Chemical Vapor Deposited Zinc Sulfide

Chemical Vapor Deposited Zinc Sulfide

John McCloy and Randal Tustison

SPIE PRESS

Bellingham, Washington USA

Library of Congress Control Number Data

McCloy, John
Chemical vapor deposited zinc sulfide / John McCloy and Randal Tustison.
p.; cm.
Includes bibliographical references and index.
ISBN 978-0-8194-9589-1
1. Chemical vapor deposition. 2. Zinc sulfide. 3. Chemical processes–infrared materials. I. Title.
TP1750.W55 2013
542–dc23

2013932605

Published by

SPIE—The International Society for Optical Engineering
P.O. Box 10
Bellingham, Washington 98227-0010 USA
Phone: +1 360 676 3290
Fax: +1 360 647 1445
Email: spie@spie.org
Web: http://spie.org

Printed in the United States of America.
First printing

Contents

Preface

Zinc sulfide (ZnS) has shown unequaled utility for infrared windows that require a combination of long-wavelength infrared (8–12 μm) transparency, mechanical durability, and elevated temperature performance. Its unique set of properties extends its usefulness to electroluminescent phosphors, optical thin films used for filters and antireflection (AR) coatings, as well as various other opto-electronic applications. High-optical-quality, chemical vapor deposited ZnS windows several millimeters thick transmit visible light and so have received attention as candidates for multi-spectral windows.

Naturally occurring zinc sulfide is well known as the primary ore of zinc. The common names for the cubic form of ZnS all come from its superficial resemblance to galena (lead sulfide, PbS), but ZnS does not yield any metal when smelted. It was therefore called "blende" or "zincblende" (from the German *blenden*, "to deceive" or "to blind"), or "sphalerite" [from the Greek σφαλερόζ (*sphaleros*), "deceptive" or "treacherous."][1] A special white, transparent, or colorless variety of sphalerite from Franklin, New Jersey, and Nordmark, Sweden, is called cleiophane, which is nearly pure ZnS with only traces of cadmium. Mineral sphalerite tends to have a large component of iron and manganese, and some specimens are very black, so-called "black jack." Mineral cleiophane and sphalerite exhibit different-colored fluorescence under short-wavelength and long-wavelength ultraviolet light, and are of interest to the mineral collector. Wurtzite is a less common hexagonal form of ZnS, named after the French chemist Charles-Adolphe Wurtz (1817–1884) by C. Friedel when it was first identified from a Bolivian silver mine. Mineral hexagonal zinc sulfide containing significant amounts of cadmium is known as pribramite. Hexagonal zinc oxysulfide has been called voltzite or voltzine, though these terms have been used to describe a lead oxysulfide as well.

Bulk ZnS for infrared windows is traditionally manufactured by chemical vapor deposition (CVD) in large reactors. Deposition temperature and mole fractions of the reactants, H_2S gas and Zn vapor, have a large influence on

[1] Mellor, J.W., "Zinc and Cadmium Sulphides," in *A Comprehensive Treatise on Inorganic and Theoretical Chemistry*, 586–612, Longmans, Green, and Co., London (1956).

visible scatter and absorption. These effects have been ascribed to electronic defects in the bandgap, hexagonal phase ZnS, and residual porosity, but the exact mechanisms have never been adequately explained.

A multispectral form of ZnS can be created by taking traditionally grown polycrystalline CVD ZnS, which is visibly yellow and opaque, and subjecting it to a post-deposition heat treatment under pressure. The heat and pressure result in recrystallization of the CVD ZnS, large grain growth, and a visibly clear and colorless product. The kinetics of this post-process, as well as the dependence on the platinum foil that typically encases the ZnS during heat treatment, remain poorly understood. It is known that CVD materials grown under different conditions do not behave identically when subsequently heat treated.

The purpose of this book is to review the physical properties of CVD ZnS and their relationship to the chemical vapor deposition process that produced them. We begin with the physics and chemistry of ZnS itself, including its many polytypes. This establishes a basis for understanding the defect structure and how it influences observed properties. Attention is then turned to the CVD process and the resulting forms of ZnS with properties that vary widely with processing conditions. To understand these variations, an in-depth look at the material microstructure follows, including the effects of post-deposition heat treatments.

For optical applications, the optical transmittance is of primary importance. ZnS intrinsically exhibits very broadband transparency beginning in the ultraviolet and extending through the infrared. This intrinsic transparency, coupled with modest mechanical durability, makes it unique among available infrared window materials. CVD ZnS optical properties are discussed, including the effects on these optical properties of post-deposition heat treatment, with comments on mechanisms for transparency improvements.

Finally, because the CVD process itself is central to the development of this material, a brief history of this process is presented, beginning with its use in the 19^{th} century as a coating technology. The evolution of CVD as a bulk-materials process came later, and only by the mid-twentieth century was it beginning to be utilized to produce CVD-formed products (most notably pyrolytic graphite). This development was an important milestone, as it put in place the process technology that was critical to the subsequent development of CVD ZnS. We offer this information as a historical note to explain the success of the CVD ZnS process as well as subsequent improvements in the process, including post-deposition heat treatments, but will not focus explicitly on the CVD process technology used to produce ZnS commercially today.

John McCloy
Randal Tustison
March 2013

List of Figures

List of Tables

Acknowledgments

We would like to thank the University of Arizona, particularly Prof. Donald Uhlmann, for providing the opportunity to gather much of the material contained in this book in preparation of a doctoral thesis (McCloy, 2008), and Raytheon Company for allowing and encouraging its publication. Of course, this book would not be possible without the many contributions from our current and former colleagues and their work on this subject. In particular we have benefited from discussions with Barney DiBenedetto and Chuck Willingham, both of whom were instrumental in the development of CVD ZnS, as well as the late Jim Pappis who was a mentor and friend to many of us. This text also benefitted from conversations with Stan Waugh, Tony Capriulo, and Andre Morrisette, as well as access to Raytheon Company archival material in reconstructing the development of CVD ZnS at Raytheon. Many colleagues at Raytheon and elsewhere have assisted us over the years in collecting the data presented herein, and they are too numerous to list here.

The authors would also like to acknowledge the reviewers of the manuscript, whose thorough reading and insightful comments added to this text. We also thank the editors from SPIE Press, especially Scott McNeill, who turned our manuscript into this book. Any remaining errors are ours, and we encourage the finding of these to be brought to our attention at jsmccloy@alum.mit.edu for correction.

Finally and most importantly, we thank our families for their support during the preparation of this book, especially our wives, Kay Tustison and Christy McCloy, for their patience and encouragement. Much of what we do would not be possible otherwise.

Chapter 1
Physics and Chemistry of ZnS

This chapter discusses the background of the relevant physics and chemistry of ZnS. The crystallography of ZnS is reviewed first, including details on its polytypes and the cubic-to-hexagonal phase transformation; then the basic electronic and vibrational structures are reviewed, including the electronic band structure and the infrared and Raman active phonon modes. The importance of defects in ZnS is discussed, including native defects as well as oxygen, hydrogen, and transition metal inclusions.

1.1 Crystallography

Zinc sulfide (ZnS) occurs naturally in the common mineral sphalerite, though the ore form typically contains a large amount of iron, manganese, or cadmium impurities. Zinc sulfide, whose phase diagram can be found in Ref. 1, occurs in two polymorph crystal structures.[2] The first is sphalerite (structure 3C or β face-centered cubic phase), also known as zincblende, which is the isotropic cubic structure and the most important structure for optical materials. The second is wurtzite (structure 2H or α hexagonal close-packed phase), which is the anisotropic hexagonal structure and the high-temperature form. Wurtzite single crystals can be formed by quenching from high temperatures above 1020 °C, though they frequently have a large volume fraction of stacking faults. Rhombohedral phases have also been reported but are most common as higher-period polytypes.[3,4] Two other forms of the zinc sulfide structure exist only under high pressure. The rocksalt structure forms from sphalerite or wurtzite at pressures of 12–65 GPa,[5,6] which at higher pressures forms a distorted orthorhombic structure.[7]

Bonding in zinc sulfide can be described as partially covalent and partially ionic. The radius ratios of the two ions is 0.402 for coordination number (CN)=6 (denoted as VI in parentheses) (Zn^{2+}(VI)/S^{2-}(VI) = 0.74 Å/1.84 Å) or 0.326 (Zn^{2+}(IV)/S^{2-}(VI) = 0.60 Å/1.84 Å) when Zn is CN=4 (denoted as IV in parentheses). These values are intermediate between the geometry-limiting configurations described by Pauling for octahedral coordination (CN=6;

ratio = 0.414) and tetrahedral coordination (CN=4; ratio = 0.225) in a strictly ionic solid.[8] The high polarizing power of Zn^{2+} and the polarizability of S^{2-} leads to the ionic character of the bonding. However, ZnS is considerably covalent, and its bonding can be, too.[9] The Madelung constant describing the ratio of Coulomb energy of the Zn-S ion pair in a lattice to that of the isolated pair at the same separation is 1.63806 for sphalerite and 1.64132 for wurtzite.[8]

The phase transition requires rearrangement of ions in the lattice; however, the ions must have sufficient mobility to rearrange. This can occur at higher or lower temperatures than are normally stated as the thermodynamic transition temperatures.[10] The low-temperature cubic phase invariably contains some domains of hexagonal material. Deformed sphalerite specimens with high dislocation density transform to wurtzite at higher temperatures when reheated due to reduced ion mobility. At temperatures of 1020 °C and above, the ions have vibrational energy sufficient to rearrange the whole crystal when it is not overly disordered. In other words, sphalerite might be able to thermodynamically transform to wurtzite at lower temperatures locally, but kinetically the process is relatively slow until approximately 1000 °C, where there is sufficient thermal energy for rapid rearrangement.

1.1.1 Stoichiometry and oxygen impurity

Scott and Barnes[11] have claimed that the fugacity of oxygen is not a controlling factor in sphalerite–wurtzite equilibrium, at least below 900 °C, but rather the fugacity of sulfur. Wurtzite on average is said to be sulfur deficient (i.e., zinc rich) relative to sphalerite and its defects are sulfur vacancies, whereas sphalerite is relatively sulfur rich (i.e., zinc deficient) and its defects are zinc vacancies, with overall nonstoichiometry estimated at 0.9 atomic percent (at. %). Whereas in pure stoichiometric ZnS the cubic-to-hexagonal transition is said to occur at 1020 °C, it has been reported that wurtzite can be formed at temperatures as low as 200 °C in a sulfur-deficient environment, while sphalerite persists to temperatures above 1240 °C in a zinc-deficient environment. Other sources cite the extent of the off-stoichiometry or width of the "line compound" in chalcogenides to be 0.01–0.0001 at. %.[12] Yet another source states that the maximum amount of excess sulfur in ZnS is 0.035 at. % ($8.7 \times 10^{18}/cm^3$) but only approximately 0.0035 at. % ($8.7 \times 10^{17}/cm^3$) for excess zinc.[13] Of course, these small fractions of off-stoichiometry are stated for thermodynamic equilibrium. Many samples in the literature whose stoichiometry has been reported, such as those made by chemical vapor deposition, were clearly not in chemical equilibrium when they were assessed.

It has been argued that the presence of substitutional oxygen in sulfur sites leads to low-temperature stabilization of the wurtzite structure in ZnS.[11] This is not surprising because the stable form of ZnO at low temperature is wurtzite. The solubility of oxygen in wurtzite ZnS is said to be 0.6 at. %[14] and

only 0.4 at. % in sphalerite.[15] As expected, these numbers differ somewhat between authors and studies.[16] The effect of adding oxygen to wurtzite ZnS is to shrink the lattice in both the *a*-axis and the *c*-axis directions,[13] and to reduce the energy gap.[17] Dissolved oxygen is said to stabilize the hexagonal polytypes of ZnS by deforming the sphalerite lattice (which is predominantly covalently bonded) and adding an additional degree of ionicity from the ZnO. Adding oxygen to sphalerite, on the other hand, increases the interplanar distances between the closest packed planes [i.e., the (00.1) *c*-axis in wurtzite, which corresponds to the (111) axis in sphalerite].

Kroeger and Dikhoff[14] have pointed out that oxygen acts as a reducing agent for ZnS because it tends to form SO_2, leaving excess Zn in the ZnS. Similarly, sulfur acts as a reducing agent for ZnO. Therefore, as long as both sulfur and oxygen ions are present with zinc, any ZnS and ZnO will remain reduced (i.e., zinc rich). Stoichiometric compounds of ZnS or ZnO are only obtainable after prolonged treatment with sulfur or oxygen vapor, respectively, in order to remove the other phase.

1.1.2 Detailed crystallography and lattice parameter

Sphalerite does not have a center of symmetry or inversion. Thus the orientations along <111> directions of ZnS_4 tetrahedra are unique. This trait makes crystals planes versus polar opposites, and versus directions can have different physical and chemical properties. The ZnS layers can be considered as a network of permanent dipole moments that completely cancel each other in a perfect crystal. However, when mechanically distorted, these dipoles give rise to a potential and thus result in piezoelectricity from mechanical tension and compression.[18] Similarly, wurtzite does not have a center of symmetry, and it has a polar axis. The permanent dipole moments do not cancel as they do in sphalerite but rather result in a single, permanent polar axis along the [00.1] *c*-axis. Wurtzite is thus not only piezoelectric but also pyroelectric, developing charge and polarization due to heating and cooling of the crystal.[19]

Sphalerite and wurtzite are very similar structures. Both have tetrahedrally coordinated zinc surrounded by four sulfurs and tetrahedrally coordinated sulfurs surrounded by four zincs. These structures are often shown as tetrahedrons, the stacking of which differs between the two. The other ion occupies half of the tetrahedral sites. Both structures can be modeled as close-packed spheres, with sphalerite being face-centered cubic (FCC) and wurtzite being hexagonal close-packed (HCP). Figure 1.1 shows these structures.

Considerable variation is found in lattice parameter values, likely due to unknown amounts of oxygen and metallic impurities. However, the estimated best value for the lattice parameter of sphalerite is 5.4092 Å.[15] Many of the samples probably had unknown amounts of oxygen content, which

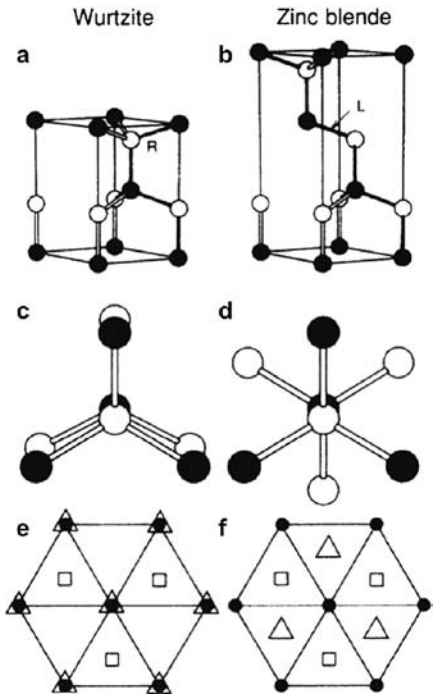

Figure 1.1 Wurtzite (left) and sphalerite (right) structures: (a) and (b) show the handedness of the interatomic bond; (c) and (d) show the "eclipsed" versus "staggered" dihedral conformations; and (e) and (f) show the layer stacking along (111) [Reprinted with permission from Yeh, C.-Y., Z. W. Lu, S. Froyen, and A. Zunger, "Zinc-blende & wurtzite polytypism in semiconductors," *Phys. Rev. B* **46**(16), 10086 (1992). Copyright 1992 by the American Physical Society.]

considerably shrinks the lattice parameter in a roughly linear fashion (Vegard's law), according to Skinner and Barton.[15] However, Chechetkina *et al.*[20] found a considerable deviation from Vegard's law in the solubility of oxygen in wurtzite ZnS.

Impurity additions of Fe, Cd, and Mn (commonly present in mineral specimens) result in additional uncertainty in measured lattice constants. A relation for estimating the lattice parameter of ZnS as a function of impurity content of FeS, CdS, MnS, CoS, ZnSe, and ZnO mole percent is shown in Barton.[21] A relation for estimating the lattice constant of ZnS based only on ZnO is shown in Morozova.[13] The lattice parameters of various natural sphalerites are reviewed in Smith.[2]

It should be recalled that Skinner and Barton[15] state the lattice parameter of cubic ZnS free of oxygen to be 5.4093 Å. Various other values are presented in the literature (see Table 1.1), which can probably be accounted for by undetermined concentrations of oxygen and other impurities. Barton and

Table 1.1 ZnS lattice parameters.

	***a* (Angstroms)**	***c* (Angstroms)**	***c/a***	**Reference, Notes**
Sphalerite $\alpha = \beta = \gamma =$ 90 deg	5.42, 5.406, 5.4109	N/A	N/A	Sharma [1]
	5.41 (*ab initio* calc.)	N/A	N/A	Wright [106]
	5.4093	N/A	N/A	Skinner [15]
	5.4050 ± 0.0030			CVD ZnS [107]
Wurtzite $\alpha = \beta = 90$ deg; $\gamma = 120$ deg			= layer repeat × $\sqrt{2}/\sqrt{3} = 2 \times 0.8166 = 1.6332$; i.e., *c* axis for 4H is 4 × 1.6332 = 6.53 Å	Ideal spherical close-packing of anions [108]
	3.8225, 3.823, 3.8226	6.2610, 6.261, 6.2605	1.6379, 1.638, 1.6378	Sharma [1]
	3.91 (*ab initio* calc.)	6.05 (*ab initio* calc.)	1.54	Wright
	3.8232, 3.8237			Skinner [15]

Skinner[21] list the lattice parameter as a function of mole percent impurity concentration as:

$$a = 5.4093 + 0.000456 * [\mathrm{FeS}] + 0.00424 * [\mathrm{CdS}] + 0.00202 * [\mathrm{MnS}] - 0.000700 * [\mathrm{CoS}] + 0.002592 * [\mathrm{ZnSe}] - 0.003 * [\mathrm{ZnO}]. \quad (1.1)$$

Morozova *et al.*[13] prefer the value of 5.4092 Å for the unaltered lattice parameter, and similarly write:

$$a = 5.4092 - 0.008584 * [\mathrm{ZnO}]. \quad (1.2)$$

Recently, McCloy *et al.*[22] presented comparisons of lattice parameter measurements with various constitutive equations for lattice parameter as well as *ab initio* calculations examining the effect of defects on the lattice parameter.

1.1.3 Polytypes and hexagonality

Besides the two main thermodynamically stable structures of sphalerite and wurtzite, zinc sulfide tends to form a large number of stable interim phases called *polytypes*.[4] Polytypes are crystal structures formed from repeated stacking of 2D "modular layers." They represent 1D disorder compared to the parent structures. Polytypes are distinct from *polymorphs*, which have well-defined stability regions separated by first-order phase transitions. By contrast, polytypes can often exist simultaneously and intergrown in the same crystal, having very similar energy in many cases. Thermodynamically, the main difference among all of the polytypes is structural entropy. For zinc sulfide, at least 194 polytypes of the crystal have been identified in three

"families" corresponding to the space group symmetry of the structure.[23] Other important materials exhibiting polytypic structures include silicon carbide and cadmium iodide.[24] For more information on polytypes in ZnS, see Ref. 16 and the references therein.

There is no agreement in detail as to how the polytypes of ZnS form as intermediate stable or metastable phases between wurtzite and sphalerite. Whether twin faulting is due to deformation, growth, or phase transformation is still debatable, and may vary considerably with local impurities, thermodynamic conditions, and material history. However, most authors are in agreement, either explicitly or tacitly, that the 2H-to-3C phase transformation in ZnS occurs by a martensitic-type mechanism. Only one source consulted[25] claims that this transformation is reconstructive.

Reasons for formation of these periodic structures of 1D disorder arise from consideration of the close-packing of equal spheres and the three crystal systems that accommodate this. Briefly, close packing can result in cubic, hexagonal, or trigonal crystal systems.[26] Cubic systems have 4-fold plane symmetry and are usually indexed to a cubic lattice, but they can also be transformed to a hexagonal lattice. Hexagonal systems have 6-fold plane symmetry and can only be described by a hexagonal lattice. Trigonal systems have 3-fold plane symmetry and can be described by a rhombohedral or hexagonal lattice. It is obvious, then, that the common lattice is hexagonal, and it is often convenient to describe all of the structures with a hexagonal basis, as is often done for studying the x-ray reflections of polytypes.

Layer arrangement and periodicity of polytypism has typically been explained by either thermodynamic or dislocation theories.[18,27–29] Thermodynamic theories attempt to explain stable polytypes by their free energy; and, for ZnS polytypes, the energies for a large range of stacking sequences are found to be very similar.[30] Thermodynamic theories alone do not explain why one polytype and not another is formed. Dislocation theories, on the other hand, easily explain the periodic sequences of polytypes. The movement of partial dislocations and the presence of a screw dislocation can model the periodicity observed in polytypes. These structural theories, however, cannot easily explain why only a few layer sequences are commonly observed.

An explanation combining elements of both these approaches has been offered by Mardix,[23] who has worked extensively with ZnS polytypes. In this model, Shockley partial dislocations glide across the basal plane and provide the mechanism by which solid-state transformations occur between the high-temperature hexagonal (2H, wurtzite) phase and the low-temperature cubic (3C, sphalerite) phase. The presence of a screw dislocation imposes periodicity on the structures, which gives rise to repetition over distances as long as hundreds of angstroms. The driving force for moving partial dislocations is the free-energy difference between the parent and transformed structures. Stability of the hexagonal phase decreases as temperature is reduced, and

hexagonal stacking sequences are replaced with cubic ones at lower temperatures. This reduction in hexagonality has been observed to occur spontaneously at room temperature.[31] The polytype structure results from local minimization of free energy in the absence of sufficient activation energy to move to still-lower energy states. Similarly, Engel[32] has shown that, using a Monte Carlo approach, the screw dislocation performs the ordering during transformation and that without it a metastable disordered cubic phase results.

Small amounts of hexagonal phase are typical in chemical vapor deposition (CVD) zinc sulfide and have been characterized as distorted layer stacking composed of stacking faults, twin boundaries, and dislocation pileups.[33] When reheated above 500 °C, the stacking faults are mobile and tend to realign toward the more-stable cubic phase.[34,35] The main polytype reported in Russian-grown CVD ZnS is the 8H polytype, which is most prevalent on the mandrel side of the chemical vapor deposited material.[36] It has been said that twinned cubic structure in polycrystalline zinc sulfide is favored by near stoichiometric ratios of zinc to sulfur.[37]

The relationship between the 3C and 2H phases can be seen in Fig. 1.2, where the 3C <111> directions and the 2H <001> directions are the close-packed ones. Additionally, Fig. 1.3 illustrates a 10H polytype, with the stacking sequence showing the relative fraction of hexagonality.

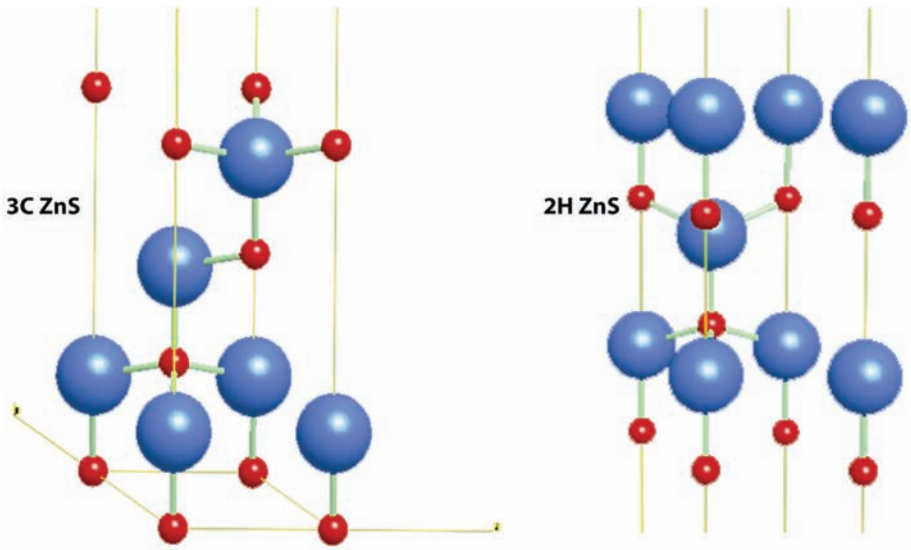

Figure 1.2 Unit cells of (left) 3C ZnS (sphalerite) and (right) 2H ZnS (wurtzite) shown with the vertical direction being the stacking direction (*c* axis of an equivalent hexagonal basis cell). The small atoms are Zn, and the large atoms are S.

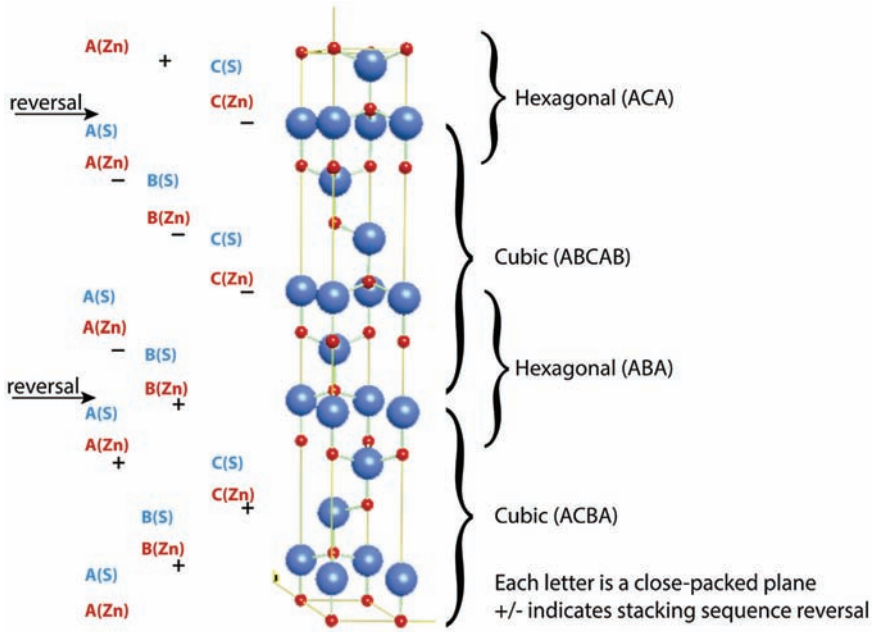

Figure 1.3 Polytype 10 H with 20% hexagonality. Vertical axis is *c* axis, which is $an\sqrt{2/3}$, where *n* is 10 in this case, and *a* is the lattice parameter in the other axis. The *c*-axis length is generally the same, with *n* varying with the repeat unit. The "+" indicates "clockwise" A→B→C→A, whereas the "−" indicates counterclockwise sequence C→B→A→C. The stacking direction is along the axis of the figure (up and down) and is the s[111] or w[00.1] *c* axis.

Bansagi *et al.*[38] and Xue and Raj[39] have suggested a simple measure of the degree of hexagonality in polycrystalline ZnS powders and hot-pressed compacts. The procedure essentially involves taking ratios of characteristic peaks in the wurtzite and sphalerite x-ray diffraction (XRD) spectra. The relative molar fraction γ of the hexagonal α phase to the cubic β phase is described by

$$\gamma = \frac{I_{28.53}^{\{\alpha(002)+\beta(111)\}}}{I_{28.53}^{\{\alpha(002)+\beta(111)\}} + I_{26.91}^{\alpha(100)}}, \tag{1.3}$$

where the subscripts are 2θ angles, and the superscripts are the characteristic planes because the $\alpha(20.0)$ and the $\beta(111)$ overlap at $2\theta = 28.53$ deg. From this it can be shown[40] that the mole fraction of the hexagonal phase is given by

$$\alpha = 1.84(1 - \gamma), \tag{1.4}$$

where the constant is determined for the value of γ when there is no cubic phase ($\beta = 0$) from standard powder-diffraction patterns. Hexagonality γ has been determined for a variety of commercial and research grades of ZnS, and has been shown to be a good indicator of relative visible transmittance.[41,42]

1.1.4 Phase transformation and twinning

A displacive (martensitic) transformation has no structural change in the first coordination sphere, no bonds are broken, and it requires no diffusion.[43] The reduction in free energy in moving from the high-temperature phase to the low-temperature phase is accounted for by changes in the second and higher coordination sphere, resulting in a denser structure with lower specific volume. Transformations of this type usually result in twinning within the martensite phase. Commonly encountered martensitic transformations in ceramics include cubic-to-tetragonal $BaTiO_3$ and tetragonal-to-monoclinic ZrO_2.

Martensitic phase transformations can be driven by two different forces.[44] Like all phase transformations, the reduction of bulk free energy per unit volume as the parent phase transforms is the primary driving force. However, because the new phase induces a shape change, there are shear and dilational stress terms in the driving force as well. Therefore, martensitic transformations can be induced by applied stress, as is seen with ZnS.[45] Stated another way, a martensitic transformation can be considered a spontaneous plastic deformation (i.e., shape change) in response to a bulk free energy change and/or an applied mechanical force.

Because it becomes critical in CVD ZnS processing, the effect of mechanical stresses on the phase transformation of ZnS is further considered. Many have argued that the transformation to a twinned sphalerite structure is accomplished by deformation twinning, either due to mechanical stress or to local thermal strains during growth.[46,47] This transformation has been recently demonstrated on wurtzite nanobelts, which begin taking on the sphalerite phase at pressures of 6.8 GPa and are converted completely to the cubic phase at 11.4 GPa, as shown by x-ray diffraction.[48]

Deformation twinning without any other mechanism has been demonstrated in sphalerite crystals using mechanical indentation with translational shear of 0.4084 times the lattice parameter, with the twin plane, the shear plane, and the shear direction.[49] Twinning sets in about the same fraction of the melting point as did slip. Some theories of transformation require a recrystallization and dislocation motion involving ordering of the crystal through dislocation glide at high temperature.[47] This passage of dislocations and its effect on the transformation of the 2H to the 3C phase has been observed directly.[29]

Deformation faults were shown to nucleate the 2H-to-3C phase transformation at low temperatures (400–750 °C), resulting in a twinned cubic crystal with regions of perfect cubic order of sizes corresponding to initial fault separation distance.[18] If few layers exist between faults, cubic regions grow together to form large domains. If more layers intervene, cubic regions either grow together to form "microtwins" at twin boundaries if the orientation is correct or else they are separated by a thin hexagonal lamella or fault. This microtwinning has been said to give rise to "false hexagonality" in x-ray diffraction studies.[45]

In a few cases it has been observed that application of pressure alone can perfect the cubic crystal, removing twin boundaries and stacking faults. In one case, the transformation was shown to be permanent due to plastic deformation by the movement of partial dislocations with Burgers vector.[45] In another case the effect on stacking faults was elastic and reversible with application of uniaxial pressure.[50] It has also been observed that crushing (used to prepare samples for powder x-ray diffraction) or even sieving through a fine metal screen has the effect of reducing the amount of hexagonal phase in a sample.[51]

Other observations of twinned sphalerite bear mention. It is not surprising that twinning on ZnS sphalerite planes is so common because the stacking fault energy is <6 mJ/m^2 (or <5 meV/atom), considerably smaller than for any other II-VI or III-VI sphalerite structure compound.[52] Twins in mineral ZnS have been observed in TEM to vary from a few angstroms to 100 nm in width and are organized into "blocks" where the slip planes meet with other slip planes.[47] The study of synthetic wurtzite nanobelts has resulted in an assessment of two ways of converting wurtzite to sphalerite: one by the transformation of three layers of wurtzite into a twinned cubic structure, the other involving the transformation of four layers of wurtzite resulting in a stacking fault.[48]

The effect of impurities on twinning in sphalerite has recently been considered in detail. The chemistry of twin boundaries of sphalerite crystals from Kosovo was studied using TEM, electron energy loss spectroscopy (EELS), and energy-dispersive spectroscopy (EDS).[53] Twinning was observed at regular intervals ranging from a few nanometers to several millimeters, which is said to be due to growth faults because the crystals are tabular. Using difference spectra to differentiate the small signal of the boundary from that of the surrounding grains, it was found that the twin boundaries were preferentially depleted of sulfur and enriched in zinc, oxygen, manganese, iron, and copper. The depletion of sulfur at the twin boundary along with enrichment in oxygen is consistent with the tendency of hexagonal stacking layers (i.e., the local twin boundary) to form under these conditions.[11]

Electronically, twins can have unique behavior. The stacking fault (twin) layer is effectively hexagonal wurtzite. Because hexagonal ZnS has a larger electronic bandgap than cubic ZnS, the cubic region separated by a stacking fault becomes a quantum well for electrons.[54] Additionally, because wurtzite is piezoelectric and polar, a static charge will build up on the stacking fault with a sign reversal between the interior and the surface of the fault. Thus the semiconductor nature of ZnS combined with simultaneously occurring structures results in what can only be defined as a semiconductor hetero-structure with all of the associated band structure implications. It is to these matters of electronic structure that we now turn.

1.2 Electronic and Vibrational Structure

1.2.1 Electronic structure

Zinc sulfide is a direct bandgap II-VI semiconductor with a room temperature bandgap of about 3.8 eV. The band structure of the hexagonal phase can be considered a perturbation of the cubic crystal field. The reduction in symmetry in the hexagonal structure results in additional valence and conduction bands due to the removal of degeneracy (see Fig. 1.4).

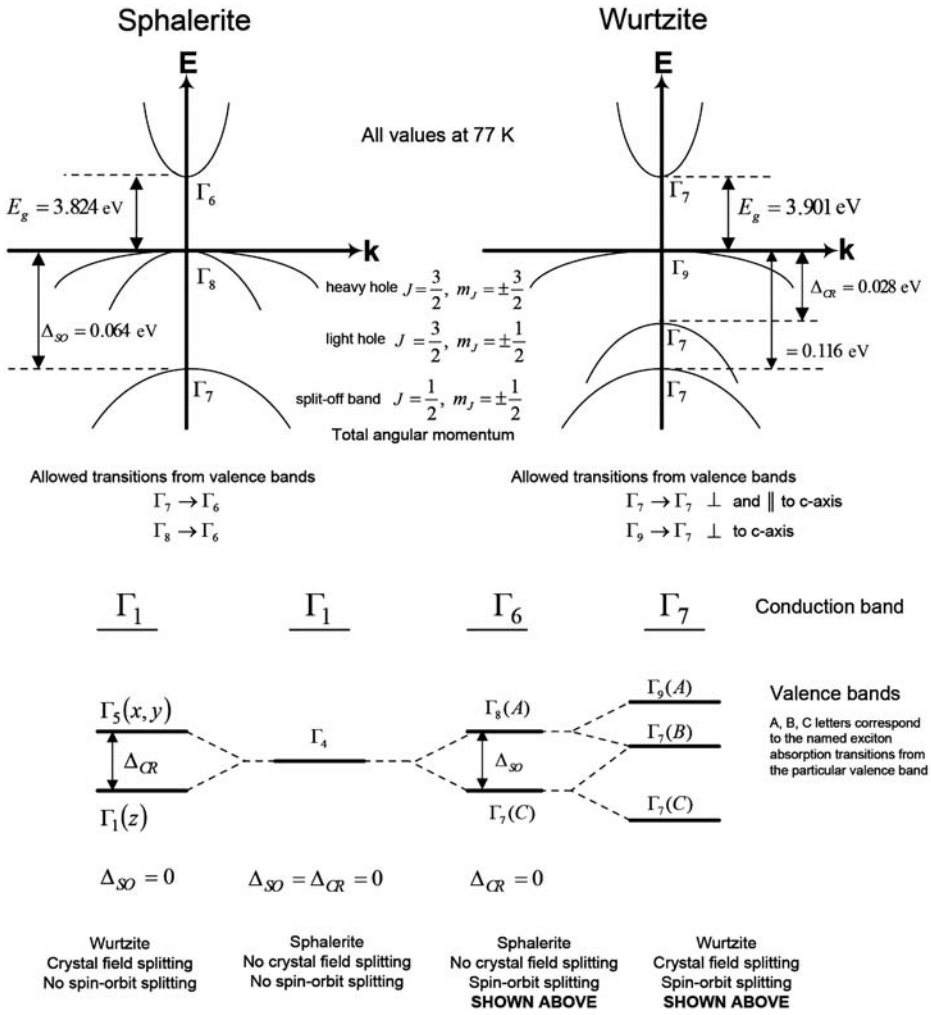

Figure 1.4 Band structure of sphalerite and wurtzite ZnS at zone center; the above shows the crystal field splitting and spin-orbit splitting of the bands in wurtzite and sphalerite, after Segall[102] and Birman.[103] Note that *J* refers to the total angular momentum of the spin-orbit coupling. Values for the valence band splitting and bandgap are from Morozova[13] and are stated at 77 K.

Intrinsic ZnS has an electrical resistivity of 10^{14} ohm-cm,[55] and at very high resistivities (above ~10^{10} ohm-cm) ZnS behaves as an insulator. However, it can be n-type doped with group-III elements such as aluminum and gallium to provide resistivities as low as 10^2 ohm-cm.[56] The latter method has been investigated for the production of blue LEDs of the metal-insulator-semiconductor (MIS) type.[55] The luminescent properties of zinc sulfide are highly dependent on controlled doping and removal of impurities.

The band structure of the two forms of ZnS and the corresponding density of states as calculated by the *ab initio* quantum-mechanical Vienna Ab initio Simulation Package (VASP) are shown in Fig. 1.5. The density of states shown can also be understood in the context of a linear combination of atomic orbitals (LCAO) model. The lowest valence band is composed primarily of the S-3*s* electrons, the middle valance bands have primarily Zn-3*d* character, and the upper valance bands have S-3*p* character. Conduction bands are derived from the Zn-4*s* electrons. Comparisons to other calculations from the literature are shown for sphalerite (Fig. 1.6) and wurtzite (Fig. 1.7).

The difference in band structures between sphalerite and wurtzite can be appreciated by considering the two types of valence band splitting. Spin-orbit splitting in sphalerite results in a lower energy split-off band and two hole

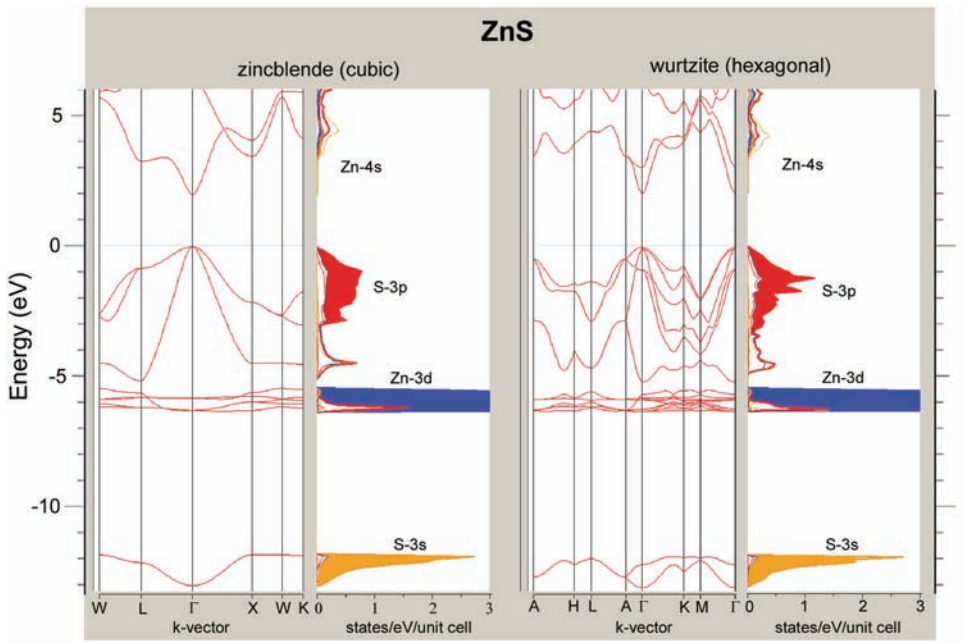

Figure 1.5 Energy band structure and density of states for sphalerite and wurtzite ZnS, as calculated by MedeA VASP using the generalized gradient approximation (GGA), which always underestimates the bandgap. Calculated GGA bandgap for sphalerite/zincblende is 2.01 eV, and for wurtzite is 2.07 eV.

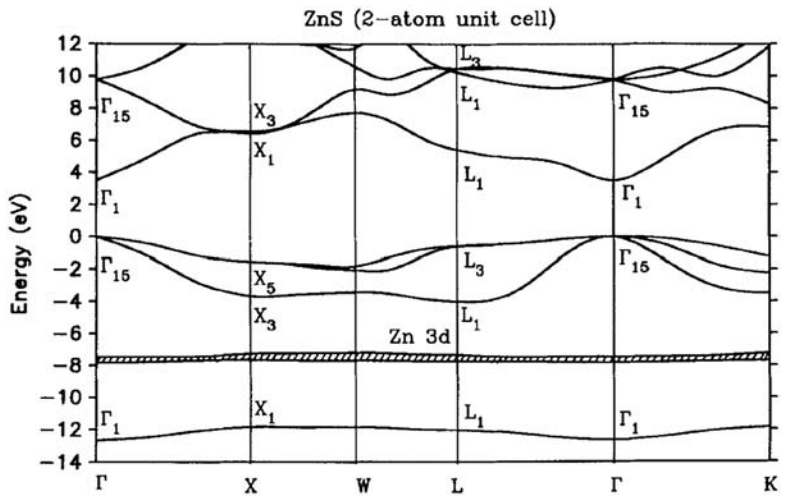

Figure 1.6 Cubic ZnS by LCAO method (image from Marshall[104] used with permission; copyright 1992 John Wiley & Sons).

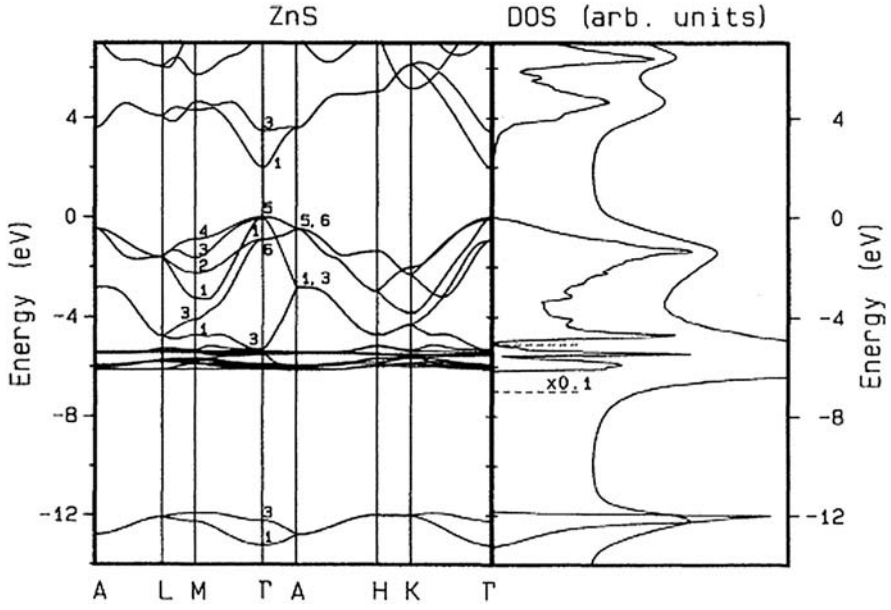

Figure 1.7 Hexagonal ZnS by *ab inito* local density approximation (image from Schroer[105] used with permission; copyright 1993 American Physical Society).

bands (light hole and heavy hole) that are degenerate at the gamma point in the Brillouin zone. Crystal-field splitting removes the degeneracy in the hole bands and results in three valence bands. A schematic of the splitting and its effect on the character of the bands is shown in Fig. 1.4 along with the

simplified band structures around the gamma point, the total angular momenta, and the irreducible representations of the symmetry.

1.2.2 Vibrational structure

The *ab initio* computed phonon density of states and phonon dispersion (as shown for cubic ZnS in Fig. 1.8) agrees fairly well with that derived by neutron diffraction (Fig. 1.9).[57] The computations were done using the MedeA platform with VASP and PHONON packages.

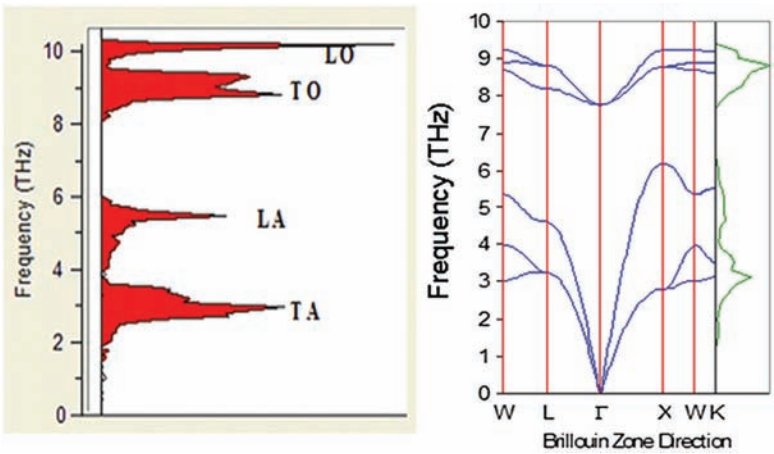

Figure 1.8 Phonon density of states for ZnS and calculated dispersion.

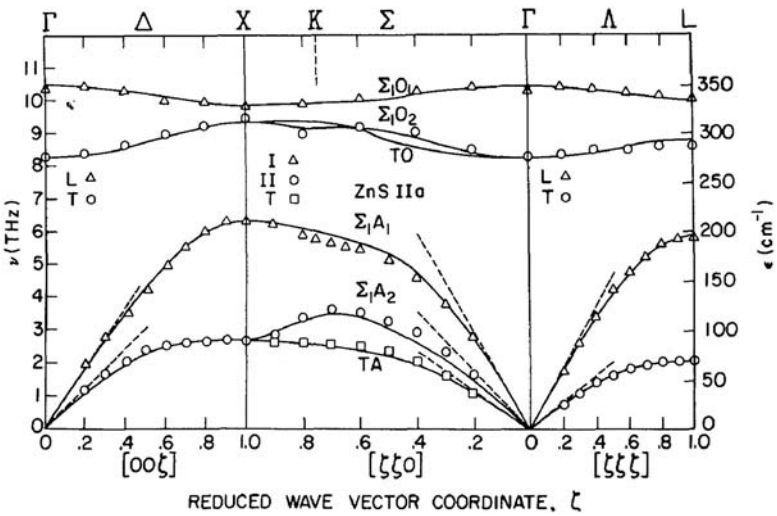

Figure 1.9 10-parameter valence-shell phonon model based on neutron diffraction data for ZnS (image from Vagelatos[57] used with permission; copyright 1974 American Institute of Physics).

The infrared absorption spectrum of CVD ZnS has been investigated in detail due to its usefulness as an infrared window in the 8–14-μm-wavelength atmospheric transparency region. Early in its development as a window, the absorption coefficient was measured by laser calorimetry at available wavelengths (2.7, 3.8, 5.25, 9.27, and 10.6 μm) and also deduced from emittance measurements (8, 9, and 10 μm).[58] More recently, clear and colorless grade (HIPed CVD ZnS) has been measured at Johns Hopkins Applied Physics Laboratory by broadband Fourier transform infrared (FTIR) spectrometry and laser transmissometry (at 0.633, 3.39, and 10.6 μm) up to 500 °C.[59] A corresponding semiempirical, multi-phonon absorption model has been derived in Hahn *et al.*[60] Hemispherical total emittance versus temperature and normal spectral emittance versus wavelength is compiled in Touloukian,[61] clearly illustrating the Restrahlen band or longitudinal optical phonon resonance around 30 μm.

The Brillouin-zone critical-point phonons for ZnS have been reviewed. Selection rules in sphalerite structures have been elicited using group theory.[62,63] For phonon assignment in Raman and infrared absorption spectra, it has become common to consider "characteristic" zone-edge phonons rather than critical-point phonons. This treatment assumes that for processes involving ≥ 3 phonons, selection rules (determining symmetry points for allowed transitions) can be ignored. Assignments of spectral features are then simplified as sums and differences of the characteristic phonons.[64] For ZnS, these characteristic zone-edge phonons are longitudinal optical (LO) 330 cm^{-1}, transverse optical (LO) 295 cm^{-1}, longitudinal acoustic (LA) 193 cm^{-1}, and transverse acoustic (TA) 83 cm^{-1}. These characteristic phonons have been used for calculating the higher-order phonon frequencies observed in the infrared absorption edge of ZnS.[65] Further details on the phonons and absorption coefficient in ZnS are found in the appendix on engineering properties.

The wurtzite phonon structure has been probed by absorption spectroscopy from 350–775 cm^{-1} at room temperature, and the features assigned to sum and difference combinations of two and three characteristic phonons.[66] Hexagonal and cubic Raman spectra have been compared, showing identical LO phonon frequency (351 cm^{-1}) for the two structures and only slightly different transverse optical (TO) frequency (276 cm^{-1} for cubic versus 273 cm^{-1} for hexagonal).[67,68]

The sphalerite phonon structure for a single-crystal sample has been probed by polarization-controlled Raman spectroscopy using both 488-nm and 514.5-nm excitation, and the resulting transition selection rules are discussed.[69] More recently, the Raman scattering of cubic ZnS was extended to isotopic compositions of Zn and S, and probed as a function of temperature and pressure at two excitation wavelengths, namely 514.5 nm and 647.1 nm.[70] It was found that the line width of the TO phonon varied strongly with isotopic mass and pressure. The intensity of the TO line, which is much

weaker than the LO line, is lost to the background at 300 K when excited with the red (647.1 nm) laser due to destructive interference with background phonons. In ZnS nanoparticles, additional transitions ascribable to surface modes of the particles have been reported.[71]

1.3 Important Defects and Chemistry

1.3.1 Native defects

Luminescence-based analytical techniques are very sensitive to defects and so can provide experimental evidence of electronic effects in both pure and doped ZnS. There are several kinds of important electronic defects in semiconductors such as ZnS. Native defects in ZnS include zinc vacancies (V_{Zn}) and interstitials (Zn_i), sulfur vacancies (V_S) and interstitials (S_i), and antisites such as a zinc atom in a sulfur lattice site (Zn_S). Isoelectronic defects are substitutional defects with the same valence as the atom being replaced. An important isoelectronic impurity defect that is inevitably present in ZnS is oxygen on a sulfur lattice site (O_S).

II-VI and III-V semiconductors almost invariably form off-stoichiometry, causing electronic defects in the energy gap.[72] As stated previously, the estimated extent of the off-stoichiometry in ZnS, at least in natural sphalerites and wurtzites, is 0.9 at. %.[11] In materials with a Zn-rich stoichiometry, having more Zn^{2+} ions and fewer S^{2-} ions (and hence empty sulfur lattice sites), sulfur vacancies ($V_S^{\cdot\cdot}$) or zinc interstitials ($Zn_i^{\cdot\cdot}$) will create donor levels close to the conduction band. Similarly, materials with S-rich stoichiometry will have zinc vacancies (V_{Zn}'') or sulfur interstitials (S_i'') that will act as acceptors with defect levels close to the valence band. The tendency toward one or the other of these conditions will depend on the partial pressures of the two components. Equilibrium concentrations of the intrinsic defects will depend on the temperature (i.e., of deposition or subsequent annealing) and activation energy of formation. Growth at high sulfur vapor pressure favors V_{Zn}' and $Zn_i^{\cdot\cdot}$, whereas growth at large excess zinc vapor pressure favors V_{Zn}'', Zn_i^x, V_S^x, and $Zn_i^{\cdot\cdot}$ native defects.

ZnS has a thermodynamic tendency to be Zn-rich and thus be an n-type semiconductor due to the relative magnitude of the reaction constants of zinc and sulfur condensation and evaporation.[73] This has been determined by assuming Schottky defects and intrinsic defects, and solving for the equilibrium concentration of charged defects versus partial pressures of zinc and sulfur. The driving force for Zn richness due to electronic defect equilibrium is in addition to that already mentioned, relating to the chemical tendency for Zn richness due to the presence of oxygen. There has been considerable disagreement in the literature as to which point defects are responsible for the n-type conductivity in ZnS, depending on whether the assumptions emphasize Schottky or Frenkel disorder.

Some argue that the intrinsic donors come from primarily interstitial Zn atoms and a relatively smaller number of sulfur vacancies.[74] Sulfur vacancy sites, when available, tend to be filled by oxygen, especially after heat treatment. The presence of interstitial zinc is supported by self-diffusion experiments and electrical conductivity experiments from annealing in zinc vapor.[13] Researchers who focus on the interstitial zinc defect tend to see Frenkel disorder as particularly important.

The presence of zinc vacancies, even in zinc-rich sphalerites, is supported by emissions from ZnS annealed in sulfur vapor.[13] The only vacancy point defect with optical transitions in the visible part of the spectrum is V_{Zn}', which has a transition from the conduction band to the acceptor level in the blue (~ 2.7 eV or 460–470 nm at 77 K). Transitions to and from $V_S^{\cdot\cdot}$, $V_S^{\cdot}$, and V_{Zn}'' all lie in the infrared.[13] IR emission bands and their assignments include 820–850 nm ($V_S^{\cdot\cdot}$, $V_S^{\cdot}$, O_i), 950–1100 nm (V_{Zn}'', V_{Zn}'), 1200–1300 nm ($V_S^{\cdot\cdot}$, $V_S^{\cdot}$), 1400–1600 nm (V_{Zn}''), and 1900–2950 nm (V_{Zn}', O_i).

Others see this sulfur vacancy as the primary donor defect in ZnS. Sulfur vacancies—though considered by some to be rare in intrinsic material—are created easily with irradiation, creating the so-called "F^+ center," which is a charged sulfur vacancy ($V_S^{\cdot}$).[54,75] Equilibrium analyses considering the Schottky defect as the controlling one in ZnS show that singly charged sulfur vacancies ($V_S^{\cdot}$) are dominant.[76] High sulfur vapor pressures are therefore necessary for making stoichiometric material.

Liquid-nitrogen temperature absorption measurements in neutron-irradiated and Zn-vapor-treated ZnS have identified a number of intrinsic defect bands thought to be related to the sulfur vacancy.[77] These authors doubt the importance of a zinc interstitial because there is evidence that optical effects of zinc Frenkel pairs (i.e., Zn_i and V_{Zn}) produced by irradiation are annealed away at room temperature. Very high energy absorptions near the band edge at 3.5 eV (354.7 mm) and 3.2 eV (388.0 nm) are believed to be due to an exciton bound to a neutral donor F center (V_S^x) and an exciton bound to an ionized donor F^+ center ($V_S^{\cdot}$), respectively. Absorptions at 1.75 eV (709.4 nm) and 2.7 eV (459.8 nm) are thought to be due to hole transitions. Absorptions at 2.3 eV (539.8 nm) and 2.9 eV (428.1 nm), observed by several researchers, are thought to be due to the F^+ center ($V_S^{\cdot}$) itself. The latter absorption was observed by Lewis *et al.*[78] at 80 K for CVD ZnS, in addition to another absorption in very highly colored material at 2.5 eV (497 nm), which may be related to a zinc hydride defect. The 2.9-eV absorption was also observed at room temperature by Collins *et al.*[79] in CVD ZnS grown at very high temperatures (950 °C); the yellow color of this material was said to be due to sulfur vacancies.

Excitons are electron-hole pairs bound by Coulombic forces. Energetically, exciton levels are located just below the conduction band edge, but they exist only near the Brillouin zone center (gamma point) because the electron-hole pair motion is coupled and must conserve momentum. Excitons in ZnS

are of the Wannier type, meaning that their orbital radius (i.e., the separation distance of the electron and hole) is much greater than the lattice spacing. Excitons have a binding energy (ground-state energy) that keeps the electron and hole separated, which is related to the dielectric strength of the medium in which they are present. The binding energy of an exciton determines whether it will be observable at a given temperatures, as thermal energy greater than the binding energy will dissociate the exciton. The exciton binding energy for ZnS at room temperature is 40–41 meV for wurtzite[72,80] and ~36 meV for sphalerite.[72]

1.3.2 Oxygen impurity

Oxygen is thought to be ubiquitous in as-prepared ZnS that has not been treated by annealing in sulfur vapors. Morozova *et al.*[13] claim that oxygen is present in ZnS in concentrations greater than $10^{18}/cm^3$ but more frequently 10^{19} to $10^{20}/cm^3$. It has been suggested that substitutional solid solutions $ZnS{\cdot}O_S$ only form when the material is grown with excess zinc, as the V_S tend to be filled with oxygen to form O_S, and the Zn_i lattice distortion is compensated for by the lattice contraction due to O_S.[81] In melt-grown crystals, oxygen present in excess of the solubility limit has been shown to segregate into layers parallel to the planes that have compositional fluctuations with respect to oxygen and a $ZnO{\cdot}S$ phase.[13]

In ZnS, the conduction band can be considered as consisting of monovalent zinc ions (Zn^+) because $Zn^{2+} + e = Zn^+$.[14] A larger Zn^+ ion will distort the lattice and hence will prefer to be associated with a smaller anion such as oxygen in a sulfur site. The isoelectronic defect of oxygen can thus be thought of as an electron trap because it captures an electron due to short-range Coulomb potential from the difference in electronegativity between the sulfur and oxygen. Because isoelectronic oxygens have electrons already associated, they tend to capture holes leading to a bound exciton.[13] The character of the luminescence for an isoelectronic center is very different than that for donor–acceptor pairs because the latter involve long-range Coulombic forces.

Studies of the effects of high pressure on cathodoluminescent spectra have lent insight into changes that occur during hot isostatic pressing of CVD ZnS. Diffusion of oxygen, which is suspected to congregate at the grain boundaries (probably in sulfur sites), is much faster than interstitial zinc diffusion at high pressures.[82] Changes in emission spectra of Zn-rich CVD ZnS after pressure treatment are thought to be due to in-diffusion of oxygen and out-diffusion of interstitial zinc.[82] Undissolved oxygen that had previously accumulated at stacking faults (twin boundaries), where it was optically inactive, moves into the lattice during dislocation motion, where it creates an optically active defect center.[13]

ZnO has been known to precipitate out, both in ZnS[80] (forming ZnO·S) and in ZnSe[83] (forming ZnO·Se). Absorption spectra of these CVD samples are said to show characteristic absorption bands in the 5–7 μm range, which are often masked by the larger 6-μm absorption, currently thought to be due to Zn-H.

Because ZnS forms a solid solution with oxygen, dissolving about 1 mol% O, ZnS-O can be hard to detect and will not appear as a separated phase in x-ray diffraction.[14] There has been some debate as to whether the weak extrinsic absorption in CVD ZnS around 9.1 μm (1100 cm^{-1}) is due to ZnO,[58] Si-O,[35] or SO_3^{2-}.[84] Absorption bands in ZnSe between 850–1100 cm^{-1} have been attributed to ZnO.[83] Low-temperature deposits ($\leq$670 °C) are said to have higher [O] present. Annealing in Zn vapor increases dissolved oxygen and decreases density, whereas annealing in S vapor reduces dissolved oxygen to 10^{18} cm^{-3} but does not affect density.[13] Additionally, the ZnS-O solid solution is said to be noticeable in photoluminescence, as a red shift to the free exciton due to the bandgap shrinkage of ZnS from accommodation of oxygen.[17,82] diBenedetto *et al.* experimented with deliberate doping of CVD ZnS with oxygen, which produced colorless material with lower visible scatter than material grown using only hydrogen sulfide and zinc.[85]

1.3.3 Hydrogen impurity

The effect of hydrogen in many semiconductors has been well documented, and its amphoteric character (acting sometimes as a donor and sometimes as an acceptor) makes it particularly difficult to study.[86,87] The bulk of CVD ZnS is grown in the presence of hydrogen in some form because the primary reaction for creating ZnS gives off hydrogen:

$$Zn\ (g) + H_2S\ (g) \Rightarrow ZnS\ (s) + H_2\ (g). \tag{1.5}$$

The existence of a Zn-H type vibration at 1608 cm^{-1} (6.22 μm) was predicted based on similar hydride molecules.[88] In early CVD ZnS it was observed that there was a strong absorption band around 6 μm that was attributed to some kind of zinc hydride.[85] Later, Lewis *et al.*[78] described the hydrogen defect in detail and correlated it to forward visible scattering, color, and the presence of a sulfur vacancy. Conclusively, they measured the evolution of hydrogen from CVD ZnS upon heating using mass spectrometry, correlating the loss of hydrogen to the disappearance of the 6-μm absorption after heating. Several hydrogen-containing defects have been proposed recently for CVD ZnS, and their formation energies calculated by *ab initio*.[22]

In the earlier CVD work, hydrogen was deliberately added to a deposition run (#ZS-117), resulting in material with more visible scattering than average and a very deep 6-μm band.[85] In a complementary run (#ZS-118), the normal

process gases were supplemented with oxygen, and the material produced was colorless, had almost no 6-μm absorption, and had less scatter than average. Similar results with oxygen had been found for CVD ZnSe by the Raytheon group.

Hydrogen also seems to have other effects in ZnS, specifically with regard to the grain structure. As already indicated, it has been postulated that hydride segregates toward the grain boundaries, resulting in luminescence quenching. It has further been shown that the presence of hydrogen tends to limit the grain size in CVD ZnS.[89] In these experiments, doping with iodine prevented the incorporation of hydrogen and resulted in larger-grain material. Some work has been performed comparing the transformation of hexagonal to cubic ZnS in atmospheres of O_2, H_2S, H_2, and He.[90] The rate of transformation was shown to be influenced by defect formation, which depended on firing atmosphere, as well as bulk diffusion of S_2^- and O_2^- anions.

1.3.4 Transition metals

Various metal-impurity atoms have been said to stabilize either the cubic or hexagonal phases of ZnS, but one main effect of these metal impurities is to change the solubility of oxygen. This, in turn, has the larger effect of changing interplanar distances and stabilizing a particular crystallographic polymorph. Of course, the impurity content directly affects the lattice constant, and the relation of lattice constant to concentration of common impurities has been related by Barton and Skinner.[21] Preferential stabilization of a particular lattice requires impurity density (of any kind) $\geq$0.01 at. %.[13]

Iron and manganese are the two main impurities in mineral sphalerite. Phase diagram studies of the FeS–ZnS and MnS–ZnS systems have shown that increasing amounts of iron or manganese lower the transformation temperature for hexagonal to cubic transition.[91] Where multiple polytypes are found together in natural ZnS, they have differing concentrations of iron, and the degree of hexagonality of polytypes correlates with iron content across source localities.[92] Solid solutions of up to 16 at. % Fe substituting for Zn have shown increased lattice constant, increased hardness, and decreased infrared transmission.[93] Additions of iron, manganese, and cadmium lower the phase transition temperature to the hexagonal phase.

Additions of silver and copper in ZnS have been shown to increase the transition rate to the cubic phase.[51] The proposed mechanism is the exothermic formation of unspecified Ag and Cu sulfides in the bulk of the powder-processed phosphor compact. The energy released on precipitation of Ag–S or Cu–S provides enough energy to produce stable nuclei of the cubic phase of ZnS in wurtzite below the transformation temperature. These cubic ZnS nuclei then grow, consuming wurtzite and releasing energy as the more-stable phase at low temperature.[94] This energy from the transition serves to further nucleate cubic phase ZnS, resulting in a self-sustaining transformation

that proceeds at a rapid rate. A particular sequence of quenching from high temperature followed by annealing was found to be the most-effective means of rapid conversion to cubic phase ZnS. Another study on ZnS:Cu suggested that it is the nuclei of Cu-S and not the energy released that starts the phase transformation.[95] This only happens when heating in the presence of H_2S, whereas heating in air does not induce the transition to cubic, presumably due to the inhibiting effects of oxygen. Finally, the presence of small amounts of Cu_2S in ZnS were shown to inhibit the transformation to the hexagonal phase at high temperatures.[96]

Many of the common dopants in ZnS are transition metals that form divalent cations and substitute for Zn^{2+}. Dopant atoms are usually substitutional, though in rare cases and high doping levels they can be interstitial. Substitutional atoms that are not isoelectronic have an effective charge relative to the normal charge at the lattice site. Conventionally, these charged defects are indicated using Kroger–Vink notation.[25,43]

Zinc sulfide is a very effective host for phosphors and lasers. Much is known about the luminescence of ZnS, as it has been used as a phosphor for over one hundred years.[72] As a phosphor for cathode ray tubes, ZnS has been routinely doped with Au, Ag, and Cu. It has been shown that small amounts of these and other dopants can strongly affect the microstructure of ZnS crystals by inducing twins, polytypes, and other lattice defects.[97] ZnS doped with Ni has been used as an x-ray phosphor screen material.[98] Recently, there has been investigation of ZnS, ZnSe, and ZnTe as laser hosts doped with divalent ions of Cr, Co, Ni, and Fe.[99] Divalent manganese doped ZnS has been the primary material for direct current and alternating current electroluminescence display devices for decades.[100]

The most important kind of luminescence in ZnS is known as broadband or deep-center luminescence, where "deep" refers to the location of the defect levels as lying deep within the forbidden energy gap. The term "center" refers to the fact that these defects are usually complexes with multiple species spatially associated within a radius of second- or third-nearest neighbor in the lattice. The most commercially important ZnS phosphors use transition metal ion dopants to achieve these deep levels, though rare earths are occasionally used as well.[72] Transition-metal ion energy levels in ZnS and other II-VI semiconductor hosts have been well studied,[101] though the exact mechanisms of certain luminescence behavior has been hotly debated.

References

1. Sharma, R. C. and Y. A. Chang, "The S-Zn (Sulfur-Zinc) System," *J. Phase Equilibria* **17**(3), 261–266 (1996).
2. Smith, F. G., "Structure of zinc sulfide minerals," *Am. Mineralogist* **40**, 658–675 (1955).

3. Buck, D. C. and L. W. Strock, "Trimorphism in Zinc Sulfide," *Am. Mineralogist* **40**, 192–200 (1955).
4. Trigunayat, G. C., "A survey of the phenomenon of polytypism in crystals," *Solid State Ionics* **48**(1–2), 3–70 (1991).
5. Ves, S. et al., "Cubic ZnS under pressure: optical-absorption edge, phase transition, and calculated equation of state," *Phys. Rev. B* **42**(14), 9113–9118 (1990).
6. Jaffe, J. E., R. Pandey, and M. J. Seel, "Ab initio high-pressure structural and electronic properties of ZnS," *Phys. Rev. B* **47**(11), 6299–6303 (1993).
7. Desgreniers, S., L. Beaulieu, and I. Lepage, "Pressure-induced structural changes in ZnS," *Phys. Rev. B* **61**(13), 8726–8733 (2000).
8. Carter, C. B. and M. G. Norton, *Ceramic Materials: Science and Engineering*, Springer, New York (2007).
9. Barsoum, M. W., *Fundamentals of Ceramics*, Series in Materials Science and Engineering, Taylor & Francis, New York (1996).
10. Krongauz, V. G., S. N. Verkhovskii, V. I. Vinnikova, and M. P. Borovitova, "A Polymorphic Transition in Crystalline ZnS," *Inorg. Mater.* **13**(8), 1122–1124 (1977).
11. Scott, S. D. and H. L. Barnes, "Sphalerite–wurtzite equilibria and stoichiometry," *Geochimica and Cosmochimica Acta* **36**, 1275–1295 (1972).
12. Stevenson, D. A., "Diffusion in the Chalcogenides of Zn, Cd, and Pb," in *Atomic Diffusion in Semiconductors*, D. Shaw, 449–541, Plenum Press, London (1973).
13. Morozova, N. K., V. A. Kuznetsov, and M. V. Fok, *Sul'fid tsinka. Poluchenie i opticheskie svoistva [Zinc Sulfide: Preparation and Optical Properties]*, Nauka, Moscow (1987).
14. Kroeger, F. A. and J. A. M. Dikhoff, "The Function of Oxygen in Zinc Sulfide Phosphors," *J. Electrochem. Soc.* **99**(4), 144–154 (1952).
15. Skinner, B. J. and P. B. Barton, Jr., "The Substitution of Oxygen for Sulfur in Wurtzite and Sphalerite," *Am. Mineralogist* **45**, 612–625 (1960).
16. McCloy, J., "Properties and Processing of Chemical Vapor Deposited Zinc Sulfide," Ph.D. diss., University of Arizona (2008).
17. Morozova, N. K. and M. M. Veselkova, "Variation of the bandgap of zinc sulfide upon doping with oxygen," *J. App. Spectroscopy* **34**(6), 685–690 (1981).
18. Roth, W. L., "Crystallography," in *Physics and Chemistry of II-VI Compounds*, M. Aven, and J. S. Prener, 117–164, North-Holland, Amsterdam (1967).

19. Yacobi, B. G. B., "The nature of the pyroelectric effect of faulted ZnS," *J. Appl. Phys.* **47**(4), 1243–1247 (1976).
20. Chechetkina, E. A., Y. M. Khozhainov, S. S. Galaktionov, and A. A. Bundel, "Solubility of ZnO in ZnS (Wurtzite)," *Inorg. Mater.* **14**(8), 1086–1088 (1978).
21. Barton, P. B. Jr. and B. J. Skinner, "Sulfide Mineral Stabilities," in *Geochemistry of Hydrothermal Ore Deposits*, H. L. Barnes, 236–333, Hold, Rinehart, and Winston, Inc., New York (1967).
22. McCloy, J., W. Wolf, E. Wimmer, and B. Zelinski, "Impact of hydrogen and oxygen defects on the lattice parameter of chemical vapor deposited zinc sulfide," *J. Appl. Phys.* **113**, in press (2013).
23. Mardix, S., "Polytypism: A controlled thermodynamic phenomenon," *Phys. Rev. B* **33**(12), 8677 (1986).
24. Verma, A. R. and P. Krishna, *Polymorphism and Polytypism in Crystals*, Wiley Monographs in Crystallography, John Wiley & Sons, New York (1966).
25. Chiang, Y.-M., D. P. Birnie, and W. D. Kingery, *Physical Ceramics: Principles for Ceramic Science and Engineering*, MIT Series in Materials Science and Engineering, John Wiley & Sons, New York (1996).
26. Allen, S. M. and E. L. Thomas, *The Structure of Materials*, MIT Series in Materials Science and Engineering, John Wiley & Sons, New York (1999).
27. Sebastian, M. T. and P. Krishna, "An X-ray diffraction study of faulting in single crystals of cubic ZnS grown from the vapour phase," *Philosophical Magazine A* **49**(6), 809–821 (1984).
28. Geilikman, M. B., "Mechanisms of Polytype Stabilization During Wurtzite-Sphalerite Transition," *Phys. and Chem. of Minerals* **8**, 2–7 (1982).
29. D'Aragona, F. S., P. Delavignette, and S. Amelinckx, "Direct evidence for the mechanism of the phase transition wurtzite - sphalerite," *Physica Status Solidi (a)* **14**, K115–K118 (1966).
30. Engel, G. E. and R. J. Needs, "Total energy calculations on zinc sulphide polytypes," *J. Phys.: Condensed Matter* **2**(2), 367–376 (1990).
31. Kiflawi, I., Z. H. Kalman, and Y. Sonnenblick, "Direct observation of polytype transformations in a vapour-phase grown ZnS crystal," *J. Crystal Growth* **34**, 145–148 (1976).
32. Engel, G. E., "Simulation of polytype formation in zinc sulphide," *J. Phys.: Condensed Matter* **2**(33), 6905–6919 (1990).
33. diBenedetto, B. A., J. Pappis, and A. J. Capriulo, "Chemical Vapor Deposition of IR Materials for Reconnaissance," AFAL-TR-72-309 (1972).

34. Hill, J., K. L. Lewis, and A. Cullis, "The Defect and Band Structure of CVD-Grown Zinc Sulphide," Proc. Electrochemical Society, 6th International Conference on Chemical Vapor Deposition, 276–282 (1977).
35. Lewis, K. L. and J. Hill, "The Effect of Impurities on the Optical Properties of CVD ZnSe and ZnS," *Proc. Electrochemical Society* **79-3**, 629–631 (1979).
36. Mironov, I. A. et al., "Physico-Mechanical and Structural Properties of Polycrystalline Zinc Sulfide Obtained by Different Methods," *Sov. J. Opt. Technol.* **59**(7), 417–421 (1992).
37. Yu, H. et al., "The study of the relationship between inside defects and optical properties of CVD ZnS," *Proc. SPIE* **4231**, 224–230 (2000) [doi: 10.1117/12.402804].
38. Bansagi, T., E. A. Secco, O. K. Srivastava, and R. R. Martin, "Kinetics of hexagonal-cubic phase transformation of zinc sulfide in vacuo, in zinc vapor, and in sulfur vapor," *Can. J. Chemistry* **46**(18), 2881–2886 (1968).
39. Xue, L. A. and R. Raj, "Superplastic deformation of zinc sulfide near its transformation temperature (1020 °C)," *J. Am. Ceram. Soc.* **72**(10), 1792–1796 (1989).
40. Xue, L. A. and R. Raj, "Effect of hot-pressing temperature on the optical transmission of zinc sulfide," *Appl. Phys. Lett.*, **58**(5), 441–443 (1991).
41. McCloy, J. and R. Korenstein, "Variability in Chemical Vapor Deposited Zinc Sulfide: Assessment of Legacy and International CVD ZnS Materials," *Proc. SPIE* **7302**, 73020M (2009) [doi: 10.1117/12.819559].
42. McCloy, J., R. Korenstein, and B. Zelinski, "Effects of Temperature, Pressure, and Metal Promoter on the Recrystallized Structure and Optical Transmission of Chemical Vapor Deposited Zinc Sulfide," *J. Am. Ceram. Soc.* **92**(8), 1725–1731 (2009).
43. Kingery, W. D., H. K. Bowen, and D. R. Uhlmann, *Introduction to Ceramics*, 2nd Ed., Wiley–Interscience, New York (1976).
44. Balluffi, R. W., S. M. Allen, and W. C. Carter, *Kinetics of Materials*, Wiley–Interscience, New York (2005).
45. Kulakov, M. P. and S. Z. Shmurak, "Structural changes in ZnS crystals on account of partial dislocation movement," *Physica Status Solidi (a)* **59**, 147–153 (1980).
46. Fleet, M. E., "Structural transformations in natural ZnS," *Am. Mineralogist* **62**, 540–546 (1977).
47. Akizuki, M., "Investigation of phase transition of natural ZnS minerals by high resolution electron microscopy," *Am. Mineralogist* **66**, 1006–1012 (1981).

48. Wang, Z. et al., "Morphology-tuned wurtzite-type ZnS nanobelts," *Nature Materials* **4**, 922–927 (2005).
49. Churchman, A. T., G. A. Geach, and J. Winton, "Deformation Twinning in Materials of the A4 (Diamond) Crystal Structure," *Proc. R. Soc. London, Sect. A* **238**(1213), 194–203 (1956).
50. Omel'chenko, S. A. and M. F. Bulanyi, "Reversible changes in the structure of zinc sulfide crystals during elastic deformation," *Phys. Solid State* **39**(7), 1091 (1997).
51. Aven, M. and J. A. Parodi, "Study of the Crystalline Transformations in ZnS:Cu, ZnS:Ag, and ZnS:Cu,Al," *J. Phys. and Chem. of Solids* **13**, 56–64 (1960).
52. Takeuchi, S., K. Suzuki, and K. Maeda, "Stacking-fault energy of II-VI compounds," *Philosophical Magazine A* **50**(2), 171–178 (1984).
53. Srot, V. et al., "Stacking faults and twin boundaries in sphalerite crystals from the Trepca mines in Kosovo," *Am. Mineralogist* **88**, 1809–1816 (2003).
54. Neumark, G. F., "Defects in wide bandgap II-VI crystals," *Mater. Sci. and Eng. R: Reports* **21**(1), 1–46 (1997).
55. Suzuki, S., S. Kitagawa, H. Iwata, and Y. Sasaki, "Structure and resistivity of heat-treated polycrystalline zinc sulfide prepared by chemical vapor deposition," *J. Crystal Growth* **134**, 67–74 (1993).
56. Thomas, A. E., G. J. Russell, and J. Woods, "Preparation of Low-Resistivity Zinc Sulphide," *J. Crystal Growth* **63**, 265–275 (1983).
57. Vagelatos, N., D. Wehe, and J. S. King, "Phonon dispersion and phonon densities of states for ZnS and ZnTe," *J. Chem. Phys.* **60**(9), 3613–3618 (1974).
58. Klein, C. A. et al., "Lattice Absorption, Phonon Assignment, and Image-Spoiling Properties of CVD ZnS in the Infrared," in *Laser Induced Damage in Optical Materials (NBS Special Publication 541)*, 86–98, National Bureau of Standards, U. S. Department of Commerce, Washington, D.C. (1978).
59. Blodgett, D. W., M. E. Thomas, D. V. Hahn, and S. G. Kaplan, "Longwave infrared absorption properties of ZnS and ZnSe," *Proc. SPIE* **5078**, 137–147 (2003) [doi: 10.1117/12.487874].
60. Hahn, D. V., M. E. Thomas, and D. W. Blodgett, "Modeling of the frequency- and temperature-dependent absorption coefficient of long-wave-infrared (2–25 um) transmitting materials," *Appl. Optics* **44**(32), 6913–6920 (2005).
61. Touloukian, Y. S., Ed., *Thermophysical Properties of Matter-Thermal Radiative Properties - Nonmetallic Solids*, John Wiley & Sons, New York (1972).

62. Birman, J. L., "Theory of Infrared and Raman Processes in Crystals: Selection Rules in Diamond and Zincblende," *Phys. Rev.* **131**(4), 1489–1496 (1963).

63. Yu, P. Y. and M. Cardona, *Fundamentals of Semiconductors: Physics and Materials Properties*, 3rd Ed., Springer, Berlin (2005).

64. Bendow, B., H. G. Lipson, and S. P. Yukon, "Multiphonon absorption in highly transparent semiconducting crystals," *Phys. Rev. B* **16**(6), 2684 (1977).

65. Klein, C. A. and R. N. Donadio, "Infrared-active phonons in cubic zinc sulfide," *J. Appl. Phys.* **51**(1), 797–800 (1980).

66. Marshall, R. and S. S. Mitra, "Optically active phonon processes in CdS and ZnS," *Phys. Rev.* **134**(4A), A1019–A1025 (1964).

67. Arguello, C. A., D. L. Rousseau, and S. P. S. Porto, "First-Order Raman Effect in Wurtzite-Type Crystals," *Phys. Rev.* **181**(3), 1351 (1969).

68. Brafman, O. and S. S. Mitra, "Raman Effect in Wurtzite- and Zinc-Blende-Type ZnS Single Crystals," *Phys. Rev.* **171**(3), 931 (1968).

69. Nilsen, W. G., "Raman spectrum of cubic ZnS," *Phys. Rev.* **182**(3), 838–850 (1969).

70. Serrano, J., A. Cantarero, M. Cardona, N. Garro, R. Lauck, R. E. Tallman, T. M. Ritter, and B. A. Weinstein, "Raman scattering in beta-ZnS," *Phys. Rev. B* **69**, 014301-1–04301-11 (2004).

71. Xu, J., H. Mao, Y. Sun, and Y. Du, "Surface vibrational mode of ZnS nanoparticles," *J. Vac. Sci. Technol. B* **15**(4), 1465–1467 (1997).

72. Yen, W. M., S. Shionoya, and H. Yamamoto, Eds., *Phosphor Handbook*, 2nd Ed., Laser and Optical Science and Technology Series, CRC Press, Boca Raton, FL (2007).

73. Wiedemeier, H., "Thermodynamic Estimations of Defect Equilibria and Vacancy Concentrations in ZnS," *Zeitschrift für anorganische und allgemeine Chemie* **632**(10-11), 1717–1727 (2006).

74. Morozova, N. K. and O. N. Morozova, "Phase Diagram of Equilibrium Point Defects and Deviations from Stoichiometry in Zinc Sulfide," *Inorg. Mater.* **17**(8), 989–993 (1981).

75. Schneider, J. and A. Rauber, "Electron Spin Resonance of the F-Centre in ZnS," *Solid State Comm.* **5**, 779–781 (1967).

76. Gurvich, A. M. and R. V. Katomina, "Influence of the positions of levels of intrinsic defects on the deviations from stoichiometry and the electrical conductivity of zinc and cadmium sulfides," *Sov. Phys. Semicond.*, **5**(7), 1189–1195 (1971).

77. Matsuura, K., I. Tsurumi, and F. Takeda, "Optical absorption and lattice defects induced by neutron irradiation and heat treatment in ZnS crystals," *Physica Status Solidi (a)* **28**(1), 379–385 (1975).
78. Lewis, K. L., G. S. Arthur, and S. A. Banyard, "Hydrogen-related Defects in Vapour-Deposited Zinc Sulphide," *J. Crystal Growth* **66**, 125–136 (1984).
79. Collins, A. K., R. L. Taylor, X. Zhang, and B. D. Bartolo, "Optical Characterization of Polycrystalline ZnS Produced Via Chemical Vapor Deposition," Proc. Electrochemical Society **PV 90-12**, 626–633 (1990).
80. Morozova, N. K. et al., "Transformation of Luminescence Centers in CVD ZnS Films subject to a high hydrostatic pressure," *Sov. Phys. Semicond.* **38**(1), 36–41 (2004).
81. Morozova, N. K., I. A. Karetnikov, V. V. Blinov, and E. M. Gavrishchuk, "A Study of Luminescence Centers Related to Copper and Oxygen in ZnSe," *Sov. Phys. Semicond.* **35**(1), 24–32 (2001).
82. Morozova, N. K. et al., "Pressure and Temperature Effects on Point-Defect Equilibria and Band Gap of ZnS," *Inorg. Mater.* **40**(11), 1138–1145 (2004).
83. Morozova, N. K., V. G. Plotnichenko, E. M. Gavrishchuk, and V. V. Blinov, "Absorption Spectrum of ZnO Precipitates in ZnSe," *Inorg. Mater.* **39**(8), 783–787 (2003).
84. Hertl, W., "Surface chemical properties of zinc sulfide," *Langmuir* **4**, 594–598 (1988).
85. diBenedetto, B. A., J. Pappis, and A. J. Capriulo, "Chemical Vapor Deposition of Multispectral Windows," AFAL-TR-73-252 (1973).
86. Myers, S. M. et al., "Hydrogen interactions with defects in crystalline solids," *Rev. Mod. Phys.* **64**(2), 559–617 (1992).
87. Van de Walle, C. G. and J. Neugebauer, "Hydrogen in Semiconductors," *Annu. Rev. Mater. Res.* **36**(1), 179–198 (2006).
88. Khan, M. A., "New Band Systems of ZnH and ZnD in the Far Ultraviolet Region," *Proc. Phys. Soc. London* **80**, 599–607 (1962).
89. Iwata, H., S. Suzuki, and Y. Sasaki, "Iodine related grain growth in vapour deposited ZnS," *J. Crystal Growth* **125**, 425–430 (1992).
90. Sakaguchi, M. and T. Hirabayashi, "Role of firing atmosphere on the rate of transformation of ZnS crystal," *J. Appl. Phys.* **44**(6), 2530–2532 (1973).
91. Knitter, S. and M. Binnewies, "Der Chemische Transport von Mischkristallen in den Systemen MnS/ZnS,FeS/ZnS und FeS/MnS," *Zeitschrift für anorganische und allgemeine Chemie* **625**, 1582–1588 (1999).

92. Balabin, A. I. and R. O. Sack, "Thermodynamics of (Zn,Fe)S sphalerite: A CVM approach with large basis clusters," *Mineralogical Magazine* **64**(5), 923–943 (2000).

93. Dicarlo, J., M. Albert, K. Dwight, and A. Wold, "Preparation and properties of iron-doped II-VI chalcogenides," *J. Solid State Chem.* **87**(2), 443–448 (1990).

94. Gashurov, G. and E. Banks, "The Role of Copper in the Transformation of Hexagonal Zinc Sulfide," *J. Electrochem. Soc.* **114**(11), 1143–1148 (1967).

95. Nickerson, J., P. Goldberg, and D. H. Baird, "The Influence of Copper on Structural Transformations in ZnS:Cu,Cl," *J. Electrochem. Soc.* **110**(12), 1228–1230 (1963).

96. Sakaguchi, M., M. Ohta, M. Satoh, and T. Hirabayashi, "The Phase Transformation during Crystallization of ZnS," *J. Electrochem. Soc.* **124**(4), 550–553 (1977).

97. Shuyuan, Z., G. Changxin, L. Bilin, and T. Shun, "A high-resolution electron microscopy study of microstructure of ZnS powder phosphors with different dopants," *Philosophical Magazine A* **62**(4), 387–394 (1990).

98. Cullity, B. D. and S. R. Stock, *Elements of X-ray Diffraction*, 3rd Ed., Prentice Hall, New York (2001).

99. DeLoach, L. D. et al., "Transition Metal-Doped Zinc Chalcogenides: Spectroscopy and Laser Demonstration of a New Class of Gain Media," *IEEE J. Quantum Electronics* **32**(6), 885–895 (1996).

100. Bringuier, E., "Tentative Anatomy of ZnS-type Electroluminescence," *J. Appl. Phys.* **75**(9), 4291–4312 (1994).

101. Majewski, J. A., "Electronic structure of transition metal impurities in zinc sulphide," *Physica Status Solidi B* **B108**, 663–672 (1981).

102. Segall, B., "Band Structure," in *Physics and Chemistry of II-VI Compounds*, 3–72, M. Aven, and J. S. Prener, Eds., North-Holland, Amsterdam (1967).

103. Birman, J. L., "Polarization of Fluorescence in CdS and ZnS Single Crystals," *Phys. Revi. Lett.* **2**(4), 157 (1959).

104. Marshall, T. S. and T. M. Wilson, "Ab initio factorized LCAO calculations of the electronic band structure of ZnSe, ZnS, and the (ZnSe) (ZnS) strained-layer superlattice," *Intl. J. Quant. Chem.* **44**(S26), 687–701 (1992).

105. Schroer, P., P. Kruger, and J. Pollmann, "First-principles calculation of the electronic structure of the wurtzite semiconductors ZnO and ZnS," *Phys. Rev. B* **47**(12), 6971–6980 (1993).

106. Wright, K. and R. A. Jackson, "Computer simulation of the structure and defect properties of zinc sulfide," *Journal of Materials Chemistry* **5**(11), 2037–2040 (1995).

107. Shchurov, A. F. et al., "Structure and Mechanical Properties of Polycrystalline Zinc Sulfide," *Inorg. Mater.* **40**(2), 96–101 (2004).

108. Durovic, S., P. Krishna, and R. Pandey, "Layer Stacking," in *International Tables for Crystallography C: Mathematical, Physical*, 744–765 (1999).

Chapter 2
Technical Issues in Processing of CVD ZnS

2.1 Introduction

In order to appreciate the complexities associated with chemical vapor deposition of ZnS and the subsequent heat treatment of the material, one must first examine the characteristics and reactions of the main components of the system (Zn, S, H_2S, and Ar). Trace components in the gas system (e.g., H_2O, H_2, and O_2) that provide alternative reaction paths must be considered as well.

It is well known that the presence of hydrogen is a controlling factor for the chemical potential of sulfur, and hydrogen has been widely used in this respect to study the reactions of sulfides in the geochemical field,[1] where the reaction is $2H_2S = 2H_2 + S_2$. This reaction determines the fugacity (i.e., activity at low pressure) for sulfur. Increasing the $[H_2]/[H_2S]$ ratio in the gas phase must then lower the partial pressure of sulfur and further prevent the H_2S from dissociating.

For ZnS, the reaction of sulfur with zinc to form ZnS, $2Zn + S_2 = 2ZnS$, is known as univariant because at constant temperature and pressure it depends only on the activity of sulfur.[2] The free-energy change for the sulfidation of zinc, per the equation above, has been shown by Vaughan[2] to be

$$\begin{aligned} \Delta G^{\circ}_{rxn,II,25-420C}(kJ) &= \Delta H_{rxn,II,25-420C} - T\Delta S_{rxn,II,25-420C} \\ &= -537.88 + 0.19\mathrm{T(K)}, \\ \Delta G^{\circ}_{rxn,II,420-1200C}(kJ) &= \Delta H_{rxn,II,420-1200C} - T\Delta S_{rxn,II,420-1200C} \\ &\quad -548.87 + 0.21\mathrm{T(K)}. \end{aligned} \tag{2.1}$$

These values agree with those in commercial thermodynamic properties databases.[3] This database also includes thermodynamic data for the similar formation of ZnO. That ZnO has a lower-standard-state Gibbs energy of formation implies that, other factors being equal, zinc has a preference for oxygen over sulfur.

The presence of oxygen in ZnS has been alluded to before in the context of luminescence. Because ZnS forms a solid solution with oxygen, dissolving about 1 mol% O, ZnS-O can be hard to detect and will not show up as a separated phase in x-ray diffraction.[4] There has been some debate as to whether the weak extrinsic absorption in CVD ZnS around 9.1 μm (1100 cm^{-1}) is due to ZnO,[5] Si-O,[6] or SO_3.[2–7] Absorption bands in ZnSe between 850–1100 cm^{-1} have been attributed to ZnO.[8] Low-temperature deposits (≤670 °C) are said to have higher [O] present. Annealing in Zn vapor increases dissolved oxygen and decreases density, whereas annealing in S vapor reduces dissolved oxygen to 10^{18} cm^{-3} but does not affect density.[9] Additionally, the ZnS-O solid solution is said to be noticeable in photoluminescence, as a red shift to the free exciton due to the bandgap shrinkage of ZnS from accommodation of oxygen.[10] As mentioned in Chapter 1, diBenedetto *et al.* have experimented with deliberate doping of CVD ZnS with oxygen, which produced colorless material with lower visible scatter than material grown using only hydrogen sulfide and zinc.

2.1.1 Vapor phase equilibrium

Homogeneous decomposition of hydrogen sulfide is severely restricted below 500 °C, and at 800 °C conversion to the elemental components is only 25% at 110-kPa pressure (825 torr).[11] Trace amounts of O_2 are known to greatly accelerate the decomposition of H_2S at high temperature (> ~2100 °C).[12] It has been observed that when H_2, O_2, and H_2S are present in equal volumes, the H_2S will be oxidized before the H_2.[13] However, the reaction mechanisms in the H_2S-O_2 system are very complex, and at least thirty possible reactions have been identified involving several paths.[14,15]

Sulfur vapor is extremely complex in its constituency, as it exhibits a number of allotropes, the distribution of which varies strongly with temperature. At low temperatures, S_8 is the most stable species, with significant fractions of S_7 and S_6, but above 720 °C S_2 becomes the most prevalent species.[16] Reaction enthalpies for conversion from S_8 to lower molecular weight forms have been reviewed recently, comparing experimental and calculated values.[17] S_2 is the largest mole fraction above 1000 K,[18] and individual sulfur atoms are unlikely to be present at temperatures lower than 2000 K due to their high enthalphy of formation.[17] However, a different conclusion was reached by Wiedemeir[19] in studying the reaction of ZnS, who stated that sulfur atoms were an important fraction of the equilibrium gas phase above the ZnS reaction from H_2S and Zn.

The equilibrium composition of the gas phase above ZnS in the presence of H_2, H_2O, and CO_2 has been investigated recently using a total energy minimization method[19] (see Figure 2.1). The study began by simulating the equilibrium vapor phase composition above ZnS(s) including all of the allotropes of sulfur along with zinc and zinc sulfide. It was found that Zn and

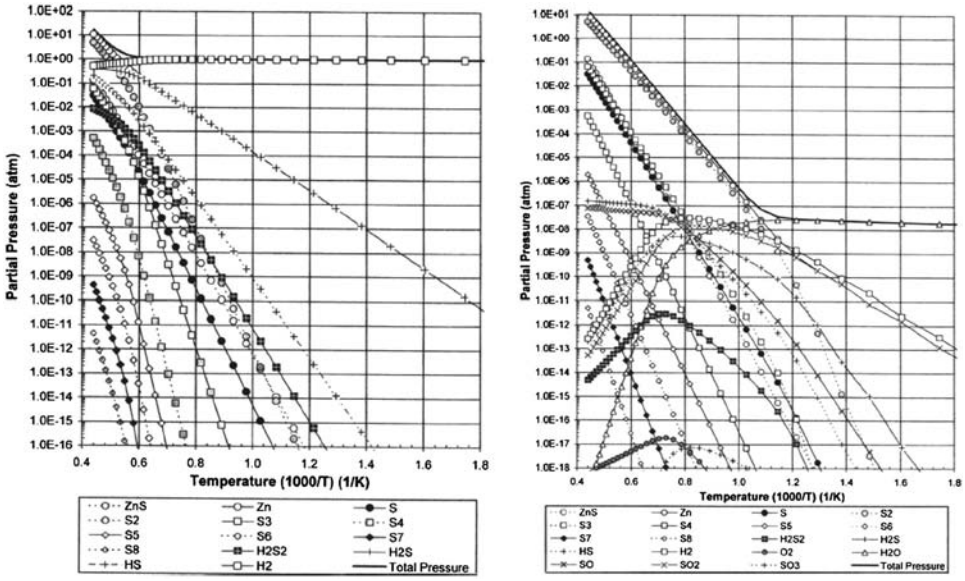

Figure 2.1 Calculated partial pressure of species in a ZnS chemical vapor reaction in the presence of hydrogen (left) or water (right) (image from Wiedemeier[19] used with permission; copyright 2006 American Vacuum Society).

S_2 are the dominant species by several orders of magnitude and are very close in partial pressures throughout the simulated temperature range (~588–2000 K). A simulation was then performed assuming the addition of 10^{-3} atm (~1 torr at 298 K) of H_2 gas, which significantly changed the equilibrium such that the dominant species below 1000 °C are H_2 and H_2S, followed by Zn, and then HS or S_2, depending on the temperature. The partial pressure of zinc (p_{Zn}) was significantly greater than the partial pressure of sulfur (p_{S_2}). Additions of H_2 gas at the 10^{-8} atm (~10^{-5} torr) level did not significantly alter the equilibrium of the ZnS (s) system alone, but larger concentrations on the order of 1 atm (~10^3 torr) of H_2 resulted in even more depletion of sulfur gas in the vapor. Similar results were found when adding 10^{-8} atm (at 298 K) of H_2O(g), in that the sulfur was much depleted below about 700 °C, and the major constituents of the vapor in order of concentration were H_2O, H_2, SO_2, Zn, S_2, and H_2S, with the order differing slightly with temperature. When both H_2O and H_2 were added at the 10^{-3} atm (at 298 K) level, the vapor was almost entirely H_2O and H_2, with concentrations of H_2S and Zn being next. Finally, the addition of 10^{-8} atm (at 298 K) of H_2O(g) and H_2 along with 10^{-5} atm (~10^{-2} torr at 298 K) of CO_2 resulted in an extremely complex equilibrium consisting of CO_2 and CO, with Zn and S_2 being the next greatest component and very close in concentration due to sublimation down to about 650 °C when H_2O(g), H_2, COS, and H_2S become important. In this last case, only at temperatures below 560 °C is there a return to the $p_{Zn} \gg p_{S_2}$.

This example illustrates the profound effect of trace impurity gases in vapor equilibria. Conventional vacuum deposition reactors that do not use careful outgassing techniques can expect to have 10^{-8} atm of $H_2O(g)$ and H_2 from the chamber walls, along with 10^{-5} atm of CO_2 in a continuous supply from pumps, furnaces, and graphite crucibles.[19] If the deposition system is dynamic, it is unlikely to be at equilibrium. Defect concentrations will be inhomogeneous and vary spatially in the chamber. Overall, any present $H_2O(g)$ and H_2 will lower the chemical potential of sulfur by forming gases with sulfur, leaving a great excess of zinc in the vapor. Assumptions in this study included a congruently vaporizing ZnS (i.e., Zn and S ratios upon sublimation are equal) and that no other solid phases were formed. This already has limited applicability to the CVD ZnS system because ZnO and Zn-H species were not considered. However, this study is one that must be performed and compared to experimental mass spectrometer data from actual CVD depositions.

2.2 Chemical Vapor Deposition of ZnS

Chemical vapor deposition methods of zinc sulfide can be separated into static and dynamic methods, as well as transport methods and conventional methods.[20] Static methods involve sealing the reactants in a furnace, whereas dynamic methods involve continuously feeding reactants and removing spent gases. Transport CVD requires combining solids of ZnS with hydrochloric acid vapor (for example) to produce zinc chloride and hydrogen sulfide gases that are held at a high temperature. These gases are then recombined such that the ZnS solid re-deposits in a bulk solid on substrates at a lower temperature, leaving hydrochloride acid that can be evaporated off. The process works well for growing small single crystals and some polycrystalline material, but it is limited in the size of parts that can be grown: zinc sulfide grown this way tends to have undesirably large grain size.

The standard dynamic ZnS CVD process as practiced today involves a liquid zinc metal that combines with hydrogen sulfide gas in a higher-temperature deposition area; the growth of ZnS proceeds by the reaction

$$\mathrm{Zn\ (g) + H_2S\ (g) \Rightarrow ZnS\ (s) + H_2(g).} \tag{2.2}$$

Hydrogen gas is given off in the process, some of which ends up being incorporated in the solid ZnS, especially at lower deposition temperatures.

ZnS CVD growth is carried out in a hot-wall CVD reactor, with a heated retort of zinc metal, hydrogen-sulfide gas injectors, and argon carrier gas for the vapors.[21] Complex models of the transport phenomena have been simulated recently that show dependence of geometries on deposition rates.[22,23] Despite this, the details of the reaction kinetics, thermodynamics, and transport phenomena are still poorly understood today.

2.2.1 Homogeneous and heterogeneous CVD reactions

There is considerable debate as to how the ZnS forms. The relative importance of the homogeneous versus heterogeneous reaction in CVD ZnS has never been resolved. CVD processes in general can be completely homogenous, completely heterogeneous catalytic, or in between.[24] The fact that CVD reactions generally show deposition of material on all internal surfaces and not just those that are meant to catalyze the reaction suggests that CVD reactions typically involve at least some homogeneous reaction.[25]

In a *homogenous* reaction, ZnS forms in the gas phase and either condenses into a powder or diffuses to the substrate to form a film.[25] Higher gas-phase concentrations (supersaturation) will favor self-collisions of gaseous products and powder formation, wheras low concentrations favor diffusion and film formation. With a cold-wall CVD process, the diffusion to the substrate is known as thermophoresis and is used in producing silica optical waveguide fiber. The CVD ZnS process, however, is a hot-wall CVD process. In recent modeling of ZnS growth using transition state theory (TST) to estimate the configuration of transition state complexes between H_2S and ZnS, Sharifi[26] assumed that ZnS forms in the gas phase and then diffuses and deposits on the substrate. It has been argued that the gas phase reactions in ZnS are undesirable from an optical standpoint, and that heterogeneous reactions and low growth rates are preferred to produce a more-cubic material.[27] There is experimental evidence that gas phase nucleation and heterogeneous deposition do occur in CVD ZnS under certain conditions, resulting in some hexagonal material. Figure 2.2 shows electron micrographs

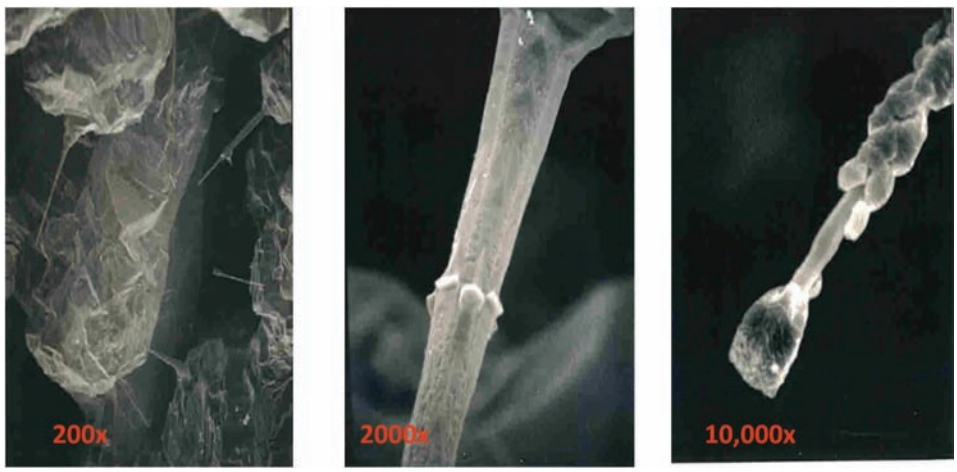

Figure 2.2 Evidence of gas phase nucleation of ZnS_xSe_{1-x} particles which then stick to hexagonal needles and become incorporated into bulk CVD material (photos courtesy of Barney diBenedetto, c. 1973).

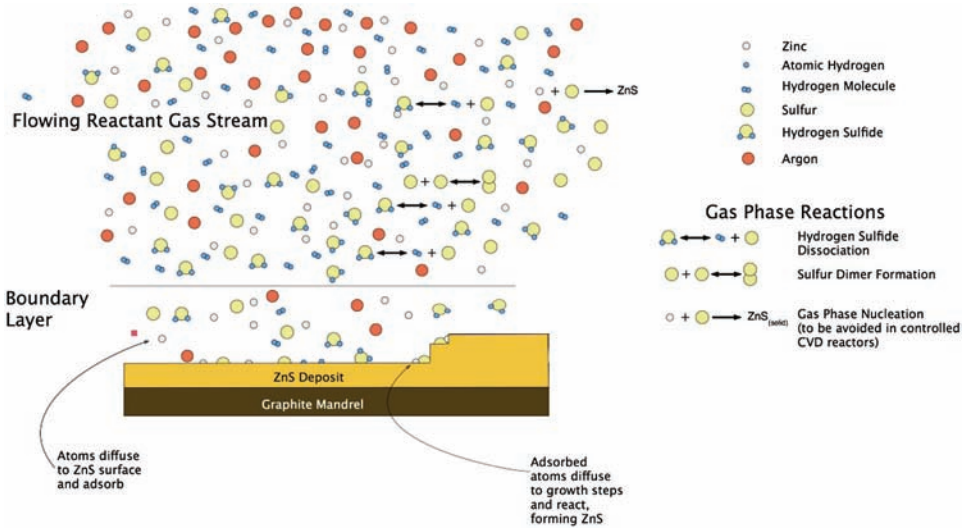

Figure 2.3 Illustration of the proposed model of ZnS growth; H_2S adsorbs to the surface and reacts with Zn. Gas phase reactions also produce ZnS that diffuses to the surface. Possible other reactions involve H or H_2, O_2 and H_2O, or gas phase ZnH_2 (figure courtesy of C. Willingham of CBWTechservices).

of CVD ZnS_xSe_{1-x} produced by Raytheon, wherein it is apparent that hexagonal needles nucleated in the gas phase, and then additional particles agglomerated or grew onto these needles, which ultimately became incorporated into the bulk CVD body.

Others have proposed that *heterogeneous* reactions are more important (or at least more desirable) for ZnS, where the hydrogen sulfide adsorbs to the graphite surface and then breaks apart, leaving the sulfur behind where it bonds to the zinc and releases hydrogen.[28] This process is depicted in Figure 2.3. This mechanism should be more important at lower temperatures and would be more affected by the stability of the H_2S (and hence the H_2 content). Note that conditions that favor the highest growth rates do not favor the best intrinsic optical quality (i.e., low hexagonality fraction).

2.2.2 Commercial CVD reactor considerations

From the very beginning, it was discovered that CVD growth of bulk ZnS was fraught with process sensitivity.[29] The primary measure of the optical quality of CVD ZnS has always been its visible color and scatter, with several groups having produced transparent, colorless, or near-colorless material without postprocessing.[30,31] However, the literature is inconsistent as to the optimal processing conditions for repeatable production of intrinsically high-optical-quality CVD ZnS. The main variables affecting the properties of the material have been established, although the physics of the interactions are poorly

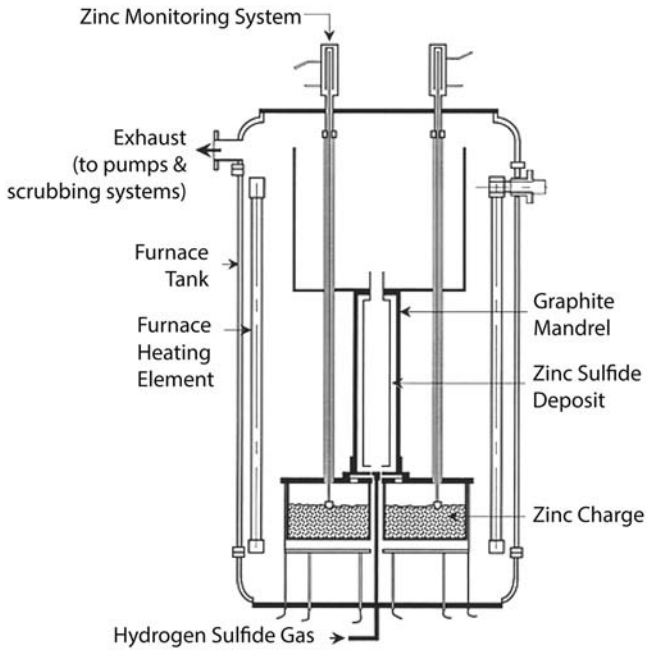

Figure 2.4 Schematic of ZnS reactor.

understood. The deposition temperature, which is the substrate or mandrel temperature of the hot-wall reactor, has been varied successfully from as low as 450 °C to as high as 950 °C.

A schematic cross-section of a typical CVD reactor for producing ZnS is shown in Fig. 2.4. Early on, many of the technical issues associated with CVD growth were encountered, including plugging of injector nozzles, thickness nonuniformity, etc. (see Chapter 5).

2.2.2.1 Mandrels

The choice of mandrel material can be considered a catalyst of the surface reaction for the first material to be deposited. Early on, alumina, fused silica, and molybdenum were investigated and found to be too reactive, affecting either the deposited ZnS material or the reusability of the mandrel.[20] Graphite mandrels with graphite release coatings were found to be the most durable and nonreactive, and are still commonly used today. The use of graphite versus tantalum substrates was recently investigated to determine any differential effect on optical properties, and none was found.[32] Therefore, it can be concluded that the initial mandrel material is relatively unimportant to the quality of the ZnS material, and noncatalytic unreactive substrates are preferred. Initial experiments by Raytheon with mandrel materials are discussed in Chapter 5. Additionally, in the interest of making near-net-shaped precision optics (both

hemispherical domes and conformal optics), much research has been undertaken in CVD mandrel materials and coatings,[33,34] focusing on the ability to make precision replicated parts with tight tolerances.

2.2.2.2 Deposition stress and thickness uniformity

Later researchers expounded on other process parameters—notably stress-induced bowing, which was thought to be caused by one of a number of factors, including coating on a graphite mandrel, growth stresses, trapping of process gases between the mandrel and depositing material, thermal expansion mismatch between mandrel and ZnS deposit, Zn condensation under the deposited material, and deposition geometry.[21,35] It has been found that bowing can be mitigated to an extent by starting the ZnS deposition at a higher temperature and then slowly reducing the temperature to the ideal degree after the first layers are deposited.[21,36] Additionally, it was found by several groups that the flow patterns of the vapors in the reactor, especially around the mandrels, influence the thickness as well as the optical quality.[21-23,31,37-39]

2.2.2.3 Deposition temperature, pressure, and reactant ratios

Deposition temperatures (i.e., hot-wall mandrel temperatures) can range from 300–1200 °C under very low total reactor pressures, on the order of 40 torr (~5 kPa or ~0.05 atm). It was found that the grain size of the polycrystalline ZnS was highly dependent on deposition temperature, with higher-temperature deposition resulting in larger grain size[40,41] (see Figs. 2.5 and 2.6). Standard CVD ZnS varied in visible color from colorless to yellow to orange to red to brown to black, and was generally opaque (i.e., highly scattering) to the eye.

Reactant molar ratios in the range of Zn/H_2S of 0.1 (very sulfur rich) all the way to 4.5 (very zinc rich) have been tried with generally acceptable long-

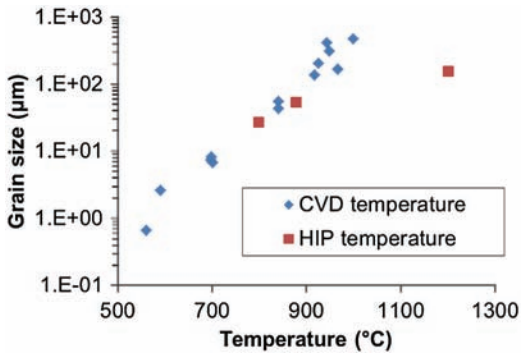

Figure 2.5 Grain size versus CVD deposition temperature and HIP temperature (data from Savage[40]).

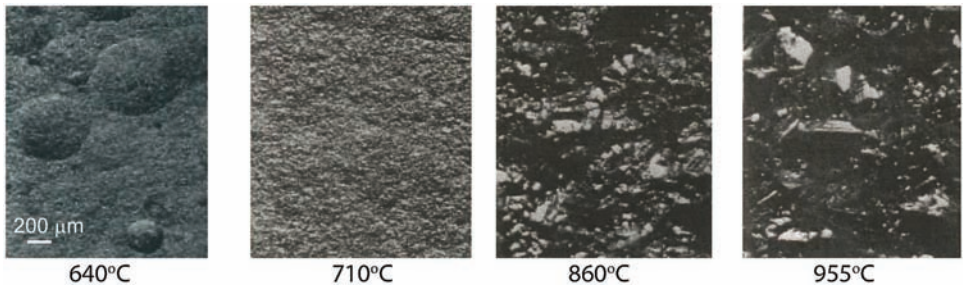

Figure 2.6 Grain size evolution with deposition temperature (image from Lewis[41] used with permission; copyright 1984 The Electrochemical Society).

wavelength infrared (8–14 μm wavelengths) properties for all cases but with highly variable visible-to-mid-wavelength infrared (0.4–5 μm wavelengths).[42] Reactant flow rates (metered rates of argon carriers for Zn vapor and H_2S) seem to have more effect on the deposition thickness uniformity than specifically on the visible transmission. It was shown by diBenedetto *et al.*[43] that areas where the sulfur partial pressure are higher, such as near the H_2S inlet jets, result in ZnS material that is higher in sulfur and has poorer optical quality (i.e., more scatter). This might suggest that vapor far from the H_2S injectors would have less sulfur, be more zinc rich, and thus potentially have higher optical quality.

2.2.2.4 Deposition rate

A Russian study on CVD ZnS has investigated the rate-controlling step in the deposition of ZnS from H_2S over a range of total system pressures (1–72 torr) and temperatures (550–850 °C) in Zn-rich reactant stoichiometry.[44] The total rate constant k_t, defined by the mass transfer in the gas phase k_g, and the first-order chemical reaction k_r at the substrate were studied. ZnS deposit thickness as a function of distance from the injectors was used to compute the gas-phase diffusion coefficient of the limiting species (H_2S) and the effective mass-transport-rate constant k_g of the heterogeneous reaction. A first-order reaction-rate constant k_r with respect to H_2S was assumed for the chemical reaction. Other studies have looked at the very important commercial constraint of deposition rate and its relation to process parameters.[39,45,46]

The study found that the mass-transfer-rate constant strongly increased with temperature in ZnS, suggesting large activation energy for mass transfer. This is in marked contrast to CVD ZnSe, where k_g was found to be independent of temperature (i.e., nonactivated).[44] At 750 °C, k_t was found to be nearly independent of system pressure from 10–70 torr, unlike the situation of ZnSe at 645 °C. This pressure independence of the growth-rate CVD ZnS suggests that growth is kinetically limited and not boundary-layer diffusion limited as in ZnSe. This chemical control on the growth kinetics of ZnS holds

even at temperatures as high as 750 °C for concentrations of the limiting reactant H_2S gas of 3.5×10^{-5} mol/L. Growth rates at this temperature over the pressure range studied were 2.3×10^3 mm-L/hour-mol and varied less than 25% over this pressure range, well within the error of the measurement of deposition thickness.

In comparing CVD ZnSe and CVD ZnS, the authors state that ZnS deposition is *kinetically controlled* over a much-larger range of temperatures and reactant dilutions (i.e., total system pressure) than ZnSe. Note that this study focused on *deposition rate*, concluding that rate was relatively insensitive to total system pressure (which includes an argon carrier) and temperature. However, it is likely that optical properties, particularly at short wavelengths, are much more sensitive to these parameters than overall growth rate.

2.2.2.5 Porosity

An Israeli group has recently provided a detailed description of the microstructure of CVD ZnS.[32] The authors show that the intrinsic visible-through-mid-wavelength infrared transparency is improved when going from 650–730 °C deposition temperatures (Zn/H_2S ratios are not specified). Pores were found in decreasing numbers with increased distance away from the mandrel and with increased deposition temperature. Pore size was in the range of 50–200 nm, according to scanning electron microscopy (SEM), and varied not with distance from mandrel or deposition temperature but only with gas flow rate and total system pressure. No significant changes in porosity were noted when using tantalum mandrels versus graphite ones.

These authors suggest that these observations can be explained by a *heterogeneous* ZnS reaction model where gases such as H_2S and H_2 adsorb to the mandrel substrate where ZnS material is deposited around them, creating pores.[32] Higher temperatures make the adsorption of gas molecules less likely. Increased temperatures on the growth surface of ZnS versus the mandrel (due to exothermic reactions producing ZnS and lower thermal conductivity of ZnS) are invoked to explain the decrease in porosity at distances away from the mandrel. Because mandrel material did not affect observed porosity, adsorption of the gas was believed to be controlled by the arrival of the gas to the substrate, and so should be influenced only by the pressure and flow rate.

A research group at the IKhVV RAN (Institute of the Chemistry of High-Purity Substances, Russian Academy of Sciences, Nizhnii Novogorod), where both CVD ZnS and CVD ZnSe are still produced, have published similar studies.[47] CVD ZnS samples were produced under various deposition temperatures, total pressures (of argon carrier gases), and H_2S concentrations, and density was measured for calculations of porosity.[48] Each of the parameters was only varied by itself while the other two conditions were held constant, so the results can be somewhat misleading. For example, porosity was seen to increase with increasing deposition temperature, which is

completely opposite to the results presented by the Israelis.[32] However, the role of pressure is clearer, with low total pressures favoring kinetically controlled heterogeneous surface nucleation, whereas higher pressures result in homogenous gas phase reactions. Similarly, kinetics control deposition reactions at low temperatures, mass transport across the boundary layer controls reactions at intermediate temperatures, and thermodynamics generally controls reactions at the highest temperatures.[21]

The role of porosity in determining the optical properties of CVD ZnS is disputed in the literature. For example, Bredikhin *et al.*[49] suggest that visible and near-infrared scattering in HIPped CVD ZnS can be explained by distributions of faceted pores (5 nm to 5 μm in size). On the other hand, McCloy[50] shows that CVD ZnS scattering cannot be explained by pores, whereas powder hot-pressed ZnS scattering can be explained by pores. Although it seems clear that porosity is indeed an important consideration in bulk commercial CVD ZnS growth, it is as yet unclear what the role of this is in determining the transmittance of CVD ZnS.

2.2.3 Summary

ZnS is made commercially by low-pressure hot-wall CVD from zinc vapor and hydrogen sulfide gas. Deposition of ZnS probably occurs by a combination of (1) homogeneous gas-phase reactions where particles diffuse to the substrate and (2) heterogeneous reactions at the growth surface. The nature of these reactions determines the microstructure, growth rate, and optical quality. The main impurities in CVD ZnS are believed to be oxygen and hydrogen, though the relative quantity and identity of all the gas species in the deposition chamber is not known. The presence of porosity in some CVD ZnS is believed to be related to the adsorption of gas molecules on the growing solid surface and subsequent trapping of gas as material is deposited around them. CVD ZnS thus produced is yellowish and opaque in the visible, requiring additional postprocessing to be usable as windows in the visible and near-infrared. Nevertheless, CVD ZnS is an excellent material for long-wavelength-infrared applications without additional treatment, and is currently used for windows and domes requiring transmission in that spectral region.

2.3 Heat Treatment of CVD ZnS

Various heat treatment protocols have been used on CVD ZnS in an attempt to produce clear and colorless material from the visible through the long-wave infrared. These treatments can be separated into those that involved only heating (i.e., annealing) and those that also involved pressure (i.e., hot isostatic pressing). Additionally, over the years, attempts have been made to

understand the impact of furnace atmosphere on material properties such as optical quality and mechanical hardness.

2.3.1 Annealing

Many annealing experiments were done in the early trials,[27] and several observations bear repeating. Materials were annealed in air, vacuum, hydrogen, hydrogen sulfide, sulfur, and zinc vapors in an effort to remove the color and reduce the optical scattering in the visible and infrared. Material response to annealing treatments was found to depend on CVD deposition conditions. Type "A" CVD ZnS material had high visible scatter (e.g., run #ZS-39[29]) was deposited above 750 °C, had no 6-μm absorption, and would not improve upon annealing under any known conditions. Type "B" material was deposited at temperatures <700 °C (e.g., run #ZS-45 deposited at 550 °C[29]), had good visible clarity, a large 6-μm absorption, brownish color, and deposition rates of ~0.002" per hour.

For annealing studies, samples were placed in a quartz tube, and the tube was sealed or left open to the atmosphere (in the case of air annealing). In the type "B" materials that improved upon annealing, heat treatment in atmospheres of vacuum, air, zinc, and sulfur all reduced the 6-μm absorption. The best annealing results were obtained with sulfur (at 500 °C for 125 h) or air (not specified, but either 500 °C for 125 h or 750 °C for 24 h).[29] For these samples, transmission was improved from the visible through the infrared, and the absorption band was completely eliminated. Hydrogen sulfide anneals were attempted later and were found to eliminate the color, but they increased the scattering as compared to the starting material.[27]

The hexagonal-to-cubic phase transformation has been studied by annealing powders (starting composition was 20% sphalerite and 80% wurtzite) in vacuum, zinc vapor, or sulfur vapor at various temperatures between 800–900 °C.[51] The rate of the transformation was determined by changes in peak heights by x-ray diffraction, monitoring the reduction of the (10.0) and (10.1) wurtzite peaks and the growth of the (111) sphalerite peak as the material becomes more cubic. Results were modeled using a second-order kinetics expression with terms for fraction unreacted and for density of transformed nuclei. Transformations from vacuum and sulfur vapor anneals were said to be controlled by nucleation of new regions of cubic phase. Concentrations of nuclei for phase transformation were found to be independent of temperature. A higher concentration of nuclei was found for annealing in sulfur vapor than in vacuum, explained as being due to adsorption of sulfur on the ZnS surface causing increased transformation rates. Above 0.5 atm of sulfur, the adsorption is saturated, and no further increase in transformation rate was achieved.

The rate of transformation in Zn vapor was well modeled by a first-order rate expression for 3D diffusion in a sphere.[51] The proposed mechanism

involved 60-deg rotation of the zinc tetrahedron along the *c* axis of wurtzite. This "diffusion" of three zinc atoms in the basal plane of wurtzite changes the *c*-axis stacking sequence from ABA to ABC, thus converting the wurtzite structure to sphalerite structure. If the levels of excess zinc are too high, this mechanism is not efficient, as shown by the decrease in transformation rate above 0.3 atm of Zn atmosphere.

2.3.2 Hot pressing and sintering of ZnS powders

Before addressing hot isostatic pressing (HIPing) of CVD ZnS directly, it is useful to examine temperature and pressure parameters in powder hot pressing and sintering. This processing, while very different than HIPing of CVD ZnS, lends significant insight into the effects of temperature and pressure on the phase transformation in ZnS.

Various samples of Kodak polycrystalline hot-pressed ZnS (IRTRAN 2) with average grain size of 1.9 μm were subjected to uniaxial compression strains at temperatures just above and just below the phase transition temperature (~1020 °C).[52] (Note that these samples were originally hot pressed from powders when they were made by Kodak, but this particular study was conducted by hot pressing these already dense polycrystalline samples again.) When samples were hot-pressed above the transformation temperature (1050 °C), there was evidence of superplasticity, an influence on the transformation kinetics, and an exponential increase in the hexagonal phase content of the resulting material. Hot pressing below the transformation temperature (975 °C) produced no additional hexagonal phase (IRTRAN 2, ZnS starts out with approximately 5% hexagonal phase). However, dynamic recrystallization and extensive cubic phase twinning took place at this temperature as flow stress from deformation reached a peak value. For the 975 °C samples, true stresses were calculated to be in the range of 90–140 MPa (13–20 ksi), depending on the strain rate used. Note that this temperature and pressure condition, which produced recrystallization in hot pressing, is very similar to the conditions used commercially in hot isostatic pressing of CVD ZnS.

Recent sintering studies of monodispersed submicron ZnS powders also provide information on the effect of temperature on phase transformation in ZnS.[53] Sintering temperatures from 900–1250 °C were investigated, and x-ray diffraction measurements were made of the sintered bodies. There was no evidence of hexagonal phase peaks in material sintered at 900 °C, and the wurtzite (10.0), (10.1), and (10.3) reflections only appear in material sintered at 1000 °C or higher. ZnS powder sintered at 1250 °C is almost entirely hexagonal phase, showing only a very small diffraction peak of the sphalerite (111) plane. These results suggest that heat-treatment temperatures below 1000 °C without pressure would not create additional hexagonal phase in ZnS.

2.3.3 Hot isostatic pressing

The application of HIPing to CVD ZnS has been found to increase the visible and near-infrared transmission to levels identical to that achievable from the best single-crystal ZnS. Typical temperatures and pressures used are 990 °C at 15–30 ksi. As discussed in the previous section, analogous to powder processing, this temperature should prevent formation of hexagonal phase, and this pressure should induce dynamic recrystallization and extensive twinning, which is exactly what is observed. HIPed ZnS has been shown to have slightly different property values for Young's modulus, Poisson's ratio, and thermal conductivity. The microstructure of HIPed ZnS is significantly different than that of the as-deposited CVD material. This is discussed in detail in Chapter 3.

HIPing has traditionally been applied in materials processing to remove porosity and increase density of metals and ceramics.[54] Densification can typically be achieved by temperature alone (sintering) or by pressure alone (cold isostatic pressing), but the application of heat and pressure together reduces the necessary level of both. The temperature used for a HIP process is generally at least half the melting point of the material in order to lower the yield strength and raise the diffusivity of the material, thus allowing pore closure and densification. The pressure is generally chosen such that it is greater than the reduced yield point of the material at the process temperature. This amount allows plastic flow due to high-temperature creep processes such as dislocation creep (slip, climb), lattice diffusion (Nabarro–Herring) creep, and grain boundary (Coble) creep.

HIPing causes grain growth and can influence phase transformations due to the high pressure.[54] By itself, the pressures in HIPing, 100–200 MPa (~15–30 ksi), are generally not enough to cause phase transformations. However, for the ZnS system as an example, the sphalerite cubic structure is denser than the hexagonal wurtzite structure and thus is more thermodynamically favorable at moderately high pressures. The transformation of the cubic to hexagonal phase ZnS near the transformation temperature is impeded by high pressure because the volume must increase to convert to the hexagonal phase.[10]

HIPing is a thermomechanical process with both consolidation and heat transfer occurring simultaneously.[54] Constitutive equations, generally applicable to powder consolidation, have been developed that describe the various microscopic mechanisms contributing to densification rate, including power-law creep, boundary diffusion, volume diffusion, and diffusional flow. Microscopic models depend on three variables: pressure, temperature, and relative density, which can be plotted in various ways on densification maps. Macroscopic models, more empirical in nature, better describe the relationship of strain and strain rate to densification and densification rate, and thus better account for shape change.

Additionally, grain growth can occur faster with HIPing, as impurity diffusion is increased at higher temperatures, and grain boundaries may no longer be pinned by precipitates but may migrate. Specific HIPing schedules must consider the densification mechanism and the thermal conductivity so as to prevent thermal cracking, especially in ceramics.

The impact of HIPing on diffusion is difficult to discern because high temperatures generally increase diffusion, whereas high pressures generally decrease diffusion. A number of studies have been conducted looking at "self-diffusion" of Zn and S in ZnS as well as a number of dopants and defects. These studies consist of calculations as well as measurements. McCloy[55] summarized these diffusion coefficients in a convenient table.

2.3.3.1 Creep, densification, and diffusion

Different plastic deformation and densification mechanisms are operative in ceramic processing depending on temperature and applied stress. Generally speaking, high pressures and low temperatures favor power-law (dislocation) creep mechanisms, whereas low pressures and high temperatures favor diffusion-controlled mechanisms.[56] On a creep-deformation map of temperature versus stress, the temperature is plotted as "homologous temperature," which is the temperature normalized by the melting point (T/T_m), and the stress is plotted normalized to the shear modulus of the material (τ/μ).

For a polycrystalline ceramic, high stresses result in dislocation glide. The Peierls–Nabarro (frictional) stress is the force needed to move a dislocation along the slip plane.[56] Regardless of temperature, the deformation mechanism is dislocation glide above the Peierls' stress and below the theoretical shear stress. The Peierls' stress is given by

$$\tau_f = \mu \exp\left(\frac{-2\pi w}{b}\right), \tag{2.3}$$

where μ is the shear modulus, w is the dislocation width, and b is the magnitude of the Burgers vector of the dislocation. For covalent ceramics, $w \sim b$, and for cubic ZnS, $\mu = 33$ GPa.[56] Therefore, for ZnS, the Peierls' stress is 61.6 MPa (8.9 ksi), which, normalized to the shear modulus, is 0.0019 or $\sim 10^{-3}$.

At low stresses, diffusional creep mechanisms are dominant. For polycrystalline ceramics, the mechanism of lattice (or volume) atomic diffusion (Nabarro–Herring creep) is favored at high temperatures, whereas grain-boundary diffusion (Coble creep) is favored at lower temperatures. Although both mechanisms can be operative at the same time, when the temperature is higher than 40–50% of the melting point, lattice diffusion is usually assumed to be dominant. The melting point of ZnS is 1830 °C,[20] so the transition point for lattice diffusion in ZnS should be approximately 732–915 °C.

Karaksina *et al.*[57] studied the recrystallization of CVD ZnS with samples that were subjected to high-pressure HIP at various temperatures between

810–1100 °C. Grain size change due to recrystallization was modeled as a power-law function of time. The power-law exponent for ZnS recrystallization was found to be 0.1 (considered a low value for ceramics), presumably due to a high density of structural defects that slow the grain boundary motion. The power law also contains a prefactor with a temperature-dependent activation energy term.

Grain size was found to increase rapidly after the first hour of HIPing ($T \geq 940$ °C) and then increase very slowly with time up to 25 h. The effect of HIP pressure on grain size in the range of 90–200 MPa was very minimal, with grain sizes increasing with pressure only about 10% in this range for a 980 °C, 16-h HIP. The change in grain size (from the original CVD material) was plotted versus temperature in an Arhennius-type analysis for samples HIPed at 180 MPa (26 ksi) for 3 h. A change of slope was found at 985 °C, indicating a recrystallization mechanism with different activation energy. Between 810–985 °C, the activation energy for grain size change was 150 kJ/mol, which was attributed to grain boundary diffusion. Between 985–1100 °C, the activation energy was 550 kJ/mol, which was attributed to volume diffusion of Zn in ZnS.

Activation energies for diffusion of Zn in ZnS in the literature vary widely (see Refs. 55 and 58), and both of the activation energies from the recrystallization study cited above are higher than the generally accepted values for Zn interstitial diffusion in ZnS. However, the larger activation energy at the higher temperatures suggests a smaller diffusion coefficient, and lattice diffusion coefficients are smaller than grain-boundary diffusion coefficients. Thus, the conclusions seem reasonable, but the authors neglect the important role of pressure in plastic deformation because diffusion will be reduced at high pressures.

The relative role of diffusion versus plastic deformation at these higher temperatures is unclear. Both mechanisms seem to be important, with some authors emphasizing diffusion[59] and others plastic deformation.[57] It still remains to be clarified how much of the recrystallization is due to the pressure (i.e., a deformation mechanism) and how much is due to the temperature alone (i.e., a diffusion mechanism). Given the fact that the Peierls' stress for ZnS is much lower than typical HIP pressures, it seems likely that dislocation motion would play a significant role at all temperatures.

2.3.3.2 Considerations for commercial HIPing of CVD ZnS

Several best practices have been indicated in the literature to produce high-quality clear and colorless HIPed CVD ZnS. Careful control of the temperature profiles and cooldown rate after HIPing has been shown to be required to ensure low-stress parts that exhibit acceptable stress birefringence.[60] It has also been noted that the starting composition of the CVD ZnS influences the HIP process and that some reactant molar ratios

(e.g., near-stoichiometric versus Zn-rich) might be more suitable for subsequent HIPing.[36,61] There is considerable disagreement in the literature about how the HIP process produces microstructural change, however,[62] and the dependencies likely rely on details of the starting defect populations and locations, including impurities such as oxygen. These points are further discussed in Chapter 4.

2.3.4 Summary

CVD ZnS is radically transformed by heat treatment with annealing or hot isostatic pressing. HIPing produces the most dramatic transformation in optical and mechanical properties. Multiple mechanisms are operating during the HIP to change the microstructure of ZnS. Grain boundary and lattice diffusion are important for redistribution and/or removal of oxygen and hydrogen impurities. Strain from high pressure in HIPing and hot pressing assists in the martensitic transformation from hexagonal to cubic packing in ZnS. Optical transmission in HIPed ZnS is increased to single-crystal levels, and electronic defect equilibria changes produce new luminescence behavior.

References

1. Sack, R. O. and D. S. Ebel, "Thermochemistry of Sulfide Mineral Solutions," *Rev. Mineralogy & Geochem.* **61**, 265–364 (2006).
2. Vaughan, D. J. and J. R. Craig, *Mineral Chemistry of Metal Sulfides*, Cambridge University Press, Cambridge, U.K. (1978).
3. Roine, A., "HSC Chemistry 5.11 for Windows," computer program (2002).
4. Kroeger, F. A. and J. A. M. Dikhoff, "The Function of Oxygen in Zinc Sulfide Phosphors," *J. Electrochem. Soc.* **99**(4), 144–154 (1952).
5. Klein, C. A. et al., "Lattice Absorption, Phonon Assignment, and Image-Spoiling Properties of CVD ZnS in the Infrared," *Laser Induced Damage in Optical Materials (NBS Special Publication 541)*, 86–98, National Bureau of Standards, U. S. Department of Commerce, Washington, D. C. (1978).
6. Lewis, K. L. and J. Hill, "The Effect of Impurities on the Optical Properties of CVD ZnSe and ZnS," Proc. Electrochemical Society **PV 79-3**, 629–631 (1979).
7. Hertl, W., "Surface chemical properties of zinc sulfide," *Langmuir* **4**, 594–598 (1988).
8. Morozova, N. K., V. G. Plotnichenko, E. M. Gavrishchuk, and V. V. Blinov, "Absorption Spectrum of ZnO Precipitates in ZnSe," *Inorg. Mater.* **39**(8), 783–787 (2003).

9. Morozova, N. K., V. A. Kuznetsov, and M. V. Fok, *Sul'fid tsinka. Poluchenie i opticheskie svoistva [Zinc Sulfide: Preparation and Optical Properties]*, Nauka, Moscow (1987).
10. Morozova, N. K. et al., "Pressure and Temperature Effects on Point-Defect Equilibria and Band Gap of ZnS," *Inorganic Materials*, **40**(11), 1138–1145 (2004).
11. Karan, K., A. K. Mehrotra, and L. A. Behie, "On Reaction Kinetics for the Thermal Decomposition of Hydrogen Sulfide," *AIChE Journal* **45**(2), 383–389 (1999).
12. Higashihara, T., K. Saito, and H. Yamamura, "S_2 Formation during the Pyrolysis of H_2S in Shock Waves," *Bull. Chem. Soc. Japan* **49**(4), 965–968 (1976).
13. Mellor, J. W., "Hydrogen Sulphide," in *A Comprehensive Treatise on Inorganic and Theoretical Chemistry*, 114–154, S. Se, Ed., Longmans, Green, and Co., London (1956).
14. Tsuchiya, K., K. Kamiya, and H. Matsui, "Studies on the oxidation mechanism of H_2S based on direct examination of the key reactions," *Inter. J. Chem. Kinetics* **29**(1), 57–66 (1997).
15. Frenklach, M., J. H. Lee, J. N. White, and W. C. Gardiner, "Oxidation of hydrogen sulfide," *Combustion and Flame* **41**, 1–16 (1981).
16. Greenwood, N. N. and A. Earnshaw, "Sulfur," in *Chemistry of the Elements*, Pergamon Press, Oxford, U.K. (1984).
17. Steudel, R., Y. Steudel, and M. W. Wong, "Speciation and Thermodynamics of Sulfur Vapor," *Topics in Current Chemistry* **230**, 117–134 (2003).
18. Rau, H., T. R. N. Kutty, and J. R. F. Guedes De Carvalho, "Thermodynamics of sulphur vapour," *J. Chem. Thermodynamics* **5**(6), 833–844 (1973).
19. Wiedemeier, H., "Computational analysis of solid-vapor equilibria for ZnS and SrS phosphor synthesis conditions," *J. Vac. Sci. & Technol. A* **24**(3), 450–458 (2006).
20. Steele, S. R. and J. Pappis, "Chemical Vapor Deposition of IR Materials," F33615-70-C-1577 (1971).
21. Goela, J. and R. L. Taylor, "Monolithic material fabrication by chemical vapor deposition," *J. Mater. Sci.* **23**, 4331–4339 (1988).
22. De, A. K., K. Muralidhar, V. Eswaran, and V. K. Wadhawan, "Modeling of transport phenomena in a low-pressure CVD reactor," *J. Crystal Growth* **267**, 598–612 (2004).
23. Sharifi, Y. and L. E. K. Achenie, "Effect of substrate geometry on the deposition rate in chemical vapor deposition," *J. Crystal Growth* **304**(2), 520–525 (2007).

24. Bryant, W. A., "Review: The fundamentals of chemical vapour deposition," *J. Mater. Sci.* **12**, 1285–1306 (1977).
25. Sladek, K. J., "The Role of Homogeneous Reactions in Chemical Vapor Deposition," *J. Electrochem. Soc.* **118**(4), 654–657 (1971).
26. Sharifi, Y. and L. E. Achenie, "Using density functional theory to postulate a mechanism for zinc sulfide formation in a CVD reactor," *J. Crystal Growth* **307**(2), 440–447 (2007).
27. diBenedetto, B. A., J. Pappis, and A. J. Capriulo, "Chemical Vapor Deposition of Multispectral Windows," AFAL-TR-73-252 (1973).
28. Willingham, C. B., "Hot isostatic pressing of ZnS," personal communication (2007).
29. diBenedetto, B. A., J. Pappis, and A. J. Capriulo, "Chemical Vapor Deposition of IR Materials for Reconnaissance," AFAL-TR-72-309 (1972).
30. Collins, A. K., R. L. Taylor, X. Zhang, and B. D. Bartolo, "Optical Characterization of Polycrystalline ZnS Produced Via Chemical Vapor Deposition," Proc. Electrochemcial Society **PV 90-12**, 626–633 (1990).
31. Campbell, A. and C. Hayman, "Manufacturing Aspects of Zinc Sulphide," *Proc. SPIE* **0915**, 79–83 (1988) [doi: 10.1117/12.945544].
32. Drezner, Y., S. Berger, and M. Hefetz, "A correlation between microstructure, composition and optical transparency of CVD-ZnS," *Mater. Sci. and Eng. B* **87**, 59–65 (2001).
33. Goela, J. S. and J. Askinazi, "Fabrication of conformal ZnS domes by chemical vapor deposition," *Proc. SPIE* **3705**, 227–236 (1999) [doi: 10.1117/12.354627].
34. Goela, J. S., J. Askinazi, and B. Robinson, "Mandrel reusability in precision replication of ZnS conformal domes," *Proc. SPIE* **4375**, 114–127 (2001) [doi: 10.1117/12.439167].
35. Goela, J. and R. L. Taylor, "Large scale chemical vapor deposition," Proc. ASME Thermal Engineering, 623–629 (1987).
36. Goela, J. S. and Z. Salihbegovic, "Low-scatter, high-quality water clear zinc sulfide " CVD, Inc., U.S.A., USPTO 6,083,561 (2000).
37. Vandenbulcke, L., "Theoretical influence of the chemical vapour deposition processes on the thickness and structural uniformity of the deposits," *Thin Solid Films* **102**(2), 149–160 (1983).
38. Ungarish, M., "Modeling the growth of zinc sulfide by CVD," Proc. Sixth European Conference on Chemical Vapour Deposition, 32–41 (1987).
39. Nisenholz, Z. et al., "Windows for infra-red and visible light produced by chemical vapor deposition of ZnS," *Israel J. Technol.* **24**, 627–632 (1988).

40. Savage, J. A., K. L. Lewis, A. M. Pitt, and R. H. L. Whitehouse, "The role of a CVD research reactor in studies of the growth and physical properties of ZnS infrared optical material," *Proc. SPIE* **0505**, 47–51 (1984) [doi: 10.1117/12.964625].
41. Lewis, K. L. et al., "The Mechanical Properties of CVD-Grown Zinc Sulphide and their Dependence on the Conditions of Growth," Proc. Electrochemical Society **PV84-6**, 530–545 (1984).
42. Pickering, M. A., R. L. Taylor, J. Goela, and H. D. Desai, "Effect of Process Conditions and Chemical Composition on the Microstructure and Properties of Chemically Vapor Deposited SiC, Si, ZnSe, ZnS and ZnS_xSe_{1-x}," Proc. Materials Research Society **250**, 145–160 (1992).
43. diBenedetto, B. A. and J. Pappis, "Chemical Vapor Deposition of Multispectral Domes," AFML-TR-75-27 (1975).
44. Gavrishchuk, E. M. and E. V. Yashina, "The Growth Mechanism of Zinc Sulfide from the Gas Phase," *Vyskochistye Veshchestva* **328**(5), 36–39 (1994).
45. Braudeau, P., G. Keller, and J. Torre, "Chemical vapor deposition of IR-transmitting zinc sulphide," *J. Phys. Colloques* **47**(C1), C1-193–C1-196 (1986).
46. Yang, Y. et al., 工艺参数对 "CVD ZnS 沉积速率的影响 [Effect of technical parameters on deposition rate of CVD ZnS]," 人工晶体学报 [*Journal of Synthetic Crystals*] **33**(2), 238–240 (2004).
47. Gavrishchuk, E. M. and E. V. Yashina, "Zinc sulfide and zinc selenide optical elements for IR engineering," *J. Opt. Technol.* **71**(12), 822–827 (2004).
48. Devyatykh, G. G., E. M. Gavrishchuk, A. N. Fatenkov, and E. V. Yashina, "The Effect of CVD Conditions on the Porosity of Zinc sulfide," *Inorg. Mater.* **31**(8), 936–938 (1995).
49. Bredikhin, V. et al., "Optical losses in polycrystalline CVD ZnS," *Inorg. Mater.* **45**(3), 235–241 (2009).
50. McCloy, J., "Semi-empirical Scattering Model for Chemical Vapor Deposited Zinc Sulfide," *Proc. SPIE* **7302**, 73020W (2009) [doi: 10.1117/12.819536].
51. Bansagi, T., E. A. Secco, O. K. Srivastava, and R. R. Martin, "Kinetics of hexagonal-cubic phase transformation of zinc sulfide in vacuo, in zinc vapor, and in sulfur vapor," *Can. J. Chem.* **46**(18), 2881–2886 (1968).
52. Xue, L. A. and R. Raj, "Superplastic deformation of zinc sulfide near its transformation temperature (1020) °C)," *J. Am. Ceram. Soc.* **72**(10), 1792–1796 (1989).
53. Kim, Y.-D., K. Sonezaki, H. Maeda, and A. Kato, "Sintering behaviour of monodispersed ZnS powders," *J. Mater. Sci.* **32**, 5101–5106 (1997).

54. Atkinson, H. V. and S. Davies, "Fundamental Aspects of Hot Isostatic Pressing: An Overview," *Metallurgical and Materials Transactions A* **31A**, 2981–3000 (2000).
55. McCloy, J., "Properties and Processing of Chemical Vapor Deposited Zinc Sulfide," Ph.D. diss., University of Arizona (2008).
56. Carter, C. B. and M. G. Norton, *Ceramic Materials: Science and Engineering*, Springer, Berlin (2007).
57. Karaksina, E., V. Ikonnikov, and E. Gavrishchuk, "Recrystallization behavior of ZnS during hot isostatic pressing," *Inorg. Mater.* **43**(5), 452–454 (2007).
58. Wright, K. and R. A. Jackson, "Computer simulation of the structure and defect properties of zinc sulfide," *J. Mater. Chem.* **5**(11), 2037–2040 (1995).
59. Yashina, E. V., E. M. Gavrishchuk, and V. B. Ikonnikov, "Mechanisms of Polycrystalline CVD ZnS Densification during Hot Isostatic Pressing," *Inorg. Mater.* **40**(9), 901–904 (2004).
60. Goela, J. S., "Low-stress, water-clear zinc sulfide," CVD, Inc., U.S.A., USPTO 6,221,482 (2001).
61. Taylor, R. L., M. J. Lefebvre, P. E. Price, and M. M. Maderazzo, "Erosion-Resistant FLIR Window: Colorless ZnS," F33615-81-C-5076 (1984).
62. Lewis, K. L. et al., "Toughening Effects Induced in Zinc Sulfide by Hot Isostatic Pressing," *Proc. SPIE* **0683**, 64–71 (1986) [doi: 10.1117/12.936417].

Chapter 3
Structure and Microstructure

Before delving into the details of the physical structure of ZnS, it is important to make some statements about terminology. CVD ZnS has many hierarchies of observable structure and so careful use of nomenclature must be maintained in order to avoid confusion. Figure 3.1 shows these scales of structure and the typical techniques used to access information about them. This chapter will start at the atomic scale and work up to the macroscale.

3.1 Atomic Structure

In this section the crystallographic structure of ZnS is presented using data from x-ray and electron diffraction. X-ray diffraction studies show evidence of hexagonality in many if not all of the samples, disordering in the closest-packed direction, and crystallographic texturing. Electron diffraction presents evidence of the nanoscale twinning of ZnS creating hexagonal layers (stacking faults) between regions of cubic sphalerite ZnS.

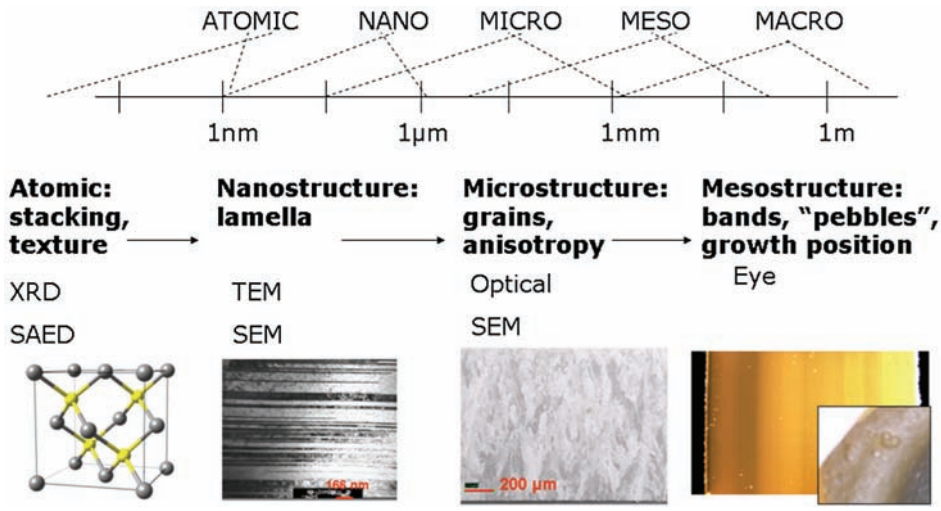

Figure 3.1 Hierarchies of structure in CVD ZnS (from McCloy[6]).

3.1.1 X-ray diffraction

X-ray diffraction has been performed on numerous samples of as-deposited and heat-treated ZnS to investigate any differences that might suggest mechanisms for visible scattering. Both polycrystalline bulk samples and powdered samples were investigated by McCloy and reported here.[2]

3.1.1.1 Polycrystalline sample diffraction and texture

For ease of understanding, the results of the polycrystalline samples will each be discussed very briefly, with comments as to how they relate to the other samples. Figure 3.2 shows all of the polycrystalline XRD samples plotted together with circles to denote specific features that are discussed in the text. Graphs are offset so as to more easily display the features. Commonly observed planes of both sphalerite and wurtzite ZnS appear at the top of the figure for reference. The description starts with the sample at the bottom of the figure and works upward. The number corresponding to the figure is indicated, followed by the full sample name and an abbreviation. Only the distinguishing XRD features of each sample are discussed. When referring to specific planes, "s" indicates cubic sphalerite, and "w" indicates hexagonal wurtzite. In general, all of the following samples can be considered predominantly cubic phase (see also Table 3.1).

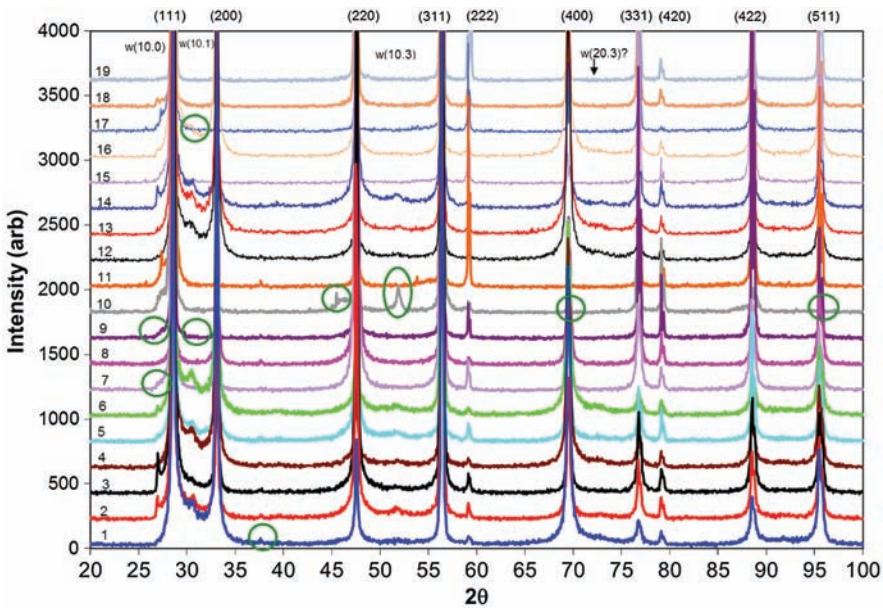

Figure 3.2 X-ray diffraction of polycrystalline specimens of ZnS. Some notable features are circled for particular samples as described in the text.

Table 3.1 XRD-derived parameters. Data taken from McCloy[2,3]. Symbol "-" indicates not measured. Note that all samples were measured as-received, except 1) DOW/Rohm&Haas samples that were commercial CVD grade and subsequently heat treated as indicated and 2) Raytheon legacy CVD material that was HIPed as indicated.

		α_{hex}%	%{001} Texture	%{111} Texture	Lattice parameter	β_{ext} at 1064 nm (cm^{-1})	Re-crystallized?
Raytheon 990°C-Pt-10h	HIP	0.8	2	49	5.411	0.04	Yes
Rafael	HIP	0.7	12	31	5.410	0.11	Yes
DOW/Rohm&Haas Cleartran	HIP	1.3	0	96	-	0.01	Yes
Vitron	HIP	1.3	-	-	5.410	0.26	Yes
DOW/Rohm&Haas 750°C-Pt-16h	HIP	2.2	55	9	5.413	2.56	No
DOW/Rohm&Haas 750°C-Ag-16h	HIP	0.4	4	24	5.413	0.21	Yes
DOW/Rohm&Haas 850°C-24h	Ann	2.1	11	15	5.414	0.60	Yes
Raytheon red	CVD	2.3	16	28	5.414	0.29	No
Raytheon elemental	CVD	3.2	38	7	5.411	0.72	No
Chinese elemental	CVD	4.6	-	-	5.404	0.34	No
II-VI	CVD	9.8	34	18	5.410	2.02	No
Rafael	CVD	5.5	-	-	5.412	2.51	No
Kodak (IRTRAN2)	HP	2.6	15	16	5.406	6.61	No
Sumitomo	HP	23.7	-	-	-	22.0	No
MTI	XL	5.7	-	-	5.411	0.09	N/A
Fairfield	XL	2.7	-	-	-	0.12	N/A

1. CVD, Rohm & Haas 2004 lot (RH-04): Very broad background around the s(111) close-packing direction; evidence of a broadened peak around the w(10.1) plane; a very weak unidentified peak around 2θ=37.8 deg was observed in this and most of the other ZnS samples, which was not found in non-ZnS materials tested in this diffractometer. The s(222) and s(331) peaks seem a bit less intense than average.
2. CVD, Rohm & Haas 2005 lot (RH-05): Broad background around the s (111) direction, but with a sharp peak in the w(10.0) side and a broader one in the w(10.1) side. Some evidence of the w(10.3) peak at around $2\theta = 52$ deg is observable as well in this sample.
3. CVD, Rohm & Haas 2006 lot (RH-06): Very sharp peak at w(10.0), and only a weak background at w(10.1).
4. CVD, Raytheon c1980s (Raytran®ZnS): No evidence of a feature at w (10.0) but very broad background on the long-angle side of s(111) and noticeable peak at w(10.1). The s(222) peak seems a bit less intense than average, and the s(400) is exceptionally strong.
5. CVD, II-VI-Infrared (II-VI): A hint of a step at w(10.0), and a noticeable step at w(10.1).
6. CVD, Princeton Scientific FLIR grade (PS): No peak at w(10.0), but broad background between s(111) and s(200) and sharp peak at w(10.1).
7. CVD, Raytheon Red (Red): Very slight step at w(10.0) that is accentuated when longer integration times (step scans) are used. No features at w (10.1), and very little broadening of s(111).
8. CVD, Raytheon Elemental c1990s (eZnS®): No peaks at w(10.0) or w (10.1), and very little broadening of s(111). Very little s(222) peak.
9. Annealed, Rohm & Haas 2006, annealed in vacuum 850 °C for 24 h (RH-06 Anneal): No peaks at w(10.0) or w(10.1). Slight broadening around s(111).
10. HIPped, Raytheon CVD, Pt HIP at 1045 °C (HIP 1045): This sample was in a HIP run where the temperature controller failed and the experimental temperature reached to 1045 °C, above the transformation temperature for wurtzite. A small shoulder is evident in the w(10.0) position but not much broadening around the s(111), which is also the w(00.2). There is also a considerable broad background between $2\theta = 45.4$ deg and 47.2 deg, just to the short-angle side of the s(220), which is also the w(11.0) plane. The w(10.3) is now a very sharp peak, and the s(400) and s(511) have disappeared completely.
11. HIPed, Raytheon Multispectral ZnS, Pt HIP at 990 °C (M/S Grade® ZnS): The most-obvious change with this sample is the huge intensity increase in the s(111) and s(222) as compared to all of the other peaks, which is not very evident from this particular figure. This is no doubt due to the recrystallization favoring large twinned crystallites. There remains a sharp peak at $2\theta = 27.35$ deg, which could be the w(10.0) peak. There is a

small, unidentified blip at $2\theta = 54.85$ deg along with the one at 37.8 deg observed in most samples.

12. CVD, Rohm & Haas 2006 core, mandrel side (RH-06 core bottom): Very broad background between s(111) and s(200), with a hint of a peak where w(10.1) should be above the background. The s(222) peak is very weak.
13. CVD, Rohm & Haas 2006 core, middle (RH-06 core middle): Very similar to number 12 but with a bit more sharpening of the w(10.1) area and of the s(222) peak.
14. CVD, Rohm & Haas 2006 core, growth side (RH-06 core top): Clear w(10.0) sharp peak along with less broadened but still evident w(10.1) and evident w(10.3). The s(220) peak is much stronger than in the previous two samples, which grew first in the CVD chamber and thus were held at growth temperature for longer.
15. HIP, Ag foil, 750 °C, 16 hours, RH-06 starting material (Ag foil): No peaks or broadening where w(10.0) and w(10.1) should be. Very low-intensity s(200) and s(400) peak.
16. HIP, no metal, 750 °C, 16 hours, RH-06 starting material (HIP no foil): Identical sample to number 15 except that it is treated with no metal. Very broad background between s(111) and s(200) where w(10.1) should be. The s(200) and s(400) peaks are very intense, especially compared to number 15. This sample did not fully recrystallize with the heat treatment.
17. HIP, Co foil, 950 °C, 12 hours, RH-06 starting material (Co foil): Small shoulder and peak where w(10.0) should be. Low-intensity s(200) and s(400) similar to the silver foil sample.
18. CVD, Rafael msZnS: s(220) is strongest intensity line, where an identified sample peaked at $2\theta = 28.8$ deg with intensity about half that of the s(111) peak.
19. IRTRAN 2, hot-pressed ZnS: s(111) is strongest intensity line. Sample appears similar to standard powder pattern.

Figure 3.3(a) compares the diffraction pattern of a typical as-deposited CVD sample versus a typical multispectral ZnS sample. When each is normalized to its peak intensity, the reduction in the line intensities [reflections s (200) and s(400)] and the s(311) and s(511) reflections is striking. By inspecting the points for the powder diffraction file, it can be seen that the multispectral ZnS, which has recrystallized after HIP, is strongly textured on planes. Even when normalized, the other peaks are not as intense as they should be according to the powder pattern. Figure 3.3(b) shows the difference that the silver foil has in changing the diffraction pattern of samples HIPed at 750 °C for 16 h with silver foil and without any metal (HIP33none). The silver-foil sample was recrystallized, and the sample HIPed without metal was not fully recrystallized as evidenced by the strong visible scattering. The sample HIPed with no metal at this low temperature appears crystallographically very similar to the un-HIPed standard ZnS shown in Fig. 3.3(a). The quantitative texture analysis

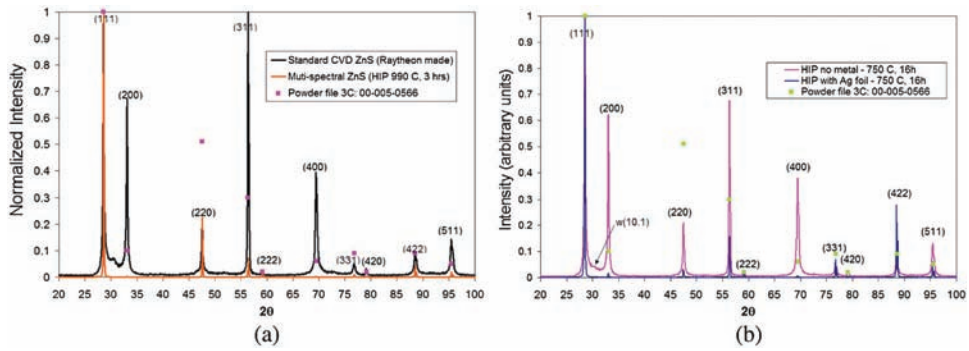

Figure 3.3 XRD comparisons for CVD versus HIP CVD. Intensities for the polycrystalline samples are normalized to the strongest peak in each case. The intensities of the nontextured powder pattern are shown for reference. All indexed peaks are for sphalerite. (a) CVD versus Pt high-T HIP; (b) silver versus no metal HIP; these samples had the same HIP treatment at 750 °C for 16 h. Note that the sample HIPed with no metal still shows signs of wurtzite w(10.1) and texturing like the as-deposited CVD material. The powder pattern is shown for reference.

confirmed that without the silver foil, there was a lack of conversion from the predominant texture of as-deposited samples to the predominant texture of HIPed fully recrystallized samples. In the silver-foil case, there is a strong, residual (422) reflection or a texture, which is removed when the samples are fully HIPed at high temperature (i.e., 990 °C) as in Fig. 3.3(a). Presumably the high temperature along with the pressure allows the dislocations to move and recrystallization to take place more completely in shorter times. These results are discussed in more detail elsewhere,[1,3] and the calculated textures agree with those stated in the literature for HIPed and CVD ZnS.[4,5] It has also been observed that both the cubic and hexagonal textures vary as a function of deposition time, with certain peaks being accentuated depending on their position along the growth direction (see Fig. 3.4).[6]

Various quantitative analysis can be performed on the polycrystalline XRD data to characterize disorder and phase composition.[2] Disordering on the close-packed direction, defined as the integrated area of the (111) sphalerite reflection divided by the fitted background area,[2,5] was found to vary substantially among the as-deposited CVD materials. The disorder in the close-packed direction was essentially absent in the transparent as-deposited samples (i.e., elemental ZnS and red ZnS) and the heat-treated samples (with the exception of the no metal, low temperature 750 °C HIP, which is considered to be unrecrystallized and more like standard CVD ZnS). Lattice parameter measurements were conducted on a limited number of samples using a high-angle alumina peak as a standard to assess angular error.[3] The lattice parameter measurements fundamentally lend support to the notion that CVD ZnS in all of its forms has considerable amounts of substitutional oxygen in sulfur sites, which reduces the lattice parameter.[1,2]

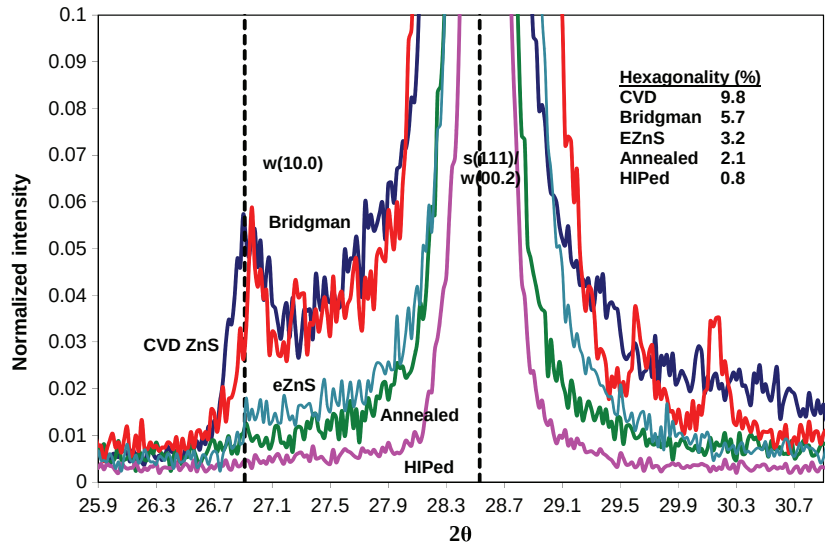

Figure 3.4 Close-up of powder XRD showing the regions used for consideration of hexagonality. Samples indicated are Bridgman (MTI), CVD ZnS (II-VI), eZnS, Annealed (RayCVD, 850C-24h), and HIPed (RayCVD, 990C-Pt-10h).

3.1.1.2 Powder diffraction and hexagonality

The considerable variability found in these polycrystal diffraction experiments, especially around the areas where wurtzite reflections can be identified, led to the investigation of ZnS using powder diffraction.[2] The purpose was to eliminate any effects of preferred orientation and allow the x-ray to have access to all of the possible planes. There was a concern that grinding would convert hexagonal phase to cubic to some extent. Even if this were the case, there was enough difference in the hexagonality of the measured samples that the powder diffraction was useful. The results of this series of experiments can be summed up very simply.

All of the powdered samples measured fell nicely into three groups considering the diffraction around the closest-packed planes. Intensities of the other peaks were very similar if not identical, as expected from powder diffraction, though some evidence of minor powder orientation in the sample holder resulted in relative peak intensities being somewhat different than the powder diffraction file data for cubic (sphalerite) ZnS. The first classification group consisted of all of the heat-treated samples—annealed Rohm & Haas (same sample as the TEM, 850 °C, 24 h in vacuum furnace), multispectral ZnS (990 °C Pt HIP), and two Vitron HIPed samples [one their commercial multispectral material (VIT-CLR), and the other their special no-Pt HIP material (VIT-HH)]. None of these samples showed evidence of a w(10.0) peak or any broadening around s(111) or near w(10.1). Note that in this group

of samples, all had fully recrystallized. It is likely that heat-treated samples that had not fully recrystallized would still show some hexagonal peaks and would not be classed in this group. The appearance of a very weak shoulder in the annealed sample places it on the borderline with the next group.

The second group consisted of as-deposited samples that are intrinsically highly transparent without heat treatment, including red ZnS, elemental ZnS, Chinese ZnS, Raytheon standard ZnS (which was very transparent compared to other "standard ZnS" samples), and Bridgman single crystal. These samples all had a small shoulder in the w(10.0) position. It is interesting that the single crystal would be in this group, but the literature reports that fully cubic single crystals are almost impossible to make and invariably contain some number of stacking faults and disordered hexagonal regions. The red ZnS powder sample had one unidentified peak at $2\theta = 40.57$ deg.

The final group included all of the CVD materials that appear opaque in the visible. This included the Vitron FLIR grade (i.e., yellow standard ZnS), Rohm & Haas 2004 and 2005 lots (which appeared different when investigated as polycrystals), and six samples from the Rohm & Haas 2006 core (two orientations each from the mandrel, middle, and growth side of the core). These samples all appear nearly identical, showing a sharp peak in the w(10.0) position with no other broadening in other wurtzite positions.

A close-up of the region of the XRD spectrum used for determining hexagonality is shown in Fig. 3.4, indicating the narrowing of the s(111) and absence of the w(10.0) peak in heat-treated samples. As-deposited CVD ZnS was determined to have about 2–5 mole percent hexagonality, fully transformed HIPed ZnS has less than 1.0 mole percent hexagonality, and red and elemental ZnS are intermediate.[1] Comparison between XRD texture, hexagonality (α), and optical extinction measured at 1.064 μm (β_{ext}) is shown in Fig. 3.5.

The core-sample comparison is particularly interesting because core-sample diffraction measurements were taken using polycrystals as well (see Fig. 3.6). From the powder diffraction, it was seen that the amount of the hexagonal phase is essentially identical among all of the parts of the core. From the polycrystalline diffraction, it can be seen that hexagonal wurtzite has a preferred orientation that is different in various parts of the core because the relative intensities of the wurtzite peaks and disordered background varies with positions in the core. Texture data supports the crystallographic differences in core position, even in the cubic phase,[2,3] but the overall phase composition seems to be the same, according to this powder diffraction.

3.1.2 Electron diffraction

A systematic study of CVD and HIPed CVD ZnS using TEM has been performed.[2] Some micrographs were indexed per the usual methods[7] and by comparison to other published electron diffraction patterns of ZnS. The

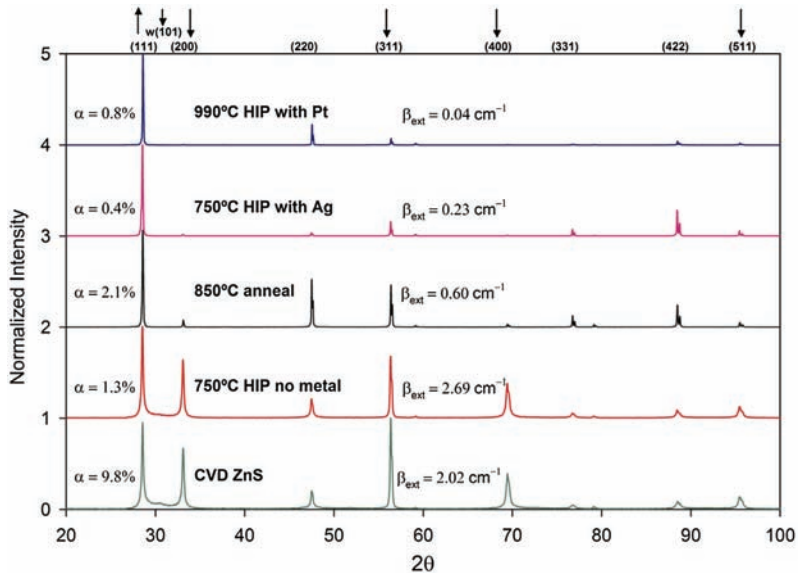

Figure 3.5 Comparison of XRD texture, hexagonality (α), and optical extinction measured at 1.064 μm (β_{ext}) for various samples. Arrows at the top of the figure show the trend change in the XRD peaks from bottom to top. Certain texture changes are associated with recrystallization, which in turn can be associated with reduction in hexagonality and extinction (optical scattering).

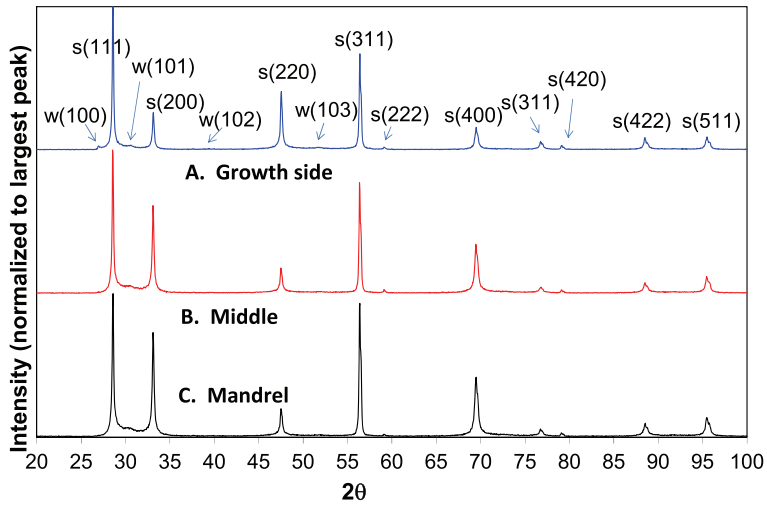

Figure 3.6 Variation in XRD spectra with respect to position in the growth direction. Intensities have been normalized to the largest peak, which is the s(111) here.

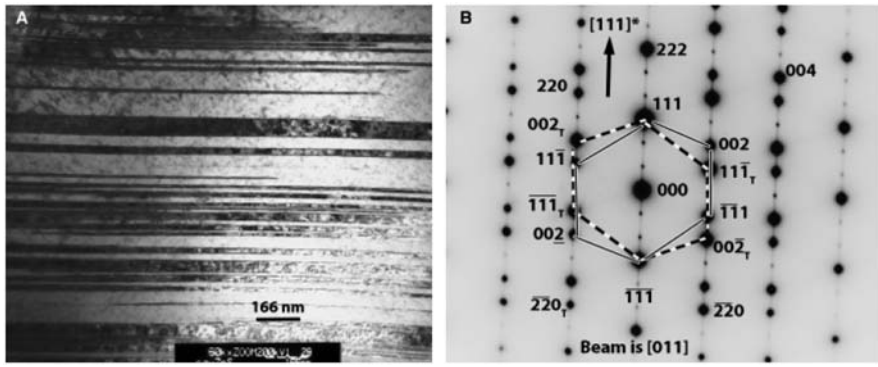

Figure 3.7 Raytheon ZnS 60-k× TEM and SAED of highly twinned region. Subscript "T" indicates twin. The [111] reciprocal lattice row is indicated as [111]*. There are two sets of twins diffracting here, as shown by the two hexagons in the indexed pattern. Some of the other spots cannot be assigned to the cubic lattice, but the whole of the hexagonal lattice is not diffracted either. This suggests simultaneous presence of cubic and hexagonal layers with some disorder in addition to the cubic twinning, which is a single hexagonal sequence (image from McCloy[1] used with permission; copyright 2009 John Wiley and Sons).

most-obvious feature of the diffraction patterns was their evidence for cubic sphalerite twinning. This was apparent at many scales in the as-deposited CVD samples and at a single (larger) scale for the HIPed samples. Also possibly evident in the as-deposited samples was the simultaneous presence of wurtzite phase or at least some hexagonal stacking not associated with twins. The exact nature of the atomic arrangement is still not fully understood.

Fig. 3.7 shows a selected-area electron diffraction (SAED) pattern. Only a few diffraction patterns were taken, but the general results are consistent within the as-deposited samples. In this pattern the splitting of spots from twinning is apparent. The pattern is very similar to those patterns shown by Ma *et al.*[8] from their nanobelts that had coexisting twinned cubic and hexagonal ZnS phases, and Hao *et al.*[9] from their nanowires periodically twinned every 4 nm. The one difference between this pattern and the aforementioned one is that only some of the hexagonal spots seem to be present in this pattern. The spots in the horizontal row of the beam axis should be hexagonal structure spots, but the ones that should be between the twins are not evident. This may be indicative of stacking disorder and imperfect hexagonal phase.

Other diffraction patterns presented in Ref. 2 suggest the existence of cubic regions with twins or hexagonal orientation with some cubic spots. In the former case, similar results have been shown by x-ray precession diffraction pattern from Fleet.[10] TEM diffractions from Holt and Culpan[11] also show similar patterns, but theirs are very streaked along the [111]* reciprocal lattice

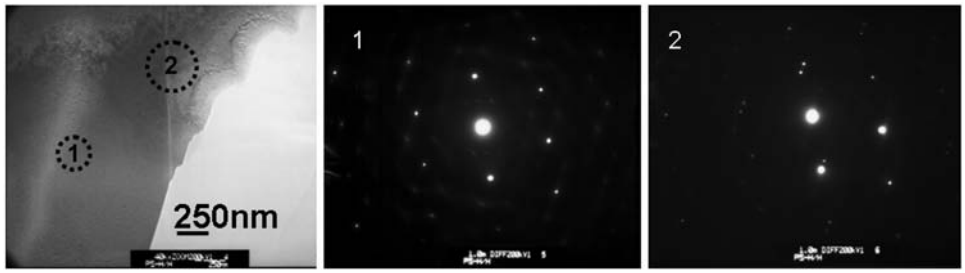

Figure 3.8 Princeton Scientific ZnS 40-k× TEM and SAED of two regions. Region 1 is a bulk crystal region, and region 2 is on a thin twin. Both areas appear cubic.

row, and they indicate that the 6H polytype would produce nearly the same pattern because it is a regularly twinned structure. Streaking is usually caused by disordering along that particular reciprocal lattice vector. In the latter case of hexagonal regions with cubic spots, similar patterns were presented for wurtzite single crystals by Blank *et al.*,[12] and for wurtzite nanobelts by Wang *et al.*.[13] Blank has indexed the pattern in a way that appears to represent the beam direction. In some patterns, the spots that should be absent for pure hexagonal but that may appear due to double diffraction (see Edington[7]) are present. This behavior might once again indicate disordering, with twinned cubic and hexagonal phases occurring together.

Figure 3.8 shows the effect of hot isostatic pressing, with large fault-free regions with some vague double-diffraction spots and thin twin bands remaining. Note the complete absence of fine twinned lamella and disordered regions that are typical of the as-deposited CVD materials. In general, the diffraction patterns of the HIPed or annealed samples were very uninteresting compared to the standard CVD ZnS samples. The regions all appear cubic, but the beam direction was not determined and patterns were not indexed. A few twins were evident, as shown in the previous sections as well, but in general the nanostructure was uniform and cubic.

Together with the microstructural images (discussed in the following section), these diffraction results suggest that CVD ZnS is composed of fine nanosized twins arranged in domains, then grains. The stacking is predominantly cubic, heavily twinned, and contains some other hexagonal stacking disorder. Heat-treated ZnS that is HIPed above ~ 750 °C or annealed above ~850 °C is at least somewhat recrystallized. This recrystallization eliminates most if not all of the nanostructured twins, leaving large, fault-free cubic regions. The grains are twinned on a larger scale, and fully recrystallized HIPed ZnS shows strong texturing from these mesoscale cubic twins. As there are fewer twins in HIPed ZnS, there are fewer hexagonal layers (twin boundaries), and so the overall hexagonality of the recrystallized HIPed ZnS is lower than for CVD ZnS.

3.2 Nanostructure and Microstructure

An overall comparison of CVD ZnS and HIPed CVD ZnS micro- and nanostructure is shown in Fig. 3.8. With simple etching and a light microscope, commercial-grade CVD ZnS can be seen to consist of 5–10 μm "grains" that are more or less equiaxed when viewed on the plane perpendicular to the growth direction in the CVD chamber (referred to by some authors as the "transverse section" or the "plane section"). When viewed perpendicular to this (referred to by some authors as the "longitudinal section" or the "cross-section"), the "columns" show an aspect ratio of approximately 10 times the "grain size" [see Figs. 3.9(a) and (c)]. Although many authors use the term "columnar" for this structure, it is strictly not correct, as columnar structures are more typical of magnetron-sputtered thin films and do not have the "fan-like" structures shown here, but they are very regular and encompass the entire thickness of the film.[14] It is likely that these elongated grains are nucleated by gas-phase-created ZnS or impurities that fall onto the substrate. These protrude farther into the gas stream, exacerbating the nonuniform growth front visible on the surface and resulting in faster growth along these grains. Temperatures are not low enough for rapid nucleation all across the surface for standard ZnS (mandrel or deposition temperature ~670–720 °C). Red ZnS is deposited at approximately 600 °C, does not show this elongated structure in the growth direction, has smaller grains by a couple of microns, and has a different crystallographic texture than standard ZnS.[3] The grain structure looks identical in both the parallel and perpendicular planes. These results collectively suggest that nucleation is more continuous in this material, resulting in fine-grained isotropic materials. This has been reported for continuously nucleated CVD ZnSe as well.[14]

Microstructural images and crystallographic considerations suggest that the preferred growth during the CVD deposition is on "atomically rough" (i.e., not close-packed) planes,[5] which encourages formation of kinks and dislocations, and results in increased rates of nucleation and growth.[15] The resulting CVD microstructure is composed of a complex hierarchy, starting with nanometer-scale lamellae that assemble into domains of which several form a grain. Each hierarchical level is separated by stacking faults or other nonequilibrium boundaries. For standard CVD ZnS there are finer scales of structure that are only visible using SEM or TEM. Looking perpendicular to the growth direction, within each "grain" there appear fine striations or layers (called "bands" by some authors but called "lamellae" here to distinguish from mesoscopic bands described later), and the grain boundaries can be seen to be very irregular (i.e., not in obvious crystallographic orientations or facets). Other authors have described the lamellae within grains as being the "growth layers" in ZnS on the order of 600–800 nm in thickness.[5] Close inspection shows that these layers are parallel within a grain but have different orientations between

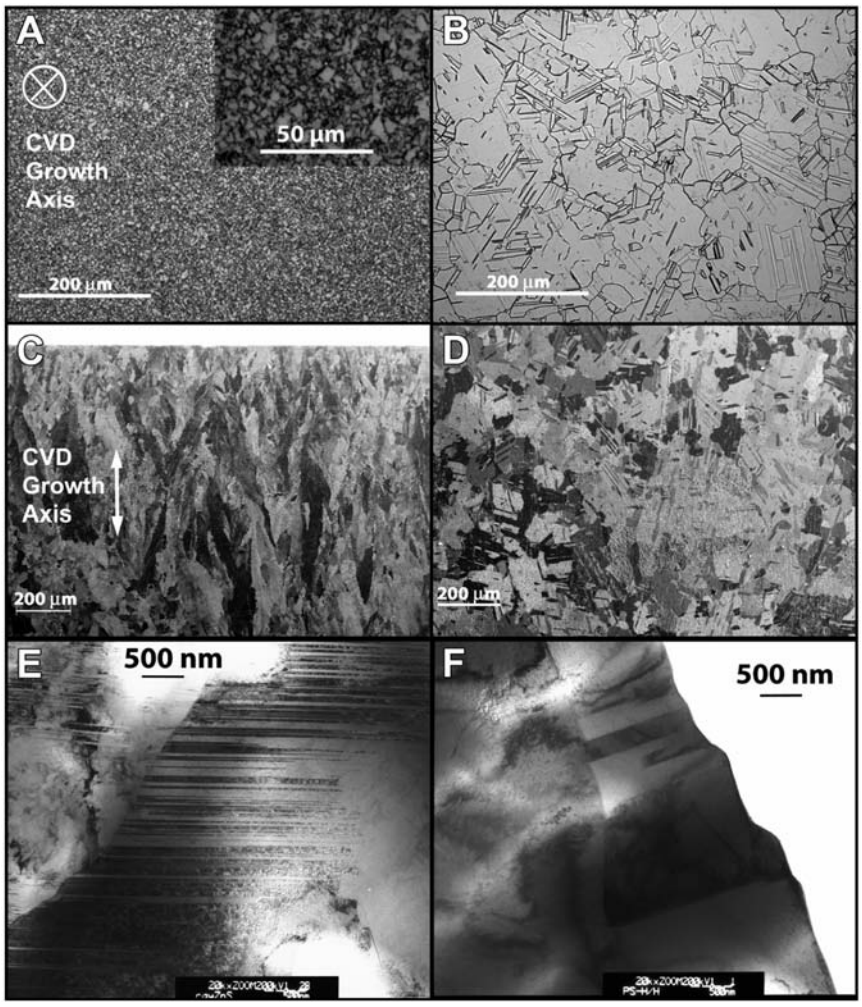

Figure 3.9 CVD ZnS (left) versus HIPed CVD ZnS (right) at various length scales: (A) and (B) optical micrographs perpendicular to the growth direction; (C) and (D) SEM (secondary electron) images parallel to the growth direction; and (E) and (F) TEM (bright field) images in cross-section orientation. Note the major presence of lamellae in CVD ZnS that are absent or at a much-larger scale in HIPed ZnS; dark regions with wavy boundaries in 2F are bend contours due to sample thickness differences from the ion mill, and white regions indicate burn-through of the ion mill or breakage (image from McCloy[1] used with permission; copyright 2009 John Wiley and Sons).

grains. This is also evident when looking at a highly etched grain boundary under high-magnification SEM. These fine growth layers appear as individual fibrous lamellae that are locally oriented (i.e., like bundles of logs).

Transmission electron microscopy gives additional insight into the lamellae observed in high-magnification SEM.[2] TEM images were taken at

magnifications between 10,000–80,000×. All of the as-deposited CVD samples investigated (including several suppliers of standard ZnS, elemental ZnS, six positions and orientations of the cores, and red ZnS) had essentially indistinguishable nanostructures. The structure consisted of parallel layers (lamellae) with widths of 10–90 nm arranged in blocks, which were further arranged into subgrains or "domains." Contrast between the layers is believed to be due to diffraction contrast.[12] No precipitates were observed on any boundaries, and no pores were observed. The layers terminate at boundaries where a new set of parallel layers takes off at a different angle, often the mirror of the angle of the previous side of the boundary. At the highest magnifications, the curved incoherent boundaries at the tips of twins can be observed. These layers are believed to be crystallographic twins on planes (Fig. 3.7). Some of the micrographs, particularly those of red ZnS (Ref. 2) but also in other CVD ZnS, illustrate how the growth-layer sets are stacked on top of each other at different angles. Figure 3.10 illustrates these features at magnifications of 10k× to 80k× for Raytheon CVD ZnS samples. Other CVD ZnS TEM micrographs are shown in Ref. 2 and exhibit similar features to those shown here.

The microstructure of the HIPed material does not typically contain all of the original hierarchical structure, but rather it consists of large, perfect, single-crystallite grains separated by low-angle twin boundaries (hexagonal stacking faults). The extent of the recrystallization depends on various factors, including as-deposited chemical composition of the CVD material along with temperature, gas atmosphere, pressure, and duration of the HIP process. Grain growth during HIPing in argon is believed to occur via a widening of the columnar grains until grains are equiaxed, with twins appearing roughly parallel to the original columns.[16] Some intermediate microstructures have been observed with HIP temperatures of 840–880 °C and pressures of 180 MPa, where coarse 30-μm grains coexist with fine 3–5 μm grains.[17] Fully recrystallized samples from higher-temperature HIPs (940–985 °C) consist of

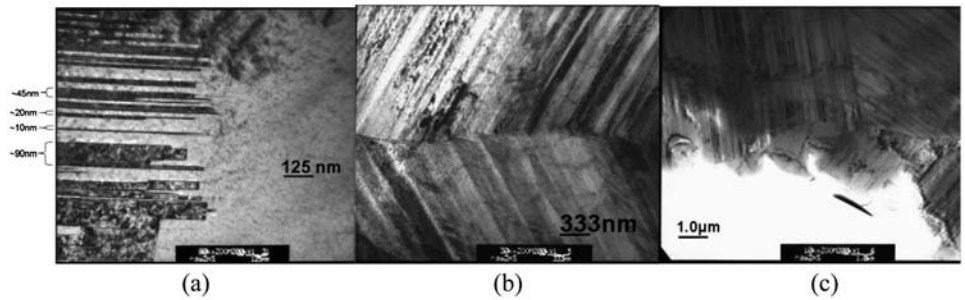

Figure 3.10 TEM image of Raytheon CVD ZnS at (a) 80 k×, (b) 30 k×, and (c) 10 k×. Note the similarity of structure and contrast at all levels of magnification.

"mosaics" of twinned textured crystallites. Higher-temperature HIP runs of 1030 °C (above the transition temperature to the hexagonal phase) result in euhedral grains with 120-deg sharp-tilt boundaries. These euhedral grains, by definition, are evidence of crystal growth unconstrained by adjacent crystals with crystallites, and hence are bounded by characteristic facets.

Hot isostatic pressing of ZnS produces recrystallization and grain growth. The grain morphology is completely different, consisting of angular plates with no remaining exaggerated grain size in the CVD growth direction [see Figs. 3.9(b), (d), and (f)]. In the case of HIPed ZnS, the contrast is somewhat better using a light microscope rather than using SEM because HIPed ZnS is typically colorless and very transparent in the visible. Thus, only a few SEM pictures [Fig. 3.9(d)] were taken, as sample preparation for optical microscopy was easier, and large areas could be investigated quickly [Fig. 3.9(b)].

Transmission electron microscopy of heat-treated CVD ZnS, either annealed or HIPed, showed a vastly different nanostructure than that of as-deposited CVD material [see Fig. 3.9(f)]. All or almost all of the fine layer structure has disappeared; in its place are large areas of seemingly layer-free ZnS. Because larger defect-free areas were available for imaging, the thickness contrast ("bend contours") from the uneven ion milling is more evident in these samples. There are twin boundaries, but crystallites are on average very large, 300–1000 nm or larger. The nanostructures for recrystallized annealed and HIPed ZnS seem to be very similar if not the same. Also, from the two samples investigated, the presence of the metal layer in heat treatment does not appear to have had a significant effect on this nanostructure.

3.2.1 Recrystallization as a result of heat treatment of CVD ZnS

One of the most useful results of the investigation of the etched ZnS was the photographic capture of samples that had only partially recrystallized, including lower temperature HIP experiments with *no* metal foils [see Fig. 3.11(a)].[1] A comparison of recrystallization trends at 750 °C is instructive in comparing the effects of annealing, HIPing, and the presence of metals during heat treatment.[2,18] At 750 °C, a 12–16 h treatment produces *some* recrystallization when HIPed with sputtered Ag or with no metal, but *full* recrystallization occurs when HIPed with Ag or Pt foil. Vacuum annealing with sputtered cobalt at 750 °C for 96 h produced only slight *coarsening* of the grains without recrystallization. However, no metal is required to achieve recrystallization at 850 °C in the anneal furnace and 900 °C in the HIP, based on inspection of the samples in Figs. 3.11(b) and (c). There was not a concerted attempt to find the lowest temperature for full recrystallization without metal in the HIP, but it is somewhere between 750–900 °C. A temperature of 850 °C or possibly lower seems likely, given the experiences in the annealing furnace and the additional pressure acting as a driving force for recrystallization in the HIP.

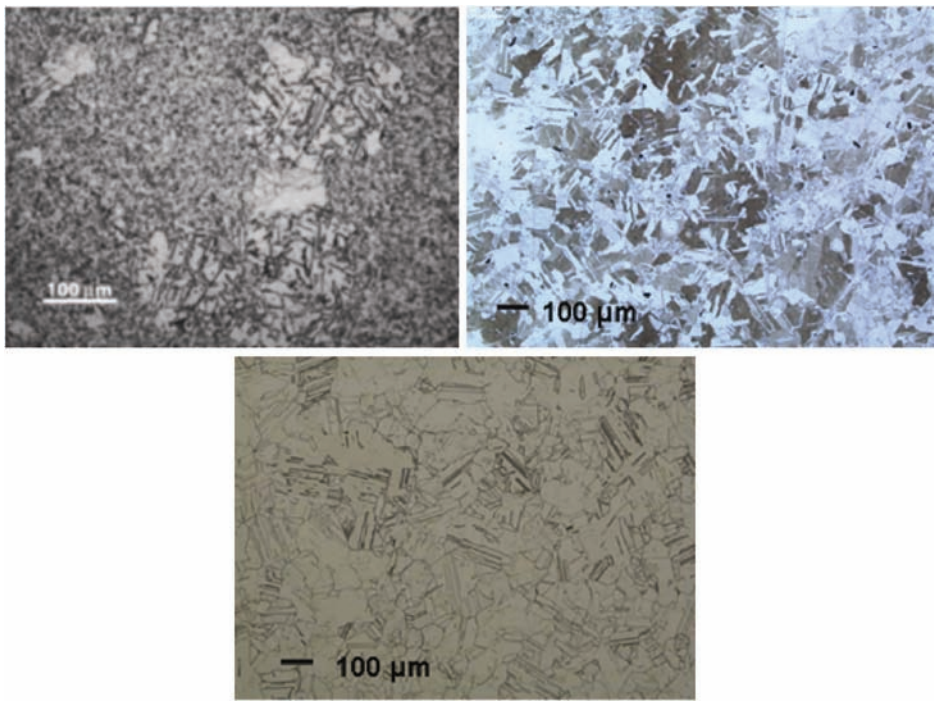

Figure 3.11 Etched, heat-treated ZnS samples recrystallized without metal: (UL) Etched, HIPed ZnS (750 °C, 16 h, no metal foil) showing partial recrystallization; (UR) vacuum anneal (850 °C, 24 h); and (B) hot isostatic press (900 °C, 32 h). Note that the transmission of the HIPed sample was superior, with an extinction coefficient at 1064 nm of 0.17 cm^{-1} versus 0.60 cm^{-1} for the annealed sample, even though the HIPed sample was ~1 mm thicker.

Although only some of the samples were etched, others with similar conditions had high visible transmission, indicative of full recrystallization throughout the entire thickness of the part. The partially recrystallized samples have very poor visible and near-infrared transmission due to scattering. Once the full recrystallization had been identified as key, it was used as a diagnostic of the microstructure. Microstructures that have recrystallized appear similar, regardless of whether pressure was applied during heat treatment, whether metal was used or not, what metal was used if any, or the process of employing the metal.

The observation of the threshold temperature effect on recrystallization led to an interest in determining the mechanism of recrystallization and the role of the metal on the recrystallization. The role of the metal foils in recrystallization has been discussed at length previously.[18] It was previously unknown whether recrystallization proceeded from the surfaces or whether it nucleated homogeneously in the bulk. Samples were prepared to attempt to

observe the results of an "interrupted HIP." Rather than etching the plane on which the metal treatment is applied, in this case the samples were cross-sectioned and etched so that the through-thickness could be viewed. Metal treatment was applied to only one side so as to also compare any recrystallization on the metal versus bare side. The first batch of samples was HIPed at 900 °C for 1 h. A second batch was done with a subset of materials at 750 °C for 2 h to assess the effect of temperature.

The results of the high-temperature interrupted HIP[18] can be summarized as evidence for a homogeneous nucleation of recrystallization throughout the bulk combined with heterogeneous nucleation of recrystallization at the surface near certain metals but not others. The most dramatic example of this surface-induced crystallization is the example of ZnS HIPed with the copper foil, which is shown in Fig. 3.12. In this figure, the face in contact with the copper surface has been recrystallized, and grains have grown markedly. On the surface without metal, some recrystallization has taken place but to an

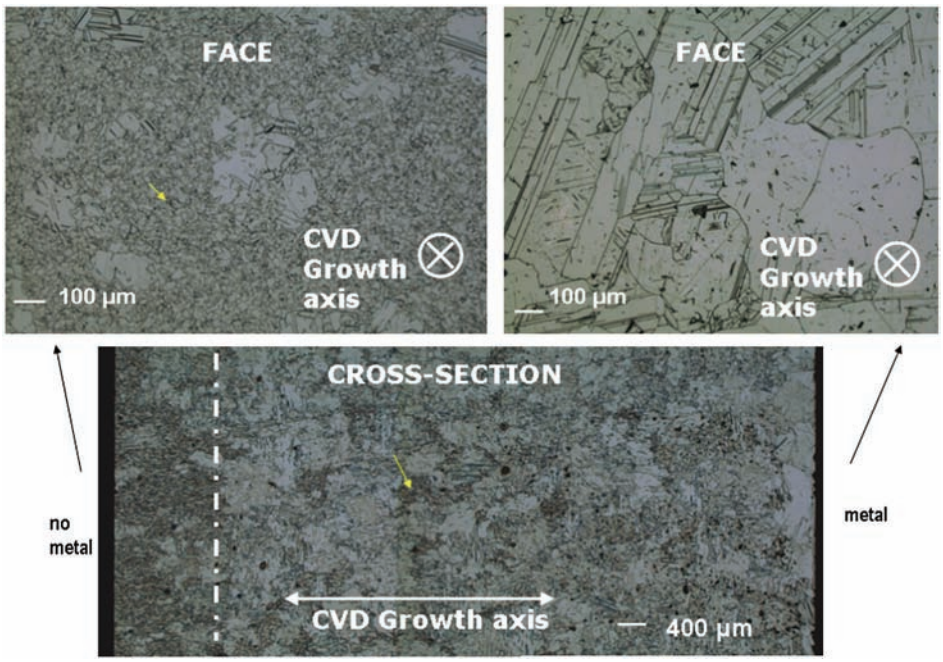

Figure 3.12 Recrystallization of sample exposed to Cu foil in 900 °C interrupted HIP: (UL) face unexposed to metal; (UR) face exposed to copper foil; (B) cross-section showing the recrystallization through the bulk and possible evidence of a recrystallization "front" (dotted line) that moved from the metal side to the nonmetal side. Regions of new grain recrystallization are evident even in advance of the "front," suggesting some component of homogeneous bulk recrystallization at this temperature. Regions that appear unrecrystallized are indicated by small arrows. The CVD growth axis for the upper two figures is perpendicular to the plane of the image, and in the bottom figure is in the plane of the image.

extent similar to the bulk. In the cross-section, it can be seen that the recrystallization is relatively complete throughout the bulk with the exception of a narrow region near the surface without metal. This suggests that the recrystallization may have propagated from the surface in contact with the metal.

Due to the short duration of the heat treatment at 900 °C, recrystallization had not gone to completion (with a possible exception of the Pt sample that appears almost fully recrystallized, including the side not exposed to the Pt). Surfaces in contact with Pt, Cu, and Ni were more fully recrystallized than the surfaces without the metal treatment. In the samples exposed to metals that were promoters of recrystallization, there is evidence of a recrystallization "front" that propagated through the material from the metal-exposed surface to the unexposed surface.

The low-temperature-interrupted HIP at 750 °C provided additional insight. The intent was to eliminate the effects of the homogenous recrystallization that occurred in the bulk due to thermally induced recrystallization. Pt, Cu, Ni, Ag, and C (grafoil) foils were placed on one side of individual samples. A control sample with no metals was HIPed with the others at 750 °C for 2 h. As summarized previously, the Ni, Pt, and Cu all showed evidence of surface recrystallization while samples with grafoil or with no metals did not recrystallize. It was further shown that, at least with Pt, the recrystallization is promoted even if the Pt is not in direct contact with the ZnS,[18] suggesting the importance of some gas-phase transport, but the exact mechanisms are still unknown.

Further work was performed to understand the role of the foils in recrystallization. Pieces of used foil of Pt, Pd, Ag, Au, Ni, Cu, Fe, and Co, having been in contact with ZnS samples during HIPing, were placed in the SEM for imaging and chemical identification using x-ray microanalysis through energy dispersive spectrometry (EDS). These same foils were also examined using x-ray diffraction (XRD) to identify the structure of any materials on the foil. Co and Fe foils, which were "ineffective" at recrystallizing ZnS when HIPed at 750 °C, showed evidence of vapor phase deposited ZnS, whereas "effective" Ni, Pt, Pd, and Cu showed evidence of sulfides of these metals attached to the foil.[2,18] Au foils, though effective at recrystallization, did not show any sulfide formation, and Ag foils showed sulfides on only some occasions. The metals that actively react with sulfur (Pt, Pd, Ag, Cu, and Ni) appear to have the most effect on the recrystallization behavior of CVD ZnS. The iron group materials, Fe and Co, only cause a precipitation of vapor phase ZnS crystals, with the cobalt foil favoring the creation of cubic ZnS and the iron foil favoring the creation of hexagonal ZnS. At this time it is not clear why these two metals produced different ZnS structures, as the treatment temperature (950 °C) was the same in both cases.

3.2.2 Effects of HIP on mechanical properties

The relationship between mechanical properties and microstructure in both CVD ZnS and HIP CVD ZnS has been closely examined. Grains of as-deposited CVD ZnS are "columnar," with the long axis of the grain oriented perpendicular to the mandrel.[19] Grain size generally scales with deposition temperature for unHIPed material. Average grain sizes (columnar cross-sections) range from 2 μm in the lowest-temperature deposits up to over 200 μm for high-temperature deposits.[20]

HIPing of ZnS has been shown to dramatically affect mechanical properties. HIPing reduces hardness and strength, and increases fracture toughness relative to starting CVD material. Direct comparison is not always straightforward, however, because commercial CVD ZnS has a 2–8 μm average grain size, and commercial HIP CVD ZnS has a 20–150 μm average grain size. Compared to CVD ZnS of comparable grain size, hardness in HIPed ZnS is unchanged, whereas indentation toughness is increased due to a higher density and higher elastic modulus in recrystallized material.[21] Young's modulus increases about 15% after HIPing, from 75 GPa to 87 GPa, possibly due to the reduction of charged grain-boundary defects that scatter phonons.[22] Density in CVD ZnS reportedly increases from 4.085 ± 0.001 before HIPing to 4.095 ± 0.001g/cm^3 after HIPing,[5] though in practice there is a wide variability and overlapping range of density for CVD and HIPed material. Room-temperature thermal conductivity increases from 17 W/(m·K) for CVD ZnS to 27 W/(m·K) for HIPed ZnS due to removal of impurities, perfection of the crystallites, and increased grain size.[23,24] Thermal conductivity of ZnS produced by various methods has been reviewed and shown to also follow this trend.[25] See the appendix for further discussion on hardness, toughness, and the elastic properties of ZnS.

Strength is decreased from about 83 MPa before HIPing to 53 MPa after HIPing (~65% reduction).[21] Published strength numbers for these materials vary somewhat due to surface conditions, residual stress, and test conditions. Fractography performed on HIPed ZnS indicates that failure still occurs predominantly from surface flaws,[24] so ascribing lower strength to HIPed ZnS simply due to grain size is not supportable. However, it has been shown that fracture data of CVD ZnS can be well modeled using a bimodal Weibull distribution function, indicating two flaw populations with critical sizes ~20 μm and ~15 μm, which are too large to be assigned to grain boundaries in CVD ZnS with grain size ~8 μm.[26] Similar analyses have not yet been performed for HIPed ZnS, so it may be that some fractures in a distribution could be due to grain-size effects, as has been suggested for CVD ZnSe,[26] which has a microstructure similar to HIPed ZnS composed of large twins with very little "columnar" anisotropic growth. Increased strength of CVD ZnS over HIPed ZnS may be due to residual stresses, present from the CVD process in the as-deposited material, which are released when the material is

HIPed;[27] (HIP temperatures are higher than original CVD ZnS deposition temperatures). There is additional evidence that hydrogen, present in CVD ZnS material and removed with HIPing, may strengthen grain boundaries.[28]

Grain growth during HIPing has been ascribed to various processes. Savage *et al.*[16] suggest that stacking faults become mobile above 500 °C and that defect clusters diffuse towards the surface. Hydrogen and excess Zn leaving the lattice provide the driving force for grain growth. Vacancy-mediated pore coalescence[29] and diffusional processes[17] have also been invoked as the main driving forces for HIPing, with plastic deformation playing a secondary role in microstructural development. McCloy *et al.*[1] have argued for a stronger role for plastic deformation in HIPing of ZnS involving dislocation motion along active slip planes. Additionally, these authors argue the possible importance of diffusion-induced recrystallization during HIPing, where oxygen present at grain and twin boundaries represent the misfit solute that diffuses out and results in crystallographic texture change of the recrystallized material.[1] Finally, a polytype-induced, exaggerated grain-growth mechanism is offered, where a pressure-induced martensitic phase transition occurs, converting hexagonal stacking layers to cubic ones and accompanied by redistribution of oxygen impurities away from grain and twin boundaries.[1] It is apparent from this brief discussion that the mechanisms involved in converting CVD ZnS to HIPed ZnS are complicated, and the resulting changes in mechanical properties require further study to determine the HIP processing limitations for maintaining good mechanical properties while still achieving the desired optical transparency.

3.3 Mesostructure and Macrostructure

At the macroscopic scale, CVD ZnS can be seen to have striations or bands as well as "globules" (botryoidal structures) from anomalous growth at heterogeneities in the growth process. Both banding and "globules" are most readily viewed in thin specimens in transmitted light (see Fig. 3.13). The possible origins of banding and the botryoidal structure and their effects on optical properties have recently been discussed.[6]

Banding in CVD material is visible in transmitted light when viewing orthogonal to the growth direction. Striations have been observed in visible[30] and electron microscopy[11] in single-crystal vapor-grown ZnS, and were tentatively ascribed to contrast induced by polytypes or to faulted bands inducing internal electrical fields. Similar bands of differing coloring in natural sphalerites were found not to correlate with iron impurity content but to have other unknown origins.[31] Nanoscale striations (crystallographic twins) have also been observed for CVD ZnS in SEM[1,32] and TEM,[1,33,34] and have been invoked in understanding the optical losses through scattering.[32,35]

Macroscopic structure in CVD ZnS material exhibits characteristic features that are typical of bulk materials grown with CVD. The yellow

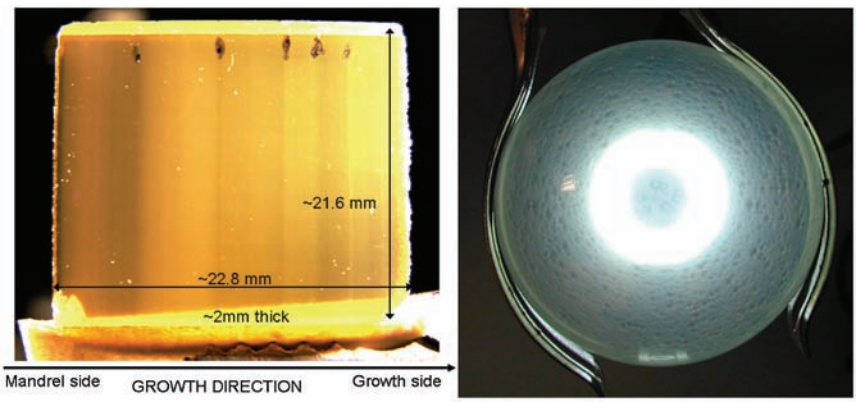

Figure 3.13 Macroscopic features in polished CVD ZnS: (L) View of growth layers of CVD ZnS in the plane parallel to the growth direction. The divisions of the "bands" are evident in the vertical direction in this photograph. This sample was taken from one of the "cores" representing approximately 20 days of growth in the CVD chamber. (R) View of inhomogeneities in elemental ZnS hemisphere using transmitted light. They are difficult to photograph but can be seen as dark specks or regions in the part (sometimes mistaken for water residue marks). These are believed to be due to the nodules or globules that grow anomalously during CVD.

material in transmitted visible light often displays patchy dark regions that appear as spherical features on the order of a few millimeters in diameter. Original nucleation of these structures is thought to be from particles present on the mandrel surface, and growth proceeds from these heterogeneous nucleation sites. These areas protrude farther into the reactant gas stream and so become preferentially built up. The surface morphology of vapor-grown material has been modeled.[36] It was shown that a flat growth front is unstable in growth conditions that are not purely kinetically limited. Whenever there is a degree of diffusion control, where the reactant must be transported to the surface, the concentration gradient in the growth front will result in "domes" at the growth front. A mathematical model was generated that well describes this surface behavior from supersaturated reactant gases such as those used with CVD ZnS and the resulting surface morphology described earlier.

At the limit of long deposition times, the growth surface of CVD ZnS is bumpy and nodular (see Fig. 3.14).[37] These structures have been variously referred to as "haystacks",[38] "pebbles",[39] "botryoidal hillocks",[20] "spicular" growth,[40] "globules",[40] "cone-like",[41] "cauliflower," "rosettes," "petals," and even "alligator skin."

It was recently found that this macrostructure influenced material-removal rates in CVD ZnS (manufactured by II-VI Infrared) by magneto-rheological finishing (MRF).[42] Shape, areal density, and intensity of the "decorated" structure emphasized by MRF polishing were different for mandrel-side and growth-size CVD ZnS surfaces. Material on the mandrel

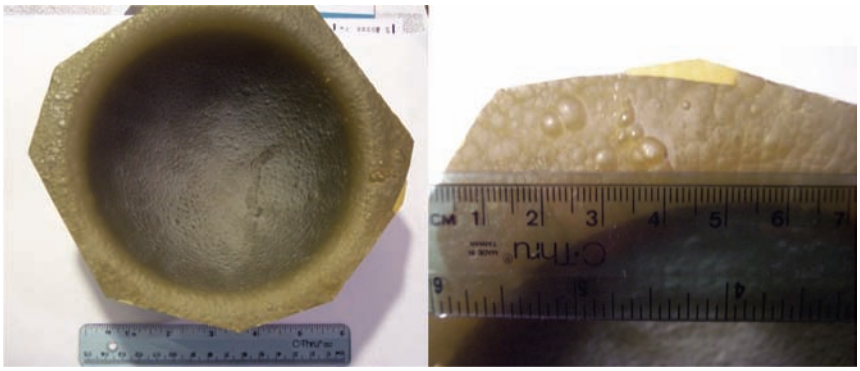

Figure 3.14 Nodular growth on the surface of CVD ZnS away from the mandrel.

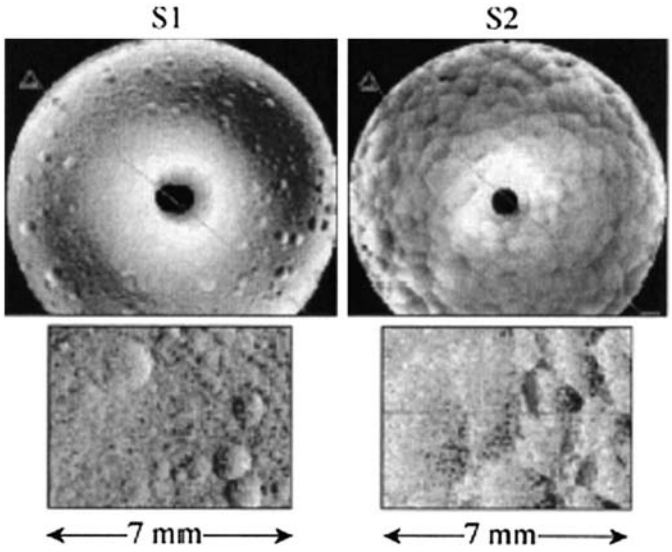

Figure 3.15 Interferometric images of opposite sides of a 20-mm thick CVD ZnS disk after removing 1.5 μm using magnetorheological finishing (image from Kozhinova[42] used with permission).

side was yellowish and, with polishing, showed distinct circular "craters" of <1 mm in diameter, which were only visible using interferometry (Fig. 3.15). Material on the growth side was orangeish and, with polishing, showed large overlapping "petals," some >5 mm in diameter, which were visible to the unassisted eye as well as to interferometry. These structures are explained as resulting from "cones" of material that increase in diameter from the mandrel side to the growth side and are probably associated with the anomalous, exaggerated grain growth visible in cross-sectioned material.

The origin of the visible scattering and differences in mechanical removal rate for CVD ZnS are as yet poorly understood. New characterization

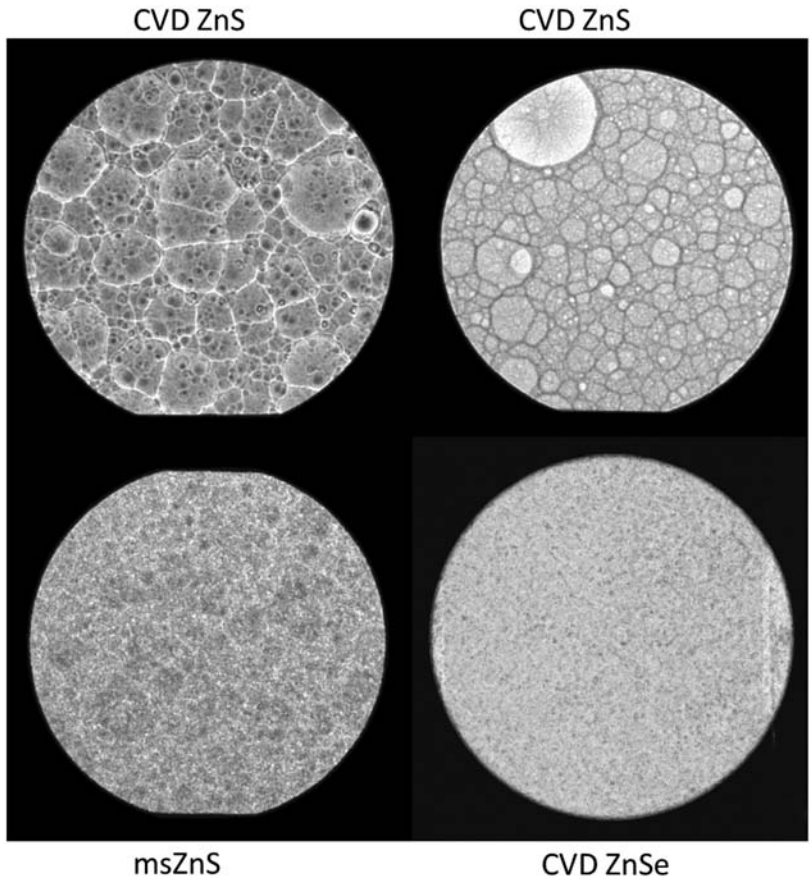

Figure 3.16 110-MHz scanning acoustic microscope images. Sample diameter ~25 mm, with the acoustic image showing the entire sample.

techniques such as scanning acoustic microscopy (SAM) has shown that the nodular structure in CVD ZnS results in different acoustic properties, such that this structure can be easily imaged (Fig. 3.16). Recall that the grain size in commercial-grade CVD ZnS is ~8 μm, so the observed acoustic structure on the ~millimeter scale cannot be attributed to grains. Even after HIPing and recrystallization, the presence of these macrostructures is still evident in SAM, in contrast to CVD ZnSe, which does not show evidence of this superstructure (Fig. 3.16). The fine granularity in these SAM images, including that for CVD ZnSe, is due to the grains on the scale of ~10 μm (slightly bigger for CVD ZnSe). It should be noted that recent work has shown that anisotropy in crystallographic texture (i.e., in the planar versus columnar direction) is present even in HIPed ZnS,[43] and occasionally HIPed ZnS will still show occasional scattering centers that can be identified as residual features of this type.

Very recent work[41] using high-resolution electron backscatter diffraction (EBSD) has dramatically shown that the cone-like structures are polycrystalline areas with differing <001> textures along the growth direction. The main difference between these neighboring regions is their preferred orientation with respect to the <001>. This work also demonstrated the complexity of the CVD hierarchical structure, showing different grain sizes and preferred orientations at the growth substrate in the first 1.7 cm deposited and in regions deposited later. Lamellar boundaries were shown to be Σ3-type twin boundaries on the {111} plane, as expected. Unexpectedly, some grains were found to change their misorientation as a function of time up to 30 deg. The mechanism believed to cause all of the complex structure in CVD ZnS is strain relaxation during CVD growth.[41]

For clear-grade ZnS in particular, manufacturers often specify other qualitative defects as well. In many cases, these indications (e.g., "haze") are based on criteria established for optical glasses, and the phenomenology for these macroscopic defects is poorly documented and understood in the open literature. Inclusions in large domes can include graphite from the mandrels, fibers, and other debris. Gavrishchuk *et al.*[44] have calculated the maximum possible volume fraction of inclusions in cubic ZnS to achieve an extinction coefficient of 10^{-3} cm^{-1} due to scattering as determined by Mie theory. By these methods, the authors determined the limits for inclusion density for wavelengths >0.5 μm. Zinc inclusions are acceptable at 0.3 parts per billion volume (ppbv), pores at 8 ppbv, and wurtzite inclusions at 60 ppbv. For longer wavelengths (>2 μm), more inclusions are acceptable, with Zn at 50 ppbv, pores at 40 ppbv, and wurtzite at 2500 ppbv. These authors also include the curves for estimating the acceptable concentration or volume fraction of inclusions as a function of inclusion size.[44]

References

1. McCloy, J., R. Korenstein, and B. Zelinski, "Effects of Temperature, Pressure, and Metal Promoter on the Recrystallized Structure and Optical Transmission of Chemical Vapor Deposited Zinc Sulfide," *J. Am. Ceram. Soc.* **92**(8), 1725–1731 (2009).
2. McCloy, J., "Properties and Processing of Chemical Vapor Deposited Zinc Sulfide," Ph.D. diss., University of Arizona (2008).
3. McCloy, J. and R. Korenstein, "Variability in Chemical Vapor Deposited Zinc Sulfide: Assessment of Legacy and International CVD ZnS Materials," *Proc. SPIE* **7302**, 73020M (2009) [doi: 10.1117/12.819559].
4. Mironov, I. A. et al., "Physico-Mechanical and Structural Properties of Polycrystalline Zinc Sulfide Obtained by Different Methods," *Sov. J. Opt. Technol.* **59**(7), 417–421 (1992).

5. Shchurov, A. F. et al., "Structure and Mechanical Properties of Polycrystalline Zinc Sulfide," *Inorg. Mater.* **40**(2), 96–101 (2004).
6. McCloy, J., E. Fest, R. Korenstein, and W.H. Poisl, "Anisotropy in structural and optical properties of chemical vapor deposited ZnS," *Proc. SPIE* **8016**, 80160I (2011) [doi: 10.1117/12.886138].
7. Edington, J. W., *Electron Diffraction in the Electron Microscope*, Macmillan, London (1975).
8. Ma, C., D. Moore, J. Li, and Z. Wang, "Nanobelts, nanocombs, and nanowindmills of wurtzite ZnS," *Adv. Mater.* **15**(3), 228–231 (2003).
9. Hao, Y. et al., "Periodically Twinned Nanowires and Polytypic Nanobelts of ZnS," *Nano Lett.* **6**(8), 1650–1655 (2006).
10. Fleet, M. E., "Structural transformations in natural ZnS," *Am. Mineralogist* **62**, 540–546 (1977).
11. Holt, D. B. and M. Culpan, "Scanning electron microscope studies of striations in ZnS," *J. Mater. Sci.* **5**(7), 546–556 (1970).
12. Blank, H., P. Delavignette, R. Gevers, and S. Amelinckx, "Fault Structures in Wurtzite," *Physica Status Solidi (b)* **B7**(3), 747–764 (1964).
13. Wang, Z. et al. , "Morphology-tuned wurtzite-type ZnS nanobelts," *Nature Mater.* **4**, 922–927 (2005).
14. Hartmann, H., L. Hildisch, E. Krause, and W. Mohling, "Morphological stability and crystal structure of CVD-grown zinc selenide," *J. Mater. Sci.* **26**, 4917–4923 (1991).
15. Kingery, W. D., H. K. Bowen, and D. R. Uhlmann, *Introduction to Ceramics*, 2nd Ed., Wiley-Interscience, New York (1976).
16. Savage, J. A., K. L. Lewis, A. M. Pitt, and R. H. L. Whitehouse, "The role of a CVD research reactor in studies of the growth and physical properties of ZnS infrared optical material," *Proc. SPIE* **0505**, 47–51 (1984).
17. Karaksina, E., V. Ikonnikov, and E. Gavrishchuk, "Recrystallization behavior of ZnS during hot isostatic pressing," *Inorg. Mater.* **43**(5), 452–454 (2007).
18. McCloy, J. and R. Korenstein, "The Effect of Metal on the Formation of Multispectral Zinc Sulfide," *Proc. SPIE* **7302**, 73020N (2009) [doi: 10.1117/12.819461].
19. Devyatykh, G. G., E. M. Gavrishchuk, and E. V. Yashina, "Effect of Deposition Conditions on the Microstructure of CVD ZnS," *Inorg. Mater.* **32**(6), 667–669 (1996).
20. Lewis, K. L. et al., "The Mechanical Properties of CVD-Grown Zinc Sulphide and their Dependence on the Conditions of Growth," Proc. Electrochemical Society **PV84-6**, 530–545 (1984).

21. Lewis, K. L. et al., "Toughening Effects Induced in Zinc Sulfide by Hot Isostatic Pressing," *Proc. SPIE* **0683**, 64–71 (1986) [doi: 10.1117/12.936417].
22. Shchurov, A. F. et al., "Effect of Hot Isostatic Pressing on the Elastic and Optical Properties of Polycrystalline CVD ZnS," *Inorg. Mater.* **40**(4), 336–339 (2004).
23. Harris, D.C., *Materials for Infrared Windows Domes: Properties and Performance*, SPIE Press, Bellingham, WA (1999) [doi: 10.1117/3.349896].
24. Henneman, L. et al., "Thermal, Structural and Optical Properties of Multispectral Zinc Sulfide," Proc. 11th DoD Electromagnetic Windows Symposium (2006).
25. Lugueva, N. V. and S. M. Luguev, "The Influence of Structural Features on the Thermal Conductivity of Polycrystalline Zinc Sulfide," *Phys. Solid State* **44**(2), 260–265 (2002).
26. Klein, C., "Flexural strength of infrared-transmitting window materials: bimodal Weibull statistical analysis," *Opt. Eng.* **50**(2), 023402 (2011) [doi: 10.1117/1.3541804].
27. Mecholsky, J. J., Jr., "Grain size effect and toughness in CVD ZnS and HIP'd CVD ZnS," personal communication (2008).
28. Wimmer, E., "Atomistic Modeling of Zinc Sulfide," personal communication (2007).
29. Yashina, E. V., E. M. Gavrishchuk, and V. B. Ikonnikov, "Mechanisms of Polycrystalline CVD ZnS Densification during Hot Isostatic Pressing," *Inorg. Mater.* **40**(9), 901–904 (2004).
30. Schanda, J., M. Somogyi, and M. Gal, "Domain phenomena in ZnS single crystals," *J. Luminescence* **1-2**, 51–60 (1970).
31. Roedder, E. and E. J. Dwornik, "Sphalerite color banding: lack of correlation with iron content, Pine Point, Northwest Territiories, Canada," *Am. Mineralogist* **53**, 1523–1529 (1968).
32. Karaksina, E., T. Gracheva, and D. Shevarenkov, "Structural defects in CVD ZnS," *Inorg. Mater.* **46**(1), 6–10 (2010).
33. Hill, J., K. L. Lewis, and A. Cullis, "The Defect and Band Structure of CVD-Grown Zinc Sulphide," Proc. Electrochemical Society **PV 77-5**, 276–282 (1977).
34. Yu, H. et al., "The study of the relationship between inside defects and optical properties of CVD ZnS," *Proc. SPIE* **4231**, 224–230 (2000).
35. McCloy, J., "Semi-empirical Scattering Model for Chemical Vapor Deposited Zinc Sulfide," *Proc. SPIE* **7302,** 73020W (2009) [doi: 10.1117/12.819536].

36. Gavrishchuk, E., P. L. Krupkin, and L. A. Kuznetsov, "Surface morphology of vapor-grown layers," *Inorg. Mater.* **33**(11), 1117–1120 (1997).
37. Goela, J. and R. L. Taylor, "Monolithic material fabrication by chemical vapor deposition," *J. Mater. Sci.* **23**, 4331–4339 (1988).
38. Adler, W. F., J. C. Botke, and T. W. James, "Response of Infrared-Transparent Materials to Raindrop Impacts," Effects Technology, Inc.; contract F33615-78-C-5143 (1979).
39. Zwaag, S.v.d. and J. E. Field, "Liquid jet impact damage on zinc sulphide," *J. Mater. Sci.* **17**(9), 2625–2636 (1982).
40. Campbell, A. and C. Hayman, "Manufacturing Aspects of Zinc Sulphide," *Proc. SPIE* **0915**, 79–83 (1988) [doi: 10.1117/12.945544].
41. Zscheckel, T., W. Wisniewski, and C. Rüssel, "Microstructure and Texture of Polycrystalline CVD-ZnS Analyzed via EBSD," *Adv. Functional Mater.* **22**(23), 4969–4974 (2012).
42. Kozhinova, I. A. et al., "Minimizing artifact formation in magnetorheological finishing of chemical vapor deposition ZnS flats," *Appl.Opt.* **44**(22), 4671–4677 (2005).
43. Biswas, P. et al., "Effect of post-CVD thermal treatments on crystallographic orientation, microstructure, mechanical and optical properties of ZnS ceramics," *J. Alloys and Compounds* **496**(1-2), 273–277 (2010).
44. Gavrishchuk, E., L. Ketkova, O. Lazukina, and M. Churbanov, "Effect of heterophase inclusions on the optical losses in high-purity IR optical materials," *Inorg. Mater.* **43**(3), 227–232 (2007).

Chapter 4
Optical Transmission

The primary usability assessment of ZnS for multispectral-infrared window applications is its transmission of light in the visible and near-infrared portion of the electromagnetic spectrum (0.4–2 μm wavelength). For this reason, measurements are routinely taken from the band edge in the ultraviolet to the limit of standard laboratory monochrometer equipment (frequently 2.5 μm). Infrared transmission is also taken due to the presence of extinction in transmission in standard as-deposited CVD ZnS out to at least 7-μm wavelength. Additionally, the association of the 6-μm absorption with visible color has been repeatedly stated in the literature (e.g., Ref. 1), and this feature is the most-prominent one in the infrared spectrum of red ZnS and elemental ZnS particularly.

It should be noted that transmission measurements that are to be interpreted quantitatively require careful preparation and measurement protocol. It has been found that surface roughness and wedge in the samples to be measured must be carefully controlled to get reproducible results, especially in the visible and near-infrared. Wedge in the part being measured is routinely kept below five arcmin to avoid these issues. Additionally, direct comparison of two samples where several-percent transmission difference is of interest may require polishing the samples all on the same block throughout each step of the polishing process. The effect of a poor surface polish has been shown to reduce the transmission at 1-μm wavelength as much as 10% in 0.14"-thick samples. It has also been shown that re-polished parts had significantly improved transmittance without having appreciably changed thickness. In the long-wavelength infrared, the effect of unintentional tilt (i.e., the effect of slight differences in how the sample was held in the fixture) has been shown to vary the transmission measurement by 4% and sometimes more across the entire spectrum. In the visible, tilt was readily identified by the periodic oscillations in the transmission due to the etalon effect.

One quick way of assessing the quality of the measurement is to plot the measured data versus the maximum transmittance based on the index of refraction:[2]

$$T_{\max} = \frac{2n}{n^2 + 1}, \tag{4.1}$$

where T is the transmittance (a number between zero and one), and n is the index of refraction, which is a function of wavelength. Tabulated index data or those based on fitted Sellmeier dispersions can be used. In this prediction the transmittance is only based on the reflection from the two surfaces, and extinction by absorption and scatter are neglected. Some of the FTIR measurements frequently indicate transmittances higher than the theoretical maximum, denoting a measurement with some tilt.

Samples were polished as much as possible to similar thicknesses in the data reported here so that direct comparisons can be made using transmission graphs. Because the samples were never exactly the same thickness, and because it was sometimes desirable to assess process progression as a function of thickness, extinction coefficients were calculated and used as a metric. The wavelength of interest in this case was 1.064 μm, the Nd:YAG solid-state-laser line. The extinction coefficient was calculated as follows:

$$\alpha = \frac{1}{L} * \ln\left[\frac{(1-R)^2}{2(T/100)} + \sqrt{R^2 + \frac{(1-R)^4}{4(T/100)^2}}\right], \tag{4.2}$$

where β is the extinction coefficient (in cm^{-1}), L is the sample thickness, T is the measured transmittance in percent, and R is the single-surface reflectivity in air calculated from the index of refraction (real part n and imaginary part k, which can be neglected in this low-absorbing region):

$$R = \frac{(n-1)^2 + k^2}{(n+1)^2 + k^2} \approx \frac{(n-1)^2}{(n+1)^2}. \tag{4.3}$$

The same equation rearranged is the familiar one for calculating the transmission of an absorbing window:[2]

$$T(\%) = 100 * \frac{(1-R)^2 e^{-\alpha L}}{1 - R^2 e^{-2\alpha L}}. \tag{4.4}$$

It should be reiterated that β is the *extinction* coefficient and thus includes the effects of both absorption and scattering. This is a critical distinction in ZnS, as the effects of absorption at the ultraviolet edge can be eliminated by heat treatment while at the same time accentuating the effects of scattering.[3] This has been demonstrated in the heat treatment of transparent red ZnS, where the color can be removed but at the expense of producing a white, scattering ZnS.

For many years, scattering has been implicated as being responsible for the low visible and near-infrared transmission of CVD ZnS. For the purposes

of CVD ZnS, scattering could be due to (1) pores,[4] (2) hexagonal-phase ZnS in a cubic matrix, (3) metal impurities, or (4) refractive index inhomogeneity due to differential incorporation of impurities such as oxygen.[5] The driving force for scattering is ultimately the difference in refractive index between the matrix (cubic ZnS) and the scatterer. The largest index difference from the ZnS matrix would be air (pores), and the smallest difference would be local density fluctuations or birefringence due to stacking differences (i.e., hexagonal layers) or chemistry differences (i.e., oxygen in sulfur sites).

4.1 Experimental Transmission Curves

4.1.1 Single-crystal ZnS

A thorough evaluation of transmission in CVD ZnS has been undertaken by McCloy[23] and is described here. Transmission of single-crystal ZnS (Bridgman melt grown) was tested alongside single-crystal ZnO (hydrothermally grown) and CVD ZnSe. The ZnS crystal (110) plane sample was largely cubic, but in x-ray diffraction was shown to have some hexagonal component.[3] The ZnO crystal was a (00.1) *c*-axis plane, and no difference was seen in transmission with light originating at the zinc-terminated surface versus the oxygen-terminated surface. The ZnSe sample was polycrystalline CVD material. Single-crystal ZnSe was not readily available, and this particular sample was thick and somewhat scratched, so the infrared transmission is lower than expected due to surface scattering. Other than this, the average transmission in the transparency region for all samples can be seen to be due mainly to reflection because the refractive index is highest in ZnSe, followed by ZnS and ZnO.

Comparison of the transmission of zinc with increasingly heavier anions is illustrative of trends in II-VI materials. Figure 4.1 is a composite of UV-VIS-NIR and FTIR spectrometer measurements. The figure is labeled with characteristic multiphonon absorptions and their assignments for ZnO,[6,7] ZnS,[8] and ZnSe.[9] Note that considerable disagreement among various sources was found on multiphonon assignment, particularly for ZnO,[10] and preference was given to more recent articles. The effect of the heavier anion moving the infrared transmission cutoff to longer wavelengths is clearly evident.

Figure 4.2 shows the effect of the electronic bandgap on the ultraviolet transmission cut-on wavelength. Of the three materials, ZnS has the largest electronic bandgap, followed by ZnO and ZnSe. The measured room-temperature ultraviolet (UV) cut-off, defined as the last spectrometer data point before a negative transmission value is recorded, was 340 nm (3.65 eV) for ZnS, 387 nm (3.20 eV) for ZnO, and 473 nm (2.62 eV) for ZnSe. These bandgap values are slightly smaller than the usually accepted numbers (e.g., Ref. 11), but these samples were fairly thick, and the ZnSe material was not the purest available.

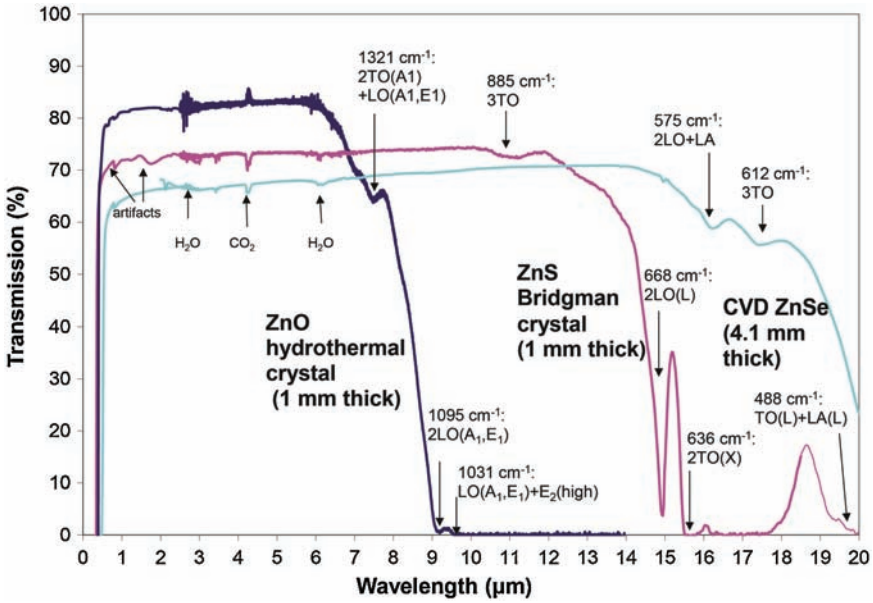

Figure 4.1 Transmission of ZnO, ZnS, and ZnSe. Note that the features below 6 μm are measurement artifacts due to gases in the spectrometer (H_2O, CO_2) as well as grating/detector changes. Significant multiphonon features are labeled.

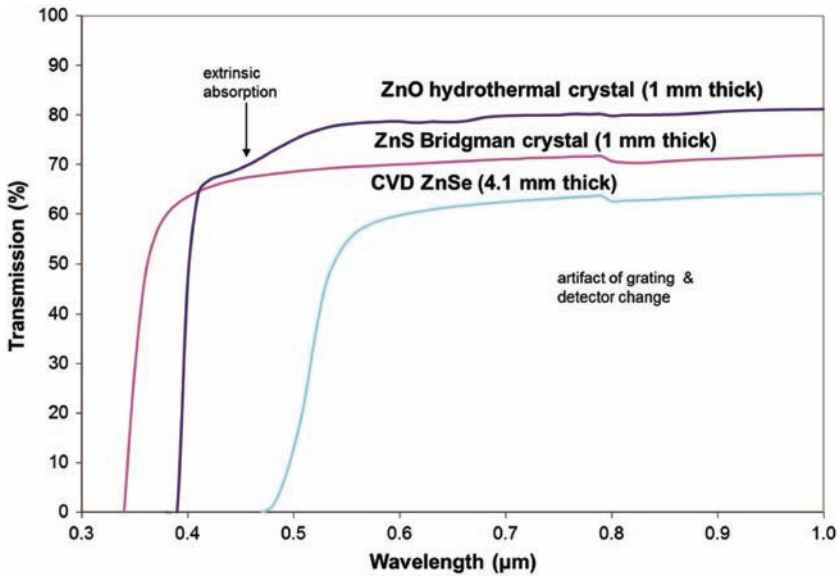

Figure 4.2 Band-edge transmission of ZnO, ZnS, and ZnSe.

4.1.2 Polycrystalline ZnS, no postprocessing

CVD ZnS materials without heat treatment vary widely in their visible and near-infrared transmission and their presentation of the 6-μm absorption band.[3] Many researchers have shown the effects of deposition temperature on the presence of the 6-μm absorption band and associated scattering, but definitive conclusions regarding the interplay of reactant stoichiometry and deposition temperature on the transmission are lacking.[12–16]

Samples from several suppliers of standard CVD ZnS were measured for transmission, including legacy Raytheon (Raytran®), Vitron, Rohm and Haas, II-VI, Rafael, and Princeton Scientific. Additionally, legacy Raytheon CVD materials, namely red ZnS and elemental ZnS, were compared to current commercially available standard ZnS. Samples were obtained of Chinese ZnS made by a process similar to elemental ZnS.[17] Two powder hot-pressed ZnS samples were obtained: one made by Eastman Kodak in the 1950s and marketed as IRTRAN 2,[18] and the other made recently by Sumitomo Japan. Finally, two samples of single-crystal ZnS were obtained: one produced by the Bridgman method and sold by MTI, and the other made by an undisclosed process (Fairfield Crystal).

It was expected that, among the various materials, there would be variation in the amount of transmission loss in the visible and near-infrared (due to scattering), the visible coloration (due to position of the band edge), and intensity of the 6-μm absorption band. These variations might be expected due to differences in impurity levels of hydrogen and oxygen, different manufacturing processes (e.g., CVD with H_2S, CVD with H_2, hot pressing from powders), and different heat treatments. A summary of transmission measurements and calculated extinction coefficients is shown in Table 4.1.

Transmission differences of the main classes of CVD ZnS are compared in Fig. 4.3. Materials were of comparable thickness, so transmission graphs can be compared directly. The curve labeled "1" is multispectral ZnS, which is CVD ZnS that has undergone a high-temperature (~990 °C) HIP step with platinum foil. Note that the transmission is very high through the visible, and there is no absorption around 6 μm. The curve labeled "2" is red ZnS, which is CVD ZnS deposited at a very low temperature (~640 °C) with a very high excess of zinc. Note the low extinction in the visible region, though the position of the band edge at ~400–415 nm accounts for the color (see Ref. 3). In red ZnS the 6-μm absorption band is very wide and deep, and is resolved into two sharp minima (see Fig. 4.5). The curve labeled "3" is elemental ZnS, which is CVD ZnS made from reacting hydrogen and sulfur together directly before mixing with zinc vapor. Note that there is some extinction in the visible, and the 6-μm absorption band is present and weakly resolved into three lines (see Fig. 4.5). Finally, the curve labeled "4" is standard CVD ZnS produced from commercial hydrogen sulfide gas and zinc vapor. Note the

Table 4.1 Transmission and absorption for various ZnS samples tested. Type of material listed as CVD (chemical vapor deposited), HIP (CVD+hot isostatic press), XL (single crystal), or HP (hot pressed powder). Note that when comparing transmission values, pay close attention to sample thickness because transmission varies with sample thickness. Extinction coefficients (β) are independent of thickness, but have a larger contribution due to surface scattering for thin samples.

				$T_{1.064}$/ $\beta_{1.064}$	$T_{3.39}$/ $\beta_{3.39}$	$T_{6.0}$/ $\beta_{6.0}$	$T_{10.6}$/$\beta_{10.6}$
		Thickness (mm)	**UV edge (nm)**	$n = 2.288$	$n = 2.255$	$n = 2.240$	$n = 2.192$
Theoretical (no scatter, phonon abs)	Type	n/a	340	73.5%	74.1%	74.5%	75.5%
Vitron FLIR	CVD	2.00	380	28.7% / 4.59	68.5% / 0.38	62.8% / 0.82	72.5% / 0.20
DOW/ Rohm & Haas	CVD	4.64	382	16.9% / 3.11	56.9% / 0.55	60.8% / 0.42	68.4% / 0.21
Rafael CVD	CVD	2.49	361	50.9% / 1.42	65.9% / 0.45	70.4% / 0.22	70.8% / 0.25
II-VI Infrared	CVD	4.89	383	26.8% / 2.02	61.0% / 0.38	60.9% / 0.40	64.8% / 0.30
Princeton Scientific FLIR	CVD	5.13	390	8.4% / 4.18	54.3% / 0.59	50.9% / 0.72	64.7% / 0.29
Raytheon Red	CVD	3.18	400	67.0% / 0.27	72.2% / 0.08	48.1% / 1.33	67.9% / 0.32
Raytheon Elemental	CVD	4.64	386	55.3% / 0.59	72.9% / 0.03	59.6% / 0.46	68.7% / 0.14
Chinese	CVD	4.62	386	62.1% / 0.35	71.8% / 0.07	73.1% / 0.04	68.4% / 0.21
Raytheon Multispectral	HIP	4.64	344	72.0% / 0.04	73.6% / 0.01	74.4% / <0.01	69.2% / 0.18
DOW/ Rohm&Haas Cleartran	HIP	8.06	340	72.7% / 0.01	72.3% / 0.03	73.3% / 0.02	62.9% / 0.22
Vitron Multispectral	HIP	2.00	345	71.9% / 0.10	73.5% / 0.04	74.2% / 0.02	73.0% / 0.16
Rafael Multispectral	HIP	2.54	343	71.3% / 0.11	71.8% / 0.12	72.6% / 0.09	70.6% / 0.26
Princeton Multispectral	HIP	5.13	340	67.1% / 0.17	69.8% / 0.11	70.6% / 0.10	65.0% / 0.28
Bridgman single crystal	XL	1.00	340	73.1% / 0.04	72.8% / 0.17	73.2% / 0.16	73.3% / 0.29
Fairfield single crystal	XL	1.08	340	72.4% / 0.12	71.8% / 0.28	72.6% / 0.22	73.1 % / 0.29
Kodak IRTRAN2	HP	6.39	445	1.1% / 6.54	63.3% / 0.24	71.3% / 0.06	60.5% / 0.34
Sumitomo hot pressed	HP	2.03	400	0.8% / 22.0	53.5% / 1.56	69.5% / 0.33	69.9% / 0.37

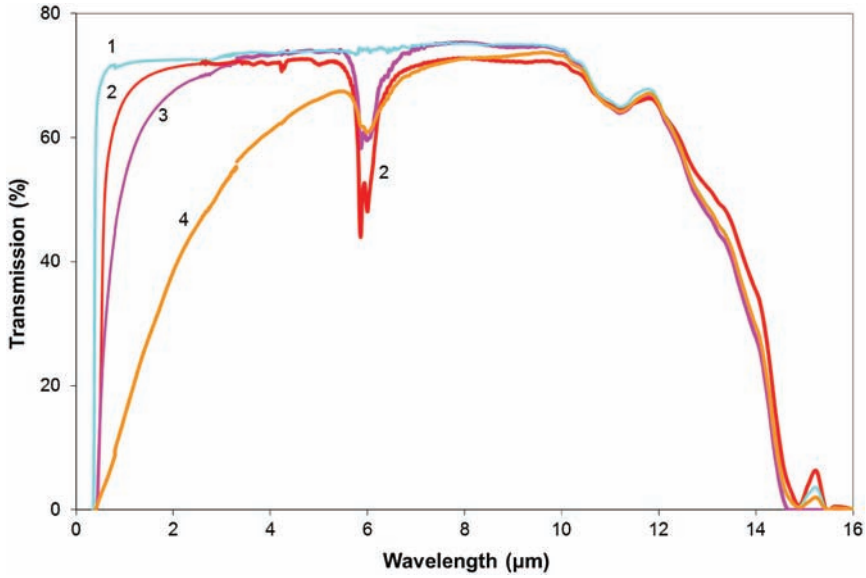

Figure 4.3 CVD ZnS transmission: (1) msZnS, (2) redZnS, (3) eZnS, and (4) stdZnS.[3]

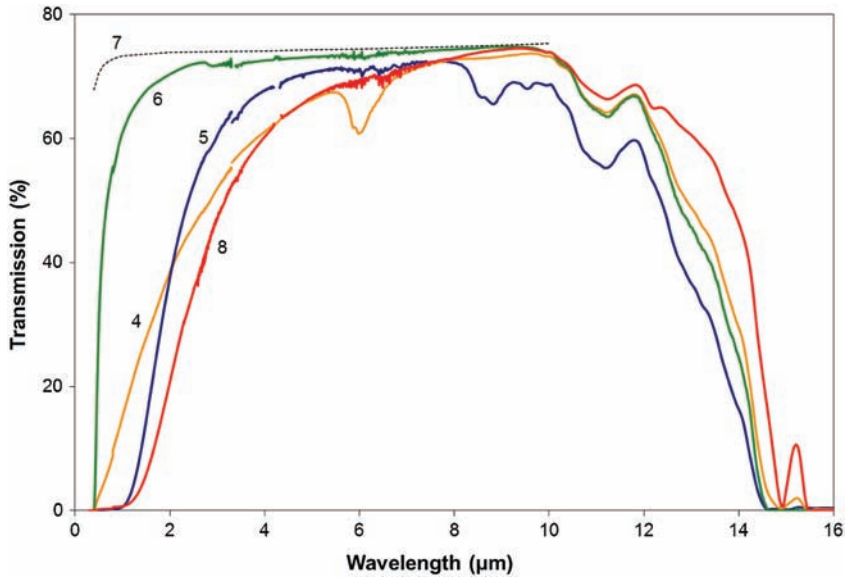

Figure 4.4 ZnS transmission: (4) stdZnS, (5) hot-pressed powder ZnS (IRTRAN2), (6) Chinese CVD ZnS, (7) T_{max} calculated per Eq. (4.1),[3] and (8) hot-pressed powder ZnS (Sumitomo).

large transmission reduction that continues through to at least 10 μm and the higher-order absorption at 6 μm superimposed on the scattering losses. Figure 4.4 illustrates transmission of other forms of ZnS. The curve labeled "4" is the same standard CVD ZnS sample as in the previous figure.

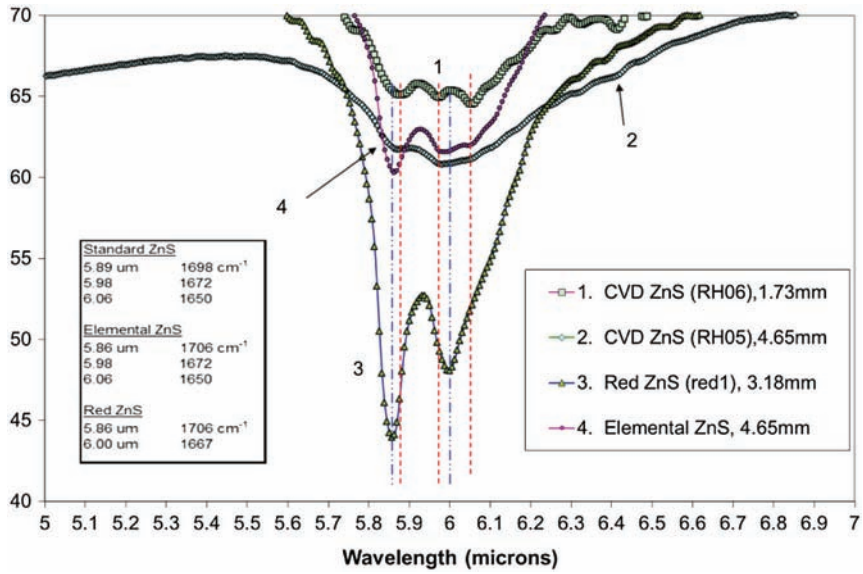

Figure 4.5 Transmission of ZnS in the vicinity of the hydride absorption.

Curve "5" is a slightly thicker hot-pressed ZnS from powder precursors. Note the different wavelength dependency of transmission loss as well as a strong extrinsic absorption at 8.9 μm. Curve "6" is the sample of ZnS produced in China, which in many respects is similar to elemental ZnS (curve "3" in the previous example) with slightly better visible transmittance for its thickness, but unlike eZnS has no 6-μm absorption. Finally, curve "7" is the reflection-only transmission (T_{max}, defined earlier) that would result if losses were only due to the refractive index. It is apparent from this comparison that all three of these materials have extrinsic losses from scattering and/or absorption in the visible and near-infrared.

The most prominent absorption feature in as-deposited CVD ZnS materials is, of course, the 6-μm absorption that has historically been assigned to zinc hydride.[1] Morozova *et al.*[19] assigned the 6-μm absorption in CVD ZnS to "imperfect ZnO" and claimed that the fine structure arising from 5–8 μm after annealing CVD ZnS[19] or CVD ZnSe[7] was due to multiphonon absorption of ZnO precipitates in these materials.

In CVD ZnS the main infrared feature is the broad absorption with one to three resolved minima at 5.9, 6.0, and 6.1 μm. This absorption was found to consist of a doublet in red ZnS and a triplet (which was often blurred into a series of weak shoulders) in CVD ZnS and elemental ZnS. *Ab initio* vibration calculations assign these absorptions to Zn-H-Zn stretch modes.[20] The doublet should be from a ZnH_2 in a sulfur site, and the triplet should be from

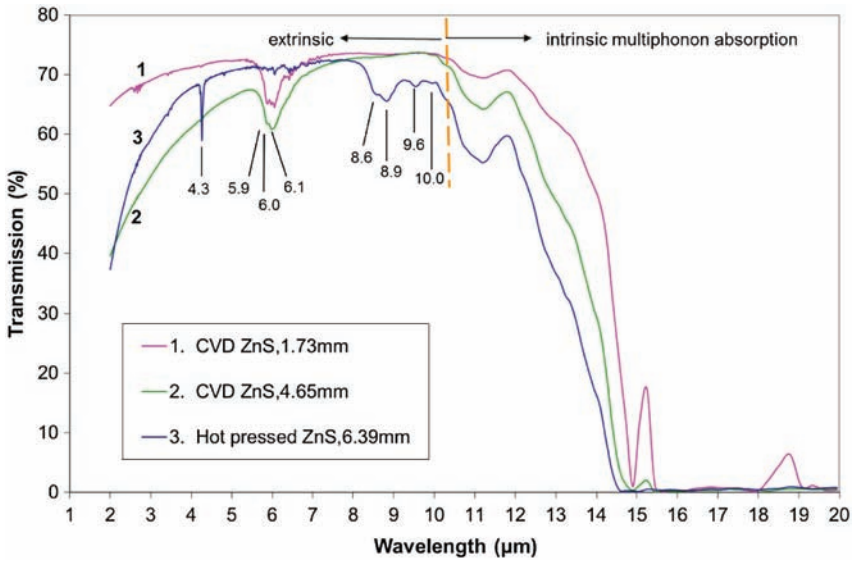

Figure 4.6 Extrinsic infrared absorptions in ZnS samples.

a ZnH_3 in a sulfur site. Figure 4.5 shows the measurements of several samples and the spectral position in wavelength and wavenumber for these vibrations.

A few other absorptions have been identified in this work for a few samples, but they have not yet been definitively assigned. Figure 4.6 shows the transmission spectra of successively thicker samples of ZnS, the first two of CVD ZnS and the third of hot-pressed ZnS. Plotting the three samples of increasing thickness allows one to appreciate the change of the multiphonon edge (wavelengths longer than 10.1 μm, which is assigned to 3LO after Ref. 21). This also helps distinguish between those absorptions extrinsic and intrinsic in ZnS. Some of these absorptions are labeled with their wavelength in microns.

In addition to differences in transmission occurring due to different fabrication processes, it has been observed that transmission can vary somewhat within CVD materials as a function of position in the deposition chamber, orientation with respect to the growth axis, and time in the growth chamber.[22] These differences are believed to be due to differences in amount of hexagonality, polycrystalline texturing, and impurity absorption, which differ spatially. Photoluminescence has been shown to be substantially different in samples from a single core of CVD ZnS, representing ~500 h of growth, depending on its layer position and orientation with respect to the CVD growth direction.[23] However, in investigating possible changes in refractive index under these conditions, it was determined that electronic defects responsible for these photoluminescence differences did not result in measurable changes in refractive index for CVD ZnS.[24]

4.1.3 Heat-treated and HIPed samples

A series of HIP runs at various temperatures was performed for CVD samples with or without the presence of metal foils. HIP pressure was maintained at 30 ksi (207 MPa). UV-VIS-NIR extinction [as calculated by Eq. (4.2)] is shown for CVD ZnS exposed to various heat treatments in Fig. 4.7.[25] It can be seen that HIP at 750 °C with no metal present does not result in transmission improvement. When its microstructure was investigated, this sample was shown not to have undergone recrystallization. By contrast, HIP at 750°C in the presence of Ag results in large transmission improvements (reduction in extinction) and is associated microstructurally with grain recrystallization as described in Chapter 3. Figure 4.7 shows the effect of this HIP condition (750 °C for 16 hours) on thick (~ 4.6 mm) CVD ZnS samples exposed to no metal, Fe, Co, Ag, and Pt. It can be seen that both Ag and Pt are effective at inducing recrystallization and thus improving transmission, whereas Fe and Co are ineffective. The effect of other metals is discussed elsewhere.

Figure 4.8 also shows that at 850 °C, no pressure is needed to improve the transmission of CVD ZnS, and the annealed sample has low extinction. This is not generally true for samples heat treated without pressure, however, as described in Section 4.2.1. HIP at high temperature (≥850 °C) does, however, effectively induce recrystallization, more so than annealing, even without the presence of metal. In general, HIP with Pt metal at high temperature (990 °C) shows the best improvement of transmission, due to the combined actions of

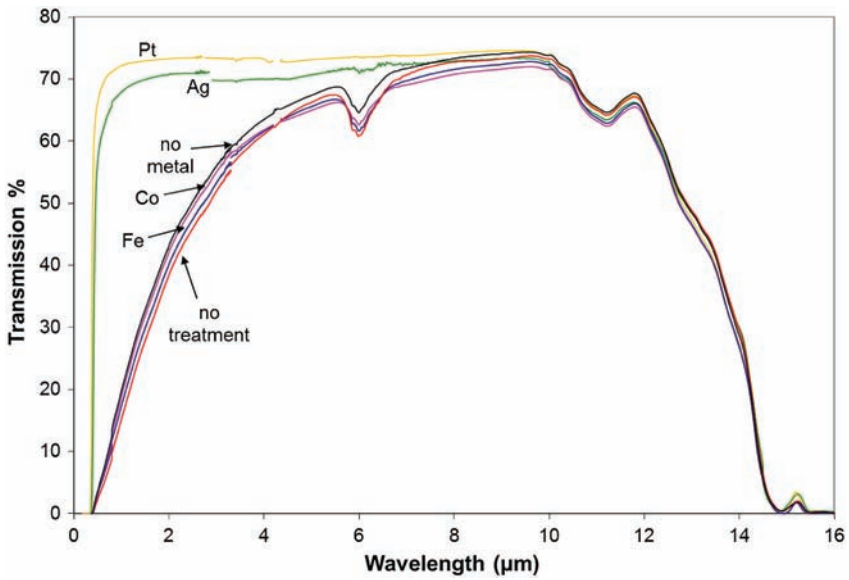

Figure 4.7 Transmission curves compared for 750 °C, 16 h with various metals. All samples were ~4.5-mm thick.

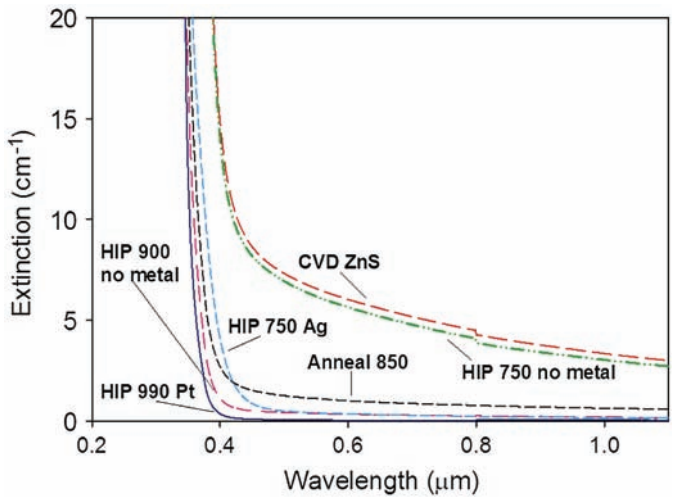

Figure 4.8 Calculated band-edge extinction for CVD ZnS and heat-treated samples (modeled after McCloy[25]).

bulk recrystallization from the temperature,[23,26] surface recrystallization from the metal,[26] and pressure-aided martensitic transformation.[25]

It is clear from the aforementioned data that the changes in transmission of ZnS with heat treatments are accompanied by many effects. Without exposure to metals, CVD ZnS can undergo recrystallization beginning at 850 °C and above. With platinum or silver foil recrystallization promoters, this recrystallization temperature can be lowered to 750 °C with complete recrystallization achievable for thick (~5 mm) samples within 16 h. No attempt was made to find a lower limit for the time of recrystallization or for a lower limit in temperature. Most likely, temperatures above the original deposition temperature (in this case ~670–720 °C) are necessary to move "frozen in" defects.

Transmission losses in the visible, other than sharp absorption lines from in-diffused transition metal impurities such as Co and Ni,[23] can be ascribed mainly to scattering. However, there is a discernible shift in the UV edge after heat treatment that can be ascribed to an electronic defect state in the bandgap of as-deposited CVD ZnS that is removed after heat treatment. It is often noted that heat treated samples (even without any metal) change from the yellowish color to white or clear after annealing or HIPing. This color change has also been observed when annealing red ZnS.[3]

4.2 Mechanisms for Transmission Improvement

The effect of heat treatments on transmission of ZnS can be separated into two effects: changes in absorption and changes in scattering. Changes in absorption can be identified by a change in the ultraviolet cut-on wavelength

near the bandgap or removal of narrow bands. Scattering can be seen as an overall reduction in transmission over a broad wavelength range. Broadband extrinsic transmission loss in the infrared can be due to either large particle scattering, free carrier absorption, or both. Particular extrinsic impurities with vibrations in the infrared, such as zinc hydride stretching or even zinc oxide lattice modes, can produce localized impurity absorptions.

4.2.1 Isothermal heat treatment

Under some conditions, isothermal annealing of CVD ZnS can produce transmission improvements, either by removing band-edge or impurity absorptions, or by increasing transmission in a broad near- and mid-infrared range.[3,23] For example, blue-shifting of the ultraviolet transmission edge after heat treatment is thought to be due to the removal of impurities of hydrogen or oxygen.[1,27] In general, however, the effectiveness of isothermal heat treatment, regardless of the atmosphere (Ar, H_2, vacuum), depends strongly on the particularities of structure in the starting material in an as-yet ambiguous way. Some speculation has been that the heat-treatability depends in part on the S/Zn ratio during growth and likely on other growth parameters.[28] It is clear, however, that for transmission improvement to take place as a result of annealing, temperature must be high enough to induce recrystallization [e.g., at least 850 °C, see Fig. 3.10(b)].[23] Calculated extinction for this annealed sample is shown in Fig. 4.8.

4.2.2 Hot isostatic pressing

Hot isostatic pressing, on the other hand, appears to be a much more "forgiving" process for transformation of CVD ZnS of all types than heat treatment without elevated pressure, generally resulting in a greatly increased transmission in the visible through mid-infrared due to reduction in scattering through a recrystallization of the microstructure and reduction in hexagonality, as described in Chapter 3. The added pressure is believed to accelerate the recrystallization, which is a martensitic transformation, and facilitate outdiffusion of impurities.[25] Additionally, the over-pressure allows higher temperatures to be used (usually 990 °C), which would otherwise sublimate the sample.[25]

The most-dramatic effect of HIPing CVD ZnS is the reduction in visible and infrared scatter, and the removal of the 6-μm absorption, resulting in transmission near if not identical to single-crystal cubic ZnS. More subtle (but perhaps more precisely telling) is the effect of HIPing on the luminescence spectra of CVD ZnS, highlighting the role of oxygen impurities. Dissolved oxygen in ZnS is thought to be detrimental to infrared transmission.[19] In Zn-rich as-deposited ZnS, changes in the cathodoluminescent spectrum after HIPing have been attributed to diffusion of interstitial zinc and oxygen from

optically inactive twin boundary sites to active sulfur lattice sites.[19] Oxygen present at stacking faults becomes mobile during the recrystallization from the HIP process and fills lattice sulfur vacancies and, in extreme cases, precipitates out a separate phase of different composition. In melt-grown crystals, oxygen-rich precipitates form at sizes ~1–10 μm and appear slightly dark in backscattered electron images, but in general they are not visible in SEM unless cathodoluminescence is used because they are compositionally different from the background by only about 1%.[29] Both the rate of diffusion and the oxygen solubility in ZnS are thought to be decreased by the high pressure during HIPing. HIP treatments at 980 °C at 21 ksi (145 MPa) provide the highest transmissions, whereas HIP treatments at 1050 °C at 14.5 ksi (100 MPa) show the largest changes in luminescence from the as-deposited material.[19] At these conditions, it is surmised that the system is in equilibrium, with high temperature causing the defect migration to speed up, and the pressure decelerating the diffusion and suppressing the phase transformation, because the hexagonal phase occupies larger volume.

The overall picture for the mechanism of transmission improvement in CVD ZnS upon HIPing is as follows. High temperatures assist in defect migration—particularly oxygen at twin boundaries as seen in TEM (Chapter 3, Refs. 19 and 30)—which may pin these boundaries during growth, resulting in a level of hexagonality and hence optical scattering (see below). Hydrogen defects are also removed, but they are important only for band-edge absorption and 6-μm absorption.[3,31] High pressures allow higher temperatures and provide an additional driving force for plastic deformation-induced recrystallization.[25,32] Hexagonality in ZnS is particularly important in the mechanisms of recrystallization due to the numerous polytypes and low energies of hexagonal-layer stacking faults in a cubic matrix.[23,33] The resulting recrystallized microstructure develops through polytype-induced exaggerated grain growth, producing the particular crystallographic texture observed in HIPed CVD ZnS samples.[25] The effect of applying particular metal foils (e.g., Pt, Ag, Pd, Au[26]) to the outside of the CVD ZnS material during HIPing is to induce recrystallization from the surface in addition to the thermally induced bulk recrystallization.

References

1. Lewis, K.L., G. S. Arthur, and S. A. Banyard, "Hydrogen-related Defects in Vapour-Deposited Zinc Sulphide," *J. Crystal Growth* **66**, 125–136 (1984).
2. Harris, D.C., *Materials for Infrared Windows and Domes: Properties and Performance*, SPIE Press, Bellingham, WA (1999) [doi: 10.1117/3.349896].
3. McCloy, J. and R. Korenstein, "Variability in Chemical Vapor Deposited Zinc Sulfide: Assessment of Legacy and International CVD ZnS Materials," *Proc. SPIE* **7302**, 73020M (2009) [doi: 10.1117/12.819559].

4. Bredikhin, V. et al., "Optical losses in polycrystalline CVD ZnS," *Inorg. Mater.* **45**(3), 235–241 (2009).
5. McCloy, J., "Semi-empirical Scattering Model for Chemical Vapor Deposited Zinc Sulfide," *Proc. SPIE* **7302**, 73020W (2009) [doi: 10.1117/12.819536].
6. Emelie, P.Y., J. D. Phillips, B. Buller, and U. D. Venkateswaran, "Free carrier absorption and lattice vibrational modes in bulk ZnO," *J. Electron. Mater.* **35**(4), 525–529 (2006).
7. Morozova, N.K., V. G. Plotnichenko, E. M. Gavrishchuk, and V. V. Blinov, "Absorption Spectrum of ZnO Precipitates in ZnSe," *Inorg, Mater.* **39**(8), 783–787 (2003).
8. Klein, C.A. and R.N. Donadio, "Infrared-active phonons in cubic zinc sulfide," *J. Appl. Phys.* **51**(1), 797–800 (1980).
9. Klein, C.A., R. P. Miller, and D. L. Stierwalt, "Surface and bulk absorption characteristics of chemically vapor deposited zinc selenide in the infrared," *Appl. Opt.* **33**, 4304 (1994).
10. Mitra, S.S. and R. Marshall, "Multiphonon infrared absorption in II-VI semiconductors," Proc. Academic Press, 7th International Conference on Physics of Semiconductors, 1085–1090 (1964).
11. Yu, P.Y. and Cardona, M., *Fundamentals of Semiconductors: Physics and Materials Properties*, 3rd Ed., Springer, Berlin (2005).
12. Campbell, A. and C. Hayman, "Manufacturing Aspects of Zinc Sulphide," *Proc. SPIE* **0915**, 79–83 (1988) [doi: 10.1117/12.945544].
13. diBenedetto, B.A., J. Pappis, and A. J. Capriulo, "Improved Large ZnS Windows," AFAL-TR-73-176 (1973).
14. Drezner, Y., S. Berger, and M. Hefetz, "A correlation between microstructure, composition and optical transparency of CVD-ZnS," *Mater. Sci. and Eng. B* **87**, 59–65 (2001).
15. Pickering, M.A., R. L. Taylor, J. Goela, and H. D. Desai, "Effect of Process Conditions and Chemical Composition on the Microstructure and Properties of Chemically Vapor Deposited SiC, Si, ZnSe, ZnS and ZnS_xSe_{1-x}," Proc. Mater. Res. Soc. **250**, 145–160 (1992).
16. Sato, T., Furukawa, and H. Kashi, "CVD-ZnS IR Dome," *J. Japan Soc. Infrared Sci. and Techn.* **11**, 44–49 (1986).
17. Fang, Z. et al., "CVD growth of bulk polycrystalline ZnS and its optical properties," *J. Crystal Growth* 237–239, 1707–1710 (2002).
18. Savage, J.A., *Infrared optical materials and their anti-reflection coatings*, Adam Hilger, Bristol, UK (1985).
19. Morozova, N.K. et al., "Pressure and Temperature Effects on Point-Defect Equilibria and BandGap of ZnS," *Inorg. Mater.* **40**(11), 1138–1145 (2004).

20. Wimmer, E., "Atomistic Modeling of Zinc Sulfide: Project 2: Interpretation of IR Absorption," personal communication (2007).
21. Klein, C.A. et al., "Lattice Absorption, Phonon Assignment, and Image-Spoiling Properties of CVD ZnS in the Infrared," *Laser Induced Damage in Optical Materials (NBS Special Publication 541)*, 86–98, National Bureau of Standards, U. S. Department of Commerce, Washington, D. C. (1978).
22. McCloy, J., E. Fest, R. Korenstein, and W. H. Poisl, "Anisotropy in structural and optical properties of chemical vapor deposited ZnS," *Proc. SPIE* **8016**, 80160I (2011).
23. McCloy, J., "Properties and Processing of Chemical Vapor Deposited Zinc Sulfide," Ph.D. diss., University of Arizona (2008).
24. Qiao, H.A., K. A. Lipschultz, N. C. Anheier, and J. S. McCloy, "Rapid assessment of mid-infrared refractive index anisotropy using a prism coupler: chemical vapor deposited ZnS," *Opt. Lett.* **37**(9), 1403–1405 (2012).
25. McCloy, J., R. Korenstein, and B. Zelinski, "Effects of Temperature, Pressure, and Metal Promoter on the Recrystallized Structure and Optical Transmission of Chemical Vapor Deposited Zinc Sulfide," *J. Am. Ceram. Soc.* **92**(8), 1725–1731 (2009).
26. McCloy, J. and R., Korenstein, "The Effect of Metal on the Formation of Multispectral Zinc Sulfide," *Proc. SPIE* **7302**, 73020N (2009) [doi: 10.1117/12.819461].
27. Kroeger, F.A. and J. A. M. Dikhoff, "The Function of Oxygen in Zinc Sulfide Phosphors," *J. Electrochem. Soc.* **99**(4), 144–154 (1952).
28. Taylor, R.L., M. J. Lefebvre, P. E. Price, and M. M. Maderazzo, "Erosion Resistant FLIR Window: Colorless ZnS," Contract: F33615-81-C-5076., CVD, Inc. (1984).
29. Morozova, N.K., V. A. Kuznetsov, and M. V. Fok, *Sul'fid tsinka. Poluchenie i opticheskie svoistva [Zinc Sulfide: Preparation and Optical Properties]*, Nauka, Moscow (1987).
30. Srot, V. et al., "Stacking faults and twin boundaries in sphalerite crystals from the Trepca mines in Kosovo," *Am. Mineralogist* **88**, 1809–1816 (2003).
31. Lewis, K.L. and G. S. Arthur, "Surface and Free Carrier Absorption Processes in CVD Zinc Selenide," *Nat. Bur. Stand. Bull.* **669**, 86–101 (1984).
32. Karaksina, E., V. Ikonnikov, and E. Gavrishchuk, "Recrystallization behavior of ZnS during hot isostatic pressing," *Inorg. Mater.* **43**(5), 452–454 (2007).
33. Karaksina, E., T. Gracheva, and D. Shevarenkov, "Structural defects in CVD ZnS," *Inorg. Mater.* **46**(1), 6–10 (2010).

Chapter 5
The Development of Chemical Vapor Deposited ZnS*

As we have seen, the chemical vapor deposition process has a profound influence on the physical and especially the optical properties of CVD ZnS. The scalability of this process was certainly a determining factor in the rapid displacement of the hot-pressed process initially used to commercially produce ZnS (IRTRAN 2). For this reason, a review of the development of the CVD process, first as an industrial process and finally as it was applied to ZnS, is in order.

This chapter recounts the events leading up to and including the development of the commercial ZnS CVD process. As Angus Macleod aptly points out in his description of the early days of optical coatings,[1] technology rarely evolves in a systematic way, being "very disorganized." Technological advancement only takes place when the climate is favorable, including the right time and place (and the individuals with the required skills are engaged), and importantly when the "subject," as Macleod calls, it is ready to receive it. Macleod argues that of these factors, climate is most important. In this sense, the climate at Raytheon Company in the 1960s was ideally suited for the development of CVD ZnS.

5.1 Chemical Vapor Deposition

The term "chemical vapor deposition" was first coined by John Blocher in 1960[2] in order to differentiate processes involving chemical reactions from those that did not (the latter being referred to as "physical vapor deposition"). It is surprising that it took so long to formalize this distinction, as the first documented recognition of CVD as a process occurred over one hundred years earlier when the chemist Robert Bunsen observed the formation of iron oxide crystals.[2]

**Material in this chapter has been approved for clearance by AFRL (case #88ABW-2012-6673).*

A summary of the conditions necessary for the implementation of the CVD process was given by Van Arkel in 1939 as follows: "the material must readily form a volatile compound which dissociates sufficiently at a temperature below the melting point of the coating material so that the partial pressure of the material in the vapor state is higher than the normal vapor pressure of the material at this temperature."[3] One of the first commercial uses of CVD occurred in the 1870s the production of carbon black using a process that we now refer to as pyrolysis[2]. The process was simple, involving the impingement of a natural gas flame on a cooled substrate (soapstone). Today, carbon-black production remains one of the largest commercial uses of this deposition technology.

Shortly after Thomas Edison patented his carbon filament incandescent lightbulb, efforts to improve the durability of the fragile filaments and hence extend their lifetime began, primarily through the application of pyrolytic forms of carbon followed by various refractory metals. The work of Sawyer and Man[4,5] is an early example. Their first patent application was in May of 1878, entitled *Improvement in Electric Lamps*. In their patent of 1880, they describe the process as follows: "(The) process is to immerse a pencil of carbon in a hydrocarbon gas or liquid and heating it to an extremely high temperature by voltaic current decomposes the surrounding matter...and deposits a perfectly homogeneous layer, generally of a bright gray color upon the exterior surface." We now recognize the bright gray color deposit as pyrolytic graphite. Similar patents quickly followed (De Lodyguine in 1893[6] and Aylsworth in 1896[7]). The drawing in the Aylsworth patent illustrates the rather simple halogen transport process used to coat carbon filaments with niobium metal (Fig. 5.1).

The next significant advancement in the evolution of CVD process technology occurred in the laboratory of chemist and industrialist Ludwig Mond and his associate Carl Langer.[8] They were studying the reaction of nickel with carbon monoxide, a process that they believed was behind the corrosion of nickel-plated plumbing. What they observed was the formation of nickel carbonyl, identified by them as nickel-carbon oxide. They went on to perfect a pyrolysis process utilizing this newly discovered "nickel-carbon oxide" to purify nickel metal as well as to coat nickel on a variety of metallic and nonmetallic substrates. This process, known today as the Mond process, made Ludwig Mond a rich man. It should be noted that in their patent describing this process,[8] they cite the deposition of free-standing nickel tubes and sheets. This is perhaps the first mention of the use of CVD to form free-standing bodies from the vapor phase. The second period in the development in carbonyl chemistry began in 1926 with the work of A. Job (see Lander and Germer[9]). In their 1949 paper, Lander and Germer report extensively on the metallic plating of Mo, W, and Cr via the thermal decomposition of carbonyls. One advantage of carbonyl processes was the fact that the majority of the processes could be performed in

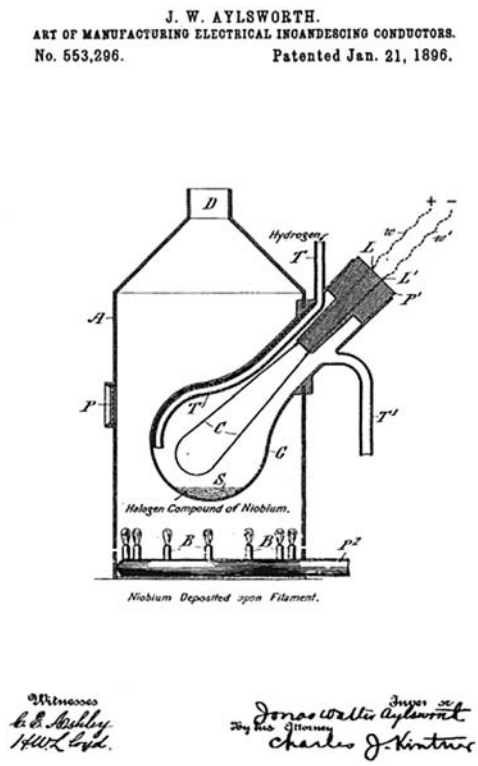

Figure 5.1 The Aylsworth vapor deposition system for coating carbon lamp filaments.

Pyrex glass reactors because the volatile compounds used typically develop the required vapor pressures below 550 °C.

The onset of World War II further stimulated efforts to produce a wide variety of refractory metal coatings using CVD. In a series of publications[3] and in the seminal text on the subject *Vapor-Plating: The formation of coatings by vapor-phase techniques*, Campbell, Powell, and Gonser[10] summarize much of the work on the formation of refractory coatings at the time, including work at the Battelle Memorial Institute, funded by the RAND Corp (called Project RAND). However, in their 1949 review they state, "the vapor-deposition processes have had only limited commercial application to date. A number of patents have been issued on the coating of wires for lamp filaments, but it is doubtful if any extensive commercial use has been made of filaments prepared in this fashion."[3]

5.2 Raytheon High-Temperature Materials

When Charles Francis Adams IV (a direct descendent of Presidents John Adams and John Quincy Adams) became president of Raytheon Company, he established Raytheon's Research Division. In his executive memorandum

of April 9, 1948, he stated: "It will be the policy to maintain a research division to handle special technical problems and research in potential fields of activity for Raytheon."[11] Among the research groups that were established within the new Research Division was the Physical Electronics Group, and under it a High-Temperature Materials laboratory. The purpose of the high-temperature materials activity was to investigate refractory materials such as pyrolytic graphite, borides, and nitrides. A 1956 trip to Alfred University convinced Raytheon that a hot-pressing apparatus and a high-temperature resistance furnace were required for "general Research Division work." Each of these were designed and built, and by 1957 work had begun on the development of processes for the production of graphite crucibles for nuclear materials research (Fig. 5.2).

By June of 1959 a High-Temperature Materials (HTM) Department was formed, splitting from the Physical Electronics Group. The HTM mission statement was to become a new product activity devoted to the preparation, study, and exploitation of pyrolytic graphite and other related high-temperature materials. While working on components for a gas-cooled nuclear reactor, Raytheon developed a production process for making pyrolytic graphite. The fact that carbon deposited at high temperatures has unusual properties had been known for some time—as evidenced by the reference to "a perfectly homogeneous layer, generally of a bright gray color upon the exterior surface" in Sawyer's 1880 patent.[5] Pyrolytic graphite is a

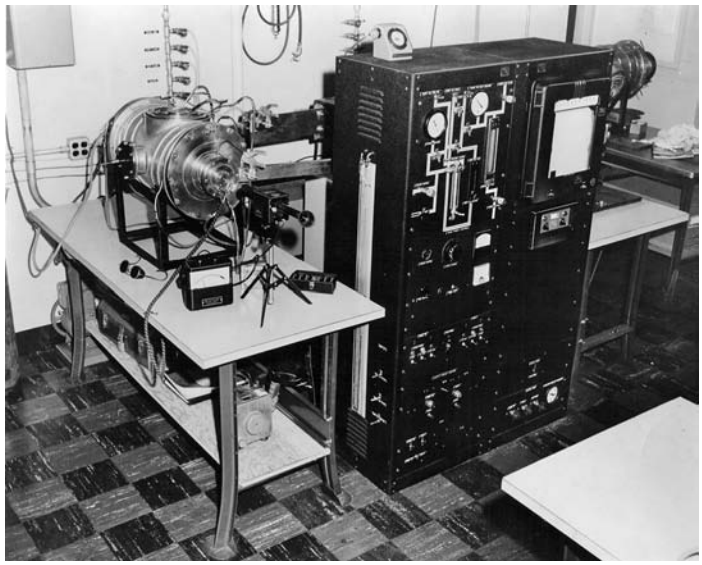

Figure 5.2 One of the 4-inch-diameter experimental reactors used to develop the pyrolytic graphite deposition process. The same reactor was eventually used to demonstrate the feasibility of CVD ZnS.

Figure 5.3 Various PG components, including rocket nozzles and nozzle inserts produced by the HTM Department.

polycrystalline form of graphite deposited from a carbonaceous vapor precursor at temperatures in excess of 2000 °C. Raytheon named this new product PYROGRAPHITE; it arguably represents the first demonstration of a commercially feasible means for producing free-standing, pyrolytic graphite (PG) parts, moving this material out of the laboratory curiosity arena. As this activity grew, a pilot manufacturing group was established in Lawrence, MA, to produce PYROGRAPHITE of many shapes and sizes (Fig. 5.3).

The HTM Department was equipped with furnaces capable of handling pieces ranging from 4–36″ in diameter and up to 4′ in length (Figs. 5.4 and 5.5).

Simultaneously, an expanded applied-research program in high-temperature materials was underway in Raytheon's Research Division in Waltham, including work on boron nitride (BN). As early as 1959, Raytheon engineers had speculated that it should be possible to pyrolize BN in the same manner as that of graphite. An apparatus was built and tested using vapor decomposition of $BCl_3 + NH_4$ in an induction furnace. The first BN depositions were made at deposition temperatures of 1900 °C. The largest percent of BN formed was amorphous, but some very dense BN was also formed on the substrate. With modifications to the "aerodynamic" or flow conditions, pyrolytic BN was deposited (x-ray diffraction confirmed the pyrographite-like structure). Raytheon's enthusiasm for this new vapor deposition process is evident in a publication by Pappis and Blum in 1961:

> "The techniques of refractory vapor deposition, originally limited to metals, appear to hold great promise as a means of forming materials which can play an important role in the space age. Recent work has demonstrated that vapor deposition techniques are applicable to many materials, including graphite, doped graphite, carbides, oxides and nitrides."[12]

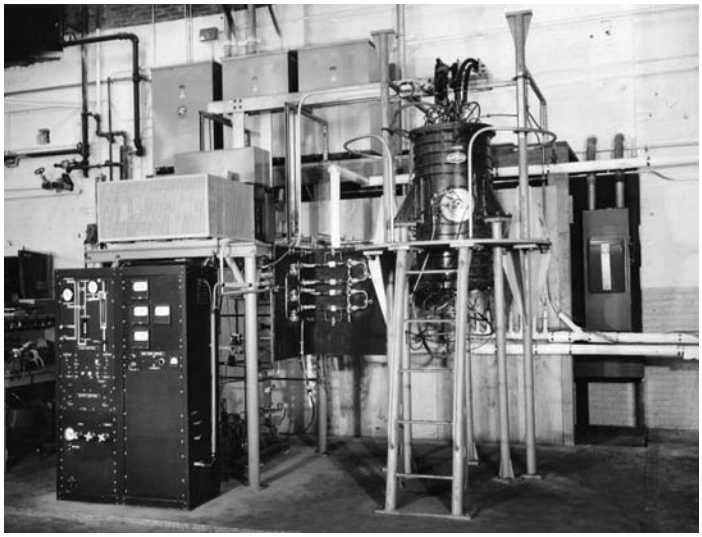

Figure 5.4 A 6″ internal diameter, PG deposition reactor in Raytheon's HTM pilot plant, circa 1960.

Figure 5.5 A large-scale, PG deposition reactor in Raytheon's HTM plant.

In addition to production, research was then extended to pyrographalloys (alloys of PG with various metals), pyrocarbides (compounds of various metals with PG) and pyrofibers (PG fibers). Beginning in 1958, Raytheon was awarded several PG-development contracts sponsored by the Special Projects

Office, Bureau of Naval Weapons (U. S. Navy), for the development of re-entry heat-sink bodies and rocket nozzle liners.[13] Pyrolytic graphite sales for the first half of 1962 were reported to be $269,179.[14]

Unfortunately, around this time three HTM employees, including the production manager, left Raytheon to start their own HTM company specifically to produce pyrolytic graphite. In addition, the U. S. Navy made a decision to use ablative materials for re-entry heat shields instead of PG because PG was significantly more expensive and difficult to integrate into systems. The loss of this business precipitated the closing of the Lawrence facility and consolidation of the remaining PG activity into the Raytheon Research Division in Waltham, MA. The newly consolidated group became the Advanced Materials Department under the leadership of Jim Pappis, the former Technical Director of HTM. Although the large reactors were left behind or sold, several of the smaller furnaces were moved to Waltham. The development and production of various high-temperature materials produced by the CVD process continued for at least 20 more years. With the consolidation of the HTM efforts came a wealth of technical knowledge specifically about CVD on a manufacturing scale and the associated reactor technology. The stage was set for the development and production of the first optical ceramic produced using CVD, namely zinc sulfide.

5.3 Raytheon CVD ZnS

Beginning in 1956,[15] Kodak developed a method of making infrared transparent ceramics using a hot-pressing technique starting with MgF_2. Leading the hot-pressing-process development at the time was Leroy Ladd, who worked on this process for a little over a year with limited success. Don Roy, who had been with Kodak since 1951, took over for Leroy, and within a couple of months had produced some "good MgF_2."[16] Following this success, Don turned his attention to ZnS, and within six months had succeeded in producing what was to become IRTRAN 2. Unfortunately, hot-pressed material had several shortcomings, including optical quality, size, and strength limitations. When the development of a hot-pressed ZnSe window for the SR71 aircraft went badly,[15,16] the Air Force became interested in alternative processes to produce the infrared windows that they needed (this occurred around 1964).[16]

As early as 1962, Raytheon foresaw the applicability of the newly developed PG vapor-deposition process to the "study of coatings for applications as electromagnetic transparent materials."[17] As mentioned at the beginning of this chapter, for product development to be successful it needs to have a user or customer at the receiving end of the development chain; in today's jargon this is called "technology pull." This technology pull came in the form of a recommendation from the Defense Department's Material Advisory Board in

the late 1960s[18] that the CVD process be considered as a way to produce long-wavelength infrared materials. The Advisory Board report concluded that the existing processes (hot pressing) would not easily produce material of the size or the overall quality required for future military systems. Importantly, the board had been impressed by the earlier work in the development and scaling of CVD processes for the deposition of pyrolytic graphite. As a result of this recommendation, the Air Force Avionics Laboratory at Wright-Patterson Air Force Base, Ohio, awarded a contract to Raytheon in May of 1970.[19] The objectives of the program were to investigate the feasibility of utilizing CVD process to fabricate materials that exhibit transmittance of 60% or greater in the 8–14-μm region of the spectrum and to determine the feasibility of scaling the CVD process to fabricate these materials in large sizes.

Raytheon chose ZnS for this feasibility demonstration. The approach was to make exploratory depositions of ZnS, believing that it could be economically and safely handled, and its properties met most of the program goals. Once feasibility had been demonstrated, $2'' \times 4'' \times 1/4''$-thick samples were to be deposited for property evaluation and sample delivery to the Air Force. The effort was to conclude with a scaling demonstration.[19]

Raytheon choose to use a dynamic CVD process, wherein fresh reactive gases are continuously fed into the furnace. The experimental deposition system is shown schematically in Fig. 5.6. Initial experiments focused on a transport method where the vapor source temperature was held higher than the substrate or mandrel temperature. Single crystals of zinc and cadmium

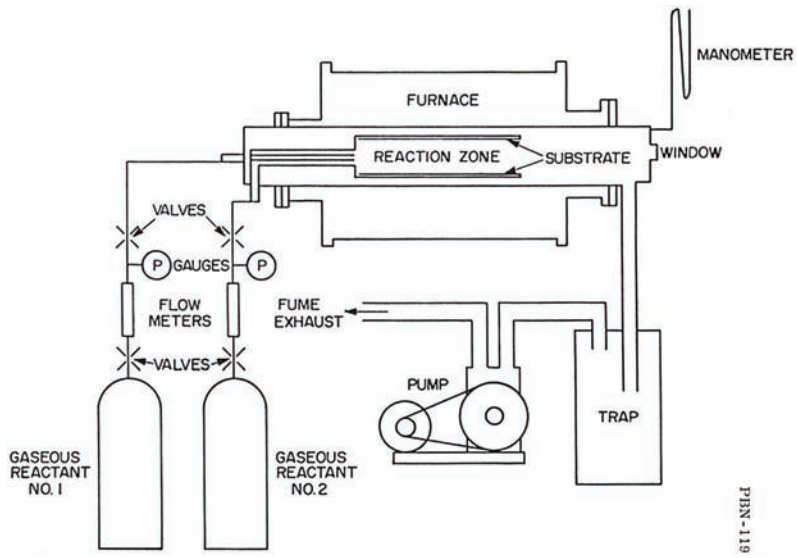

Figure 5.6 A schematic representation of a dynamic CVD deposition system.

sulfides, tellurides, and selenides had all been deposited using transport methods.[20] Dry hydrogen-chloride gas was passed over high-purity ZnS powder contained in a heated retort, generating zinc chloride vapor and hydrogen sulfide gas together with unreacted, excess hydrogen-chloride gas. A flow of helium gas was added as a diluent to improve transport efficiency and make the deposition rate more uniform over the substrate. A total of twenty deposition experiments were conducted using the transport method. During these experiments the thermal gradient between the retort and the substrate was modified, the retort design was changed to increase its capacity, and the exhaust system was modified to handle sulfur deposits that created constrictions and limited deposition time. The retort and substrate temperatures and the deposition pressures were varied. Unfortunately, ZnS material with adequate mechanical and optical properties and small grain sizes could not be produced. The excess HCl that was always present in the vapor stream was considered to be responsible for the large grain size as well as the trace amounts of chlorine found in the deposits.[19]

Attention was then turned to the more-conventional CVD approach wherein the reactants are delivered in the form of zinc vapor and hydrogen sulfide gas into the reaction chamber where ZnS is formed. Four exploratory depositions were made using this approach in the same furnace that was used for the transport CVD experiments (Fig. 5.2). Zinc pellets, 99.999% pure, were placed in the retort. Argon gas was flowed through the retort as a carrier gas. The zinc vapor flow over the substrate was controlled by restraining the argon flow and the retort temperature. Hydrogen sulfide gas was flowed through a separate inlet over the mandrel. A scrubbing system was also added to handle the effluent gases (Fig. 5.7).

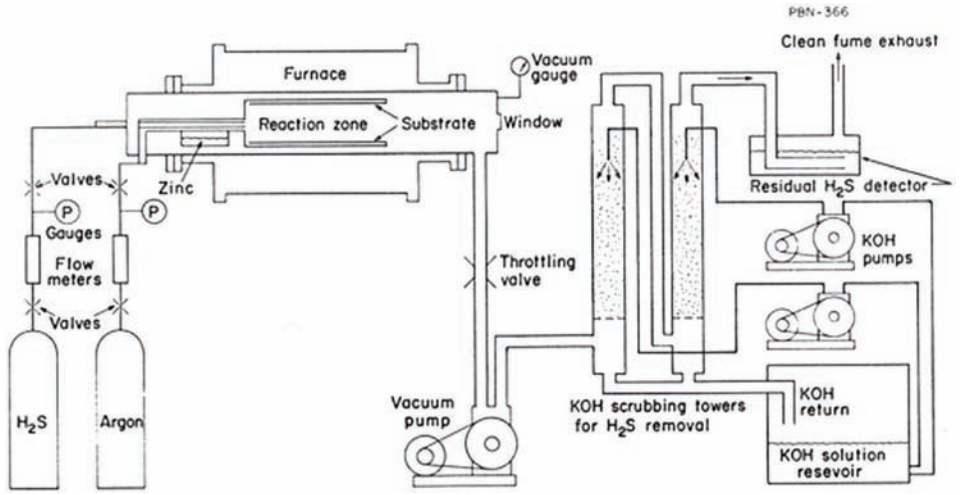

Figure 5.7 The exploratory ZnS CVD system.

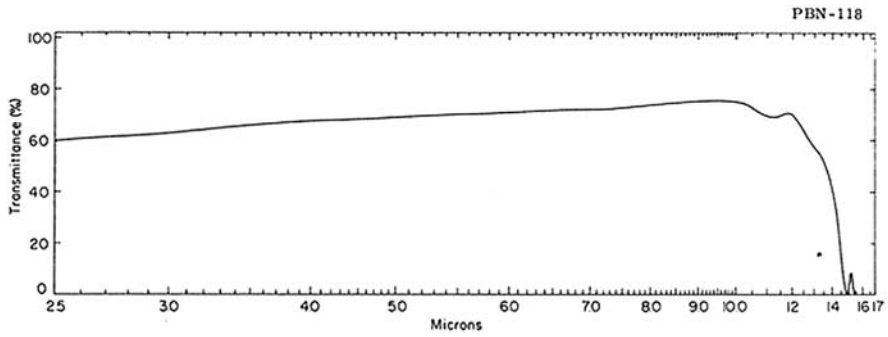

Figure 5.8 Infrared transmittance of CVD ZnS from exploratory deposition ZS-23.

The very first deposition experiment yielded material of a much-smaller grain size than had been deposited previously. By the third deposition, $1'' \times 4'' \times 1/8''$ plates were produced. The infrared transmittance and flexural strength of the material were comparable to commercially available hot-pressed ZnS (Fig. 5.8). The feasibility of depositing commercial-grade ZnS using a CVD process had been established!

To demonstrate the scalability of the process, one of the larger furnaces used in the CVD of the refractory materials was utilized with some modifications. The heating elements were first re-designed, a so-called birdcage design, and these were hung from the top of the furnace. The furnace element electrodes were changed from copper to graphite and were fed into the reactor from the top. The insulation package was reduced, allowing more internal volume for the furnace, as the deposition temperatures were significantly lower than those required for PG. Initial experiments were conducted using a mandrel that was $4'' \times 16''$. The very first experimental deposition produced good-quality, fine-grained material; however, the deposition rate was low, and the ZnS deposit was thin near the exhaust end of the mandrel (attributed to depletion of the zinc vapor). To increase the deposition rate, the zinc retort temperature was increased, resulting in a much-higher rate, encouraging investigators to increase the mandrel size again—this time to $8'' \times 16''$. However, the net result was a much-lower deposition rate even though the zinc pickup rate was high, suggesting that there was inadequate mixing of the vapors in the deposition zone. Modifications to the mandrel to encourage mixing were made, along with reductions in the retort temperature. In subsequent runs, the retort temperature and furnace pressure were optimized to deposit material over the entire mandrel area without "sooting" (gas-phase powder formation), which plagued some of the early experiments. By deposition experiment number ZS-36, a uniform, high-quality deposition was obtained at a deposition rate of 1–2 mils/h. Two $2'' \times 4'' \times ¼''$ prototype samples were produced, polished, and sent to the Air Force for evaluation. In addition, a $3.5'' \times 8'' \times 0.225''$ ZnS plate was polished to

demonstrate the feasibility of utilizing a CVD process to make large, infrared-transparent windows.

A few additional words should be said about the choice of the substrate or mandrel material. The proper choice of mandrel material is critical to the success of the CVD process, particularly when the objective is to produce free-standing material. Fused silica was initially chosen as the substrate material. While it yielded good results if it was clean and well-polished prior to deposition, it could only be used once, as the reactor environment would lightly etch the fused silica, promoting adhesion of the deposition in some areas. As a result of the large mismatch in thermal expansion coefficients, the ZnS in these areas would crack. Polished or glazed alumina eliminated the cracking problem because of the similarity in expansion coefficients. However, the ZnS strongly adhered to this substrate material and was difficult to remove. Pyrolytic graphite was used and was found to be the optimum material. Pyrolytic graphite mandrels could be reused repeatedly and were produced either by machining from plate stock or by coating graphite sheet.

The Air Force Avionic Laboratory recognized the potential of the CVD process for depositing ZnS and awarded a follow-on program in 1971 to continue the development of CVD ZnS, improving the optical properties while scaling the process to produce large windows.[21] The goal of the program was to deposit window blanks up to $14'' \times 17'' \times 1/2''$ thick. Although theoretically dense, the ZnS deposited to date had exhibited considerable scatter in the visible portion of the spectrum. There were also problems with deposits cracking as a result of mandrel design, which had to be remedied if large windows were to be produced.

To accommodate the long deposition times that were required to produce large plates of material, modifications were made to auxiliary equipment such as gas handling systems, the zinc retorts (required now to handle large quantities of zinc for extended operation while maintaining a constant temperature), and the scrubbing system that would neutralize all effluents. The reactors used in this scale-up effort are shown in Fig. 5.9.

Once these modifications were in place, 41 process evaluation runs were made. The first deposition parameter to be investigated was the deposition temperature. The reactor had been profiled and adjusted so as to control the temperature to within ± 10 °C. Deposition temperatures ranging from 500–750 °C were evaluated. It was found that material deposited below 600 °C was generally finer-grained and darker in color. Following these experiments, additional variables were explored, including furnace pressure, molar ratio of the reactant gases, H_2S/Zn, as well as temperature of the reacting gases. Additional reactants were also explored in order to reduce the scatter in the material, including additions of HCl vapor or a small addition of ZnSe, in an effort to ensure that only cubic-phase material was deposited. However, no improvement in the short-wavelength scatter was obtained in these dopant

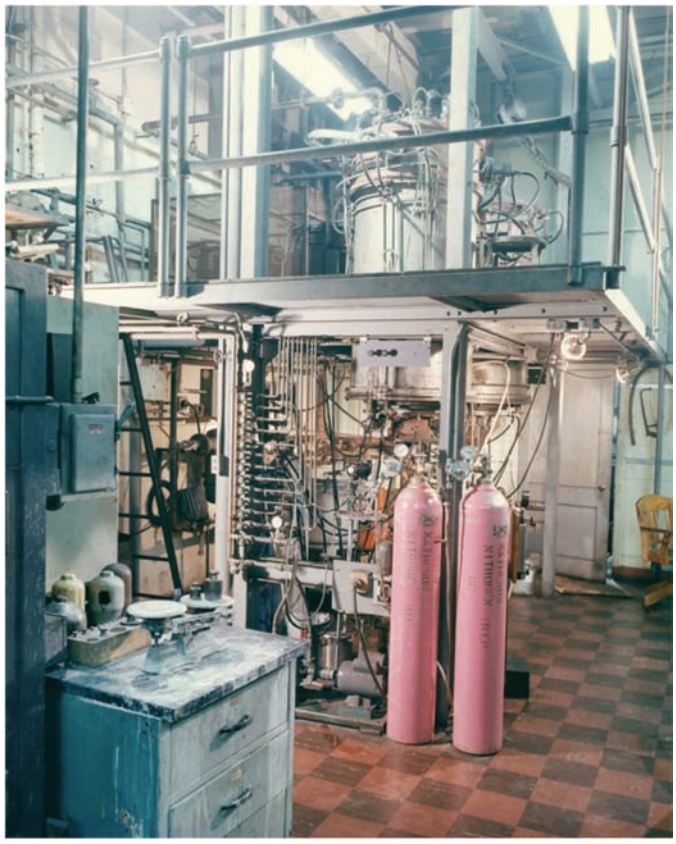

Figure 5.9 The resistance furnaces used to develop the CVD ZnS process.

experiments. Finally, refinement to the retort material and its preparation for deposition was explored. Graphite, coated with colloidal graphite, was found to be the optimum solution.

Next, scale-up experiments were conducted, beginning with an increase in deposition area from $4'' \times 9''$ to $7'' \times 16''$. Deposition conditions found to be optimum in the exploratory runs were used in the scale-up experiments. Deposition over the larger areas required a significant increase in the total reactant-gas input and retort volume as well as extending the deposition time in order to increase the thickness of the deposit. Deposition times up to 76 h were typically needed to deposit samples up to $0.375''$ in thickness. The thickness profile in these intermediate scale-up experiments was excellent; the results of deposition ZS-73 showed less than 10% thickness variation over the $7'' \times 16''$ area. Unfortunately, the extended deposition times came with issues with the clogging of the exhaust, which necessitated a redesign of the exhaust end of the furnace.

The scale-up development culminated in the deposition of 16″ × 24″ × 1/2″ plates on 16″ × 24″ × 3″ box mandrels. In total, nine deposition experiments using the large mandrels were completed. Although the optical quality of the material produced over the large areas was not as good as the best material produced during the exploratory process runs, it was deemed satisfactory for forward-looking infrared (FLIR) window applications. Window blanks were cut and ground from deposition runs ZS-91, ZS-93, and ZS-95, and submitted to the Air Force for evaluation.

The final development program began in 1973 and was completed by early 1975,[22,23] focusing on three things: zinc-sulfo-selenide solutions, continued scaling-process development, and demonstration of the production of ZnS domes. This work was very successful as well, notably yielding the first-of-its-kind, 180-deg, 9″-diameter dome.

In 1975 the first manufacturing-technology development program[24] took the development and demonstration of a commercially viable CVD ZnS process to maturation. We would now call this TRL-8. A fully automated, 52″ furnace was designed, built, and installed in the Waltham facility (Fig. 5.10).

Deposition temperature, system pressure, and reactant usage rates were all automatically controlled to predetermined values. The area of the mandrel was increased tenfold to 6000 sq. in. A new, by-flow, H_2S input-nozzle system had been developed in the smaller 17″ furnace that eliminated ZnS overgrowth on the H_2S nozzles, a critical advancement that allowed depositions to continue beyond about 100 h. The final production furnace required the use of multiple nozzles; hence, the by-flow nozzle technology was

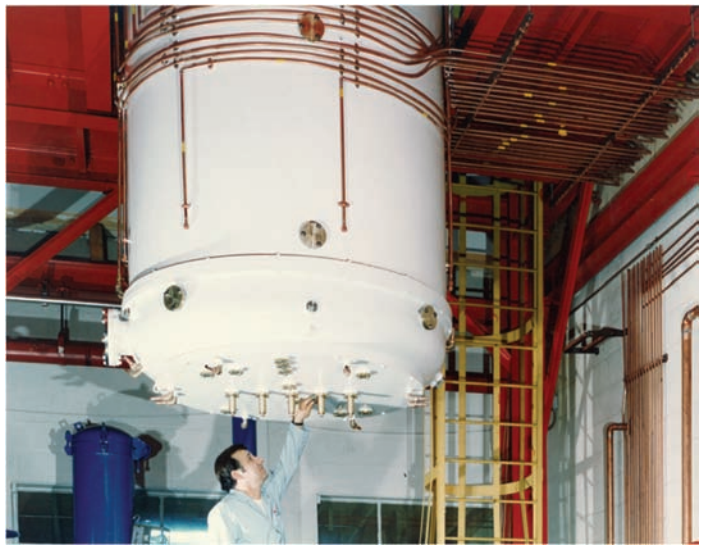

Figure 5.10 Installation of the first 52″ production furnace.

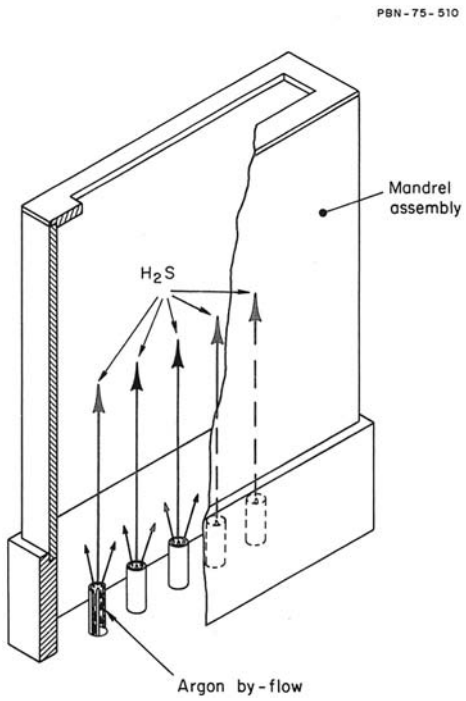

Figure 5.11 $34'' \times 34'' \times 9''$ mandrel box with five by-flow H_2S nozzles.

transferred to the $52''$ furnace. The mandrel setup for the initial series of runs in the large furnace consisted of a deposition zone with two $34'' \times 34''$ mandrel plates that were $9''$ apart in a box configuration (Figs. 5.11 and 5.12).

Optimization of the retort heaters, zinc pickup rate, nozzle hole size, back pressure in the input nozzles, as well as reactant gas temperature and molar ratio led to a successful conclusion of the scale-up, resulting in two $34'' \times 34''$ plates (Fig. 5.13).

Two more production furnaces were ultimately built and installed based on this design (Fig. 5.14), providing optical-quality ZnS for both DoD and commercial applications.

5.4 Multispectral ZnS and Elemental ZnS

By the end of 1975, Raytheon had established a ZnS production process, thereby demonstrating for the first time the capability to produce an optical material using CVD on a commercial scale. While not discussed here, the companion material, ZnSe, had also been developed in parallel for high-power laser applications (Fig. 5.15). Solid solutions of ZnS and ZnSe were explored early on by Raytheon,[21,22] and then later by other researchers,[25–28] as a means to improve the long-wave infrared transmission. These efforts,

Figure 5.12 Loading the deposition mandrel and fixturing into the ZnS reactor.

Figure 5.13 Inspection of large 34″ × 34″ CVD ZnS plate.

along with additional experiments with ZnS-CdS solid solutions,[22] suffered from high cost of starting materials, large scattering in the visible and near-infrared, and general sensitivity to processing conditions. Little benefit was gained in mechanical properties.

By 1980, the standard ZnS CVD process was well developed and being sold by Raytheon as Raytran® for both aircraft targeting pod windows and missile domes. Raytheon did not apply for any patents on the process at the time, but in late 1979 Aldinger and Werdecker, from the German

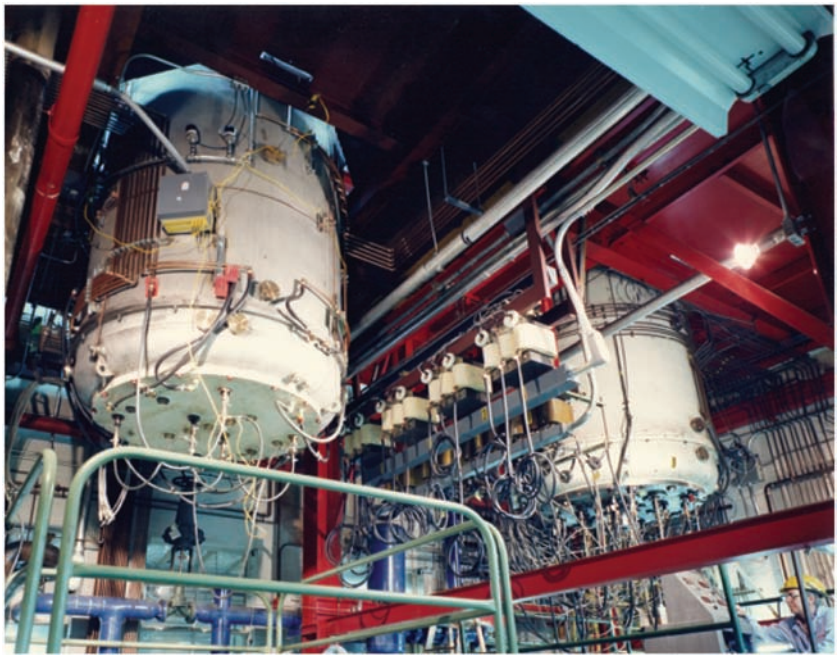

Figure 5.14 Raytheon's CVD production facility in Waltham, MA.

Figure 5.15 A large CVD ZnSe laser window produced at Raytheon, demonstrating the size and optical quality capability of the CVD process.

company W. C. Hereaus GmbH, applied for a patent entitled "Zinc sulfide bodies for optical purposes," which was granted in the U. S. at the end of 1981.[29] This patent described the use of a HIPing step after CVD of ZnS to remove the absorption around 6.3 μm and slightly improve transmission in the 0.4–0.5 μm region, at the expense of transmission in the 0.7–4.0-μm region. It had been found early on by Raytheon that annealing tended to remove the 6.3-μm absorption and produce colorless material.[21]

Starting in the late 1970s, Chuck Willingham of Raytheon was experimenting with HIPing with the CVD ZnS bodies wrapped in platinum foil, and he produced what Raytheon ultimately trademarked as Multi-spectral® ZnS. This material was highly transparent in the visible, colorless, and termed "water clear." The scatter in the visible region had been mostly eliminated. Raytheon filed a patent application on December 29, 1980 to protect their Multi-spectral® ZnS process. After almost a decade, Willingham and Pappis of Raytheon Research Division were granted U. S. patent #4,944,900 on July 31, 1990, for the HIP process on CVD ZnS.[30] The Raytheon process was notable over the German process in that it involved wrapping the yellow ZnS (or ZnSe) parts in platinum foil and subjecting them to HIP at 5–30 ksi pressures. The platinum foil was meant to prevent contamination or chemical reaction with the container (typically graphite) and to act as a procurer of outgassing agents.[31] The material produced was a so-called "water clear" transparent and colorless ZnS material that transmitted from the visible through the long-wavelength infrared regions with no significant absorptions.

Earlier in 1980, a couple of Raytheon employees left the company and set up their own small business nearby in Massachusetts called CVD, Inc. to make ZnS and ZnSe by CVD directly in competition with Raytheon. In 1983, CVD, Inc. received government development contracts to optimize the HIPed CVD ZnS, which they later trademarked as Cleartran®.[31] This product is the same one sold today, though CVD, Inc. was sold to Morton, then to Rohm and Haas, and is currently owned by DOW. In 2000 and 2001, CVD, Inc. was granted two improvement patents for the HIPed ZnS process. The first U. S. patent, USPTO 6,221,482, "Low scatter, high quality water clear zinc sulfide" (2000), specified temperature ramping protocols for the zinc retort and the mandrel temperature, as well as specific stoichiometries for the reactants.[32] The second patent, USPTO 6,221,482, "Low stress, water-clear zinc sulfide" (2001), described an increased cool-down time after HIP to prevent bowing, cracking, and stress birefringence in large plates.[33,34] Raytheon again emerged in the late 2000s with evidence that the HIP process of CVD ZnS did not require platinum but could be performed without any metals,[35] with metals other than platinum,[35,36] or with platinum reused multiple times,[37] thus controlling costs of the once-through platinum process that had come to dominate the U. S. market. It should be noted that there is anecdotal evidence

Figure 5.16 The current elemental ZnS (or eZnS®) processing facility at Raytheon Company (reprinted from Clement[39] with permission).

that some non-U. S. suppliers of multispectral ZnS do not use platinum in their HIP process.[38]

"Elemental" zinc sulfide (eZnS®) was developed at Raytheon beginning in the mid-1990s because of the concerns about storing large quantities of hydrogen sulfide gas. The process differed from previous CVD ZnS in that the hydrogen sulfide gas was made *in situ* by a gas generator from hydrogen gas and sulfur vapor (Fig. 5.16). The H_2S gas, probably with some unreacted H_2, was then delivered to the growth chamber along with the zinc vapor. Surprisingly, given deposition conditions very similar to the standard CVD process practiced commercially, the elemental ZnS product resulted in very pale yellowish material with low scatter.[39] Mechanical properties remained similar to standard CVD ZnS (Raytran®). A similar material was recently reported by a Chinese group grown by separate sources of hydrogen and sulfur.[40]

Others began to follow Raytheon's lead with their own efforts, beginning with CVD, Inc. in 1980 and II-VI, Inc. in 1983. Harris has recently written a review that chronicles these later activities.[15] Other countries have also undertaken successful efforts to establish production CVD ZnS processes, most notably efforts in the United Kingdom beginning in the late 1970s, work in the former Soviet Union and Russia from the 1970s, and more recently in Israel and the People's Republic of China, among others. Currently, commercial CVD ZnS suppliers exist in at least the following countries: United States, Germany, Russia, Israel, and China. These international efforts have been reviewed by McCloy.[41]

5.5 "Improvements" to CVD ZnS: Composites with $ZnGa_2S_4$ and Diamond

As time went by, military applications of ZnS on aircraft and missiles discovered that environmental durability was a problem. Specifically, rain erosion became a significant concern. During the 1990s, many scientists and engineers developed methods that attempted to improve the durability of ZnS, whether through covers, coatings, or treatments to the bulk ZnS itself.[34] Other less-successful methods that were investigated included grain refinement, thermal tempering, ion implantation, and pulsed electron-beam annealing.[31] The durability problem was especially acute with the Multi-spectral®-grade ZnS. It was found that the HIPing caused enough grain growth to reduce the hardness and flexural strength by about thirty percent.

One of the most promising solutions to improve durability involved treating the bulk ZnS with other metal ions that would induce compressive stresses in the surface or form other sulfides that were harder than ZnS. These strengthening methods were attempted on both standard yellow ZnS as well as the water-clear version. Cadmium was an obvious choice due to the early investigations of cadmium sulfide as an infrared material.[22,31] A series of experiments in the late 1980s by Raytheon resulted in additional patents for treating ZnS. The U. S. Patent entitled "Method of strengthening an optical body by diffusion of material to the depth of structural flaws formed in such body" was issued in January of 1994 and claimed that ZnS could be strengthened through diffusion of transmission metal ions into the surface.[42] Specifically mentioned in claims are cobalt (Co), iron (Fe), chromium (Cr), manganese (Mn), nickel (Ni), and vanadium (V). Interestingly, gallium (Ga) is mentioned in the body of the patent but not in the claims. Nickel doping of single crystals was also later described as increasing the hardness of ZnS.[43] A related patent was issued six months later based on the same original application. Entitled "Zinc sulfide bodies having improved optical transmittance characteristics and mechanical characteristics," this patent focused on the improvement of the optical transmission in the visible and near-infrared regions by diffusion of transition metals, notably cobalt, into yellow standard ZnS.[44] Over a decade later, it was shown by McCloy[45] that the cobalt in diffusion was not the cause of the transmission improvement but rather the heat treatment itself, the results of which depended strongly on the starting CVD ZnS material.

During the same period of time when Raytheon was investigating transition metal additives to ZnS, others were looking at hardening based on precipitation.[46] Finding little hope for second-phase strengthening in the CdS-ZnS system, one group turned to the $ZnS–Ga_2S_3$ system with its tetragonal zinc thiogallate ($ZnGa_2S_4$) phase.[47] It was found that adding Ga_2S_3 powder to ZnS powder and hot pressing resulted in a hardness

increase over ZnS alone, with a fracture toughness maximum around 12 mole percent Ga_2S_3.[48]

It turns out that zinc thiogallate has similar infrared transmittance to zinc sulfide, so maintaining second-phase zinc thiogallate below a particular particle size eliminates problems of optical scattering.[49] This ZnS–Ga_2S_3 powder process is the basis for two patents by Harris and Dougherty of Hughes Aircraft Company: the U. S. Patent entitled "Process for making low cost infrared windows," filed April 1994 and granted November 1996;[50] and the U. S. Patent entitled "Method for making low cost infrared windows," a division of the other patent application and granted July 1997.[51] The Hughes process involves several different embodiments. The first is co-precipitating sulfide powders containing zinc and gallium, and pressing the powder. The second is evaporating gallium on densified ZnS powder processed body. In either case, the ceramic body is HIPed to develop the zinc thiogallate phase. In a later patented embodiment (more germane to the CVD ZnS story), CVD Multi-spectral® ZnS is dipped in liquid gallium and the surface is strengthened rather than the bulk as by powder processing. This patent, "Method of treating a zinc sulfide body formed by chemical vapor deposition to increase its rain erosion durability," by Chen, Harris, and Gabelich, was filed in October 1998 as Hughes Aircraft Company but is assigned to Raytheon, who had bought Hughes in 1999 before the time the patent was issued in April 2000.[52]

Composite ceramics offered a potential for improved properties as well. Zinc sulfide–diamond composites were investigated for a time.[53-55] Diamond is a good choice for a second material because of its high hardness and similar index of refraction to ZnS. Additionally, gallium phosphide composites with ZnS were investigated by chemical vapor transport.[56] Both of these systems were powder processed, typically by hot pressing. There is promise in this area, particularly if grain sizes can be made small enough to eliminate visible scattering and if material phases can be made continuous to maximize thermal conductivity.

From the above discussions, it should be apparent that the CVD technology needed to produce electro-optic materials such as ZnS and ZnSe in unprecedented shapes and sizes had clearly been established beginning with the deposition of pyrolytic graphite at Raytheon Company. Raytheon has held a core role since the early 1970s in ZnS technology, being responsible for the introduction of platinum HIP multispectral CVD ZnS, elemental ZnS, and various improvements and additions to the understanding of the processing of CVD ZnS.

5.6 Applications of CVD ZnS

By the time that Raytheon had ceased production, a large number of windows and domes had been produced for the Department of Defense, including 400 PAVETACK (ZnS) windows, 500 F-18 FLIR windows, 1400 LANTIRN

windows, and more than 25,000 I^2R Maverick domes.[18] Other DoD systems that use CVD ZnS are Small Diameter Bomb II,[57,58] Javelin,[59] and AT FLIR,[60] to name a few.

The commercial applications for this material are many and varied, including prisms, beam splitters, optical wedges, lenses, windows, and other elements. CVD ZnS pieces are frequently used as evaporative source material due to the fact that they are fully dense and do not outgas or "spit" during evaporation, as the hot-pressed material is prone to do. Sputtering targets made from CVD material have some of the same advantages in terms of density and purity. Of course, many familiar products today incorporate ZnS films, such as retroreflective security coatings, highway signs, solar cells, antireflective coatings, solar coatings, and a wide variety of other coating products.

To this day, the maturity and properties of CVD ZnS and multispectral CVD ZnS are as-yet unmatched, particularly for broadband imaging applications extending from the visible to the LWIR portion of the spectrum.

References

1. MacLeod, A., "The early days of optical coatings," *J. Opt. A* **1**(S), 779 (1999).
2. Allendorf, M., "From bunsen to VLSI: 150 years of growth in chemical vapor deposition technology," *Electrochem. Soc. Interface* **7**(1), 36–39 (1998).
3. Campbell, I. E., C. F. Powell, D. H. Nowicki, and B. W. Gonser, "The Vapor-Phase Deposition of Refractory Materials: I. General Conditions and Apparatus," *J. Electrochem. Soc*. **96**(5), 318–333 (1949).
4. Sawyer, W. E. and A. Man, "Improvement in Electric Lamps," U.S.A., USPTO 205,144 (1878).
5. Sawyer, W. E. and A. Man, "Carbon for Electric Lights," U.S.A., USPTO 229,335 (1880).
6. De Lodyguine, A., "Process of manufacturing filaments for incandescent lamps," U.S.A., USPTO 494,150 (1893).
7. Aylsworth, J. W., "Art of manufacturing electrical incandescing conductor," U.S.A., USPTO 553,296 (1896).
8. Mond, L., "Process of depositing nickel," U.S.A., USPTO 455,230 (1891).
9. Lander, J. J. and L. H. Germer, "Plating molybdenum, tungsten and chromium by thermal decomposition of their carbonyls – Part I. Plating by pyrolysis fomr the carbonyls," *Am. Institute of Mining and Metallurgical Engineers, Technical Publication*, No. 2259, 1–42 (1947).
10. Powell, C. F., I. E. Campbell, and B. W. Gonser, *Vapor-Plating: The Formation of Coatings by Vapor-deposition Techniques*, John Wiley & Sons, New York (1955).

11. Leverton, W. F., "The Research Division," Raytheon, Internal Report to Advanced Management Program, (1959).
12. Pappis, J. and S. L. Blum, "Properties of Pyrolytic Graphite," *J. Am. Cer. Soc.* **44**(12), 592–597 (1961).
13. Blum, S. L. and J. Pappis, "Pyrographite," *Elect. Progress* **IV**(6), 2–6 (1960).
14. "The significance of a materials organization to missiles and space division," Raytheon Research Division Memorandum S-470 (September 1962).
15. Harris, D. C. "History of the development of hot-pressed chemical-vapor-deposited zinc sulfide and zinc selenide in the United States," *Proc. SPIE* **6545**, 654502 (2007) [doi: 10.1117/12.716808].
16. Roy, D., "MgF_2," personal communication (September 16, 2004).
17. Blum, S. L., "High temperature materials and ceramic activities," Raytheon Research Division Report S-439 (June 1962).
18. Pappis, J., "The development of zinc sulfide and zinc selenide by chemical vapor depositon," WL-TR-95-4082 (1994).
19. Steele, S. R. and J. Pappis, "Chemical Vapor Deposition of IR Materials," F33615-70-C-1577 (1971).
20. Nitsche, R., H. U. Bölsterli, and M. Lichtensteiger, "Crystal growth by chemical transport reactions—I: Binary, ternary, and mixed-crystal chalcogenides," *J. Phys. Chem. Solids* **21**(3–4), 199–205 (1961).
21. diBenedetto, B. A., J. Pappis, and A.J. Capriulo, "Chemical Vapor Deposition of IR Materials for Reconnaissance," AFAL-TR-72-309 (1972).
22. diBenedetto, B. A., J. Pappis, and A. J. Capriulo, "Chemical Vapor Deposition of Multispectral Windows," AFAL-TR-73-252 (1973).
23. diBenedetto, B. A. and J. Pappis, "Chemical Vapor Deposition of Multispectral Domes," AFML-TR-75-27 (1975).
24. Pappis, J. and B. A. diBenedetto, "Zinc Sulfide FLIR Windows," AFML-TR-76-226 (1976).
25. Lewis, K. L., D. J. Cook, and P. B. Roscoe, "The Structure and Optical Properties of Polycrystalline ZnS_xSe_{1-x} Prepared by Chemical Vapour Deposition," *J. Crystal Growth* **56**, 614–620 (1982).
26. Gavrishchuk, E. M., D. V. Savin, and V. B. Ikonnikov, "CVD-growth of ZnSxSe1 - x with subsequent hot isostatic pressing," *Surface and Coatings Technol.* **201**(22–23), 9385–9388 (2007).
27. Pickering, M. A., R. L. Taylor, and D. T. Moore, "Gradient infrared optical material prepared by a chemical vapor deposition process," *Appl. Opt.* **25**(19), 3364–3371 (1986).

28. Pickering, M. A., R. L. Taylor, J. Goela, and H. D. Desai, "Effect of Process Conditions and Chemical Composition on the Microstructure and Properties of Chemically Vapor Deposited SiC, Si, ZnSe, ZnS and ZnS_xSe_{1-x}," Proc. Materials Research Society **250**, 145–160 (1992).
29. Aldinger and Werdecker, "Zinc sulfide bodies for optical purposes," W. C. Hereus GmbH, U.S.A., USPTO 4,303,635 (1891).
30. Willingham, C. B. and J. Pappis, "Polycrystalline Zinc Sulfide and Zinc Selenide Articles Having Improved Optical Quality," Raytheon, U.S.A, USPTO 4,944,900 (1990).
31. Taylor, R. L., M. J. Lefebvre, P. E. Price, and M. M. Maderazzo, "Erosion Resistant FLIR Window: Colorless ZnS," F33615-81-C-5076 (1984).
32. Goela, J. S. and Z. Salihbegovic, "Low scatter, high quality water clear zinc sulfide" CVD, Inc., U.S.A., USPTO 6,083,561 (2000).
33. Goela, J. S., "Low stress, water-clear zinc sulfide" CVD, Inc., U.S.A., USPTO 6,221,482 (2001).
34. Harris, D. C. *Materials for Infrared Windows Domes: Properties and Performance*. SPIE Press, Bellingham, WA (1999) [doi: 10.1117/3.349896].
35. McCloy, J., R. Korenstein, and B. Zelinski, "Effects of Temperature, Pressure, and Metal Promoter on the Recrystallized Structure and Optical Transmission of Chemical Vapor Deposited Zinc Sulfide," *J. Am. Ceram. Soc.* **92**(8), 1725–1731 (2009).
36. McCloy, J. and R. Korenstein, "The Effect of Metal on the Formation of Multispectral Zinc Sulfide," *Proc. SPIE* **7302**, 73020N (2009) [doi: 10.1117/12.819461].
37. Korenstein, R. H., J. Patrick, S. McCloy, and C. B. Willingham, "Treatment Method for Optically Transmissive Bodies," Raytheon, U.S.A., USPTO 7,790,072 (2010).
38. McCloy, J. and R. Korenstein, "Variability in Chemical Vapor Deposited Zinc Sulfide: Assessment of Legacy and International CVD ZnS Materials," *Proc. SPIE* **7302**, 73020M (2009) [doi: 10.1117/12.819559].
39. Clement, T. J., "Elemental zinc sulfide (eZnS®) provides a clear view for missile systems' tri-mode seekers," Technology Today (Raytheon) **2**, 66 (2012).
40. Fang, Z. et al., "CVD growth of bulk polycrystalline ZnS and its optical properties," *J. Crystal Growth* **237–239**, 1707–1710 (2002).
41. McCloy, J. "International development of chemical vapor deposited zinc sulfide," *Proc. SPIE* **6545** 654503 (2007) [doi: 10.1117/12.717870].
42. Wahl, J. M., R. W. Tustison, T. Y. Wong, and C. B. Willingham, "Method of strengthening an optical body by diffusion of material to the

depth of structural flaws formed in such body," Raytheon, U.S.A., USPTO 5,281,465 (1994).

43. Wu, P., R. Kershaw, K. Dwight, and A. Wold, "Growth and Characterization of Nickel-doped ZnS single crystals," NTIS Report # AD-A199781; TR-9 (1988).
44. Wahl, J. M., R. W. Tustison, and T. Y. Wong, "Method of strengthening an optical body by diffusion of material to the depth of structural flaws formed in such body," Raytheon, U.S.A., USPTO 5,324,353 (1994).
45. McCloy, J., "Properties and Processing of Chemical Vapor Deposited Zinc Sulfide," Ph.D. diss., University of Arizona (2008).
46. Zhang, J. M., W. W. Chen, B. Dunn, and A. J. Ardell, "Phase Diagram Studies of ZnS Systems," *Proc. SPIE* **0968**, 35–40 (1988) [doi: 10.1117/12.948123].
47. Zhang, J., W. W. Chen, A. J. Ardell, and B. Dunn, "Solid-State Phase Equilibria in the ZnS-Ga_2S_3 System," *J. Am. Ceram. Soc.* **72**(6), 1544–1547 (1990).
48. Zhang, J., W. W. Chen, and A. J. Ardell, "Solid Solution Strengthening of ZnS," *Proc. SPIE* **1326**, 93–98 (1990) [doi: 10.1117/12.22486].
49. Chen, W. W., B. Dunn, and J. M. Zhang, "Experimental and theoretical studies of second-phase scattering in IR transmitting ZnS-based windows," *Proc. SPIE* **1535**, 199–208 (1991) [doi: 10.1117/12.48316].
50. Harris, N. H. and T. K. Dougherty, "Process for making low cost infrared windows," Hughes Aircraft Company, U.S.A., USPTO 5,575,959 (1996).
51. Harris, N. H. and T. K. Dougherty, "Method for making low cost infrared windows," Hughes Aircraft Company, U.S.A., USPTO 5,643,505 (1997).
52. Chen, W. W., N. H. Harris, and S. A. Gabelich, "Method of treating a zinc sulfide body formed by chemical vapor deposition to increase its rain erosion durability," Raytheon, U.S.A., USPTO 6,045,728 (2000).
53. Fujii, A. et al. "Diamond-ZnS composite infrared window," *Proc. SPIE* **4375** 206–217 (2001) [doi: 10.1117/12.439177].
54. Xue, L. A. et al., "Optical and mechanical properties of zinc sulphide diamond composites," *Acta Metallurgica et Materialia* **38**(9), 1743–1752 (1990).
55. Every, A. G., Y. Tzou, D. P. H. Hasselman, and R. Raj, "The effect of particle size on the thermal conductivity of ZnS/diamond composites," *Acta Metallurgica et Materialia* **40**(1), 123–129 (1992).
56. Han, Y. and M. Akinc, "Zinc Sulfide/Gallium Phosphide Composites by Chemical Vapor Transport," *J. Am. Ceram. Soc.* **78**(7), 1834–1840 (1995).
57. Haynes, A., "Low cost zinc sulfide missile dome manufacturing," cited January 9, 2013, http://www.armymantech.com/pdfs/LCZSulfideMDome.pdf (2012).

58. Haynes, A, "Low Cost Zinc Sulfide Missile Dome Manufacturing – report," cited January 9, 2013, http://www.dtic.mil/cgi-bin/GetTRDoc?AD=ADA480072 (2013).
59. Lyons, J., D. Long, and R. Chait, "Critical technology events in the development of the Stinger and Javelin missile systems: project Hindsight revisited," cited January 9, 2013, http://www.ndu.edu/CTNSP/docUploaded/DTP%2033%20Missiles.pdf (2006).
60. Harris, D. C., "Multi-spectral transparent materials technology, American Ceramic Society – Baltimore, June 2010," cited January 9, 2013, http://ceramics.org/wp-content/uploads/cls/cls10_d_harris.pdf (2010).

Chapter 6
Perspective and Future Work

In this final chapter we pull together all of the aforementioned investigation and attempt to present a coherent picture of the properties and processing relationships in CVD ZnS. This is broadly divided into two sections: the nature of CVD ZnS, and the nature of its transformation during heat treatments. The bulk of this chapter is an assessment of the previously presented literature and the results of investigations described herein, so copious citations and references to previous data presented will be minimized.

We begin with a discussion of the chemical, crystallographical, structural, and optical nature of the CVD ZnS material. We review the differences encountered along the different positions of the growth cores from the first to the last material to deposit. We then speculate on the nature of red ZnS and elemental ZnS, and their differences from standard yellow CVD ZnS.

The heat treatment of the above material is discussed next. We focus on the hot isostatic press and elicit the role of temperature and pressure. We relate a proposed mechanism of recrystallization and a role that the metals have in inducing it.

The chapter ends with some overall observations and conclusions. Much work has been done, but we also relate some specific examples of work yet to be done to test the conclusions and extrapolations from this work.

6.1 What Is The Nature of Standard CVD ZnS?

CVD ZnS is a polycrystalline material with multiple levels of hierarchical structure. Its typical impurities are hydrogen from the hydrogen sulfide precursor, and oxygen from process gases and the low-vacuum deposition environment. CVD ZnS consists of nanoscale twins of cubic sphalerite phase on the order of 10–100 nm separated by a hexagonal packing layer. These twins are associated into domains and finally grains, where each higher-order boundary involves disordered hexagonal and cubic packing. Strictly speaking, polytypes probably do not exist within individual crystallite lamella. Of course, the degree of ordering or disordering completely depends on the scale being considered.

CVD ZnS exhibits ~5–10 at. % of hexagonality. The hexagonal phase measured by x-ray diffraction should not be considered as a "phase" in the sense that there is a clearly identifiable region in the material with the 2H or 4H structure. It has been shown that hexagonal reflections in polycrystalline XRD and selected-area electron diffraction indicate that hexagonal packing is present. The hexagonal disorder is in a single dimension: the close-packed stacking direction. In the polycrystalline solid, the close-packing direction is not quite randomly oriented because the preferred orientation is evident in XRD, in some cases emphasizing the wurtzite (10.0) and in others the wurtzite (10.1) reflection. It is possible that some needle-like hexagonal ZnS crystals are occasionally produced in the vapor phase and then get trapped in the growing ZnS deposit or are flushed into the exhaust of the CVD chamber.[1,2]

The "grain" size of CVD ZnS, as commercially deposited around 670 °C, is 4–8 μm in the direction perpendicular to the growth direction and about ten times that in the growth direction, giving CVD ZnS a "columnar" habit. The compressive strength of CVD ZnS is considerably higher when the load is along these "columns" than when it is perpendicular to them. CVD ZnS has a preferred texture (25–60%) along the {100} planes [i.e., the (200) and (400) x-ray reflections] and to a much lesser extent {311} and {511} planes, which are at small angles to the {100} planes. In some cases the {100} texture, including both (111) and (222) reflections, is more important than the {511}.

CVD ZnS, and even vapor-grown single-crystal ZnS, shows many macroscopic "growth bands;" these bands are perpendicular to the growth direction in CVD ZnS. They probably represent slightly different chemical compositions, such as impurity content of hydrogen and oxygen. Previous researchers have suggested that banding is due to gas-phase (homogeneous) reactions, nonuniform zinc-vapor usage, or formation and dissociation of zinc hydride.[3] It was confirmed that the hydride absorption was lowest in the colorless band near the mandrel. This "growth banding" has been observed in CVD zinc sulfo-selenide, where the bands were clearly different sulfur-to-selenium ratios and had different refractive indices. In single crystals of ZnS, these bands are not always associated with different crystal structures or polytypes, but they nonetheless exhibit measurably different birefringence. The exact nature of this banding is still poorly understood.

Data presented here on the variation of properties of CVD ZnS along the growth direction (i.e., the cores) are the first such data in the literature.[4] It was shown by powder x-ray diffraction that the absolute amount of hexagonality remains unchanged from the first deposited ZnS at the mandrel to the last deposited ZnS at the growth surface. However, the texture of the material changes as the relative intensities of the different hexagonal ZnS peaks change with position in the core.

Chemically, ZnS tends to be a Zn-rich n-type semiconductor due to the relative magnitude of the reaction constants of zinc and sulfur condensation

and evaporation, and the presence of oxygen as a reducer for sulfur. CVD ZnS has been verified by energy dispersive spectroscopy to be Zn-rich as well, assuming that a Bridgman melt-grown crystal is nominally stoichiometric. CVD ZnS has the additional driving force for Zn-richness because the growth process is typically carried out at zinc-to-hydrogen-sulfide reactant ratios greater than one. Zn-rich materials tend to favor the introduction of oxygen because the material is already sulfur deficient, so sulfur vacancy sites exist, and interstitial zinc needs volume compensation by nearby sulfur vacancies or substitutional oxygen.

Competition exists for these sulfur sites during the CVD process. Hydrogen sulfide is thought to adsorb onto the growing solid body and interact with a sulfur vacancy, filling the sulfur site and giving off hydrogen.[6] Oxygen, if available, will preferentially bond to sulfur sites before hydrogen sulfide. The evolved hydrogen from the split hydrogen sulfide may react exothermically with zinc vapor in the gas phase near the growth surface to form ZnH_2, often getting incorporated into the growing solid. When deposited at temperatures up to about 850 °C, CVD ZnS shows characteristic zinc hydride absorption around 6 μm, which can be resolved into a triplet of roughly equally spaced spectral lines. This defect is believed to have the structure of $(ZnH_3)_S$ based on *ab inito* assessments.[6] Some CVD ZnS (e.g., that produced by Rafael[7]) has no 6-μm absorption. Such material can be produced by growing at higher temperatures, though it is not known if this is the case with the Rafael material.

The measurable oxygen content in CVD ZnS, about 0.2–0.4 at. %, gives rise to some of the characteristic behavior during HIPing to be discussed next. The oxygen is believed to be located both in the lattice on sulfur substitutional sites and along disordered boundaries. Oxygen preferentially inhabits sulfur sites along twin boundaries (hexagonal packing sequences), which have been shown in other studies to be sulfur deficient and oxygen rich. This preferred location is due to the smaller ion size of oxygen and the favored hexagonal structure of ZnO. Because substitutional oxygen induces lattice compression, it tends to associate spatially with other defects that stretch the lattice, such as zinc interstitials or monovalent cations such as silver. This phenomenon is referred to as the compensation of volume.

6.1.1 What is red ZnS?

What is referred to here as red ZnS is ZnS grown by CVD at low mandrel temperatures (~640 °C) at very high zinc excesses. The resulting material, when polished, varies from deep red to brownish in color. It is characteristically very low scattering in the visible and infrared but has very strong hydride absorption and a notably longer-wavelength ultraviolet edge. The "ultraviolet" edge measures at 400–415 nm, compared to 361–386 nm for standard CVD ZnS. The 6-μm absorption band is resolved into two distinct minima at different spectral positions than in standard ZnS. It has been said that the

absorption edge (and hence coloration) is tied to the hydride absorption; this was not confirmed in these experiments. A sample having been annealed at 650 °C for a total of 6 h showed an ultraviolet edge shift to 376 nm, creating a white, scattering sample that still had an unchanged 6-μm absorption.[7] This leads us to conclude that the color in red ZnS, at least, is due to the position of the band edge and the relative transmission in the various visible wavelengths.

Red ZnS is microstructurally similar to other standard ZnS but with a slightly smaller grain size. This smaller grain size does not contribute to stronger ZnS, and biaxial flexure strength is essentially the same for red ZnS and standard CVD ZnS. The grains do not have columnar behavior, however, unlike standard ZnS. The nanostructure is similar, with small twins collectively organized into larger domains and then grains. The nanostructure does seem to be more randomly oriented compared to other samples investigated. Selected-area electron diffraction showed more "spotty rings," indicative of small structures. It is conceivable that because of the low deposition temperature, red ZnS actually forms ZnS in the gas phase by homogeneous nucleation via a transition state complex and then deposits on the substrate more as a particle.[8] Alternatively, the dense isotropic polycrystalline form could be due to a kinetically limited process, where the rate of the reaction to form ZnS is the limiting factor, and increased nucleation rate inhibits anomalous grain growth seen in higher-temperature-grown ZnS.

Red ZnS has ~2 at. % hexagonality, considerably less than in standard ZnS, which is more scattering. As with elemental ZnS, the slow growth rate (<0.001″/h) probably contributed to the lower incidence of hexagonal stacking disorder. The crystallographic texture of red ZnS is substantially different from standard ZnS, with most of the texture being in the planes and much less in the planes.

The main chemical difference in red ZnS seems to be its oxygen content. Red ZnS is not any more Zn-rich than standard ZnS, at least within the limits of energy dispersive spectroscopy assessment. It does contain more oxygen, measured by Interstitial Gas Analysis (IGA) at 0.3–0.6 at. %, as expected for a lower-temperature deposition.[6] Lattice parameter measurements confirm the high presence of oxygen (as ZnO) in the concentration range measured by IGA. It is possible that the red-shifted ultraviolet edge is due to the high dissolved-oxygen content as ZnS(O). It has been reported that the red color in ZnSe is due to zinc vacancies,[27,28] but, given the way this red ZnS was grown, it seems unlikely to be the explanation for the color in this ZnS.

It is possible, but not proven, that the scattering induced by annealing red ZnS is due at least in part to precipitation of zinc-oxide particles. Some annealed red ZnS in which the 6-μm absorption has been removed shows a structure that some in the literature have claimed is due to ZnO.[5] Due to its close proximity to water bands that are difficult to remove even in a careful spectroscopic measurement, this identification is still uncertain.

6.1.2 What is elemental ZnS?

Elemental ZnS, as defined here, is any CVD ZnS formed from hydrogen and sulfur reacted just before injection into the CVD chamber to combine with Zn vapor. This is distinguished from standard (or FLIR-grade) CVD ZnS, which uses a commercial hydrogen-sulfide gas precursor. The two known versions of elemental ZnS are on average superior in visible and near-infrared transmittance to standard CVD ZnS.

It has been shown by x-ray diffraction that both Chinese ZnS (grown from the elements) and Raytheon elemental ZnS have measurably less hexagonality (estimated at 2 at. %). As a result, both show improved transmission (lower scattering) in the visible and near-infrared. In the internal surface scatter model, this is reflected by a lower "birefringence" for elemental ZnS than for standard CVD ZnS.

Elemental ZnS should be structurally similar to other CVD ZnS materials grown at similar temperatures. Recall that Raytheon's commercially produced standard CVD ZnS and elemental ZnS were both grown with a 670 °C mandrel temperature. Grain diameters for Raytheon elemental ZnS are 4–8 μm, and the material has a "columnar" grain that is about ten times as large in the growth direction. At the nanoscale, lamellar twin structures are observed with diffraction contrast in the TEM. The x-ray texture is nearly identical to standard CVD ZnS except that there is a component of texture that is not significant in standard ZnS. Elemental ZnS may be slightly denser than standard ZnS but barely within the resolution of an immersion-type measurement. Biaxial flexure strength is essentially identical to CVD ZnS.

The reason for the reduction in hexagonality in these materials can be postulated as due to several factors. First, it is highly likely that there is some unreacted hydrogen gas that is introduced into the reactor with the hydrogen sulfide, which will make the hydrogen sulfide more thermodynamically stable in the gas phase and prevent the back reaction to the elements (the low chamber pressures prevent the need to consider activity coefficients). This allows the splitting of the hydrogen sulfide to occur at the surface of the growing solid body rather than in the gas phase. Also, Raytheon elemental ZnS was historically produced at much-lower growth rates than commercial CVD ZnS (<0.001″/h versus 0.002″/h). This lower growth rate should assist in preventing hexagonal stacking disorder.

Chemically, elemental ZnS is very similar if not identical to standard CVD ZnS (i.e., made from bottled H_2S). It is zinc-rich and its measured oxygen content is the same at 0.2–0.4 at. %. The hydrogen content of Raytheon elemental ZnS is probably similar to (most) standard CVD ZnS based on the absolute depth of the 6-μm absorption. The Chinese and Raytheon elemental ZnS materials are different, however, because the Chinese ZnS shows no 6-μm absorption,[7] whereas the Raytheon elemental ZnS shows the characteristic CVD ZnS hydride absorption with three identifiable minima.

6.2 What Is the Nature of Transformation to Multispectral ZnS?

Multispectral ZnS is a desirable optical material due to its broadband transparency from the ultraviolet through the long-wave infrared. The ability to make very thick parts of conformal shapes sets CVD apart from other techniques for making ZnS. Therefore, the transformation from as-deposited scattering standard CVD ZnS is critical for applications requiring a window with visible through longwave-infrared spectral bandwidth.

Many aspects of the changes induced by HIPing on the microstructure and properties of CVD ZnS have been reviewed and assessed here. The zinc to sulfur ratio does not appear to change chemically, at least within the resolution of the EDS measurement. Hydrogen is removed by HIPing or annealing for sufficient times, as evidenced by the reduction and eventual removal of the 6-μm absorption. In the samples assessed, the overall oxygen concentration does not appear to change, measuring 0.3–0.4 at. %.

The most obvious change, other than the removal of scattering, is the complete recrystallization of the CVD ZnS after HIPing, resulting in large single-crystallite grains without nanolamellar twins. It has been shown that this process can be observed before it is complete, with the intermediate material being more scattering than the original CVD ZnS.[9] Seemingly similar multispectral ZnS can be distinguished by its crystallographic texture. Upon complete recrystallization, the HIPed ZnS is strongly textured in the planes, close to %.

In samples HIPed at low temperature without any metal present, texturing remained as if it were still CVD ZnS (i.e., predominantly texture), recrystallization did not take place or at least did not complete, and visible transmission was low and scattering.[9] Samples may have improved transmission without "full" recrystallization (defined here as having the predominant crystallographic texturing in the planes), such as those annealed at 850 °C and those HIPed with silver at 750 °C,[9] where the material is predominantly textured with being the next largest fraction.

Thus, it can be said that true "multispectral ZnS" is by definition fully recrystallized to strong texture, so a certain minimum process involving a combination of temperature, pressure, and/or metal promoter is required. Biaxial flexure testing of textured multispectral ZnS has a lower average strength and higher Weibull modulus than material HIPed at lower temperature with silver or platinum.[5] The differential crystallographic texture of the low-temperature HIPed samples and the removal of internal stresses induced during CVD deposition may be responsible for the different biaxial flexure behavior. The flaw-size to grain-size ratio is large enough in both CVD ZnS and HIPed ZnS that fracture should be governed by the polycrystalline fracture energy in both cases, and there should not be a significant grain-size effect.[10]

6.2.1 What is the HIP doing?

The hot isostatic press combines two driving forces for recrystallization: temperature and pressure. By performing annealing experiments, the effect of pressure has been independently assessed. It has already been shown that the pressures typically used in HIPing ZnS (15–30 ksi) are well above the Peierls' stress of 9 ksi necessary to move dislocations in ZnS.[9] It is thus expected that HIPed microstructures will show more signs of plastic deformation than annealed structures. An additional surprising effect of the high pressure was that it allowed higher processing temperatures to be used without evaporation of the ZnS. It was shown that a 990 °C anneal for 10 h completely evaporated 5-mm-thick samples of CVD ZnS, whereas samples held at 30 ksi for this time and temperature fully recrystallized with some subsequent grain growth.

Unlike other authors who claim to have been unable to recrystallize without applying pressure, this work observed some microstructures that did recrystallize with annealing only when temperatures were $\geq$850 °C.[9] This temperature would seem to be the threshold for thermal activation of dislocation motion involving diffusion, grain-boundary sliding, and nucleation of stress-free grains.[11] It should be recalled that lower temperatures are effective at recrystallization in the HIP when appropriate metal recrystallization promoters are used.

Fully recrystallized multispectral ZnS has a very low fraction of hexagonal phase, less than about a half an atomic percent. Because the starting material has 5–10 at. % hexagonality, the hexagonality is reduced by HIPing. Because the phase transformation is martensitic, it is expected that pressure would help induce the transformation. Cubic sphalerite is slightly denser than hexagonal wurtzite, so it is also expected that the denser phase would be slightly favored at higher pressure. Additionally, lattice diffusion will likely be important at temperatures $\geq$850 °C, so zinc diffusion and rearrangement of the zinc sublattice may also assist in transformation to the cubic phase.[12]

Recrystallization due to the HIP can be seen as a combination of diffusion and plastic deformation. The mechanism proposed here implicates oxygen as the important species that is normally at the twin boundaries, inducing hexagonal layers at the twin boundaries and contributing to nonuniform chemistry, and hence nanoscale birefringence. Careful measurements of natural sphalerites have indicated that oxygen concentrates at twin boundaries, substituting for sulfur for less than two monolayers.[13] In the model proposed here, at elevated temperatures these oxygen atoms at the boundaries can diffuse into the lattice into sulfur sites, thus unpinning the twin boundaries to move to lower-energy stacking configurations. The total energy of the system is lowered by removing the internal hexagonal surfaces and recrystallizing into large (30–100+ μm) grains that are relatively fault free. These large "perfect" crystallites are readily evident in TEM in materials

HIPed at high temperature. Grains of HIPed ZnS are irregular in shape and can consist of lathes of material with aspect ratios of up to 10.

This phenomena could fall under the heading of "diffusion-induced grain-boundary migration" (DIGM) or "diffusion-induced recrystallization." DIGM has been modeled at an atomistic level as being due to dislocation climb in the grain boundary as a result of interdiffusion (Kirkendall effect).[14] In classic DIGM, the flux of solute atoms to the boundary is not equal to the flux of matrix atoms out of the boundary, and the result is a "wavy" grain boundary due to atoms diffusing across the boundary rather than along it as in normal grain-boundary diffusion.[15] DIGM and diffusion-induced recrystallization (DIR) have been observed mostly in precipitates in metal alloys but, with very few exceptions, not at all in ceramic systems, presumably due to the requirement for charge neutrality and thus the simultaneous movement of anions and cations.[16]

DIR occurs when a misfitting solute, such as oxygen in ZnS in this hypothetical example, diffuses through a lattice, producing strain and thus nucleating new grains.[17] Solute segregation at interfaces results from elastic forces from size misfit, electrostatic interactions between charged solutes and interfaces, and dipole interactions involving electric fields at interfaces.[18] The elastic energy change that results from the movement of the solute provides the driving force for the boundary motion in the new grain. "Coherency strains" can be thought of as variable lattice parameters in nearby regions of the crystals that can be caused by various things including diffusion, phase transformation, and nucleation. Carter and Handwerker[17] have shown that morphologies of recrystallized grains depend only on elastic anisotropy and linear compressibility, each defined by a relation of the elastic tensor components. In the ideal case of DIR, for materials with elastic anisotropy of greater than one (such as ZnS), the fastest growth in strain-free crystals will be parallel to the <111> directions, and the slowest growth parallel to the <100> directions; the resulting recrystallized grains will be cuboidal.

Fully recrystallized ZnS does have a strong texture, suggesting that a mechanism like DIR could be occuring. However, the resulting structure is not cuboidal but rather elongated tabular grains. A more-likely candidate for a detailed mechanism for producing the microstructures observed in recrystallized ZnS is polytype-induced exaggerated grain growth.[19] In this model, an impurity or dopant with low solubility forms prototypic growth faults at a twin or other special boundary rather than forming a separate phase within the host. Because the symmetry of the system is altered, these polytypic sequences then grow in the direction of the fault plane (i.e., along the planes) at the expense of fault-free regions in order to minimize the total energy of the system. The result is anisotropic grain growth, which has been observed in the cubic-to-hexagonal phase transition in barium titanate and has been implicated in twining behavior in natural ZnS sphalerites.

Exaggerated or discontinuous grain growth (also called secondary recrystallization), or the coarsening of the average grain size due to preferential consumption of some grains in favor of others, has been observed in many ceramics and has traditionally been ascribed to a bimodal size distribution of grains or nonuniform pore pinning.[20] It has been shown that there is another mechanism for exaggerated grain growth, which can be explained by the presence of nanostructural polytypism in these systems, that imparts anisotropy to an otherwise isotropic grain system. This phenomenon may be able to explain the microstructure of recrystallized CVD ZnS.

Nanostructural polytypism is favored in systems where there is a very low solubility of the additive in the host material and where there is a tendency to form faults that become enriched with the additive rather than form an isolated phase,.[19] These faults tend to be low-index planes such as twin, antiphase, or inversion boundaries, and are produced (nucleated) during the initial growth and never by deformation. Examples of this phenomenon include the hexagonal-to-cubic transformation in $BaTiO_3$, where the dopants of calcium tend to segregate to polytypic faults. Polytypism in SiC has been shown to be enhanced by the addition of aluminum, and additions of SnO_2 to ZnO produce inversion boundaries. In all cases, these systems exhibit anisotropic grain growth along the polytypic faults (i.e., twin faults or inversion boundaries) when they are subsequently reheated. Resulting recrystallized microstructures can be seen to be preferentially elongated along the planes of the polytypic faults at the expense of fault-free regions. Secondary faults are sometimes produced as a result of impingement of oppositely growing domains.

No porosity was identified in any of the CVD materials used in this study. Based on this lack of evidence for porosity, a pore-closure mechanism cannot be invoked as a driving force for HIPing. It is instead suggested here that oxygen normally pins grain (twin) boundaries. At elevated temperatures, the oxygen can diffuse, boundaries can move, and grains can recrystallize. The exact threshold temperature for this unpinning mechanism cannot be separated from the threshold temperature for thermal activation of dislocation motion mentioned earlier. Other impurities such as hydrogen leave the lattice, and zinc diffusion will promote the phase transformation from hexagonal to cubic stacking by the crystallographic rotation of zinc tetrahedra. Plastic deformation (strain) will also promote the martensitic phase transformation and provide the main basis for strong texturing through slip and twinning of the cubic grains.

6.2.2 What is the metal doing?

One important factor not yet discussed is the role of the metal present during the HIPing. It has been shown by the "interrupted HIP" experiments that certain metals (Pt, Ag, Ni, and Cu) accelerate recrystallization from the contacted surface.[21] In the case of platinum and copper, the formation of a sulfide on the metal foil has been verified. Those metals that did not assist

recrystallization (Fe and Co) form only hexagonal or cubic ZnS on their surfaces after HIPing. Sputter-deposited metals on the ZnS surface do not seem to be as effective as foils in inducing the recrystallization, presumably because the in-diffusion of the metal is facilitated, which complicates the lattice restructuring and recrystallization. This could be due to the need to nucleate a metal sulfide, and the nature of nucleation sites on a foil surface and a metal coating are very different, the former having electronic surface reconstructions.

A detailed understanding of why certain metals, such as Cu, Ag, Ni, and Pt, are effective at recrystallization of ZnS whereas other metals such as Co and Fe are not effective is the subject of future work.

What is proposed here is that the so-called "active" metal recrystallization promoters, typified here by platinum, react with sulfur coming out of the ZnS during HIPing. The removal of sulfur from ZnS creates open lattice sulfur sites into which oxygen can diffuse from the twin boundaries. Dissolving the oxygen, which initially lies at the nanopolytype twin boundaries, back into the cubic lattice allows recrystallization to occur. This process creates large, new crystallites with relatively uniform oxygen concentration separated by twin boundaries enriched in oxygen. These large recrystallized grains grow to impingement along the twin boundaries and then thicken to impingement in the other direction in an anisotropic, exaggerated grain-growth mode.

HIPing or even annealing at high temperature (>850 °C) alone without a recrystallization promoter can allow the oxygen diffusion and dislocation motion necessary for recrystallization, but the promoter metal foils allow recrystallization to occur down to 750 °C or lower in the HIP. An absolute lower limit for recrystallization with the foils was not determined, but it is likely that it must be greater than the deposition temperature of the CVD ZnS (~670 °C). The time required at temperature is more for thicker samples to achieve the same effect of transmission improvement via recrystallization.

The addition of an active foil lowers the temperature required for full recrystallization as shown by a couple of examples.[21] A sample, HIPed with an inactive metal (cobalt) at 950 °C, shows texturing nearly identical to that of high-temperature, platinum-HIPed samples in addition to high visible transmission, though not quite as high as the Pt sample. A cobalt sample HIPed at 750 °C shows transmission unchanged from the original CVD ZnS, thus indicating no recrystallization. It can thus be said that cobalt is inactive at recrystallizing ZnS.

The same low-temperature (750 °C) HIP conditions with silver produce high visible transmission.[21] The texture has strongly changed in favor of {111} and {211}, those planes most associated with material fully recrystallized with platinum at high temperature. Material HIPed at 750 °C without metal has remained in the {100} texture associated with the as-deposited material. Although the microstructure of this particular sample was not investigated, a

similar sample showed only the first signs of recrystallization, and the low transmission of both samples suggests that their microstructures are similar and only beginning to recrystallize. Microstructures of samples HIPed at this temperature and time with active metals are fully recrystallized and have high visible transmission.

Additionally, both samples HIPed without foil at low temperature still show signs of hydride absorption. Because the samples of the same thickness HIPed at this temperature with Ag or Pt do not have any remnants of this 6-μm absorption, this suggests that one of the other roles of the metal foil is to facilitate removal of the hydride. Zinc hydrides present in sulfur sites will break apart, releasing the hydrogen that diffuses out of the ZnS. Zinc stays in sulfur sites as an antisite point defect, diffusing to a zinc vacancy.

One additional possible mechanism exists for the efficacy of the metal in recrystallizing the ZnS and improving its transmission. It has been shown in the literature that small amounts of metals such as copper or silver in ZnS phosphors can form sulfides during heat treating of the powders. The energy evolved from the formation of these sulfides nucleates the hexagonal-to-cubic ZnS phase transition. This behavior is more likely to be important with the sputtered metals, where intimate contact between the ZnS and metal is assured. As has been mentioned, however, these sputtered metals have a greater tendency to diffuse into the ZnS, which may create small metal particles that can have surface resonance effects that absorb in the infrared.[22] Although this was not shown in detail in this book, this surface plasmon resonance may be responsible for the infrared absorption in ZnS HIPed with silver at higher temperatures.

6.3 Conclusions

The goal of this work is to address the transmission-loss behavior of various forms of ZnS and to elucidate the mechanism of transmission improvement through HIPing in the presence of platinum.

Degradation of transmission in the visible and near-infrared can be correlated to hexagonal phase content. However, scattering cannot be modeled by a simple Rayleigh model assuming a difference in refractive index between the cubic and hexagonal phases, as the slope of the scattering is much smaller than the wavelength to the inverse fourth-power characteristic of Rayleigh scattering. A pseudo-empirical model was generated that relies on scattering at surfaces between nanosized lamella with slightly different refractive indices.[23] This model estimates the transmission of standard CVD ZnS, elemental ZnS, and multispectral ZnS very closely. No additional complexities were added to the model to account for internal electric fields, size distributions, or other features known to be present in ZnS. Adding these additional complexities to the model could allow better predictions assuming effects of coherent and incoherent multiple scattering.

The ZnS investigated in this study shows a large range of optical extinction behaviors. Hot-pressed powder ZnS (IRTRAN) showed localized absorptions from impurities and Rayleigh scattering due to pores.[23] CVD ZnS showed the unconventional scattering behavior modeled above, as well as hydride absorptions described as ZnH_2 and ZnH_3 species on sulfur sites. Samples that were stopped in the midst of recrystallization showed large-particle scattering behavior independent of wavelength. ZnS HIPed with silver at high temperature showed broadband extinction, probably due to resonance of indiffused silver particles reflecting and absorbing the infrared light.[21] This last phenomenon deserves future inquiry.

Recrystallization of the CVD ZnS, whether by annealing or HIPing, has emerged as the most-important function of the heat treatment. HIPing has the added benefits over annealing of allowing processing at temperatures that normally evaporate ZnS, as well as providing the additional driving force of pressure for dislocation motion and martensitic phase transformation. The platinum foil was found to be far from inert, as has been traditionally assumed. Although recrystallization is possible without an active metal promoter, the metal allows it to occur at lower temperatures. Other active metals aiding recrystallization have been identified; silver was the one explored most, whereas copper, palladium, gold, and nickel were discovered later and have yet to be optimized.[21] Platinum still remains the most-effective element for recrystallizing thick ZnS at low temperatures.

A large number of commercial grades of CVD ZnS have been compared using various techniques and shown to be distinctly different in terms of their defects, particularly with respect to the hydride absorption.[7] Furthermore, for the first time, the crystallographic and electronic defects of CVD ZnS have been characterized as a function of its growth position with respect to the mandrel and shown to be highly variable.[4]

Insights into the HIP process of ZnS have been offered as well. The band edge of CVD ZnS has been investigated in detail here, showing that heat treating moves the edge further into the ultraviolet and indicating an absorption phenomenon separable from visible scattering. The role of the metal has previously been described as "inert" or "protection" from the graphite-reducing environment of the HIP chamber. To the contrary, platinum and other metals have been shown to be active in the recrystallization process. Identification of the materials on the surface of the metal foils is presented for the first time, lending credence to the importance of the metal in reacting with sulfur.

6.4 Suggestions for Future Work

Despite being known as a phosphor for over 100 years, the luminescence behavior of ZnS in its various forms still defies coherent and consistent explanation. The presence of blue, green, and combination bands in various

amounts in the samples studied in this work cannot be easily explained by electronic defect models available in the literature. Better structural characterization of point defects could be gained by using photoluminescence excitation (PLE) to vary the input excitation energy for luminescence and time-resolved methods for viewing spectral shift and decay. More complicated and expensive techniques such as electron paramagnetic (or spin) resonance (EPR/ESR), positron annihilation spectroscopy (PAS), or capacitance methods such as deep-level transient spectroscopy (DLTS) provide information about defect charges due to the inclusion of electric and magnetic fields.[24] Even better are methods that combine structural and electronic knowledge of defects such as scanning cathodoluminescence spectroscopy (SEM-CL) and imaging combinations with EPR such as optically detected magnetic resonance (ODMR).[25]

Absorption and scattering measurements could also aid in understanding electronic and microstructural defects. Absorption or emissivity measurements at low temperatures on very thin samples would help determine the presence of point defects and impurities, especially those present in low concentrations.

In microscopy, more-detailed investigation of the microstructure and nanostructure of ZnS will aid in producing better scattering and diffraction models. The advent of electron backscattered diffraction (EBSD) in scanning electron microscopes allows identification of crystal orientations at the same time they are imaged.[26] This technique could lead to new insights about the texturing of CVD ZnS and the changes it undergoes during recrystallization. Careful chemical analysis of twin boundaries in CVD and HIP CVD ZnS should be carried out using transmission electron microscopy (TEM) combined with x-ray energy dispersive spectroscopy (EDS) and TEM electron energy loss spectroscopy (EELS) similar to what has been done with natural sphalerites. Convergent beam electron diffraction (CBED) in TEM may allow individual nanotwin lamella to be investigated and stacking sequences determined.

On a more-macroscopic scale, there is still work to be done in understanding the banding and growth layers in CVD ZnS. Cores of red ZnS and elemental ZnS were not available, and when they are, they should be similarly characterized. Variation in these layers could also be assessed as a function of position in the CVD deposition chamber. If possible, micro-x-ray diffraction should be used to identify any hexagonality, texture, or lattice parameter differences between the growth bands that could help explain their origin. The formation, structure, and optical properties of the macroscopic "hillocks," visible most prominently in elemental ZnS (and in standard ZnS as well, though the difficulty seeing them is due to the material's visible opacity), deserves more attention. These structures can be imaged by scanning acoustic microscopy. It may be that these features are, at their root, associated with gas-phase-created hexagonal crystallites which have embedded in the growing ZnS body.

In the areas of recrystallization promotion, there are still a number of unknowns. Further research could investigate the phase transformation using only pressure, such as with a cold isostatic press (CIP), to see if recrystallization could be induced without elevated temperature. The exact mechanism for the promotion of recrystallization by certain metals and not others needs some dedicated work. This current work has only opened the door to the possibility of understanding the roles that these and other metals have on inducing recrystallization and grain growth in CVD ZnS.

Finally, a better understanding of the chemistry of the CVD ZnS deposition chamber is sorely needed. The lack of information about the actual mechanism for ZnS formation and deposition during bulk chemical vapor deposition heeds further optimization of the process. The installation of a mass spectrometer, such as a residual gas analyzer (RGA), somewhere in the gas stream would give some insight into the species and levels of contaminants in the process. Detailed investigation of the purity of process gases such as argon, hydrogen sulfide, and hydrogen is an easy first step toward understanding the full complexity of gas species available for reaction in the CVD chamber.

6.5 Final Thoughts

We are definitely indebted to the serious work on ZnS carried out in previous generations that established the basis of understanding of the physics and chemistry of this material. In the 1960s, many corporate labs such as Westinghouse, Bell, GE, IBM, RCA, and Phillips had well-funded programs to explore ZnS as a semiconductor material and phosphor. The Raytheon Research Division developed CVD ZnS in the 1970s, but since then dedicated funding towards the understanding of ZnS has been spotty at best. We were fortunate to discover the vast Russian literature on ZnS, some previously untranslated. It is our hope that the heyday of basic science and research and development, funded and published by the government and industry, is not over but only suffering a hiatus. Much of the work described herein clearly would not have been done without the continued interest by Raytheon in CVD ZnS.

It is worth reconsidering the mineral name for cubic ZnS—"sphalerite," from the Greek σφαλερός (*sphaleros*), meaning "treacherous." The Ancients demonstrated their particular wisdom in their naming of this material, one that has required careful and diligent study in order to pry loose any of its secrets. Though known as an infrared window material for over 50 years and as a phosphor for twice that, ZnS continues to offer new surprises. With the advent of new characterization techniques to probe the chemistry and physics of its structure, ZnS is sure to be a fruitful material to study for decades to come.

Figure 6.1 Standard CVD ZnS (left) and multispectral ZnS (right) produced commercially at Raytheon. The transparency of multispectral ZnS is apparent when viewing text through a ~3-mm-thick piece.

References

1. diBenedetto, B., "On hexagonal needles in CVD ZnS & anisotropy in transmission in growth direction and perpendicular to growth direction," personal communication (2008).
2. diBenedetto, B. A. and J. Pappis, "Chemical Vapor Deposition of Multispectral Domes," AFML-TR-75-27 (1975).
3. diBenedetto, B. A., J. Pappis, and A. J. Capriulo, "Chemical Vapor Deposition of Multispectral Windows," AFAL-TR-73-252 (1973).
4. McCloy, J., E. Fest, R. Korenstein, and W. H. Poisl, "Anisotropy in structural and optical properties of chemical vapor deposited ZnS," *Proc. SPIE* **8016**, 80160I (2011) [doi: 10.1117/12.886138].
5. McCloy, J., "Properties and Processing of Chemical Vapor Deposited Zinc Sulfide," Ph.D. diss., University of Arizona (2008).
6. McCloy, J., W. Wolf, E. Wimmer, and B. Zelinski, "Impact of hydrogen and oxygen defects on the lattice parameter of chemical vapor deposited zinc sulfide," *J. Appl. Phys.* **113**, in press (2013).
7. McCloy, J. and R. Korenstein, "Variability in Chemical Vapor Deposited Zinc Sulfide: Assessment of Legacy and International CVD ZnS Materials," *Proc. SPIE* **7302**, 73020M (2009) [doi: 10.1117/12.819559].

8. Sharifi, Y. and L. E. Achenie, "Using density functional theory to postulate a mechanism for zinc sulfide formation in a CVD reactor," *J. Crystal Growth* **307**(2), 440–447 (2007).
9. McCloy, J., R. Korenstein, and B. Zelinski, "Effects of Temperature, Pressure, and Metal Promoter on the Recrystallized Structure and Optical Transmission of Chemical Vapor Deposited Zinc Sulfide," *J. Am. Ceram. Soc.* **92**(8), 1725–1731 (2009).
10. Rice, R. W., S. W. Freiman, and J. J. Mecholsky, "The Dependence of Strength-Controlling Fracture Energy on the Flaw-Size to Grain-Size Ratio," *J. Am. Ceram. Soc.* **63**(3–4), 129–136 (1980).
11. Balluffi, R. W., S. M. Allen, and W. C. Carter, *Kinetics of Materials*, Wiley Interscience, New York (2005).
12. Bansagi, T., E. A. Secco, O. K. Srivastava, and R. R. Martin, "Kinetics of hexagonal-cubic phase transformation of zinc sulfide in vacuo, in zinc vapor, and in sulfur vapor," *Can. J. Chem.* **46**(18), 2881–2886 (1968).
13. Recnik, A., N. Daneu, T. Walther, and W. Mader, "Structure and Chemistry of Basal-Plane Inversion Boundaries in Antimony Oxide-Doped Zinc Oxide," *J. Am. Ceram. Soc.* **84**(11), 2657–2668 (2001).
14. Flewitt, P. E. J. and R. K. Wild, *Grain Boundaries: Their Microstructure and Chemistry*, John Wiley & Sons, New York (2001).
15. Butrymowicz, D. B. et al., "Diffusion-induced grain-boundary migration," in *Character of Grain Boundaries*, M. F. Yan and A. H. Heuer, Eds., 202–212, American Ceramic Society, Columbus, OH (1983).
16. Handwerker, C. A., R. L. Coble, and J. E. Blendell, "Diffusion-induced grain-boundary migration and discontinuous precipitation experiments in ceramic systems," in *Character of Grain Boundaries*, M. F. Yan and A. H. Heuer, Eds., 213–223, American Ceramic Society, Columbus, OH (1982).
17. Carter, W. C. and C. A. Handwerker, "Morphology of Grain Growth in Response to Diffusion Induced Elastic Stresses: Cubic Systems," *Acta Metallurgica et Materialia* **41**(5), 1633–1642 (1993).
18. Yan, M. F., R. M. Cannon, and H. K. Bowen, "Solute Segregation at Ceramic Interfaces," in *Character of Grain Boundaries*, M. F. Yan and A.H. Heuer, Eds., 255–273, American Ceramic Society, Columbus, OH (1982).
19. Recnik, A., M. Ceh, and D. Kolar, "Polytype induced exaggerated grain growth in ceramics," *J. Eur. Ceram. Soc.* **21**, 2117–2121 (2001).
20. Kingery, W. D., H. K. Bowen, and D. R. Uhlmann, *Introduction to Ceramics*, 2nd Ed., Wiley-Interscience, New York (1976).

21. McCloy, J. and R. Korenstein, "The Effect of Metal on the Formation of Multispectral Zinc Sulfide," *Proc. SPIE* **7302**, 73020N (2009) [doi: 10.1117/12.819461].
22. Bohren, C. F. and D. R. Huffman, *Absorption and Scattering of Light by Small Particles*, John Wiley & Sons, New York (1983).
23. McCloy, J., "Semi-empirical Scattering Model for Chemical Vapor Deposited Zinc Sulfide," *Proc. SPIE* **7302**, 73020W (2009) [doi: 10.1117/12.819536].
24. Neumark, G. F., "Defects in wide bandgap II-VI crystals," *Mater. Sci. Eng. R* **21**(1), 1–46 (1997).
25. Becker, W. and H. D. Lutz, "Phase Studies in the Systems CoS-MnS, CoS-ZnS, and CoS-CdS," *Mater. Res. Bull.* **13**, 907–911 (1978).
26. Zscheckel, T., W. Wisniewski, and C. Rüssel, "Microstructure and Texture of Polycrystalline CVD-ZnS Analyzed via EBSD," *Adv. Funct. Mater.* **22**(23), 4969–4974 (2012).
27. Siche, D. and H. Hartmann, "Source-material dependent growth limitations in unseeded dissociative sublimation of ZnSe," *J. Mater. Sci.* **31**, 6171–6175 (1996).
28. Devyatykh, G. G. et al., "Deviations from stoichiometry in polycrystalline CVD zinc selenide," *Doklady Akademii Nauk* **328**(1), 56–57 (1993).

Appendix
Engineering Data

A.1 Table of ZnS Engineering Properties

Note that the values presented in this section are typical and do not necessarily reflect measured values for a particular supplier or experimental condition. A more-detailed discussion of some of these properties is provided in the following. Mechanical properties, such as strength, are very extrinsic and depend on many factors including grain size, polishing process, stressed area, etc.[1,2] An excellent meta-study on data for CVD ZnS published up to 1996 is provided by Gibson *et al.*[3] Note that particularly with CVD ZnS, but with HIPed ZnS also, some anisotropies are observed depending on the orientation of the growth direction, as discussed in Ref. 4 and below. Values included in Tables A.1 and A.2 can be taken as average data.

A.2 Elastic Properties

A.2.1 Density

The x-ray density of cubic ZnS is 4.123 g/cm^3, and for hexagonal ZnS it is 4.103 g/cm^3 based on the perfect unit cell.[5] The actual density of materials is always lower than the x-ray density due to grain boundaries and defects.[6] In practice the density of sphalerite is usually quoted as 4.09 g/cm^3 and wurtzite as 4.08. Early assessments of CVD ZnS density using toluene immersion reported an average density of 4.08 g/cm^3.[7] Later assessments of Raytheon CVD ZnS state that run-to-run density fluctuations were 4.08335 $\pm$ 0.00020 g/cm^3 or $\Delta\rho/\rho \approx 5 \times 10^{-5}$.[8] Russian researchers report an increase in density with HIPing of CVD material, raising the measured density from 4.085 $\pm$ 0.001 to 4.095 $\pm$ 0.001 g/cm^3.[9] The effect of dissolved oxygen at the level of 10^{18}/cm^3 (0.004 at. %) on density is deemed negligible, but zinc vacancy concentration in sulfur-annealed single crystals has been estimated from $\Delta\rho$ of 0.0004 g/cm^3.[5]

Twenty-two measurements were made of various ZnS samples, with most of the samples measured 4.089 $\pm$ 0.001 g/cm^3 and a few slightly more or less.[10] The large differences reported by Russian researchers between CVD and HIP

Table A.1 Elastic, mechanical, and thermal properties at room temperature (~25–30 °C).

	Property	Symbol	Units	CVD ZnS	Multispectral (HIPed) ZnS	Notes
Elastic	Density	ρ	g/cm^3	4.09	4.09	
	Young's modulus	E	GPa	74.6	87.6	
	Poisson's ratio	N	unitless	0.29	0.32	
Mechanical	Hardness, Knoop	H_K	Kg/mm^2	210–250	150–165	1,2,3
	Hardness, Vickers	H_V	Kg/mm^2	230	150	1,2,3
	Fracture toughness	K_{ic}	$MNm^{-1.5}$	0.8	1.0	1
	Strength, average		MPa	103	60-69	1,4
Thermal	Conductivity	K	W/(m·K)	16.7	27.2	
	Coefficient of thermal exapansion		$\times 10^{-6}$/ K	6.8	6.5	
	Specific heat	c_p	J/(g·K)	0.469	0.527	
	Melting point	T_m	K	1093	1093	
Electrical	Resistivity	ρ_{el}	Ω·cm	$>10^{12}$	$>10^{13}$	

1. Processing dependent
2. Load dependent
3. Stressed-area dependent
4. To convert from kg force/mm^2 to MPa, multiply by 9.80665

CVD ZnS were not observed. The HIPed samples were 0.002 and 0.003 g/cm^3 denser than the average, with an estimated error on all measurements of ± 0.001 g/cm^3. Based on the limited number of measurements, it seemed that there could be a correlation between high optical transparency in the visible and density (i.e., red ZnS, eZnS, and HIP ZnS all had densities on the high side). For engineering purposes, there is no reason to distinguish between the density of CVD and HIPed material, and the value of 4.09 g/cm^3 has been assigned for both.

A.2.2 Young's modulus and Poisson's ratio

Calculations of the elastic properties of polycrystalline ZnS have been conducted based on the single-crystal tensor properties of cubic ZnS.[11] This study showed that the calculated values for Young's modulus and Poisson's ratio of polycrystalline ZnS agree with the measured values for HIPed CVD ZnS but are about 17% higher than measured values for as-deposited CVD ZnS. The differences are explained as being due to the presence of hexagonal phase in CVD ZnS and the considerable stacking disorder. The variational principles of Hashin and Shtrickman[12] were used in this analysis, which give much better bounds than Reuss and Voigt methods for calculating bulk and shear moduli. For example, the calculated Voigt shear modulus for ZnS is 19% higher than the Reuss shear modulus, while the Hashin shear modulus is only 3% larger than the Shtrickman shear modulus. There is some indication of anisotropy in the elastic constants of CVD ZnS, particularly the Poisson's

Table A.2 Optical properties at room temperature.

Property	Symbol	λ (μm)	Units	CVD ZnS	Multispectral (HIPed) ZnS	Notes
Refractive index	n_d	0.588	unitless	2.3676	2.3675	
	n	0.633	unitless	2.3504	2.3504	
	n	1.064	unitless	2.2879	2.2883	
	n	3.39	unitless	2.2553	2.2559	
	n	10.6	unitless	2.1921	2.1925	
Thermo-optic coefficient	dn/dT	0.633	$\times 10^{-6}$/ K	54	54	
	dn/dT	1.15	$\times 10^{-6}$/ K	50	42	
	dn/dT	1.5	$\times 10^{-6}$/ K	46		
	dn/dT	3.39	$\times 10^{-6}$/ K	43	39	
	dn/dT	10.6	$\times 10^{-6}$/ K	41		
Attenuation coefficient	α	1.064	cm^{-1}	0.35–4.6	0.04	1
	α	3.39	cm^{-1}	0.03–0.59	0.01	1
	α	10.6	cm^{-1}	0.24	0.18	
Refractive index homogeneity	$\Delta n/n$	0.633	unitless		20	
	$\Delta n/n$	10.6	unitless	100		
Dielectric constant	E	1 MHz	unitless	9.67		
		400 MHz	unitless	8.7	7.8	
		14 GHz	unitless	8.7	8.5	
		35 GHz	unitless	8.35	8.39	
Loss tangent	tan δ		unitless	0.0024	0.0024	

[1]See Chapter 4 for variability in attenuation (absorption + scattering) and Section A.2 on absorption coefficient to assess bulk absorption.

ratio, due to the columnar preferential growth perpendicular to the mandrel.[13] A comparison of these values is shown in Table A.3.

The increase in Young's modulus after HIPing has been recently proposed as being due to a decrease in dangling bonds in nonequilibrium grain boundaries.[9,14] These authors corroborate this hypothesis with low-frequency dielectric-constant measurements and electron paramagnetic resonance. Note, however, that these dielectric results have not been reproduced by U. S. researchers. Elastic energy losses at the 1–2 kHz range are said to be due to the excitation of dislocations in grain boundaries.

A.3 Mechanical properties

Of all the data on optical materials, perhaps the most variable are the mechanical properties, particularly hardness, fracture toughness, and strength. Hardness depends on load type, loading rate, and stressed area. Likewise, toughness depends on pre-existing flaw size, test method, and other factors. Strength, most notoriously, depends on surface finish, subsurface flaws, stressed area, load profile, and contact stresses. Critical applications require detailed analysis of these factors, which is beyond the scope of this book. Interested readers are referred to standard references on the subject.[18]

Table A.3 Published values for Young's modulus (E) and Poisson's ratio (ν) for CVD ZnS and HIPed CVD ZnS. Static tests involve strain gauges on the tensile side of a flexural bend test. Dynamic methods are those such as ASTM E1259 that involve sound-wave propagation with noncontact transducers.

CVD ZnS	HIPed CVD ZnS	Manufacturer	Orient. (CVD)	Method	Reference
$E = 10.7 \pm 0.5$ Msi (74.1 ± 3.6 GPa)	N/A	Raytheon	Independent of orientation	Static	Wimmer[13]
$E = 10.8 \pm 0.5$ Msi (74.5 ± 3.5 GPa)	$E = 12.7 \pm 0.1$ Msi (87.6 ± 0.7 GPa)	Raytheon	Not indicated	Static	Klein[11]
$E = 12.4$ Msi (85.5 GPa) – Shtrikman limit $E = 12.7$ Msi (87.7 GPa) – Hashin limit	Single XL tensor data from Berlincourt[15]	Assumed isotropic	Calculated	Klein[11]	
$E = 11.69 \pm 0.26$ Msi (80.6 ± 1.8 GPa)	$E = 12.74 \pm 0.06$ Msi (87.8 ± 0.4 GPa)	Rohm & Haas	Not indicated	Dynamic	Henneman[16] and pers. comm.
$E = 11.3$–11.7 Msi (77.9–80.9 GPa)	$E = 12.5$–13.3 Msi (86.2–91.5 GPa)	IKhVV RAN, Russia	Not indicated	Not indicated	Shchurov[9]
$E = 11.5$ Msi (79 GPa)	$E = 12.6$ Msi (87 GPa)	IKhVV RAN, Russia	Not indicated	Not indicated	Yashina[17]
$\nu = 0.30 \pm 0.003$	N/A	Raytheon	Contraction normal to growth direction	Static	Wimmer[13]
$\nu = 0.35 \pm 0.017$	N/A	Raytheon	Contraction parallel to growth direction	Static	Wimmer[13]
$\nu = 0.29 \pm 0.1$	$\nu = 0.318 \pm 0.001$	Raytheon	Not indicated	Static	Klein[11]
$\nu = 0.318$ – Shtrikman limit $\nu = 0.314$ – Hashin limit		Single XL tensor data from Berlincourt[15]	Assumed isotropic	Calculated	Klein[11]
$\nu = 0.30 \pm 0.008$	$\nu = 0.33 \pm 0.007$	Rohm & Haas	Not indicated	Dynamic	Henneman[16] and pers. comm.

A.3.1 Hardness

Hardness relates to the resistance of a material to indenter penetration. Minimum Vickers' hardness in CVD ZnS for 10-N loads was ~1.6 GPa for 15–25-μm average grain-size material.[19] Note that data from Savage *et al.*,[23] Townsend and Field,[19] and Lewis *et al.*[21] appears to be the same data, except that the latter reference has a more datapoints for CVD ZnS as well as some data for HIPed ZnS. Hardness increased with decreasing grain size, following a Petch mechanism due to dislocation pile-ups at grain boundaries, reaching a maximum value of 2.2 GPa for 2.5-μm grain sizes[19] and 4.0 GPa for 0.5-μm grain sizes.[20] Hardness measurements for grain sizes >17 μm varied widely due to anisotropic hardness of individual grains. Though hardness appeared to increase with increasing grain size for 10-N loads, measurements using 100-N loads showed more-constant hardness at large sizes (~1.4 GPa for grain sizes >30 μm), showing that this value probably represents the hardness of single crystals (grains). Standard commercial CVD ZnS at 4–8 μm has a Vickers' hardness around 2.0 GPa for both 10-N and 100-N loads. Hardness of HIPed material is indistinguishable from hardness of unHIPed material at the same grain size, about 1.8 GPa for 150-μm grain sizes in the recrystallized HIPed material.[21] Figure A.1, taken from Ref. 22, is based on data from Refs.

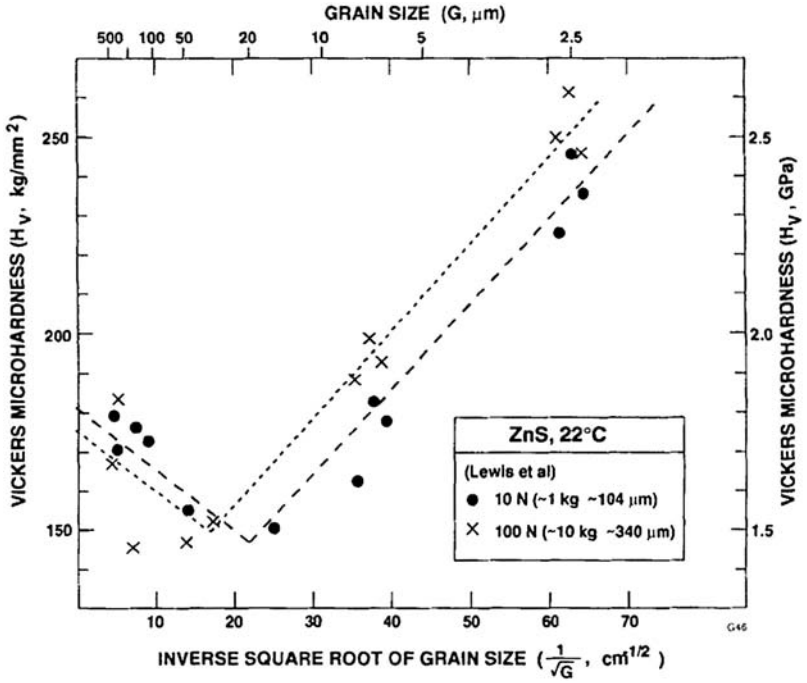

Figure A.1 Hardness as a function of grain size (image from Rice[22] used with permission; copyright 2009 John Wiley & Sons).

19, 21, and 23, and shows the minimum in hardness due to the effect of the indenter size as it relates to the grain size. A similar effect is seen with indenter toughness measurements.

Hardness versus displacement (load) rate of CVD ZnS was determined at two temperatures.[24] The material is effectively harder when impacted at higher rates. These load rates are much lower than those for real dynamic impact situations (rain, sand). The authors determined the quasistatic hardness for low-velocity impacts to be 3 GN/m^2, corresponding to a plastic strain rate of 10^4/sec for this ZnS.

A.3.2 Toughness

Fracture toughness (quoted in units of $MN \cdot m^{-1.5}$ or equivalently in $MPa \cdot m^{1/2}$), or the resistance of the material to crack propagation, has been measured for CVD ZnS by various methods. There is some indication that the toughness in CVD ZnS might be anisotropic,[25,26] but the details are not readily available in the literature. Toughness was determined by fracturing notched rings by hydrostatic expansion.[27] Samples had average grain diameters of 8 μm and aspect ratios of about 8 for the columnar structure. Expansion of the cylinders was in the direction perpendicular to the growth direction (column direction). Measured toughness was 0.75 ± 0.01 $MPa \cdot m^{1/2}$, and crack propagation was by mixed intergranular and transgranular mode. Toughness measured from double-cantilever beam experiments was determined to be 0.67 ± 0.04 and 0.69 ± 0.07 $MPa \cdot m^{1/2}$ for two different lots of CVD ZnS, with cracks propagating parallel to the growth direction.[13] Zhang and Ardell[28] found a value of toughness for CVD ZnS at "infinite crack length" of 0.86 ± 0.08 $MPa \cdot m^{1/2}$ by using a controlled flaw method and a ring-on-ring, disk-bend fracture toughness test, and although these authors mention both CVD and HIPed CVD ZnS, it is not clear from the paper for which material they are reporting the toughness. Toughness computed from fracture mechanics and from fracture surface analysis was determined to be 1.1 ± 0.1 and 1.05 ± 0.03 $MPa \cdot m^{1/2}$, respectively.[29]

Indentation fracture toughness increased with HIPing, however, for comparable grain sizes. Toughness values for CVD ZnS peak at 0.8 $MPa \cdot m^{1/2}$ for 8-μm grain-size material.[19] Materials with 2.5-μm grain size exhibit toughness of 0.6 $MPa \cdot m^{1/2}$, whereas large-grain-size material (500 μm) exhibits toughness of 0.3 $MPa \cdot m^{1/2}$.[19] Large-grain-size toughness values represent single crystals, and maximum toughness corresponds to an indenter size effect. To our knowledge, no nanoindentation studies have been published for CVD ZnS. HIPing increases the toughness in CVD ZnS for comparable grain-size material.[21] Toughness for HIPed ZnS was 0.8–1.2 $MPa \cdot m^{1/2}$ for 100-N loads compared to about 0.5 $MPa \cdot m^{1/2}$ for comparable grain sizes (~100-μm diameter) for CVD ZnS. The recrystallization of HIPed ZnS results in more pristine grain boundaries and a denser material, which tends to improve material toughness.[30]

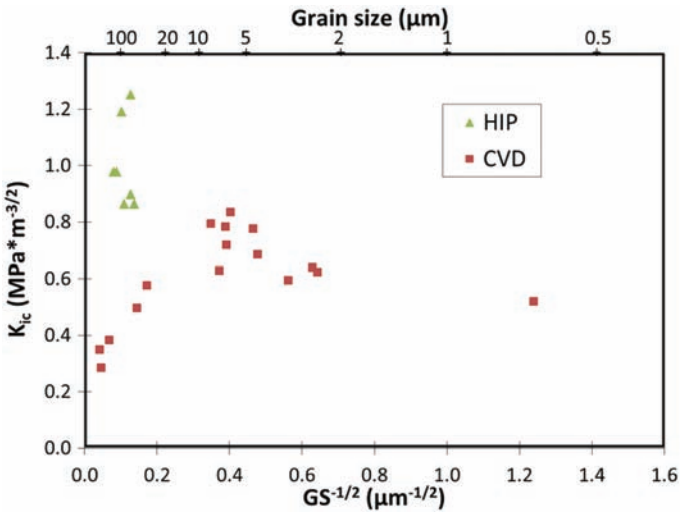

Figure A.2 Fracture toughness as a function of grain size (data from Lewis *et al.*[22]).

A grain-size to indenter-load effect can be seen in toughness determined by indentation (e.g., Vickers); see Fig. A.2. This effect is due to the relationship between the size of the indenter impression (which is also related to the load force and hardness resistance force in the material) and the material contacted by the indenter. For example, a large-grain-size material may be more likely sampled in a single grain, which would behave more like a single crystal, whereas a very small-grained material would more likely be sampled on a grain boundary. These two extremes will have different fracture toughness values due to the deformations being different mechanisms (i.e., cleavage versus grain-boundary pile-up).

Hardness of all ceramics tends to go through a minimum from single crystal to very fine grains, the effect of which is more pronounced at higher loads. Cracking depends on load, residual additives, indent geometry, surface finish (most important at low loads), porosity/density, compositional variation, phase inhomogeneity, anisotropy (single-crystal hardness can be anisotropic), and residual stress. Cracking along grain boundaries (spalling) can be exacerbated by thermal-expansion anisotropy and elastic anisotropy. For reference, ZnS has 8.4% elastic anisotropy, which is fairly high.[22]

A study was made on contact damage by Vickers indent on ZnS as a function of grain size.[26] Deformation was determined to be accommodated by plastic flow within the grains and by movement along grain boundaries. The porous zone results from shear along flow lines and from nucleation of voids where flow lines cross. All cracks nucleated from the boundary of the porous (plastic) zone or at the crossing of shear lines. Similar data was later analyzed for hardness and toughness values as a function of grain size in standard

ZnS.[19] Because many of the toughness equations involve hardness as a variable, and the latter authors found a variation in hardness with grain size, they used a toughness equation that did not have hardness in it:

$$K_c = (0.0762)P/c^{3/2}, \tag{A.1}$$

where load P is plotted against crack length $c^{(1.5)}$, and the slope is taken as toughness K_c.

Observations of Townsend and Field[19] include the lack of median cracks under the indenter for grain sizes >8 μm, and the radius of the multiple-fracture zone was taken as c for these samples. Cracks were said to nucleate from dislocation pile-ups at grain boundaries and to propagate in cleavage planes of the large grains. Measured toughness decreased for grain sizes <8 μm due to void formation under the indenter; in other words, the stored elastic energy is released after the load is removed and there is voiding underneath. The smaller grain sizes have higher values of hardness but not toughness (remember that these authors did not use hardness to calculate toughness).

This phenomenon suggests that when particles on the order of the grain size impact the part, enhanced erosion is likely. Also, indent testing may not be good for fracture-toughness measurements of intermediate grain size. The hardness is at a minimum when the indenter diameter is on the order of the grain size. The effect is more pronounced with Vickers indenters and at higher loads.

A.3.2.1 Slow crack growth

Pickles and Field[31] give data on crack velocity in ZnS as a function of stress intensity in both air and water. All surface flaws in ceramics contain residual stress unless that stress is deliberately removed.[32] This can be accomplished by annealing (though care should be made not to change the grain size of the material tested) or by carefully controlled successive grinding and polishing to remove the stressed layer. Any residual stresses in surface flaws are enough of a driving force for slow crack growth through stress corrosion.

Most slow-crack-growth parameters are tabulated without including residual stress. An equation exists to convert these parameters to a value that assumes residual stress in the flaws, which is the most common situation. The time-to-failure for a part considering crack growth is

$$\tilde{t}\, constant * \sigma^{N'}, \tag{A.2}$$

where t is the time to failure, σ is the *inert strength* (i.e., instantaneous strength), and N' is the *slow-crack-growth exponent* in the presence of residual stress. In other words, time is on the order of a constant times the inert strength raised to the slow crack growth exponent. Inert strength can be estimated if one knows the condition in which a set of data was taken [i.e., broken in air over a few seconds with relative humidity (RH) 50%], the value of N', and the relationship between N' and strength reduction factor, as shown

in Pepi.[33] For example, if the catalog measures average strength in air from testing done over a few seconds, inert strength can be obtained by scaling up by the factor on the 50% RH curve; specifically, finished fused-silica glass tested in air may have a strength of 20,000 psi, but its inert strength would be, for $N' = 28$, approximately 1.4 times higher (28,000 psi).[34]

N' can be found from N by $N' = (rN + 2) / (r + 1)$, where $r = 3$ for point flaws, which is the reality even for scratches that appear to be line (Griffith) flaws.[33] Surface flaws with their depth equal to their surface extent are called "penny" cracks. Values for the slow crack growth or stress corrosion exponent without residual stress (N) and with residual stress (N') in the surface flaws for ZnS are discussed below.

Standard ZnS:

NIST data (unpublished) but alluded to in Ref. 35. This explanation was provided by Pepi,[33] who was involved in the testing.

To obtain data on ZnS N value and strength, the following was done:

- Four-point bend flexure tests were performed on as-received (no indentation) samples. Twenty samples were used, failed in air at a fast rate (10^4 MPa per second), so measured strength is close to inert strength. Average strength is 135 MPa.
- For dynamic fatigue tests, 3-N Vickers indents were placed to ensure that cracks were parallel to the tensile stress axis. At least five specimens at each of four stress rates were broken in distilled water, with rates varying from 10^{-2} to 10^4 MPa/sec. To get indented inert strength, five specimens were tested in dry oil at 10^4 MPa/sec. The result was indented inert strength of 69 MPa.
- A plot of dynamic fatigue was prepared, and from the slope a flaw growth exponent of 57.5 was computed. Because this value contains residual stress, an N value of 76 $[(4/3)N' - (2/3)]$ is obtained.

Multispectral ZnS:

Slow crack growth was performed by SSG[33] for a different customer, so data could not be divulged. The summary of the results (Table A.4) follows:

Table A.4 Slow-crack-growth parameters for ZnS as reported in the literature. Data from Pepi[33] are the most reliable given the rigorous methodology used to obtain them.

Material	Stress corrosion parameter (n)	$N' = (r{\cdot}n + 2) / (r + 1)$, where $r = 3$ point flaws; presence of residual stress	References
CVD standard ZnS	20–40	15.5–30.5	[13]
CVD standard ZnS	Infinity	Infinity	[36]
CVD standard ZnS	76	57.5	[33]
CVD multispectral ZnS (Cleartran®)	46	35	[33]

- The multispectral ZnS testing was done on four-point bend samples in water.
- Indents could not be readily or consistently produced on these samples. Therefore, testing was performed on polished samples, ~350 over a three-year program.
- If dynamic fatigue testing with good indents was used, five samples at each of four stressing rates would be required. For polished samples with variable defects, many more samples are required to average results (about 80 samples at each of five stress rates). The actual quantity tested was dependent upon availability of material and cost of testing, but the more the better.
- This is not the best way to determine N. One would like to have consistent strength at a given stress rate, greatly reducing the number of samples required for good statistics.

A.3.3 Fracture strength

Fracture strength of ZnS has been assessed on various sample types. Most of the testing performed was ring-on-ring biaxial flexure.[1] In addition, limited experiments have been performed in compression to assess the relative strengths of the two directions in the CVD growth process.[4] Details of a comparison of ring-on-ring data from various vendors and heat treatments of CVD ZnS is provided elsewhere.[1] A model for a bimodal flaw-size distribution in ZnS has been recently proposed by Klein.[37] Other ZnS strength data was recently summarized in Harris *et al.*[38]

A probability of failure plot based on these parameters is shown in Fig. A.3. This probability is based on using the unbiased Weibull modulus to

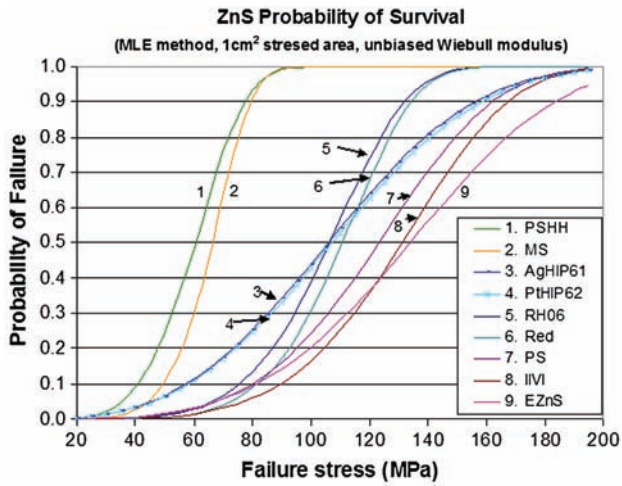

Figure A.3 ZnS biaxial flexure probability of failure versus applied stress.

account for small sample sizes. It can immediately be seen that the high-temperature HIPed samples have a relatively high Weibull modulus (slope of the probability of failure curve) with a lower scale factor (strength of the 62% point in the distribution). The lower-temperature HIPed samples, though they have a higher average strength and scale factor, have a low Weibull modulus, indicating a broad distribution of strengths (large standard deviation). All of the CVD materials have a moderate Weibull modulus and a higher scale factor than the heat-treated samples. All tests were done on the same apparatus with the same surface preparation by the same optical shop, so surface flaws should be similar for all samples. However, the different Young's modulus between as-deposited and HIPed samples (described earlier) could influence the behavior of abrasives interacting with the sample and result in a different flaw size in the CVD versus HIPed materials. The shape of the curve for the low-temperature HIPed samples suggests that they may have a fracture character intermediate between the as-deposited and high-temperature HIPed samples. At this low HIP temperature, Pt- and Ag-HIPed samples appear to be fully recrystallized with a grain size comparable to that of the high-temperature HIPed samples.[10] However, the texture analysis on similar Ag foil samples showed a somewhat intermediate crystallographic texture between CVD ZnS and high-temperature HIPed ZnS.[10]

The literature shows that the transition between the lower single-crystal fracture energy to the larger polycrystalline fracture energy is best understood in terms of the ratio of the flaw size to the grain size.[39] Ratios of about one or higher generally indicate that polycrystalline fracture mechanics should be applied. Flaw sizes in HIPed ZnS have been measured at 100–200 μm,[16] suggesting that even the relatively large-grained HIPed material is controlled by polycrystalline fracture mechanics. However, the caveat is that crystallographic texturing and preferred cleavage planes can greatly influence the transition from single-crystal to polycrystalline fracture energy.[39] CVD ZnS, such as the studied CVD ZnSe in the previous reference, has preferred texturing and a single preferred cleavage along the [110] direction. The difference in crystallographic texturing between the low-temperature and high-temperature HIPed samples can probably explain the different fracture behavior.

A.3.4 Rain and sand erosion resistance

During the 1990s, many scientists and engineers developed methods that attempted to improve the durability of ZnS, whether through covers, coatings, or treatments to the bulk ZnS itself.[40] Other less-successful methods that were investigated included grain refinement, thermal tempering, ion implantation, and pulsed electron beam annealing.[41] A detailed discussion of rain-erosion testing of CVD ZnS is beyond the scope of this text, but the reader is referred to the excellent summary on rain erosion by Gibson *et al.*[3] and the data and

discussion in Harris.[40] Some insights on ZnS with respect to rain and sand erosion have been presented in Sections A.1.1 and A.1.2. Data on transmission loss as a function of erosion are typically kept as closely guarded proprietary information by end users.

A.3.5 Laser-damage effects

A discussion of laser-damage effects on ZnS is beyond the scope of this text, but the reader is referred to the excellent summary by Gibson *et al.*[3]

A.4 Thermal Properties

A.4.1 Thermal expansion

Gibson[3] summarized data up to ~1996 and presented the following relation for mean coefficient of thermal expansion (CTE) of CVD ZnS ($T = 300$–1200 K) in ppm/K:

$$\alpha = 3.469 + (0.01737)T - (2.553\times10^{-5})T^2 + (2.015\times10^{-8})T^3 - (5.816\times10^{-12})T^4. \quad \text{(A.3)}$$

Recently, Harris *et al.*[38] measured multispectral ZnS (Cleartran®) and obtained ($T = 213$–673 K):

$$\Delta L/L_0 = -1.218\times10^{-3} + (1.496\times10^{-6})T + (1.079\times10^{-8})T^2 - (5.742\times10^{-12})T^3. \quad \text{(A.4)}$$

Additionally, when combined with previous data on standard CVD ZnS, which exists over a much-broader temperature range, Harris *et al.*[38] propose an expression for thermal expansion of either standard or clear ZnS as ($T = 90$–1255 K):

$$\Delta L/L_0 = -1.082\times10^{-3} + (3.406\times10^{-7})T + (1.461\times10^{-8})T^2 - (1.181\times10^{-11})T^3 + (3.791\times10^{-15})T^4. \quad \text{(A.5)}$$

Typical quoted values for room-temperature CTE for multispectral ZnS are slightly lower than for CVD ZnS, but new, careful measurements of standard CVD ZnS are needed to compare to the newer measurements of multispectral (Cleartran®) ZnS to fully resolve whether the small difference is real or not. Note that the most-common definition for the mean coefficient of expansion is[2]

$$\alpha_m = (\Delta L/L_0)/(T - T_0), \quad \text{(A.6)}$$

where L_0 is the length at T_0. It should be noted that the two results, Harris *et al.* (broader temperature range) and Gibson *et al.*, differ substantially at the highest temperatures, with Gibson being higher. This is presumably because Harris relied on the high-temperature data of Koenig,[42] whereas Gibson relied

on the high-temperature data of Artyukh *et al.*,[43] the latter of which is for KO-2 hot-pressed ceramic ZnS.[17,44]

A.4.2 Thermal conductivity

Thermal conductivity (κ) for standard CVD ZnS was described by Gibson *et al.*[3] ($T = 150$–1200 K) in W/(m·K) as

$$\kappa = [0.0156 + (1.44\times10^{-4})T]^{-1}. \tag{A.7}$$

Again, Harris *et al.*[38] provided reassessed temperature-dependent values but report different relations for multispectral ZnS (Cleartran®), standard ZnS, and KO-2 (Russian hot-pressed material[45]). Unlike for thermal expansion, thermal conductivity varied greatly depending on the material fabrication method. For details on the measurements and the fitting, refer to Harris *et al.*[38] and references therein.
For multispectral ZnS ($T = 233$–643 K):

$$\kappa = 71.42 - (0.1967)T + (1.921\times10^{-4})T^2 - (5.826\times10^{-8})T^3. \tag{A.8}$$

For standard ZnS ($T = 296$–811 K):

$$\kappa = 32.16 - (6.247\times10^{-2})T + (3.800\times10^{-5})T^2. \tag{A.9}$$

For KO-2 ($T = 329$–1330 K):

$$\kappa = 35.77 - (6.212\times10^{-2})T + (4.689\times10^{-5})T^2 - (1.312\times10^{-8})T^3. \tag{A.10}$$

A.4.3 Specific heat (heat capacity)

Heat capacity as a function of temperature has been reviewed in Gibson *et al.*[3] Multispectral ZnS (Cleartran®) was recently re-measured at Purdue's Thermophysical Properties Research Laboratory (TPRL)[16,38] and compared to older data from standard ZnS.[42] Heat capacity (in Joules/gram/Kelvin) as a function of temperature (213–643 K) was fit as follows:

$$\begin{aligned} c_p = {} & 0.4409 - (4.895\times10^{-4})T + (4.000\times10^{-6})T^2 \\ & -(7.780\times10^{-9})T^3 + (4.784\times10^{-12})T^4. \end{aligned} \tag{A.11}$$

A.5 Optical Properties

A.5.1 Refractive index

The most-widely cited refractive-index data on ZnS comes from Li,[46] who created the refractive-index dispersion curve used by many researchers. Li derived a ZnS refractive-index Sellmeier equation as a function of both wavelength and temperature based primarily on CVD and natural ZnS experimental data of Mell[47] and Feldman *et al.*[48] with additional consideration of other data. The generally accepted Sellmeier equation from Li,[46] valid

from $\lambda = 0.5$ μm to $\lambda = 14$ μm, and $T = 93 - 618$ K, is as follows [where $t = T(K) - 293$]:

$$n^2(\lambda, t) = C + \frac{D}{\lambda^2 - \lambda_1^2} + \frac{E\lambda_2^2}{\lambda^2 - \lambda_2^2}, \tag{A.12}$$

where

$$\lambda_1[\mu\text{m}] = 0.23979 + (4.841\times10^{-5})t;$$
$$\lambda_2[\mu\text{m}] = 36.525 + (4.75\times10^{-3})t;$$

The Sellmeier equation normally encountered for CVD ZnS is just the Li equation assumed for room temperature (i.e., $t = 0$). Other room-temperature fits of ZnS index data include a Sellmeier fit by Tatian[49] for CVD ZnS and an 11th-order polynomial fit by Debenham[50] for those measured on multispectral CVD ZnS prisms. The latter data on multispectral ZnS was fit by Klein[51] to a Sellmeier that is commonly used to represent the colorless ZnS today:

$$n^2 = 8.393 + \frac{0.14383}{\lambda^2 - 0.2421^2} + \frac{4431.0}{\lambda^2 - 36.71^2}. \tag{A.13}$$

The results of the fits by Li_{46} and Klein_{51} indicate very small differences between CVD ZnS and multispectral ZnS (see Table A.5), which probably reflect real differences and not merely differences in fitting techniques. It is

Table A.5 Refractive index values for ZnS at 20 °C. Note that differences in the fourth decimal place can readily be measured using prism coupling and minimum-deviation method.[62] Differences between CVD ZnS and multispectral ZnS should be taken as real differences. Note that values shown are calculated based on the commonly accepted Sellmeier equations as discussed in the text.

Wavelength (μm)	CVD ZnS	Multispectral ZnS
0.500	2.4200	2.4199
0.633	2.3504	2.3504
1.000	2.2921	2.2925
1.064	2.2879	2.2883
2.000	2.2647	2.2653
3.000	2.2574	2.2581
3.390	2.2553	2.2559
4.000	2.2520	2.2527
5.000	2.2463	2.2469
6.000	2.2396	2.2403
7.000	2.2319	2.2325
8.000	2.2228	2.2234
9.000	2.2123	2.2128
10.000	2.2002	2.2007
10.600	2.1921	2.1925
11.000	2.1863	2.1867
12.000	2.1704	2.1709
13.000	2.1524	2.1528

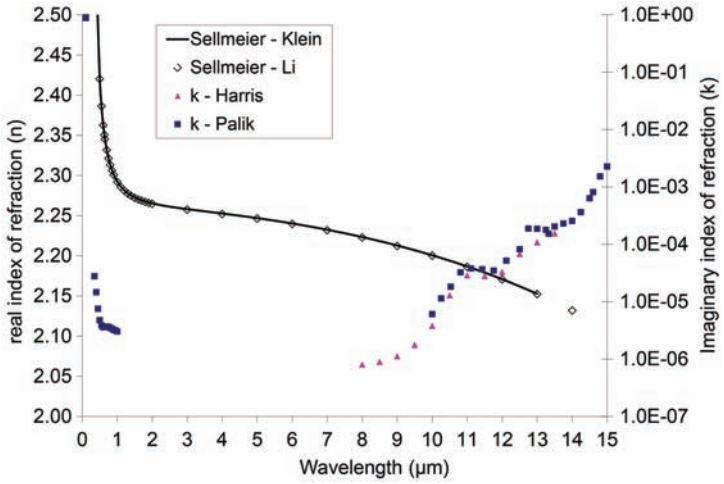

Figure A.4 Refractive index versus wavelength (μm) based on Sellmeier equations from Li[46] and Klein.[51] Data for *k* from Palik[52] and Harris *et al.*[38]

indicated, then, that at least at infrared wavelengths, the refractive index of multispectral ZnS is slightly larger than CVD ZnS, by ~ 0.0004. It is unknown whether there is lot-to-lot variation or vendor-to-vendor variation in these precision measurements. A comparison of these equations, along with data for imaginary index *k* (from Palik[52] and Harris *et al.*[38]), is shown in Fig. A.4.

Palik and Addamiano[52] provide a tabulated summary of optical constants of ZnS across the whole electromagnetic spectrum, and a representation of the refractive data is shown in Fig. A.5. The large oscillation in refractive index (~35 μm) is due to the fundamental optical phonons (i.e., the Restrahlen band).

Other notable papers on ZnS refractive index include: Bieniewski *et al.*[53] for hexagonal ZnS crystals; Ong *et al.*[54] for wurtzite thin films; Hattori *et al.*[55] and Memon *et al.*[56] for far-infrared measurements by dispersive Fourier transform infrared (FIT) measurements; Thamizhmani *et al.*[57] for far-infrared properties by THz-time domain spectroscopy; Dodge[58] for minimum-deviation-method data on CVD ZnS; Ozaki and Adachi[59] for 1.2–5.6 eV real and imaginary permittivity for cubic ZnS fitted to a damped harmonic oscillator; Tsuchiya *et al.*[60] for a model of permittivity for 0–20 eV; Rummel *et al.*[61] for index homogeneity in multispectral ZnS; Harris *et al.*[38] for recent measurements of long-wavelength infrared complex index for multispectral ZnS; and Qiao *et al.*[62] for prism coupler measurements showing the lack of refractive index anisotropy in CVD ZnS.

A.5.2 Thermo-optic coefficient

Table A.6 and Fig. A.6 display graphical and tabulated data on the change of refractive index with temperature (dn/dT) for multispectral and CVD ZnS.

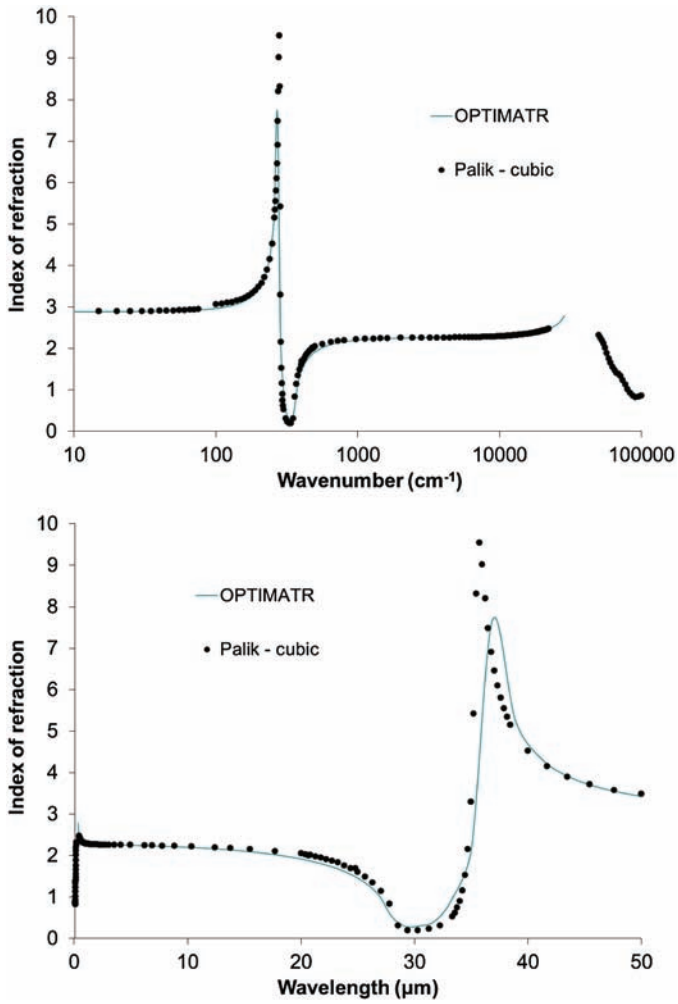

Figure A.5 Refractive index versus wavenumber (log scale) and versus wavelength (μm). Data from Palik[52] with model from OPTIMATR.[63,64]

Detailed data from Feldman *et al.*[48] on CVD ZnS (Table A.6) is in the same range as recent data from Qiao *et al.*[62] for CVD ZnS *dn/dT* at 10.6 μm and 60 °C (35–48 ppm/°C). Data from Blodgett *et al.*[65] for *dn/dT* values for multispectral ZnS (30–55 ppm/°C, depending on wavelength and temperature) is shown in Fig. A.6.

A.5.3 Absorption coefficient

Extinction coefficient values for various ZnS samples at key wavelengths are provided in Chapter 4. Some models of infrared absorption examining ZnS have been reviewed elsewhere.[64,66,67] Values for the imaginary component of

Table A.6 *dn/dT* (ppm/K) for CVD ZnS. Data from Feldman[48].

Temp °C	1.15 μm	3.39 μm	10.6 μm
−180	35	28	27
−160	37	31	30
−140	38	33	33
−120	40	35	35
−100	41	37	37
−80	42	39	38
−60	43	40	39
−40	44	41	40
−20	45	41	40
0	45	42	41
20	46	42	41
40	46	43	41
60	47	43	41
80	47	43	41
100	47	43	42
120	48	44	42
140	48	44	43
160	49	44	44
180	49	45	45
200	50	46	47

refractive index (k) and absorption coefficient were recently calculated for the scatter-free region of multispectral ZnS (above 8 μm) from transmission data by Harris *et al.*,[38] based on the assumption that refractive index follows Li's[46] equation (see Table A.7). Additionally, Blodgett *et al.*[66] measured multispectral ZnS as a function of temperature from 10–800 K, and a sampling of their high-temperature data is shown in Fig. A.8 (also >8 μm). Klocek[68] lists

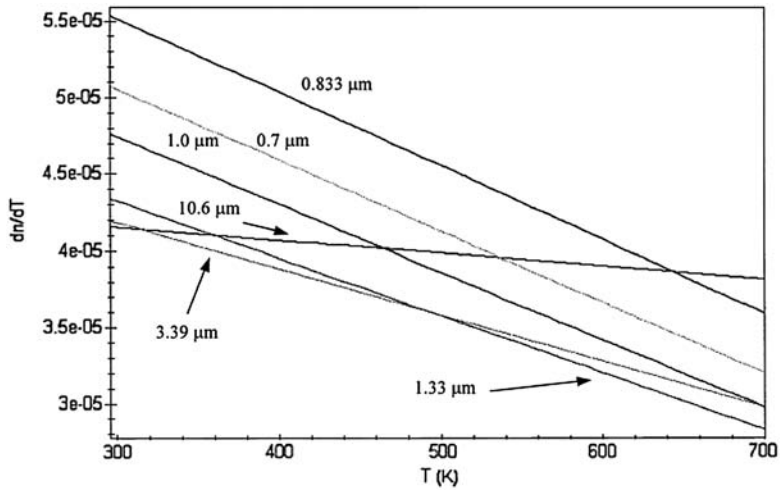

Figure A.6 *dn/dT* of multispectral ZnS (from Blodgett[65]).

Table A.7 Index (from Li at 24 °C), k, and α (cm^{-1}) for multispectral ZnS (from Harris[38]).

Wavelength (μm)	24°C			100°C			200°C		
	n	k	α (cm^{-1})	n	k	α (cm^{-1})	n	k	α (cm^{-1})
8.0	2.223	8.0×10^{-7}	0.013	2.226	3.8×10^{-7}	0.006	2.231	3.8×10^{-7}	0.006
8.5	2.218	8.9×10^{-7}	0.013	2.221	9.4×10^{-7}	0.014	2.225	9.4×10^{-7}	0.014
9.0	2.212	1.12×10^{-6}	0.016	2.216	8.5×10^{-7}	0.012	2.220	1.28×10^{-6}	0.018
9.5	2.207	1.76×10^{-6}	0.023	2.210	1.96×10^{-6}	0.026	2.214	3.18×10^{-6}	0.042
10.0	2.200	3.79×10^{-6}	0.048	2.203	6.13×10^{-6}	0.077	2.208	8.47×10^{-6}	0.106
10.5	2.194	1.29×10^{-5}	0.155	2.197	1.67×10^{-5}	0.200	2.201	2.29×10^{-5}	0.274
11.0	2.186	2.87×10^{-5}	0.328	2.190	3.98×10^{-5}	0.455	2.194	5.27×10^{-5}	0.602
11.5	2.179	2.77×10^{-5}	0.302	2.182	4.53×10^{-5}	0.495	2.186	6.76×10^{-5}	0.739
12.0	2.171	3.27×10^{-5}	0.342	2.174	4.88×10^{-5}	0.511	2.178	7.66×10^{-5}	0.803
12.5	2.162	6.76×10^{-5}	0.679	2.165	9.51×10^{-5}	0.956	2.169	1.33×10^{-4}	1.34
13.0	2.153	1.08×10^{-4}	1.05	2.156	1.63×10^{-4}	1.57	2.160	2.30×10^{-4}	2.22
13.5	2.143	1.54×10^{-4}	1.43	2.146	2.39×10^{-4}	2.23	2.150	3.53×10^{-4}	3.29
14.0	2.132	2.56×10^{-4}	2.29	2.135	3.99×10^{-4}	3.58	2.140	5.66×10^{-4}	5.08

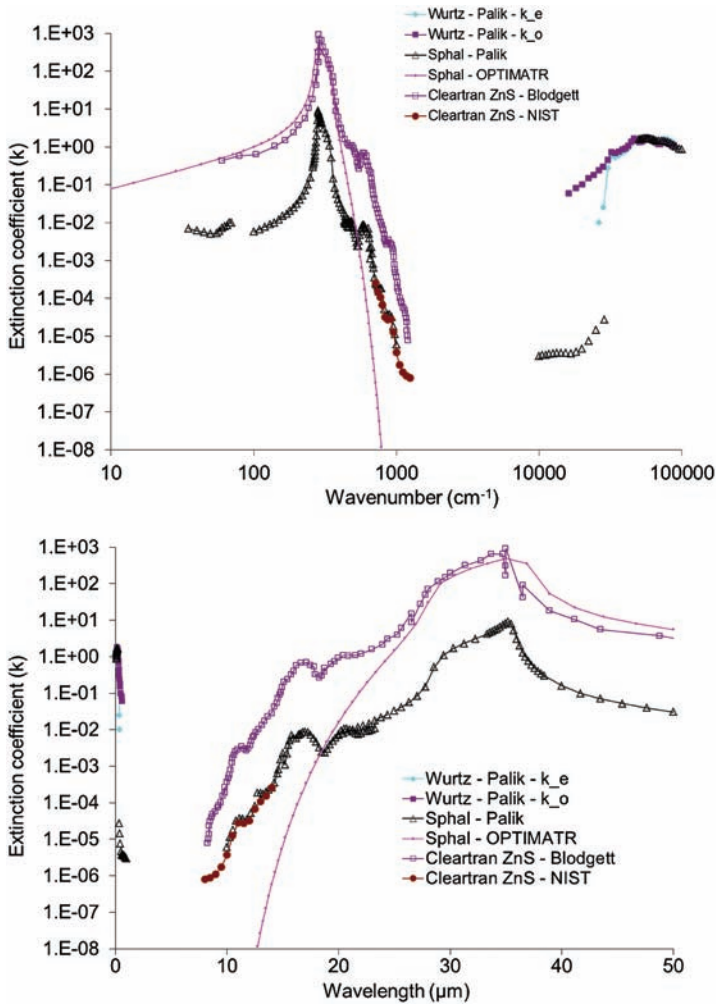

Figure A.7 Extinction coefficient (imaginary refractive index, log scale) versus wavenumber (log scale) and wavelength. Data from Palik[52] (cubic sphalerite and hexagonal wurtzite—ordinary and extra-ordinary), Harris *et al.*[38] (NIST data), Blodgett *et al.*,[66] and model from OPTIMATR.[63,64]

absorption-coefficient values for hot-pressed ZnS (IRTRAN 2) for 2–12 μm wavelengths.

Bulk absorption coefficients for wavelengths in the highly transparent region (~0.5–8 μm) are not commonly available in the literature due to the very small absorptions relative to the scatter typically encountered, especially for standard-grade CVD ZnS. The extinction coefficients k listed are on the order of 10^{-6} for this region,[52] which translates to absorption coefficients ~10^{-1} cm^{-1}, which are too high [note that the absorption coefficient, α in cm^{-1}, can be computed from the imaginary part of the refractive index

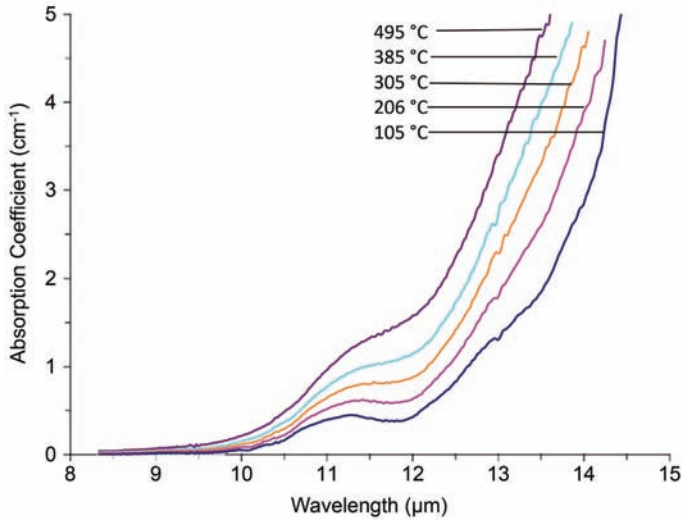

Figure A.8 Experimental absorption coefficient of multispectral ZnS as a function of temperature (data from Blodgett[66]).

(extinction coefficient) k as $\alpha = 4\pi k/\lambda$].[40] Additionally, values reported in Gibson *et al.*[3] vary from 0.03–0.5 cm^{-1} at 5 μm. Bulk absorption coefficients should be ~10^{-3} cm^{-1} and are best measured by careful calorimetric means via measuring emissivity or by laser calorimetry. Touloukian[69] gives values of 0.03–0.06 for ZnS total absorptance at 333 K and wavelengths 3–10 μm, for instance. A summary of solar absorptance, normal spectral reflectance, and normal spectral emittance for ZnS can be found in that reference as well.[69] Klein *et al.*[70] have shown that for the similar material CVD ZnSe, in which there is little bulk scatter and temperature-independent (200–400 K) surface absorption due to defects predominates at wavelengths <8 μm; this surface absorption can be detected up to 14 μm. Bulk absorption in CVD ZnSe is strongly dependent on temperature and wavelength, but its value, even at 10.6 μm, is only 4×10^{-4} cm^{-1}.[70] One might expect comparatively low values of bulk absorption in CVD ZnS in the transparency region (at least up to 8 μm, where multiphonon processes begin to be important for ZnS but not yet for ZnSe). Klocek[68] reports the following absorption coefficients for multispectral ZnS (presumably at room temperature): 1.1×10^{-3} cm^{-1} (2.7 μm), 0.6×10^{-3} cm^{-1} (3.8 μm), 1.1×10^{-2} cm^{-1} (9.27 μm), and 2×10^{-1} cm^{-1} (10.6 μm), in line with the expected ~10^{-3} for the transparency region. Ikeda *et al.*[71] recently reported absorption coefficients for multispectral ZnS at 1 μm and ~1.3 μm of <10^{-3} cm^{-1}, and these authors note that the measured internal attenuation between 0.8–1.5 μm (10^{-2} cm^{-1}) is indicative of scattering-dominated processes and not absorption. It is therefore important to realize that while bulk absorption in multispectral CVD ZnS is ~10^{-3} cm^{-1} in the transparency region,

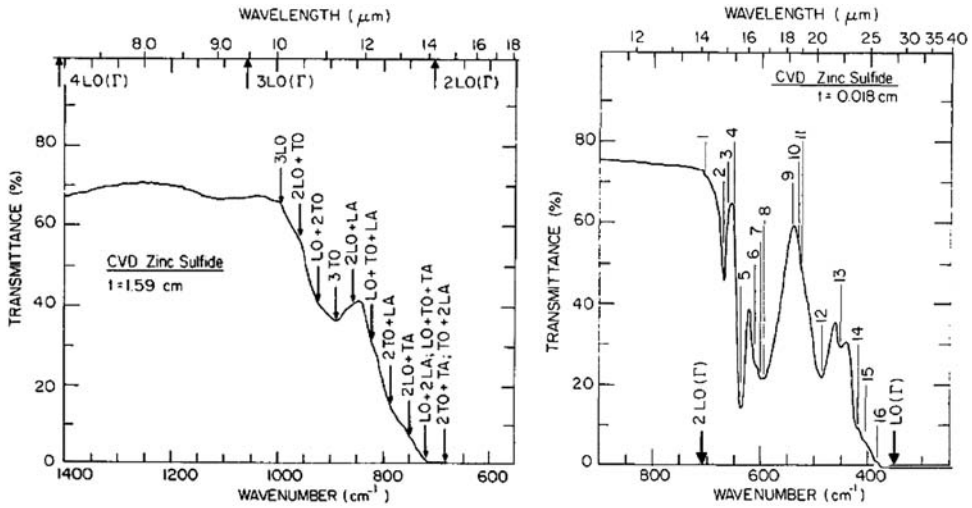

Figure A.9 Transmittance of CVD ZnS and assignment of multiphonon modes. Assignments for #1–16 are shown in Table A.8 (image from Klein[72] used with permission; copyright 1980 by the American Institute of Physics).

the losses (attenution coefficient) are actually much higher, especially below 8 μm, due to scattering.

Palik and Addamiano[52] contains a tabulated summary of optical constants of ZnS across the whole electromagnetic spectrum, including k values. A representation of this data is shown in Fig. A.7. Klein and Donadio[72] assign multiphonon modes (see Fig. A.10 and Table A.8) to CVD ZnS infrared

Table A.8 Assignments for infrared multiphonons in CVD ZnS from transmittance data (from Fig. A.9).[72]

Feature	Type	Measured position (cm^{-1})	Measured position (μm)	Phonon assignment
1	Kink	704	14.20	2LO(Γ)
2	Minimum	668	14.97	2LO(L)
3	Shoulder	662	15.11	$2O_1(W)$
4	Shoulder	650	15.38	LO(X)+TO(X)
5	Minimum	636	15.72	2TO(X)
6	Shoulder	612	16.34	$2O_2(W)$
7	Minimum	602	16.61	$2O_3(W)$
8	Minimum	596	16.78	2TO(L)
9	Kink	544	18.38	LO(X)+LA(X)
10	Shoulder	530	18.87	TO(X)+LA(X)
11	Shoulder	526	19.01	LO(L)+LA(L)
12	Minimum	488	20.49	TO(L)+LA(L)
13	Minimum	450	22.22	$O_1(W)+A_2(W)$
14	Kink	420	23.81	LO(X)+TA(X)
15	Shoulder	406	24.63	TO(X)+TA(X)
16	Shoulder	386	25.91	2LA(L)

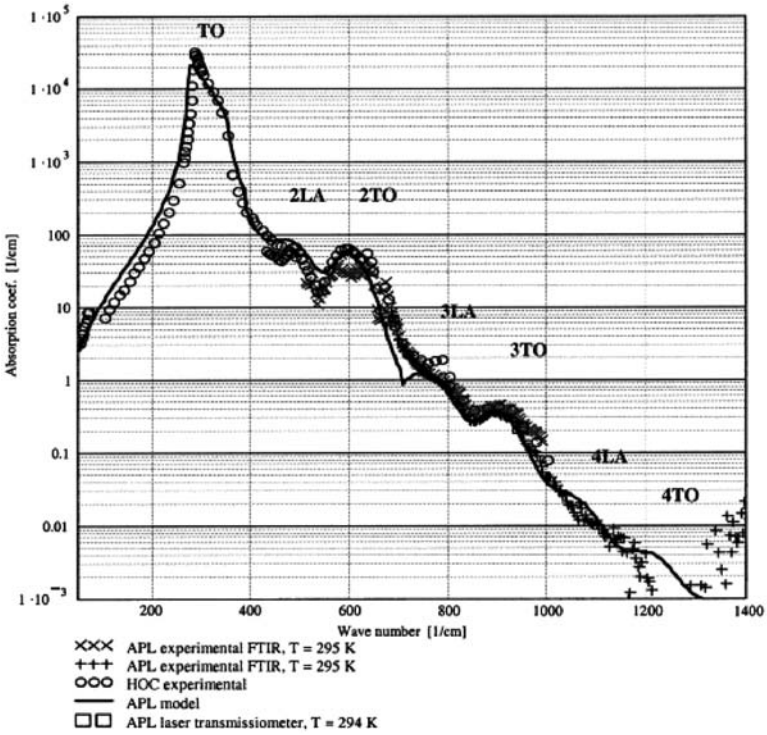

Figure A.10 Absorption coefficient as a function of wavenumber for ZnS with major phonon assignments.[66]

absorption data and find that the characteristic zone-boundary phonon modes are at the following positions: longitudinal optical (LO) = 330 cm^{-1}, transverse optical (TO) = 295 cm^{-1}, longitudinal acoustic (LA) = 193 cm^{-1}, and transverse acoustic (TA) = 89 cm^{-1}. A multiphonon model was generated by Blodgett *et al.*[66] and is shown in Fig. A.10.

On the high energy side, Ozaki and Adachi[59] (1.2–5.6 eV) and Tsuchiya *et al.*[60] (0–20 eV) include real and imaginary permittivity for cubic ZnS along with models.

A.5.4 Dielectric constant

A summary of dielectric constants from the literature is presented in Table A.9. Temperature-dependent measurements of dielectric constant and loss tangent at 35 GHz for CVD ZnS have been measured from 300–700 °C by Ho.[73] Comprehensive dielectric properties of the briefly manufactured British Aerospace CVD ZnS (amber grade, see Ref. 74) was provided by Messiak.[75]

Comparing standard CVD ZnS and multispectral ZnS, Stead and Simonis[76] report a slightly higher dielectric constant and lower loss for the

Table A.9 Dielectric constants of ZnS from the literature.

Material	Frequency (GHz)	Dielectric Constant	Loss Tangent	Test Method	Reference
IRTRAN 2 (Kodak hot-pressed ZnS)	8.5–12	8.0		Not stated	: p. 415
CVD ZnS (Russian)	10^{-6}	11.0	0.075	Capacitance measurement	
CVD ZnS (Russian)	10^{-5} to 10^{-3}	8.5–9.5		Capacitance measurement	
CVD ZnS (British Aerospace Amber)	8–12	8.02		Slotted line, short-circuited waveguide	
CVD ZnS (British Aerospace Amber)	12.5–18	8.23		Slotted line, short-circuited waveguide	
CVD ZnS (British Aerospace Amber)	35	8.39	0.0012	Open resonator	
CVD ZnS (British Aerospace Amber)	94	8.60	0.0024	Open resonator	
CVD ZnS? (stated "polycrystalline," no other information.)	18–40	8.6–8.4	0.0006–0.0012	Cavity resonator	
CVD ZnS (CVD, Inc.)	35	8.347	0.0024	Free-space transmission/ reflection	
CVD ZnS (Raytheon)	94–300	8.352	0.0032	Nondispersive Fourier transform spectroscopy	
CVD ZnS (Raytheon)	100–375	8.384–8.397	0.0018–0.0029	Dispersive Fourier transform spectroscopy	
Cubic ZnS (not stated, presumably single crystal)	0.4	7.9		Not stated	: p. 406
Cubic ZnS (not stated, presumably single crystal)	1000	8.3		Not stated	: p. 406
Multispectral ZnS (Russian)	10^{-6}	9.5	<0.01	Capacitance measurement	
Multispectral ZnS (Russian)	10^{-5} to 10^{-3}	7.5–8.7		Capacitance measurement	
Multispectral ZnS (Raytheon)	Low freq. limit	8.393 ± 0.023		Not stated	: p. 177,409
Multispectral ZnS (Raytheon)	94–300	8.410	0.0021	Nondispersive Fourier transform spectroscopy	
Multispectral ZnS (Raytheon)	High freq. limit	5.105 ± 0.033		Not stated	: p. 409

multispectral grade. A broad frequency range of dielectric constant measurements (100 Hz to 30 GHz), as well as temperature-dependent (25–250 °C) 1 kHz data, were taken on Russian-made CVD and multispectral ZnS.[77] These authors instead found a lower dielectric constant for the multispectral grade (at least at frequencies up to ~700 kHz, which they present). The dielectric-constant results on the Russian CVD ZnS are explained by appealing to a decrease in dangling bonds in nonequilibrium grain boundaries after HIPing.[9,14] These authors corroborate this hypothesis with results from low electron paramagnetic resonance and the observed increase Young's modulus after HIPing.

Recent unpublished research conducted on U. S.-produced CVD ZnS and multispectral ZnS (Rohm and Haas) did not, however, observe the strong frequency dependent results or significant differences between the two grades, contrary to what has been reported by the Russian researchers. Measurements were made by free-space measurement (4–40 GHz) and by impedance analyzer (<1 GHz). Average values for 1 kHz to 1 GHz permittivity for CVD ZnS were 8.789 $\pm$ 0.908 and 8.823 $\pm$ 0.912 for two samples, and values for multispectral ZnS were 9.000 $\pm$ 0.930 and 8.787 $\pm$ 0.908. Average values (transmission and reflection) for 4–40 GHz were 8.467 and 8.376 for CVD ZnS, and 8.419 and 8.333 for multispectral ZnS. It can be seen that there is overlap in the values for the two materials, and lot-to-lot or measurement-to-measurement variability may make them indistinguishable.

A.5.5 Scattering

Bidirectional transmittance distribution function (BTDF) and bidirectional reflectance distribution function (BRDF) measurements have been published for ZnS and multispectral ZnS. Most are in agreement that scattering in CVD ZnSe is dominated by surface scattering (in the strict sense here, from the surfaces to air), whereas scattering in ZnS in any form is dominated by bulk scattering.[66,80] Actual values for BTDF vary significantly. Mellozzi *et al.*[80] says that the scatter in CVD ZnSe is lower than in multispectral ZnS, but more recent measurements by Hahn *et al.*[81] suggest that HIPed ZnS is lower scatter than CVD ZnSe at 633 nm and 3.39 μm. The latter authors calculate scattering coefficients from BTDF data, which for 633 nm are: standard ZnS (10.2–15.8 cm^{-1}), HIPed ZnS (0.03–0.19 cm^{-1}), and CVD ZnSe (0.20 cm^{-1}). Values at 3.39 μm are standard ZnS (0.61–0.99 cm^{-1}), HIPed ZnS (0–0.11 cm^{-1}), and CVD ZnSe (0.03 cm^{-1}).[81] An empirical scattering model has also been offered, where the scattering coefficient is a constant times the wavenumber raised to a power—the constant and the power are fitting parameters to measured data.[66] Other recent scattering data have been presented by Harris *et al.*[38] for multispectral ZnS (BRDF and BTDF and total integrated scatter for 3.39 and 10.6 μm), by McCloy *et al.*[4] for CVD ZnS (BTDF and forward integrated scatter for 3.39 μm), and by Bredikhin *et al.*[82]

for CVD and multispectral ZnS (scattering indicatrix for 0.633 μm). Finally, manufacturers often use "forward scatter" as a production metric for multispectral ZnS. This measurement essentially involves shining a 6328-nm HeNe laser through a sample and measuring the scattered light in a half-cone angle of 3 deg.[83] As of this writing, manufacturer specifications are <6 cm^{-1} (Vitron), ≤ 6 cm^{-1} (II-VI Infrared), ≤ 7 cm^{-1} (Rohm & Haas/DOW), or not specified (Tydex, Rafael).

References

1. McCloy, J. and R. Korenstein, "Variability in Chemical Vapor Deposited Zinc Sulfide: Assessment of Legacy and International CVD ZnS Materials," *Proc. SPIE* **7302**, 73020M (2009) [doi: 10.1117/12.819559].
2. Huie, J., C. Dudding, and J. McCloy, "Polycrystalline Yttrium Aluminum Garnet (YAG) for IR Transparent Missile Domes and Windows," *Proc. SPIE* **6545**, 65450E (2007) [doi: 10.1117/12.719521].
3. Gibson, C. C., D. L. Taylor, and R. H. Bogaard, *Databook on Properties of Selected Infrared Window and Dome Materials*, HTMIAC Report 27, High Temperature Materials Information Analysis Center (HTMIAC), West Lafayette, IN (1996).
4. McCloy, J., E. Fest, R. Korenstein, and W. H. Poisl, "Anisotropy in structural and optical properties of chemical vapor deposited ZnS," *Proc. SPIE* **8016**, 80160I (2011) [doi: 10.1117/12.886138].
5. Morozova, N. K., V. A. Kuznetsov, and M. V. Fok, *Sul'fid tsinka. Poluchenie i opticheskie svoistva* [*Zinc Sulfide: Preparation and Optical Properties*], Nauka, Moscow (1987).
6. Smith, J. F., "Crystallography and Phase Equilibria: A Review: Part II - Space Groups and Structure," *J. Phase Equilibria and Diffusion* **25**(6), 497–506 (2004).
7. Steele, S. R. and J. Pappis, "Chemical Vapor Deposition of IR Materials," F33615-70-C-1577 (1971).
8. Klein, C. A. et al., "Lattice Absorption, Phonon Assignment, and Image-Spoiling Properties of CVD ZnS in the Infrared," *Laser Induced Damage in Optical Materials* (*NBS Special Publication 541*), 86–98, National Bureau of Standards, U. S. Department of Commerce, Washington, D. C. (1978).
9. Shchurov, A. F. et al., "Structure and Mechanical Properties of Polycrystalline Zinc Sulfide," *Inorg. Mater.* **40**(2), 96–101 (2004).
10. McCloy, J., "Properties and Processing of Chemical Vapor Deposited Zinc Sulfide," Ph.D diss., University of Arizona (2008).

11. Klein, C. A. and C. B. Willingham, "Elastic properties of chemically vapor-deposited ZnS and ZnSe," in *Basic Properties of Optical Materials*, 137–140, National Bureau of Standards, U. S. Department of Commerce, Washington, D. C. (1985).
12. Hashin, Z. and S. Shtrickman, "A Variational Approach to the Theory of the Elastic Behaviour of Polycrystals," *J. Mech. Phys. Solids* **10**, 343–352 (1962).
13. Wimmer, J. M., "Mechanical and Physical Properties of Chemically Vapor-Deposited (CVD) Zinc Sulfide," AFRL Report, U. S. Air Force Research Laboratory (1979).
14. Shchurov, A. F. et al., "Effect of Hot Isostatic Pressing on the Elastic and Optical Properties of Polycrystalline CVD ZnS," *Inorg. Mater.* **40**(4), 336–339 (2004).
15. Berlincourt, D., H. Jaffe, and L. R. Shiozawa, "Electroelastic Properties of the Sulfides, Selenides, and Tellurides of Zinc and Cadmium," *Phys. Rev.* **129**(3), 1009 (1963).
16. Henneman, L. et al., "Thermal, Structural and Optical Properties of Multispectral Zinc Sulfide," Proc. 11th DoD Electromagnetic Windows Symposium (2006).
17. Yashina, E. V., "Preparation and Properties of Polycrystalline ZnS for IR Applications," *Inorg. Mater.* **39**(7), 663–668 (2003).
18. Lawn, B., *Fracture of Brittle Solids*, 2nd Ed., Cambridge Solid State Sciences Series, Cambridge University Press (1993).
19. Townsend, D. and J. E. Field, "Fracture toughness and hardness of zinc sulphide as a function of grain size," *J. Mater. Sci.* **25**, 1347–1352 (1990).
20. Lewis, K. L. et al., "The Mechanical Properties of CVD-Grown Zinc Sulphide and their Dependence on the Conditions of Growth," Proc. Electrochemical Society **PV84-6**, 530–545 (1984).
21. Lewis, K. L. et al., "Toughening Effects Induced in Zinc Sulfide by Hot Isostatic Pressing," *Proc. SPIE* **0683**, 64–71 (1986) [doi: 10.1117/12.936417].
22. Rice, R. W., C. C. Wu, and F. Boichelt, "Hardness-Grain-Size Relations in Ceramics," *J. Am. Ceram. Soc.* **77**(10), 2539–2553 (1994).
23. Savage, J. A., K. L. Lewis, A. M. Pitt, and R. H. L. Whitehouse, "The role of a CVD research reactor in studies of the growth and physical properties of ZnS infrared optical material," *Proc. SPIE* **0505**, 47–51 (1984) [doi: 10.1117/12.964625].
24. Evans, A. G. and T. R. Wilshaw, "Quasi-static solid particle damage in brittle solids—I. Observations analysis and implications," *Acta Metallurgica* **24**(10), 939–956 (1976).

25. Kozhinova, I. A. et al., "Minimizing artifact formation in magnetorheological finishing of chemical vapor deposition ZnS flats," *Appl. Opt.* **44**(22), 4671–4677 (2005).
26. Zwaag, S., J. T. Hagan, and J. E. Field, "Studies of contact damage in polycrystalline zinc sulphide," *J. Mater. Sci.* **15**(12), 2965–2972 (1980).
27. Shockey, D. A., D. J. Rowcliffe, and K. C. Dao, "Fracture Toughness of CVD ZnS," Contract N0001-76-C-0657 (1977).
28. Zhang, J. and A. J. Ardell, "Measurement of the fracture toughness of CVD-grown zinc sulfide using a miniaturized disk-bend test," *J. Mater. Res.* **6**, 1950-7 (1991).
29. Yoder, P. L. and J. J. Mecholsky, "Fractographic analysis of chemical vapor deposited ZnS," ADA197394, Pennsylvania State University, University Park, PA (1988).
30. Mecholsky, J. J. Jr., "Grain size effect and toughness in CVD ZnS and HIP'd CVD ZnS," personal communication (2008).
31. Pickles, C. S. J. and J. E. Field, "The dependence of the strength of zinc sulphide on temperature and environment," *J. Mater. Sci.* **29**(4), 1115–1120 (1994).
32. Marshall, D. B., "Failure from surface flaws," in *Fracture in Ceramic Materials: Toughening Mechanisms, Machining Damage, Shock*, A. G. Evans, Ed., 190–220, Noyes Publications, Park Ridge, NJ (1984).
33. Pepi, J. W., "Stress corrosion in ZnS and allowable stresses in glasses and ceramics," personal communication (2006).
34. Pepi, J. W., "A method to determine strength of glass, crystals, and ceramics under sustained stress as a function of time and moisture," *Proc. SPIE* **5868**, 58680R (2005) [doi: 10.1117/12.612013].
35. Cranmer, D. C., S. W. Freiman, G. S. White, and A. S. Raynes, "Moisture- and water-induced crack growth in optical materials," *Proc. SPIE* **1330**, 152–163 (1990) [doi: 10.1117/12.22637].
36. Wahl, J. M. and R. Tustison, "Mechanical enhancement of LWIR materials via coatings," *Proc. SPIE* **1326**, 128–136 (1990) [doi: 10.1117/12.22492].
37. Klein, C., "Flexural strength of infrared-transmitting window materials: bimodal Weibull statistical analysis," *Opt. Eng.* **50**(2), 023402 (2011) [doi: 10.1117/1.3541804].
38. Harris, D. C. et al., "Thermal, structural, and optical properties of Cleartran multispectral zinc sulfide," *Opt. Eng.* **47**(11), 114001 (2008) [doi: 10.1117/1.3006123].
39. Rice, R. W., S. W. Freiman, and J. J. Mecholsky, "The Dependence of Strength-Controlling Fracture Energy on the Flaw-Size to Grain-Size Ratio," *J. Am. Ceram. Soc.* **63**(3–4), 129–136 (1980).

40. Harris, D. C., *Materials for Infrared Windows and Domes: Properties and Performance*, SPIE Press, Bellingham, WA (1999) [doi: 10.1117/3.349896].
41. Taylor, R. L., M. J. Lefebvre, P. E. Price, and M. M. Maderazzo, "Erosion Resistant FLIR Window: Colorless ZnS," F33615-81-C-5076 (1984).
42. Koenig, J. R., "Thermostructural Evaluation of Four Infrared Seeker Dome Materials," TP 6539 Part 2, Naval Weapons Center, China Lake, CA (1985).
43. Artyukh, E. P., L. G. Bochkareva, and F. K. Volynets, "The linear thermal expansion coefficient of condensed zinc sulfide (KO-2) optical ceramics," *Sov. J. Opt.* Technol. **42**(1), 52–53 (1975).
44. Mironov, I. A. et al., "Physico-Mechanical and Structural Properties of Polycrystalline Zinc Sulfide Obtained by Different Methods," *Sov. J. Opt. Technol.* **59**(7), 417–421 (1992).
45. McCloy, J., "International development of chemical vapor deposited zinc sulfide," *Proc. SPIE* **6545**, 654503 (2007) [doi: 10.1117/12.717870].
46. Li, H. H., "Refractive index of ZnS, ZnSe, ZnTe and wavelength, temperature dependence," *J. Phys. Chem. Ref. Data* **13**(1), 103–150 (1984).
47. Mell, Z., "Brechung und Absorption des Lichtes in der Zinkblende bei Temperaturen bis zu 700°C," *Phys* **16**, 244 (1923).
48. Feldman, A., D. Horowitz, R. M. Waxler, and M. J. Dodge, "Optical Materials Characterization," *Natl. Bur. Stand.* (*U.S.*) *Tech. Note* **993**, 63 (1979).
49. Tatian, B., "Fitting refractive-index data with the Sellmeier dispersion formula," *Appl. Opt.* **23**(24), 4477–4485 (1984).
50. Debenham, M., "Refractive indices of zinc sulfide in the 0.405-13-μm wavelength range," *Appl. Opt.* **23**(14), 2238–2239 (1984).
51. Klein, C. A., "Room-temperature Dispersion Equations for Cubic Zinc Sulfide," *Appl. Opt.* **25**(12), 1873–1875 (1986).
52. Palik, E. D. and A. Addamiano, "Zinc Sulfide (ZnS)," in *Handbook of Optical Constants of Solids, Volume 1*, E. D. Palik, Ed., 597–615, Academic Press, New York (1980).
53. Bieniewski, T. M. and S. J. Czyzak, "Refractive Indexes of Single Hexagonal ZnS and CdS Crystals," *J. Opt. Soc. Am.* **53**, 496–497 (1963).
54. Ong, H. C. and R. P. H. Chang, "Optical constants of wurtzite ZnS thin films determined by spectroscopic ellipsometry," *Appl. Phys. Lett.* **79**(22), 3612–3614 (2001).
55. Hattori, T., Y. Homma, A. Mitsuishi, and M. Tacke, "Indices of refraction of ZnS, ZnSe, ZnTe, CdS, and CdTe in the far infrared," *Opt. Comm.* **7**(3), 229–232 (1973).

56. Memon, A. and D. B. Tanner, "Far-Infrared Dielectric Function of Zincblende ZnS," *Physica Status Solidi B* **128**(1), 49–52 (1985).
57. Thamizhmani, L., A. K. Azad, J. Dai, and W. Zhang, "Far-infrared optical and dielectric response of ZnS measured by terahertz time-domain spectroscopy," *Appl. Phys. Lett.* **86**(13), 131111-3 (2005).
58. Dodge, M. J., "Refractive properties of CVD Zinc Sulfide," *Natl. Bur. Stand. Spec. Pub.* **509**, 83–88 (1977).
59. Ozaki, S. and S. Adachi, "Optical Constants of Cubic ZnS," *Jap. J. Appl. Phys.* 32, 5008–5013 (1993).
60. Tsuchiya, T., S. Ozaki, and S. Adachi, "Modeling the optical constants of cubic ZnS in the 0–20 eV spectral region," *J. Phys.: Condensed Matter* **15**(22), 3717 (2003).
61. Rummel, S. P., H. E. Reedy, and G. L. Herrit, "Residual stress birefringence in ZnSe and multispectral ZnS," *Proc. SPIE* **2286**, 132–141 (1994) [doi: 10.1117/12.187335].
62. Qiao, H. A., K. A. Lipschultz, N. C. Anheier, and J. S. McCloy, "Rapid assessment of mid-infrared refractive index anisotropy using a prism coupler: chemical vapor deposited ZnS," *Opt. Lett.* **37**(9), 1403–1405 (2012).
63. JHU/APL, "OPTIMATR," optical materials computer program (1991).
64. Thomas, M. E., *Optical Propagation in Linear Media: Atmospheric Gases and Particles, Solid-State Components, and Water*, JHU/APL Series in Science and Engineering, J. R. Apel and K. Moorjani, Eds., Oxford University Press, New York (2006).
65. Blodgett, D. W., D. Yang, S. C. Walts, and M. E. Thomas, "Measurement of the temperature-dependent refractive index and relative photoelastic constant of zinc sulfide," *Proc. SPIE* **4375**, 224–234 (2001) [doi: 10.1117/12.439179].
66. Blodgett, D. W., M. E. Thomas, D. V. Hahn, and S. G. Kaplan, "Longwave infrared absorption properties of ZnS and ZnSe," *Proc. SPIE* **5078**, 137–147 (2003) [doi: 10.1117/12.487874].
67. Hahn, D. V., M. E. Thomas, and D. W. Blodgett, "Modeling of the frequency- and temperature-dependent absorption coefficient of long-wave-infrared (2–25 μm) transmitting materials," *Appl. Opt.* **44**(32), 6913–6920 (2005).
68. Klocek, P., *Handbook of Infrared Optical Materials*, Vol. 30, Marcel Dekker, New York (1991).
69. Touloukian, Y. S., Ed. *Thermophysical Properties of Matter-Thermal Radiative Properties - Nonmetallic Solids*, John Wiley & Sons, New York (1972).

70. Klein, C. A., R. P. Miller, and D. L. Stierwalt, "Surface and bulk absorption characteristics of chemically vapor deposited zinc selenide in the infrared," *Appl. Opt.* **33**, 4304 (1994).

71. Ikeda, Y. et al., "Zinc sulfide and zinc selenide immersion gratings for astronomical high-resolution spectroscopy: evaluation of internal attenuation of bulk materials in the short near-infrared region," *Opt. Eng.* **48**(8), 084001 (2009) [doi: 10.1117/1.3206734].

72. Klein, C. A. and R. N. Donadio, "Infrared-active phonons in cubic zinc sulfide," *J. Appl. Phys.* **51**(1), 797–800 (1980).

73. Ho, W. W., "Millimeter-wave dielectric properties of infrared window materials," *Proc. SPIE* **0750**, 161–165 (1987) [doi: 10.1117/12.939871].

74. Campbell, A. and C. Hayman, "Manufacturing Aspects of Zinc Sulphide," *Proc. SPIE* **0915**, 79–83 (1988) [doi: 10.1117/12.945544].

75. Messiak, W., "A report on the 5th European EM Windows Conference," 3rd DoD EMD&W Symposium, (1989).

76. Stead, M. and G. Simonis, "Near millimeter wave characterization of dual mode materials," *Appl. Opt.* **28**(10), 1874–1876 (1989).

77. Shevarenkov, D. and A. Shchurov, "Dielectric properties of polycrystalline ZnS," *Semiconductors* **40**(1), 33–35 (2006).

78. Shimabukuro, F. I., S. L. Johns, and H. B. Dyson, "Complex permittivities of IR window materials in the frequency range 18–40 GHz," *Internatl. J. Infrared and Millimeter Waves* **12**(6), 601–609 (1991).

79. Afsar, M. N. and K. J. Button, "Millimeter-wave dielectric measurement of materials," Proc. IEEE **73**(1), 131–153 (1985).

80. Melozzi, M., A. Mazzoni, and G. Curti, "Bidirectional transmittance distribution function measurements on ZnS and on ZnS Cleartran," *Proc. SPIE* **1512**, 178–188 (1991) [doi: 10.1117/12.47160].

81. Hahn, D. V., D. D. Duncan, and D. W. Blodgett, "Imaging Performance of Candidate Longwave Infrared Window Materials," Proc. 9th Department of Defense Electromagnetic Domes and Windows Conference (2002).

82. Bredikhin, V. et al., "Optical losses in polycrystalline CVD ZnS," *Inorg.* Mater. **45**(3), 235–241 (2009).

83. Goela, J. S. and Z. Salihbegovic, "Low scatter, high quality water clear zinc sulfide" CVD, Inc., U.S.A., USPTO 6,083,561 (2000).

Index

John S. McCloy is currently a senior research scientist at Pacific Northwest National Laboratory (PNNL) and the team leader of the Glass and Materials Science Team in the Radiological Materials and Technology Development Group. He received his Bachelor of Science degree from the Massachusetts Institute of Technology in 1996, and his M.S. and Ph.D. degrees (in Materials Science and Engineering) from the University of Arizona in 2007 and 2008. Prior to joining PNNL, he was a senior engineer at Raytheon Missile Systems (Tucson, AZ), where he worked for eight years as a design and manufacturing engineer in the Opto-Mechanical Design department and the Electro-Optics Precision Assembly factory. His specialties included infrared materials, optics and sensor development, cryogenics, and multifunctional electromagnetic materials. In 2008, Dr. McCloy moved to PNNL, where his current research interests are in radiation effects on materials, electrical and magnetic transport phenomena, and chemistry and applications of glasses. His technical expertise is in the area of materials characterization of vibrational, electronic, and magnetic properties of solids, and the processing of transparent ceramic and glass materials. Dr. McCloy has over 50 publications in the open literature and is a member of the American Ceramic Society, SPIE, and Sigma Xi.

Randal Tustison is Principal Fellow and Materials Technology Director at Raytheon Integrated Defense Systems. He has been involved in the development of infrared transparent materials and thin films for much of his career, with a special focus on the development of high-durability infrared coatings and processes for their application to infrared materials like ZnS. He holds a B.S. degree in Physics from Purdue University, and M.S. and Ph.D. degrees in Materials Science and Metallurgical Engineering from the University of Illinois. Prior to joining Raytheon, he was a Research Associate in the Physics Department at the Massachusetts Institute of Technology. He is a member of the American Vacuum Society, where he is past president of the Vacuum Technology Division. He has served on the DoD Militarily Critical Technology Working Group—Optical Materials and is currently on the Industrial Advisory Board of the Center for High-rate Nanomanufacturing and the Executive Advisory Board of the Nanomanufacturing Center at the University of Massachusetts in Lowell, MA. Dr. Tustison is currently Program Committee Co-Chair of SPIE's Window and Dome Technologies and Materials XII Conference (and past editor of volumes VI through XII of the proceedings). He is the author of over 30 publications and holder of twelve patents related to infrared optical materials.